UNIVERSITAT
JAUME·I

Advanced Flow platforms for Sustainable Processes

Diego Iglesias

Supervisors:

Víctor Sans Sangorrín

Marcileia Zanatta

Castellón de la Plana, December 2024

inam
Institute of Advanced Materials
UJI Castelló

Programa de Doctorado en Química Sostenible

Escuela de Doctorado de la Universitat Jaume I

Advanced Flow platforms for Sustainable Processes

Memoria presentada por Diego Iglesias para optar al grado de doctor/a por la Universitat Jaume I

Doctorando	**Directores**	
Diego Iglesias	**Víctor Sans Sangorrín**	**Marcileia Zanatta**

DIEGO|
IGLESIAS|
BERNARDO

Firmado digitalmente
por DIEGO|IGLESIAS|
BERNARDO
Fecha: 2024.12.17
22:02:18 +01'00'

VICTOR|
SANS|
SANGORRIN

Firmado
digitalmente por
VICTOR|SANS|
SANGORRIN
Fecha: 2024.12.18
12:24:26 +01'00'

MARCILEIA|
ZANATTA

Firmado digitalmente por
MARCILEIA|ZANATTA
Fecha: 2024.12.18 11:13:00 +01'00'

Castelló de la Plana, Diciembre 2024

Financiación

La actividad investigadora desarrollada ha sido llevada a cabo gracias a la financiación de los siguientes proyectos:

- Integrating Design Across the Scales (IDEAS). Generalitat Valenciana. (CIDEGENT 2018/036)
- Fabricación Avanzada Para Procesos de Cristalización de Perovskitas (NIRVANA). Ministerio de Ciencia, Innovación e Universidades (PID2020-119628RB-C33).

Agradecimientos

A lo largo de la vida, especialmente en investigación, compartes momentos con muchísima gente. Lo percibas o no, muchos de ellos acaban teniendo algún impacto. Hay veces que es evidente, pero también se quedan pequeños hábitos o gestos que moldean tu forma de hacer las cosas sin que te des cuenta, por lejos que puedan estar haberse ido. Dar las gracias de forma explícita muchas veces se nos olvida en el día a día, muchas veces lo damos por sentado por rutina, pero momentos como sentarse a escribir esto son buen momento para aprovechar; más ahora a final de año, que se siente doblemente cierre.

Empezando por el grupo, donde siempre he estado cómodo. Al "hacer la ciencia", los directores son los que ayudan a colocar los cimientos sobre los que construir tu forma de enfocarla. Muchas gracias a Víctor y Marci por el apoyo, la confianza, la guía, el estar siempre ahí para revisar lo que surgiera en cualquier momento. También muchas gracias a Cristopher y Simone, porque básicamente sin vosotros mucho de esto no hubiera sido posible o hubiera sido muchísimo más difícil. Pero también quiero dar las gracias al resto de compañeros de laboratorio y despacho durante estos años, Ileana, Sara y Gianluca.

Pasando al INAM, quiero dar las gracias por la confianza en al inicio cuando entré, que creo que a la larga ha dado sus frutos. Es un gran lugar para la ciencia, pero también lo que destaca es que también lo es para las personas. Para aguantar todo lo que trae el día a día, que no son pocos los problemas, hace falta un buen ambiente, sea por los laboratorios o en las comidas, y todos estos años he estado siempre cómodo y aprendiendo constantemente de cualquier cosa. En particular hay que dar las gracias a Loles, un pilar fundamental para el instituto, por todo lo que hace por nosotros, su apoyo y consejos. Y a Elena, nuestra directora, por lo pendiente que está de todo y lo mucho que ha luchado.

Ya saliendo de la ciencia, aunque sin salirnos de la UJI, gracias Rubén, María, Elisa y Yasmina por seguir tras tantos años ahí (factorizando), aunque a veces seamos un tanto desastre en regularidad y otras cosas. Y también al sector salonero, que, aunque estemos desperdigados, siempre está bien comentar cualquier cosa o reunirse, aunque sea en medio de la nada rodeados de alcachofas.

Decía antes lo de que muchas veces hay huellas que quedan sin que te des cuenta y con la familia pasa justo eso. Tanto los Iglesias como los Bernardo, los que están y los que hace muchos años que se fueron, puedo ver cosas de como soy que vienen de vosotros, gracias. Y también gracias a los González, que ya son muchos años, he visto a todos los niños prácticamente nacer y crecer, y sé que siempre habrá un hueco para mí. Por supuesto, gracias a mi padre, Ramón, y mi hermana, Marina, por el apoyo y compañía durante toda mi vida, que han hecho posible llegar hasta aquí y, aunque no lo vea, dedicarle esto a mamá.

Paula, te dejo al final porque es difícil concebir esto sin ti, apoyándonos mutuamente en todo momento, creando cosas únicas. Tras cada jornada, lo primero era salir y llegar para verte enfrascada en mil cosas, es prácticamente imposible separarlo, por eso también quería que la portada de este *zine* fuera tuya. El año empezará con esto, pero espero que depare muchas más cosas: Recorreremos las tierras, cruzaremos los mares y surcaremos los cielos, ya sabes como sigue.

“On that day, I bid you remember this… That no matter how far your journey may take you, you stand where you stand by virtue of the road you walked to get there.”

FFXIV. Reflections in Crystal.

Scientific contributions

During the development of the present thesis (thesis by compendium), the results obtained have allowed to publish the following list of research articles that conform it:

1. Alvarez, E.; Romero-Fernandez, M.; Iglesias, D.; Martinez-Cuenca, R.; Okafor, O.; Delorme, A.; Lozano, P.; Goodridge, R.; Paradisi, F.; Walsh, D. A.; et al. Electrochemical Oscillatory Baffled Reactors Fabricated with Additive Manufacturing for Efficient Continuous-Flow Oxidations. *ACS Sustainable Chemistry & Engineering* **2022**, *10* (7), 2388-2396. DOI: 10.1021/acssuschemeng.1c06799. Impact factor: 7.1
2. Iglesias, D.; Tinajero, C.; Marchetti, S.; Roppolo, I.; Zanatta, M.; Sans, V. Multi-step oxidative carboxylation of olefins with carbon dioxide by combining electrochemical and 3D-printed flow reactors. *Green Chemistry* **2023**, *25* (23), 9934-9940, 10.1039/D3GC03360K. Impact factor: 9.3
3. Iglesias, D.; Tinajero, C.; Luis-Gómez, J.; Aranda, C. A.; Martinez Cuenca, R.; Zanatta, M.; Sans, V. 3D printed flow reactors for the synthesis of single crystal perovskites. *Materials Today Energy* **2024**, *39*, 101476. DOI: 10.1016/j.mtener.2023.101476. Impact factor: 9.0
4. Iglesias, D.; Tinajero, C.; Marchetti, S.; Luis-Gómez, J.; Martinez-Cuenca, R.; Fuentes-Ballesteros, J. F.; Aranda, C. A.; Martínez Serra, A.; Asensio, M.C.; Abargues, R.; Boix, P. B.; Zanatta, M.; Sans, V. Digital flow platform for the synthesis of high-quality multi-material perovskites. Under submission. Pre-print. DOI: 10.26434/chemrxiv-2024-7n62r

This thesis has been accepted by the co-authors of the publications listed above that have waved the right to present them as a part of another PhD thesis.

Additionally, the work developed also contributed to the following research articles that are not included in this thesis:

1. Luangwanta, T.; Turren-Cruz, S.-H.; Masi, S.; Das Adhikari, S.; Recalde, I. B.; Zanatta, M.; Iglesias, D.; Rodríguez-Pereira, J.; Gené-Marimon, S.; Martinez-Ferrero, E.; et al. Enabling white color tunability in complex 3D-printed composites by using lead-free self-trapped exciton 2D perovskite/carbon quantum

dot inks. *Nanoscale* **2024**, *16* (21), 10262-10272, 10.1039/D4NR00707G. DOI: 10.1039/D4NR00707G.

2. Julián E. Sánchez-Velandia, Ferran Esteve, Miguel Maireles, Diego Iglesias, Nuria Martín, Marcileia Zanatta, Victor Sans, Francisco G. Cirujano, Eduardo García-Verdugo, One-pot growth of metal-organic frameworks on polymers for catalytic performance enhancement in the CO2 cycloaddition to epoxides, *Journal of CO2 Utilization* **2023**, 78, 102636, DOI: 10.1016/j.jcou.2023.102636.
3. Iglesias, Diego; Haddad, Dina; Sans, Victor; Recent Developments in Process Digitalisation for Advanced Nanomaterial Syntheses. Chemistry Methods **2022**, *2*, e202200031, DOI: 10.1002/cmtd.202200031

Resumen

La presente tesis está centrada en la digitalización de procesos químicos, a base de implementar plataformas automatizadas y tecnologías avanzadas de producción a diferentes casos de estudio. Estos casos específicos pueden ser divididos en dos áreas temáticas: “Nuevas rutas para la mejora de la sostenibilidad de procesos de síntesis”, centrada en la digitalización de rutas sintéticas (Capítulos 3 y 4), y “Desarrollo de plataformas para la cristalización de materiales avanzados, enfocada en el desarrollo de una plataforma digital para la síntesis de materiales cristalinos (capítulos 5 y 6). Las metodologías aplicadas implican la transformación de procesos discontinuos de síntesis en síntesis realizadas en flujo continuo y su mejora tecnológica. Esto requiere el diseño digital de reactores, a base de su modelado usando herramientas de diseño y su producción en el laboratorio mediante impresión 3D, además de herramientas para el control digital y automatización de las plataformas.

El **Capítulo 1** funciona como introducción para presentar los fundamentos que guiaron las decisiones tomadas al enfrentarse a los retos que aparecieron en el desarrollo de la tesis. En primer lugar, hay una introducción general, destacando el interés de la digitalización para crear procesos más sostenibles. Esto es seguido por una presentación de los fundamentos de la química en flujo. Seguidamente, los componentes necesarios para construir las plataformas de flujo se exploran en detalle y, finalmente, los fundamentos para la digitalización de dichas plataformas son presentados. En el **Capítulo 2** se establecen los objeticos de esta tesis. Adicionalmente, los objetivos específicos de cada área temática se presentan.

El **Capítulo 3** abre la sección dedicada a “Nuevas rutas para la mejora de la sostenibilidad de procesos de síntesis”. En esta sección, se desarrollan sistemas que buscan la mejora de las rutas de síntesis con la ayuda del diseño digital y la automatización de procesos. Durante este capítulo, un reactor electroquímico oscilatorio con deflectores se ha desarrollado. El reactor se diseñó con el objetivo de incrementar el transporte de masa a los electrodos durante la transformación electroquímica, mediante la combinación de deflectores y la superposición de un movimiento oscilatorio. El trabajo implicó el desarrollo conceptual preliminar, la evaluación inicial mediante simulaciones computacionales de dinámica de fluidos, la producción mediante impresión 3D y la evaluación experimental final.

El desarrollo de nuevas rutas sintéticas prosigue en el **Capítulo 4**. En él, un proceso de síntesis en flujo se desarrolló para la conversión de olefinas en carbonatos cíclicos (compuestos químicos de valor añadido), en un proceso de dos pasos consecutivos que aprovechaba el dióxido de carbono como reactivo. En el primer paso, la olefina se oxide electroquímicamente a un epóxido, con la meta de mejorar la conversión respecto procesos discontinuos. En el segundo paso, un reactor de flujo se diseño e imprimió en 3D para mejorar el mezclado de la solución que contiene el epóxido y la fase gas en la reacción de cicloadición.

El **Capítulo 5** presenta el concepto de desarrollo de plataformas para la cristalización de materiales avanzados. Durante esta sección, el trabajo se enfoca al Desarrollo de plataformas capaces de producir materiales avanzados con propiedades cristalinas mejoradas. Más específicamente, en este capítulo la Plataforma de flujo se desarrolla para apoyar la síntesis de monocristales de perovskita de alta calidad y tamaño. La combinación de flujo y el reactor impreso en 3D, con el material del cuerpo usado como herramienta para controlar el gradiente de temperatura, se hizo con el objetivo de mejorar la reproducibilidad comparado con la síntesis tradicional. Los cristales obtenidos presentaron mejoras en las propiedades de fotoluminiscencia, indicando mejoras en la calidad del cristal.

A la vista del potencial de la plataforma, durante el Capítulo 6 una nueva versión con mejoras se desarrolló. El método de calentado se optimizó para un mejor control del perfil de temperatura en la cámara de cristalización, la distribución de flujo se revisó para una mayor homogeneidad de concentración de precursores, y un sistema de control de visión se desarrolló para monitorizar el crecimiento de los cristales. Adicionalmente, se demostró como el control digital de la plataforma permite crecer cristales con composiciones variables a lo largo del tiempo sin detener los experimentos.

Finalmente, en el Capítulo 7, las conclusiones más relevantes del trabajo desarrollado durante la tesis se destacan. Cada capítulo de las dos áreas temáticas incluye la correspondiente información experimental y conclusiones más específicas.

Finally, during **Chapter 7,** the most relevant conclusions of the work carried during the present thesis are highlighted. Each chapter of the two thematic areas features the corresponding experimental information and more focused conclusions.

Summary

The present thesis is focused on the digitalisation of the chemical processes, by the implementation of automated platforms and advanced manufacturing technologies applied to different cases of study. These specific cases can be divided in two thematic areas: “New routes for improved synthesis sustainability”, focused on the digitalisation of synthetic pathways (Chapters 3 and 4), and “Development of platforms for crystallization of advanced materials”, centred around the development of digital platform for the synthesis of crystalline materials (chapters 5 and 6). The methodologies applied involve the conversion of batch procedures into continuous flow and their technological enhancement. This requires the digital design of the reactors, by modelling them using computer assisted design tools and their manufacturing onsite using 3D printing, along the use of tools for the digital control of the platforms and automation.

Chapter 1 serves as an introduction that presents the fundamentals that guided the choices made while facing the challenges appeared during the development of the thesis. First there is a general introduction, highlighting the interest of process digitalisation for creating more sustainable processes. It is followed by a presentation of the fundamentals of continuous flow chemistry. Next, the components required for the construction of flow platforms are explored in detail and, finally, the fundamentals of the digitalisation of said platforms are introduced. In **Chapter 2**, the global objectives of the thesis are stablished. Additionally, the specific objectives for the two main thematic areas are presented.

Chapter 3 is the first work of the “New routes for improved synthesis sustainability” area. In this section, systems are developed to improve the yield of chemical synthesis routes with the aid of digital design and process automation. During this chapter an electrochemical continuous flow oscillatory baffled reactor was developed. The reactor was designed with the aim of increasing mass transport to the electrodes during electrochemical transformations by combining baffles and the superposition of an oscillatory motion. The work comprised preliminary concept design, initial evaluation using computational fluid dynamics, its manufacturing using 3D printing and final experimental validation.

The work of developing new synthetic routes is continued in **Chapter 4.** Here, a flow synthetic method was developed for the conversion of olefins to cyclic carbonates (added value chemicals), in a two-step consecutive process that used carbon dioxide as feedstock.

During the first step, the olefin is electrochemically oxidated to an epoxide, with the goal of improved conversion yield compared to batch procedures. In the second step, a flow reactor was designed and 3D printed for improved mixing of the epoxide-containing solution and the gas phase during the cycloaddition reaction.

Chapter 5 introduces the concept of the development of platforms for crystallization of advanced materials. During this section, work is devoted to the development platforms capable of producing advanced materials with improved crystalline properties. Most concretely, in this chapter a flow platform is designed to aid in the synthesis of high-quality and large size perovskite single crystals. The combination of flow and the 3D printed reactor, with the material of the body as a tool for controlling the heating gradient, was made with the goal of improving the reproducibility compared to batch crystallizations of perovskites. The crystals obtained presented also increased photoluminescence properties, signalling improvements over crystal quality.

As the platform showed promising potential, during **Chapter 6** a new iteration with improved features was developed. The heating method was optimized for better control over the temperature profile in the crystallization chamber, the flow pattern was revised for a more homogeneous distribution of precursors, and a vision control system was developed to monitor the growth of the crystals. Additionally, it was demonstrated how the digital control of the platform allows to grow crystals with varying compositions over time without stopping the experiments.

Finally, during **Chapter 7,** the most relevant conclusions of the work carried during the present thesis are highlighted. Each chapter of the two thematic areas features the corresponding experimental information and more focused conclusions.

List of abbreviations and acronyms

3DP: 3D printing

AFM: Atomic Force Microscopy

AM: Additive manufacturing

BPR: Back Pressure Regulator

CAD: Computer Assisted Design

CC: Cyclic carbonate

CE: Counter electrode

CFD: Computational Fluid Dynamics

COBR: Continuous Oscillatory Baffled Reactor

CV: Cyclic Voltammetry

Da: Damköhler number

DLP: Digital Light Processing

DMSO: Dimethyl sulfoxide

DMF: N,N-Dimethyl formamide

DSC: Differential scanning calorimetry

ECOBR: Electrochemical Continuous Oscillatory Baffled Reactor

FEP: Fluorinated ethylene propylene

FFF: Fused Filament Fabrication

GDH: Glucose dehydrogenase

IPA: Isopropyl alcohol

FT-IR: Fourier transformed infrared

HOIP: Hybrid organic-inorganic perovskite

HPLC: High Pressure Liquid Chromatography

HTR: High temperature resin

ITC: Inverse Temperature Crystallization

MAX: Methylammonium halide (X= Br, Cl, I)

$MAPbX_3$: Methylammonium lead (II) halide perovskite

MeCN: Acetonitrile

MFC: Mass Flow Controller

MSLA: Masked Stereolithography

NAD^+/NADH: Nicotinamide adenine dinucleotide

NMR: Nuclear Magnetic Resonance

NRP: Normalized reactor productivity

PBR: Packed bed reactor

PID: Proportional Integral Derivative (temperature controller)

PDMS: Polydimethylsiloxane

PEEK: Polyether ether ketone

PFA: Perfluoroalkoxy alkane

PL: Photoluminescence

PTFE: Polytetrafluoroethylene

Re: Reynolds number

RTD: Residence Time Distribution

SLA: Stereolithography

SLS: Selective laser sintering

STY: Space time yield

TBA.Br/TBA.Cl: Tetrabutylammonium bromide

TBA.Cl: Tetrabutylammonium chloride

TEA.BF_4: Tetraethylammonium tetrafluoroborate

TGA: Thermogravimetric analysis

TRPL: Time-resolved Photoluminescence

THF: Tetrahydrofuran

Tris-HCl: 2-amino-2-(hydroxymethyl)propane-1,3-diol hydrochloride

TPU: Thermoplastic polyurethane

VCA: Vision computing area

WE: Working electrode

XPS: X-Ray Photoelectron Spectroscopy

XRD: X-Ray diffraction

Index

Chapter 1. Introduction

1.1 General introduction

Digital transition is one of the current key challenges of the society. Indeed, one of the main priorities of the European Union is to impulse the digital transformation of its member states, including the training of citizens to develop digital skills, the improvement of the digital infrastructure, and a complete modernisation of the economic system.[1] In this regard, the chemical industry is looking to digitalise the workflows with the aim of improving the processes in all fronts: sustainability, product quality and business model. The goal of the digitalization the chemical process is to achieve production on demand: producing chemicals with tailored properties in the exactly needed quantities, avoiding material waste and generation of stock excess. This requires the development of more robust and reproducible processes, with a higher degree of control over all the parameters.[2] To achieve this, a new series of technologies need to be implemented, and process design thoroughly studied for making the best use of them. The fundamentals and uses of some of these technologies will be explored later in more detail, but now they will be presented as a general concept for illustrating purposes.

One of the key steps is to minimize manual handling of reagents and system setup, as human interaction is a source of variability and is inherently slower than the use of automated, programmable robotic platforms.[3] Therefore, process conditions (concentration, temperature, reaction time, etc.) need to be translated into digital inputs controlled with a computer as executed by a robotic platform. In that sense, the development of microfluidic reactors has grown in interest, as they allow to perform reactions with minimal handling since the reagents are delivered by pumps.[4] Furthermore, they offer improvements in terms of output and great synergy with the implementation of in-line analytics techniques, enabling the monitorization of reactions in real-time, producing data that gives a higher degree of control and insight about intermediate steps and the final product.[5] The transition to continuous flow requires the design of reactors that make the best use of the technology, as mixing is a crucial parameter. The combination of Computer Assisted Design (CAD) and Computational Fluid Dynamics (CFD) allows to adjust the geometry of the reactor and evaluate fluid behaviour or temperature profiles before producing the reactor.[6] Thanks to this, more complex mixing strategies can be developed to improve the mixing between phases, contact with reactor surface in case of advanced functionalities, such as supported catalysts, or transport of species on electrode surface for electrochemical flow reactors. In addition, validated reactor geometries can be fabricated on-site using additive manufacturing, also known as 3D printing (3DP), in an easy rapid way, also allowing to produce geometries that would be impossible with traditional manufacturing technologies.[7]

Using all these tools, integral flow digital platforms can be developed. In first place, selected reagents, their concentration, along with reaction conditions, would be introduced via a digital interface. Next, the platform would adjust all the settings to match the required conditions and run a set of experiments, where products would be automatically collected, along a corresponding a set of data of final product and mid-process information. In this sense, inputs (reagents, reactor geometry, reaction conditions, etc.) could be correlated with outputs (product yield, particle size, physical properties, etc.) for better understanding of the process and finding the best conditions.[8] Further developments can use the generated datasets, or publicly shared data, to a full automation of the process integrating machine learning. In this case, a set of target properties can be selected and the platform would run experiments, setting up different inputs until the desired output is obtained.

In this thesis, our efforts to apply these concepts to explore new production methods in the context of sustainable chemistry will be presented. Chemical industry has a critical role in the accomplishment of climate objectives, not only for producing new and improved materials, but also because it needs to transform itself by making the processes more sustainable. Indeed, by the start of the decade it was responsible of 20% of global energy consumption and carbon dioxide (CO_2) emissions.[9] The aim should therefore be to contribute to the decarbonization by finding more energy efficient productions techniques, implement renewable energy sources, and the electrification the processes (with technologies like electrochemical synthesis routes or indirect heating).[10] Chemical waste and gas by-products, like CO_2, have to be reduced by finding more chemically efficient routes, alternative feedstocks or synthetic pathways. Alternatively, routes that recycle them to be used as feedstock for other syntheses may be researched. Additionally, the potential of materials for sustainable applications, like solar cells or electrochemical electrodes, needs to be further developed. Not only by enhancing the properties of the materials for the final applications, but also improving the sustainability of their obtention process, and enabling the scaling up for the global implementation. The methodologies developed during this thesis aim to contribute to the transformation of the chemical industry according to these guidelines.

1.2 Continuous flow chemistry

Batch reactors have been the more prevalent synthetic technology in industry.[11, 12] Reagents are loaded into a reactor, generally flasks at laboratory scale or stirred tanks in the industry, and under appropriate conditions they transform into products. Once the reaction has occurred, after what is known as reaction time, products are collected from the reactor and they must be separated from undesired compounds to proceed to the next step.[13] Despite their relevance, batch reactor may present issues with reproducibility and scalability of processes, mainly related to inhomogeneous distribution of species and temperature profiles in the reactor due to inefficient mixing.[14] This derives into variability of reaction kinetics over different locations of the reactor, with phenomena such as the formation of hotspots or points with lower interaction between phases, and as reactor scale increases this becomes more relevant issue. In the case of the synthesis of advanced materials, this is especially relevant, as their final properties are highly dependent of particle size and shape, something directly related to synthesis conditions.[14] Ultimately, a high degree of control over reaction parameters is crucial in order to avoid unreliable synthesis processes that waste resources. Furthermore, the processing time is inherently long, when the loading, temperature ramps, discharging and cleaning steps are factored in.[15]

Continuous flow processes have become of interest for the industry as solution for these matters, modernise the processes and improve overall efficiency. The broad concept of flow chemistry involves a continuous introduction of reagents and removal of products from a reactor where a transformation happens. The relationship between the flow rate and volume of the reactors is used to determine how much time the reaction mixture stays inside the reactor, in what is known as *residence time*.[16] Considering this, reaction time can be directly correlated to physical position within the reactor.[17] It should be noted that even though the use of continuous-flow reactors has been a standard on the chemical industry for decades,[12] the current use of the term *flow chemistry* mainly refers to processes that take place in small setups at laboratory scale.[18] These *flow reactors* are commonly under the millimetre range, in what is known as the domain of microreactors, albeit many principles can be also applied to reactors at the millimetre scale, also referred as mesoreactors.[19] Future developments on reactor designs aim to bring the benefits associated to microfluidics, that will be next discussed, to larger scales.

The first example of a microfluidic device is attributed to a micro-gas chromatography system developed in 1979 for gas detection, a simplified schematic can be seen in Figure 1. Thanks to photolithography, a capillary column was fabricated over a silicon substrate with a detector chip.[20] After this, during the 90s, as new tools that allowed the control and analysis of fluids in small scale appeared, the interest of developing total chemical analysis systems or *labs on a chip* grew.[21] These techniques saw a rapid development in the biological field, especially in DNA sequencing during the research of the human genome, using glass as building material.[22] Also, during this time, the first developments of applying the principles of microfluidics to flow synthesis appeared, revealing the first signs of advantages over traditional systems that will be later discussed.[23, 24] During the 2000s, polymers emerged as an alternative for fabricating reactors, and polydimethylsiloxane (PDMS) became a fundamental material for the development of microfluidic devices, first in biology[25] and eventually in chemistry,[26] although it presented compatibility issues with some organic solvents. During the last decades, microfluidics has experienced continuous developments, being applied to many different chemical processes and even industrial applications. New technologies, such as 3DP, have emerged and its application to the production of microreactors aims to further improve the field by enabling the development of new geometries for its scale up. Furthermore, 3DP is an useful asset for the rapid development and production on-site of prototypes, reactors or elements for bespoke flow chemistry systems.[27]

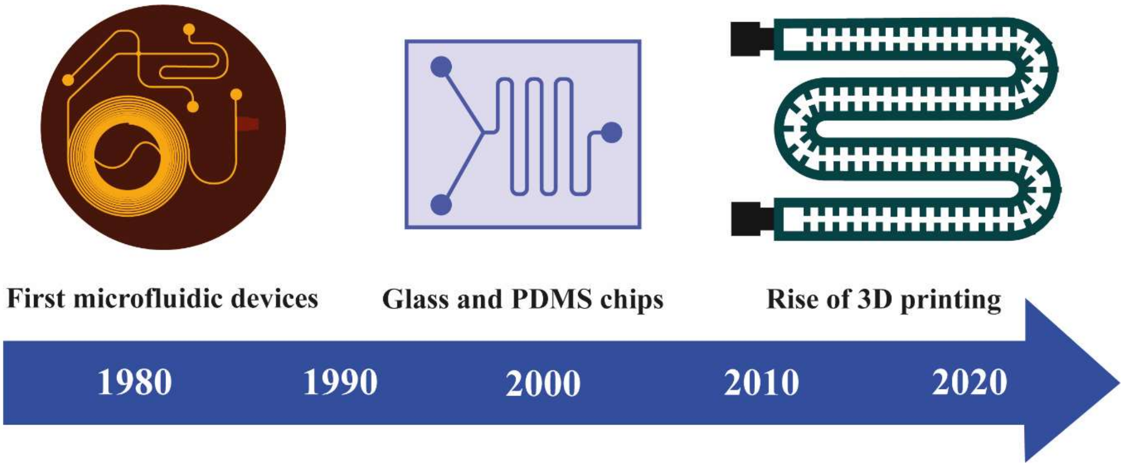

Figure 1. Timeline of the evolution of microfluidic devices.

Flow reactors present several advantages over batch due to their higher surface-area-to-volume ratios, the most notable being improvements in temperature control through enhanced heat transfer ability and mixing. The small cross sections of microreactors allow to decrease the heat transfer resistance, accelerating the heat control over the process and making temperature distribution more homogeneous, preventing the formation of hotspots that may derive into alternative reaction pathways yielding undesired products.[28] In microreactors, as flow regime is mainly laminar, mass transfer of species is controlled by diffusion, thereby an smaller channel size favours the contact between different species. However, friction between the fluid and the walls may cause differences in the velocity profile between centre and wall contacting areas, and, as scale increases, inhomogeneities may be more prominent.[19] To solve this, additional rapid mixing features can be implemented via reactor design, something that will be discussed in a later section. Additionally, flow reactors have been used for the synthesis of crystalline materials, as the described qualities can also play a role in the morphology of grown crystals,[29] particle size distribution[30] or their physical properties.[31] Overall, the benefits of flow chemistry include a higher degree of control over the synthesis process, creating a more homogeneous environment that enables higher selectivity toward desired products by reducing side reactions or low-quality products.

Flow chemistry makes it possible to carry out reactions in extreme conditions that are not possible in standard laboratory equipment, like reactions at high temperatures and pressures to accelerate kinetics that were not feasible in batch.[32] Indeed, this also enabled the development of flash chemistry, where it is possible to follow chemical pathways that make use of unstable intermediates, with lifetimes lower than a second or even in the order of milliseconds, before they decompose.[33] Another advantage of flow chemistry is safety. The reduced scale of flow reactors, and the concealed nature of the setups, makes the processes safer (especially exothermic ones), as the quantity of hazardous materials present during the reaction is lower and the risk of leakage is decreased.[32] There are synthetic routes generally discarded by the industry due to the requirement of hazardous intermediates and/or conditions, but flow setups allow to perform them in a safer environment. For example, persulphuric acid is a powerful oxidant that can decompose explosively, and thus its storage always supposes a risk. It is produced by the reaction of sulfuric acid with hydrogen peroxide, so a flow process can be designed for its generation onsite by mixing streams of both precursors and mix the resulting stream with the main reaction flow. By adjusting the stoichiometry, the produced persulphuric acid can be fully consumed minimizing the risk.[34] In the case or processes handling gases, the increased safety opens the possibility of using higher pressures that aid in the dissolution of gases into the mixture. Hazardous compounds, such as pyrophoric chemicals, can also be used more safely, and other air sensitive chemicals that can be used without the risk of degradation.[35] The improved heat control also reduces the risk of accidents caused by uncontrolled heating of the reaction mixture.[36]

Another characteristic that makes flow chemistry desirable is its potential for scaling up reactions. As stated previously, batch synthesis presents problems when scaling up, due to inhomogeneous mixing and the rapid increase of energy costs with scale.[37] In contrast, flow setups present different strategies for scaling up production. One option could be the increase of the section of the reactor, but as reactor lateral dimensions surpasses the millimetre scale there is the risk of confronting the same problems that exist in batch unless mixing strategies are implemented.[14] Another option is to connect multiple modules of the same reactor in series while proportionally increasing the flow, with the result of having the same residence time but producing a higher yield of product per unit of time. An additional strategy is the numbering-up the reactors, that consists of dividing the flow into multiple channels that run the reactions in parallel.[38] Even though this presents issues in the matter of having control over flow distribution, there are reports signalling that is possible to have up to 64 simultaneous channels via thoughtful reactor design.[39] Furthermore, once the system has achieved steady state conditions (usually considered as having pumped a minimum of 1.5 residence times), products could be obtained for an indefinite time considering starting solution is replenished and the integrity of the components is not compromised.

From a process point of view, the possibility to make consecutive reactions, with no need to isolate intermediate products, with the corresponding reduction of chemical storage, and no downtime, makes flow chemistry very desirable. However, the engineering challenges in the microscale are different from batch reactions, and possible drawbacks need to be considered when designing processes.[12] For example, as flow chemistry is mainly done in solution, the handling of solids adds another layer of complexity. One of the subsequent main issues is the clogging of channels, something that could be caused by either the use of slurries for delivering solid precursors, the accumulation of solid products (nanoparticles, crystals, polymers, precipitates, etc.) along the reactor path and walls or the precipitation of undesired species.[40] Depending on the system, different solutions have been developed such as sonication, the addition of anti-solvents[41] or the development of an agitated cell reactor.[42] Another important point is that transitioning a particular synthesis from batch to flow is non-trivial, as the search of new compatible conditions can be time consuming. In this regard, the automation of syntheses, along the implementation of design of experiments or self-optimization algorithms, can highly reduce the number of experiments required, and thus, resources for finding better conditions.[43] However, even after considering this, not all the reactions necessarily benefit from flow: slow processes that cannot be accelerated by heating or mixing are sometimes better handled by batch, especially if the industry already has the know-how for achieving an acceptable yield.[44] Therefore, the main agents currently looking for the transition into flow are industries with high added value products that justify the allocation of resources into this change. The pharmacological industry has great interest, as their products require a great number of reaction steps with their respective workups and separations, and advanced material industry looks for strict control of conditions for reproducible material properties.[45]

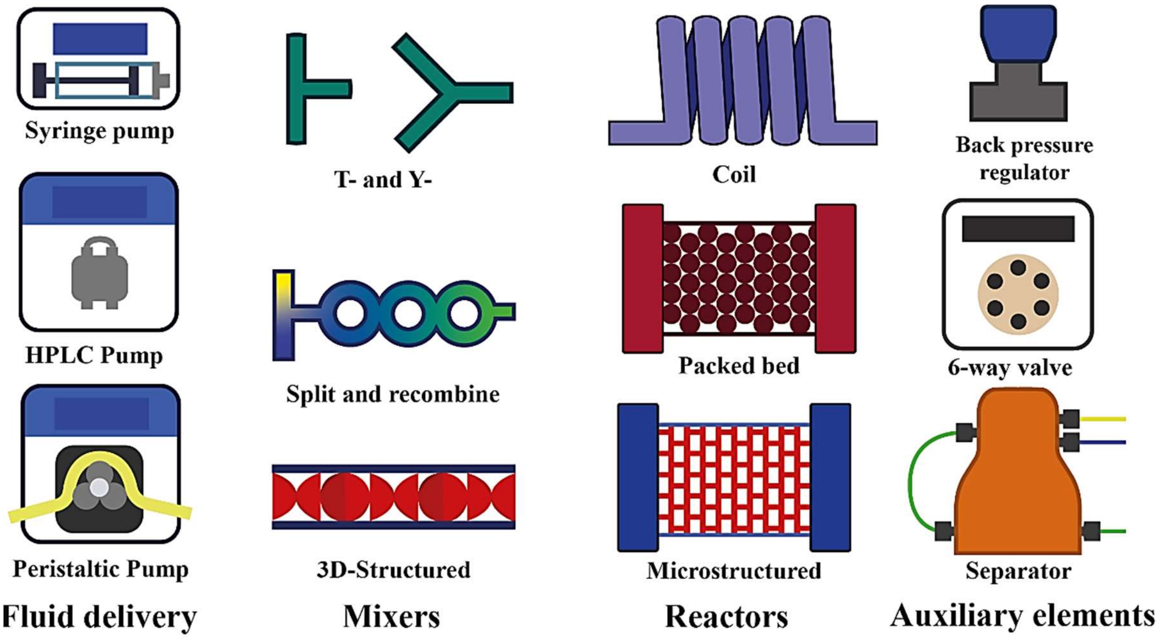

Figure 2. Schematic of different elements used in flow platform setups.

1.3 Design of flow platforms

A flow setup is constructed by arranging a series of components, each one having a different function, with the final goal of producing a transformation from initial reagents to a desired product. The most basic elements include a pump that is going to deliver the initial reagents, a reactor where the transformation will take place, and something to collect the end product. Even though a universal flow platform does not exist, the modularity of flow setups allows to tailor systems to the needs of every process in order to obtain the bests results. Figure 2 illustrates a collection of elements that can be used for construct flow setups, but the list of possible components is far greater and constantly growing. During this section, different components that conform the flow setups developed in this thesis will be explored in more detail.

1.3.1 Fluid delivery

Pumps are the motor of the flow setup; they provide the energy for moving fluids throughout the system. Depending on the phases to be delivered, the flow rate or the accuracy, different pump types should be selected. The following section collects the most used types at laboratory scale.

High pressure liquid chromatography (HPLC) pumps. Based on pistons connected to driving cams that are rotated by a motor offering a stable delivery of liquids at flows above 0.05 ml min^{-1}.[18] HPLC pumps are not suited for gas delivery, and even the presence of gas bubbles can harm the components. Low boiling points solvents such as acetone or tetrahydrofuran also present risks during their pumping, but it's possible to overcome it by degassing or implementing back pressure regulators (BPR) for avoiding boiling.[46] Taking this into consideration, HPLC pumps have been used with great success in a wide variety of processes thanks to their robustness. For example, with the aid of BPRs, Ley's group was able to dissolve CO_2 into a THF stream and successfully use them in the multistep synthesis of carboxylic acids. Reagents, including acid mixtures, were delivered at different steps thanks HPLC pumps, and purification was made downstream by including specific columns.[47] Overall, this illustrates how flow can be use in the synthesis of chemical products in a safer way. Alternatively, flow can have an influence in the crystallization process, therefore, properties of advanced materials synthesized in flow may differ from the ones made in batch, paving the way to obtain properties previously not easily obtainable. Part of the research of the Material for Advance Sustainable Production group (MASP) has been devoted to exploring this. For example, different HPLC pumps were used for combining precursors and antisolvent in for the crystallization of Sn (II)-based perovskite microcrystals. Flow rate was found to have a direct effect in crystal structure, stability and photoluminescent properties of the synthesized materials.[31]

Syringe pumps. They are generally composed of a syringe and mechanical actuator. The plunger of the syringe is mechanically displaced, therefore, volume delivered is correlated to the number of steps the motor moves. They are intended for applications when an accurate non-pulsed delivery at lower flow rates is required, mainly liquids, but the main disadvantage is that the syringe limits the maximum volume delivered until the pump needs to stop and reload. To circumvent this, two alternating syringe pumps can be used, so when the first one is emptied a second one is ready to deliver while the former one reloads. Another option consists in using the syringe pumps to load sample loops and "sandwich" the reaction sample between plugs of carrier solvent. This is used in processes that require small amounts of sample, like the evaluation of synthesis conditions for pharmacological compounds,[34] though the user must be aware that not all introduced sample might react under steady state conditions.[8] Syringe pumps have been applied in diverse applications, including organic synthesis,[48] electrochemical reduction of CO_2[49] or advanced material synthesis.[50, 51] They have also found applications as a way to introduce gas bubbles[52] (albeit other methods are more accurate) or oscillations within the flow for improvement of mixing in what is known as oscillatory reactors.[7, 53] Also, they can be used to inject a defined amount of a tracer substance for its monitoring during the performance of residence time distribution (RTD) studies, an important tool in the characterization of the mixing within a reactor that will be discussed later[7]. Another interesting property of syringe pumps is the possibility of easily programming movement sequences, something that makes them highly interesting for the development of automated flow platforms.[54, 55] Syringe pumps can even be constructed in-house with easily available parts and 3D printing for producing low cost fluid delivery devices.[56]

Peristaltic pumps. They feature a central rotor with a series of cylinders that compress a flexible tube, the substances present in the compressed area are forced to move forward, and thus they exit the tube while new reagents are introduced. As a downside of their design principle, peristaltic pumps can show noticeable flow pulses. Additionally, the material of the tubing needs to be carefully selected, since it has to be flexible while maintaining chemical compatibility, something that can be rather limiting.[41] Nevertheless, developments of new materials, like fluoropolymers, have allowed peristaltic pumps to be a robust option that can deal with viscous fluids and aggressive species, including organic solvents, organometallic compounds or even strong acids and bases.[57] Most noticeably, the pulsing nature of the pumps can be used beneficially for dealing with solids, as sedimentation or clogging can be minimized. They have also found application in organic reactions, when reagents or products have low solubility in the chosen solvent or in case oversaturated feedstocks are used, to pump the slurry without clogging issues.[58] Peristaltic pumps can also be applied to flow crystallization processes, as the aim is to generate a solid starting from a solution,[59] or in the synthesis of nanoparticles.[60] Recent developments have also found use of peristaltic pumps as gas delivery systems for low-pressure applications.[61]

Mass flow controllers (MFC). A key tool for the accurate delivery of gases. These devices consist of small section tube featuring two thermometers and a heating element, when a flow of gas is applied, a difference of temperature between the two points is generated and mass flow rate of gas can be calculated.[62] Each unique gas has a specific heat capacity value; therefore, they can be specifically calibrated to their implementation in a wide array of processes. MFCs have seen great use as a way to accurately introduce gas reagents instead of directly connecting the system to a gas pressure regulator. They have seen great application in organic reactions, highlighting the use in intermediate steps of long pharmacological synthesis routes. Kappe's group has developed a great number of works exploring multistep syntheses of pharmacological compounds, sometimes featuring MFCs for a precise delivery of gases. Some examples include the difluoromethylations employing fluoroform,[48] with the final goal of the synthesis of a treatment of the sleeping sickness, or hydrogenations mediated by an organometallic catalyst,[63] for a precursor of a treatment for asthma. MFCs can also be used as a tool for introducing an inert gas, generating a segmented gas-liquid flow that promotes mixing within each liquid plug.[64] In specific cases, the same gas that promotes internal mixing in the liquid sections can also serve as reservoir of reactive gas, either in organic reactions[61] or nanoparticle synthesis,[30] that slowly doses it into the reaction mixture.

1.3.2 Mixers

In continuous flow processes it is essential to achieve efficient mixing to prevent that heat and mass transfer limitations reduce the process efficiency in terms of conversion, yield or selectivity. The distance a molecule travels increases with the square root of time; this means that at higher volume reactors transport of species is greatly decreased.[9] In batch processes, additional means to promote the interaction between species are required, since the interaction by diffusion is highly unlikely due to the big distances. This is generally achieved by mixing by mechanical means, such as magnetic stir bars at laboratory scale or propeller blades at industrial scale.[12] In micro- and meso- fluidic reactors, due to the reduction of scale, interaction by diffusion is more feasible and additional mixing elements might not be required. In case of reactions that required additional mixing, some strategies can be implemented before the mixture enters the reactor or directly in reactor design.

The Reynolds number (*Re*) is used to characterise flow patterns.[65] This dimensionless module correlates the inertial and viscous forces interacting during the flow process. In microfluidic setups, flow generally follows a laminar regime, linked to low *Re* values. This means, that fluid is divided into infinite parallel layers that move through the reactor, as seen in Figure 3. In these cases, mixing would only occur at the frontier between layers due to molecular diffusion and, hence, the high surface area to volume ratios of microreactors are directly linked to improvements over mixing.[35] On the other extreme, at higher *Re* values, there is turbulent flow, characterised by the presence of vortices and other phenomena that increase the chaos within the flowpath.[66] At sufficiently high flow rates, an also in the presence of elements that can disturb the path, turbulences in the flow can improve the mixing between species. In the case of mixing different streams, flow paths can be easily connected by using T- or Y-mixers leading into a merged stream. Depending on the process kinetics, this could be sufficient to achieve a homogeneous distribution under low *Re* values. Alternatively, when the reactions are kinetically fast or highly exothermic, the reactors require more efficient mixing for the reactions to occur safely and efficiently. In this case, mixers with flow paths containing obstacles, curves or restrictions that induce the generation of vortexes can be implemented.[67]

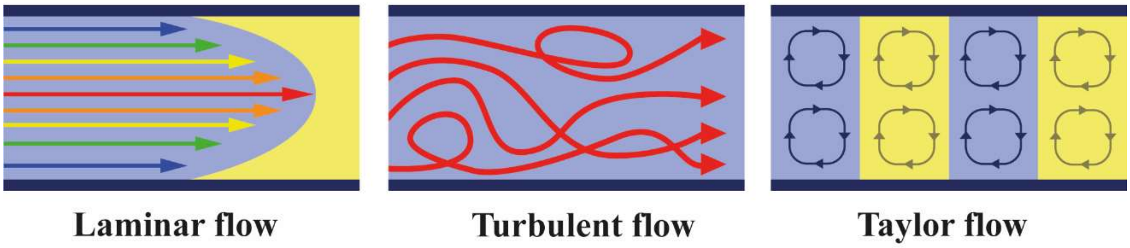

Figure 3. Different flow patterns.

Another strategy to improve mixing is to introduce secondary patterns within the flow. There are many different patterns that can be generated according to the mixer design and the relative flow rates between the different phases. One of the most remarkable ones is slug flow, also known as Taylor flow, produced by introducing perpendicularly a secondary phase into the stream, either a gas or a liquid.[68] This is done by using T-shaped mixers that result in a segmented flow where both fluids are alternating along the tubing. The formation of segments promotes vortexes that cause the recirculation of species within each of the individual fragments, increasing the mass transport and contact between slugs, as illustrated in Figure 3. This can be used either for reactions between two liquids[69] or gas and a liquid.[30] Another application of this principle is the simple addition of an inert gas to generate vortexes that enhance the mixing within the liquid plugs. This increases the yield in chemical reactions, can ensure a uniform particle growth[64] and individual droplets can even be used to run different reaction conditions for screening using a minimum amount of reagents.[43] Indeed, a really fine tuning of the mixing of plugs of solution containing material precursors, an immiscible oil, and a gas has been shown to control independently the stages of nucleation and growth of palladium nanoparticles.[60]

In order to evaluate the resulting mixing one of the most relevant tools are residence time distribution (RTD) studies[8]. In an ideal reactor, all the individual particles would have an equal residence time. However, due to causes like the generation of preferential flow paths, mixing between phases or interaction with the environment, time of residence is not homogeneous. Generally, studies are performed by injecting a tracer in the system and monitoring its concentration over time, yielding the residence time distribution function $E(t)$. Considering this, tracers must be chosen in a way they can be monitored with techniques, like UV-VIS absorption, and their behaviour within the reactor must be representative of the actual reaction mixture.[16] RTD studies are used to characterize flow patterns of the mixers, reactors, diagnose problems, compare different systems[70] or even correlate them with parameters such as conversion or dispersity of final properties.[71]

1.3.3 Reactors

Reactors are the core element of the system, where a transformation takes place under the appropriate conditions. Initial microfluidic reactors took the shape of chips made in glass or PDMS, simple tubing (in materials such steel or silica) or machined metal blocks. Even though these examples already highlighted the benefits of working at microfluidic scale, these designs sometimes lacked flexibility to be used in processes requiring fast mixing.[72] Nevertheless, chip reactors have still seen further developments, like their application in photochemistry making use of their transparency,[73] and tubing reactors remain a really useful asset in the flow chemistry toolbox thanks for their simplicity to be implemented into any setup.[18] Depending on the requirements of reactions, previously discussed mixers installed prior to the coil or chip could be sufficient for achieving a good reaction rate. Otherwise, mixing during the reaction should be carefully studied, and for a more detailed analysis the Damköhler number (*Da*) is used. This dimensionless number serves to characterize the reaction rate relative to mass transport, and is given by Eq. 1.[74]

$$Da = \frac{\chi d_t^2}{4\tau D} = \frac{Reaction\ rate}{Diffussion\ rate} \qquad \text{(Eq. 1)}$$

Where χ is related to reagent concentration and reaction rate, d_t is channel width, τ is related to mixing time and D is the diffusion coefficient. If $Da<1$, transport of species is faster than the reaction, and therefore process is limited by reaction rate. If $Da>1$, the reaction is faster than the mass transport over the reactor, and hence diffusion is limiting the process so concentration gradients could be generated.[74] In slow reactions, usually, *Da* will be lower than 1, meaning that just the use of a coil reactor or implementing T- or Y- mixers before the entrance could be sufficient. Whereas in faster reactions, mixing rate needs to be improved to avoid limitations by mass transport, therefore, reactor needs to be redesigned with more advanced mixing strategies. These strategies include the use of a segmented flow (previously discussed in the mixer section), the addition of passive mixing structures in the reactor flowpath or the use active mixing techniques.

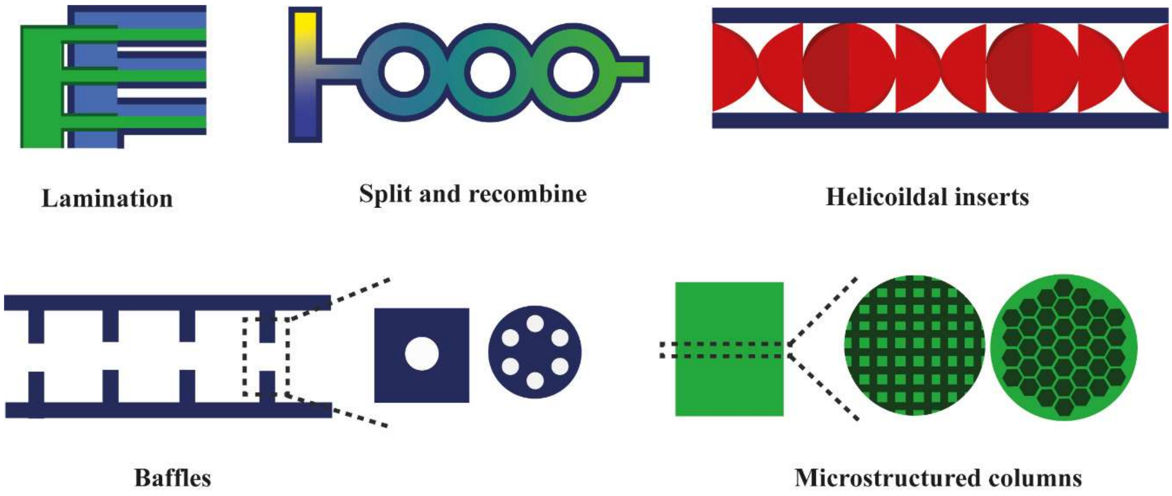

Figure 4. Different geometries designed for improved mixing.

There is a great number of possible geometries for improving mixing in microfluidic devices, but Figure 4 shows only a few examples. The most laminar-like approach to improve mixing is the split of the streams in many thin films, what is known as lamination. As diffusion is directly related to distance, by laminating and interlocking two different flow streams is possible to improve their interaction.[75] Just from transitioning from a straight line to a more sinusoidal path there could already be improvements over mixing, thanks to the sharp turns along the flow channel.[76] Another methodology of mixing is the use of split-and-recombine reactors, where the geometry forces the flow to be divided and merged, greatly increasing the interaction between streams, and, at higher Reynold numbers, vortexes can be generated due to the collision between streams.[77] Indeed, different strategies can be used in tandem in a single reactor. For example, Jensen's group developed a chip containing multiple heart shaped elements linked by thin nozzles, where the fluid has to split, follow heart shaped curves and recombine in a really thin space.[78] The previous examples were intended for 2D flow paths, but these strategies or analogous can also be applied to three-dimensional movements. Akin to the sinusoidal flow, in flow paths that follow an helicoidal shape, the swirling move can generate chaotic advection,[79] and if different helicoidal channels split and recombine continuously mixing can be further enhanced.[80] Different microstructures can be designed to generate more intricate flow paths in the three dimensions like helicoidal inserts,[67] honeycomb structures[81] or periodic structures such as gyroids.[82] The generation of complex 3D microstructures has great potential for development, but its fabrication was rather limited compared to 2D chips. Nevertheless, thanks to rapid development of 3D printing, that will be later discussed, interesting 3D structures are being studied. The MASP group has focused part of its research in the development of 3D reactors with improvement mixing capabilities like column reactors with internal grid motifs[83] or helicoidal channels featuring obstacles.[61]

Alternatively, in active mixing, an external actuator causes some perturbation in the fluid that results in enhanced mixing. The nature of the tools used for this are really diverse, like acoustic waves that generate vortexes by inducing oscillations in piezoelectric transducers or generating gas bubbles.[84] Ultrasounds can be used not only to reduce clogging of channels by resuspending solids, but also generate cavitations that produce agitation within the flow channels.[85] Working at the microscale also opens the window to more unique mixing methods like electrokinetic instabilities, that are generated by passing a flow that presents an electrical gradient (like two different streams) under an electrical field.[86] Interestingly, passive and active mixing can be combined like in the case of Continuous Oscillatory baffled reactor (COBR). In this case, the reactor structure features baffles that can generate chaotic advection by themselves, and, while the fluids are pumped through the reactor, an additional oscillatory pulsation is imposed into the flow. This results in a net flow towards the exit while, at the same time, it’s being subjected to a back-and-forth movement through constrictions that causes a recirculation of the flow, and may enhance the generation of turbulences at low values of Reynolds number[7]. In COBRs, mixing is product of the oscillatory motion, not the net flow, therefore more compact reactors can be developed and they have seen development in applications such as crystallization[53] and organic synthesis.[87] They present great potential for future developments, for example, in electrochemistry, as they enable the scaling of channel size up to multiple millimetres while retaining benefits of microfluidics.[88, 89] Alternatively, oscillation can be used as a tool to feature bead-shaped catalysts constantly agitated inside columns for increased interaction with fluids[87] or reduce clogging.[90]

Taking this information into consideration, depending on the phases of the reagents, or if additional energy sources are required for the transformation, different reactor typologies can be used for chemical transformation. Some of them will be highlighted since they were of interest during the development of the works featured in this thesis and are illustrated in figure 5.

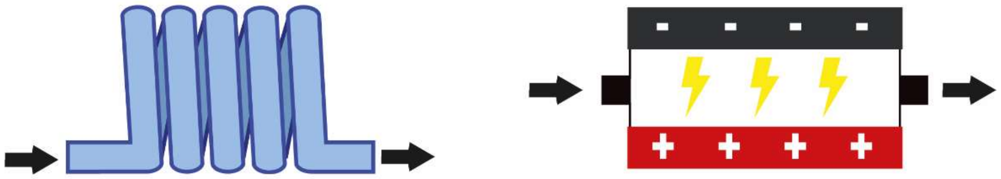

Coil reactor **Electrochemical reactor**

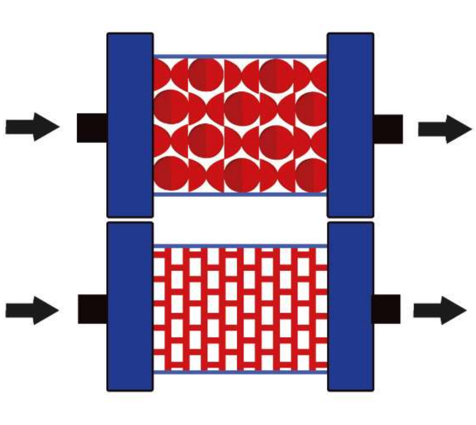

Packed bed reactor **Microstructured reactors**

Figure 5. Schematic representation of a selection of reactor typologies

Coil reactors. Commonly used thanks to their simplicity, as tubes in materials like steel, PFA of PTFE, are widely available for purchase, they only need to be cut and installed with the appropriate connection fittings. Due to the curvature of the tubing, the centripetal forces generate vortices that promote mixing,[91] albeit for intensify it, coupling with other strategies like the use of Taylor vortices may be required.[60] Tubing that is permeable to gas can be used to have tube-in-tube reactors, as a way to introduce the gas gradually into the stream with the rest of chemical compounds.[47] Transparent tubing materials, like PFA, can be also used to produce coil reactors for applications that require photochemical transformations, with the lamp either at the centre of the coil or outside. Thanks to the small diameter of the tubes, optical path lengths are greatly decreased, and therefore higher control of light irradiation over the reaction volume can be achieved resulting in more homogeneous product distribution.[92]

Electrochemical reactors. In these reactors, fluids are passed between two electrodes and chemical transformations occur at the electrode surface due to the transfer of electrons. Electrochemical reactors show great potential in the development of more sustainable processes, as they enable to carry out oxidations or reductions without the addition of catalysts or stoichiometric amounts of redox agents.[93] By carefully selecting parameters such as electrode material, electrolyte, voltage, time of residence or current density, electrochemical flow reactors can grant great selectivity toward specific products, making them of great interest.[9] As implantation of renewable energies continues, this energy can be applied as the source for the electrochemical synthesis, greatly furthering their sustainability.[10] Moreover, improvements of mass transfer of species due to flow enable the application of lower interelectrode distances and voltages compared to batch electrochemical cells, decreasing the required electrolyte concentration.[94] Typically, flow electrochemical cells feature two parallel plates and flow fluids pass in the available space between them. Flow path can be designed to increase residence time or improve mixing, generally applying 2D mixing strategies like split and recombine of channels. There are other possible geometries, like a cylindrical cell with concentric electrodes developed by Cantillo and co-workers, intended for more temperature and pressure conditions compared to the, usually, gentle conditions for electrochemical reactions.[95] The development of 3D geometries can further improve transport of species between electrodes, in that sense, the design of oscillatory baffled reactors[89] or the development electrodes featuring geometries that promote mixing[96] can increase the production of electrochemical flow reactors. Overall, electrochemical flow reactors show promising potential for the synthesis of chemical compounds and the scaling up of production.[97] Some of the main challenges are the management of gas byproducts inside the cell and the increase of substate concentration.

Packed bed reactors. They generally consist of columns filled with beads of a material, and some kind of filter or frit at the extremes. Fluids pass through the empty spaces available between beads, resulting in a flow path full of obstacles that induce the generation of turbulences that can be used to enhance mixing.[98] Packed bed reactors are generally used in heterogeneous catalysis, with the beads serving as a tool for supporting the catalyst in place while the reaction mixture passes through.[34] Alternatively, when solid reagents want to be used but there only required in one step of the synthesis, packed beds can also can be used as a way to use them while avoiding a separation step.[99] In case of working with gases that have low solubility in liquids, the small distances inside the reaction enable a high interaction between gas, liquid and catalyst not possible in batch. This can be done either using fine powders[100] or porous beads that generate intricate paths.[101] One issue they present is possible flow irregularities due to the formation of preferential paths, for that reason microstructured reactors have emerged as an alternative.

Microstructured reactors. These reactors are designed to include features that alter the flow path for generating flow instabilities that enhance mixing. The basic principles remain the same as in packed bed reactors, but the goal is to have a higher degree of control over flow behaviour as the randomness inherent to the packing of beads is eliminated. One of the first developments trying to overcome the issues of packed bed reactors was the use of monolithic structures, in materials like ceramic or metals, with commonly a grid-like structure that resulted in several square channels.[102] However, with de advent of 3D printing, more diverse structures are being developed. For example, helical inserts combining different rotations can force the fluid in different directions with great success.[103] Other options include honeycomb arrangements,[81] spiralling channels[61] or more complex geometrical figures like gyroids.[82] Microstructured reactors not only can enhance mixing, but they also can also serve as supports for heterogeneous catalysts, as produced structures can be further modified to immobilize catalysts of great use either in single-phase[81] or multi-phase reactions.[104] They can also play an active role in electrochemical reactors, as demonstrated by Wessling and co-workers, where helicoidal inserts were fabricated in metal for also being used as electrodes.[96]

1.3.4 Auxiliary elements

Other elements might be included in the setup to control and influence the specific process needs. Although the list could be longer, some selected examples relevant to this thesis are presented.

Sample loops and 6-way valves. Sample loops consists in sections of tubing isolated from the main circuit, while 6-way valves are rotational valves featuring 6 ports that are connected in pairs. Once the valve is rotated, the connected pairs change, hence the sample contained in the loop can be introduced into the main circuit and immediately bypassed again. They might be required when dealing with small amounts of reagents, like during the evaluation of reaction conditions while minimizing the sample amount per run.[8] This also offers great synergy with automated platforms, as different samples can be introduced with an autosampler and collected.

Back pressure regulators (BPR). Devices used to control the upstream pressure; they feature a valve that opens once a minimum pressure threshold is surpassed. They can be fixed-pressure cartridges or adjustable by regulating the pressure of a diaphragm[18]. There are also electronic versions of these devices for active pressure regulation, and some manufacturers are recently developing applications to also use their peristaltic pumps as BPRs.[105] They are of great use for stabilizing pressure in processes featuring gasses for ensuring uniform plug size distribution,[64] additionally, they can also be used to improve gas solubility in liquids[47] or to increase the boiling point of solvents.[46]

Heating and cooling elements. The reduced scale of flow reactors enables alternative heating solutions, as heat can be applied more effectively to the reaction mixture with less energy consumption. This heating can be electrified, making the process more sustainable as those alternative methods can be powered by renewable electricity. For example, reactors can be heated by heat generated with electrical resistances distributed to the desired areas through heat conductive parts.[106] Another available option is to generate controlled temperature currents of either hot or cold air surrounding the reactor.[75]

Separators. Devices that feature a membrane designed to separate different polarity liquid phases, but also gasses can be separated from the liquid phase. They can be used in biphasic liquid reactions for separating the phase containing the product from the others.[107] In case of gas-containing fluid stream that is going to be connected to an inline detector, such as a UV detector, it can be used to remove gas bubbles that might cause interferences.[100] Or for telescoped reactions, it can be used to separate some species before entering the next stage of the process. For example, Wirth's group reported a strategy for fluorination chemistry that removes the dangerous hydrofluoric acid by implementing a liquid-liquid extraction. A mediator species is electrochemically generated, the hydrofluoric acid byproduct is extracted with water and the mediator proceeds to be mixed with the target substrate.[108] In the case of electrochemical devices, another solution is to use porous electrodes, that allow the removal of gas bubbles from the solution.[109]

1.4 Digitalisation of flow platforms

The digitalisation of different components allows achieving a further degree of control over continuous-flow processes. This will enable the automation of the workflow, minimizing human intervention, and to generate relevant process data in real-time which might be used for machine learning-based modelling.[110] With this, it would be possible to achieve the rapid optimisation of process conditions,[111] target properties,[112] and the discovery of novel materials[113] or reactions.[114] During the following section, concepts needed to develop more digital processes will be discussed.

1.4.1 Digital reactor design

During the section dedicated to reactors, it was established that mixing was a key element in the development of efficient flow syntheses. Depending on the reaction, coil reactors or mixing achieved through T-mixers might not be sufficient. Packed bed reactors can be used to generate chaotic advection, albeit they cause variability issues due to the randomness intrinsic to the packing that might generate suboptimal pathways, also known as channelling.[115] This variability can present itself in differences on residence times for gases and liquids, mass or heat transfer, and overall can lead to poor reproducibility between experiments.[61] In order to overcome this, microstructured reactors have been developed over the last years, as their geometry can be finely tuned to control fluid dynamics and heat distribution along reactor profile.

Computer-Aided Design (CAD) are a series of technologies that enable the development of models, either 2D or 3D, for industrial applications. Even if there are applications that can be used for 3D modelling, the software developed for CAD requires an accurate control over the dimensions of the design, as they need accurately transferred into production of the object. In a broad sense, these tools are used for creating solid bodies with a series features that give the model its particular shape. These features are generally created by performing an operation over a 2D drawing, these operations can result in the addition of material (create bodies by extruding, revolving…), removal (hollowing solid pieces, make holes, …) or other transformations (bend pieces, multiply features, make threads…). Some CAD commercial software examples include Solidworks[116] or Autodesk Fusion 360,[117] alternatively many open-source alternatives, like FreeCAD[118] are available. Figure 6A shows an electrochemical reactor where many different components, including the flow cell, the housing and gaskets were modelled with CAD software and later printed. The software enabled the production of pieces with dimensions tailored to already available electrodes and connector pieces, while also including advanced mixing features, like baffles. However, complex periodic structures that can be interesting for improving mixing and surface area, like gyroids,[82] might require a huge number of operations in the mentioned programs. These bodies can be described by mathematical expressions, so alternatives such as Python-based scripts[119] or commercial software like Hyperganic HyDesign[120] for their generation with detailed measurements have been developed. Finally, one of the issues that CAD reactor design might face is the weight of having to add another skill to researcher's repertoire. To face that, initiatives like ChemSCAD exist for making the development of custom reactors easier, as the software allows to design it by selecting the needed pieces,[121] or CAD files could be provided in publications to aid in the reproduction of results.[8]

Using the designed models is possible to accurately manufacture the reactor through different methods, in that sense 3D printing has gained great interest as a technique for this and it will be discussed in more detail later. Moreover, the same 3D model can be used for a preliminary evaluation of their properties through simulations employing Computational Fluid Dynamics (CFD). In CFD simulations, the provided model is transformed into a mesh that is comprised by a number of discrete elements, or cells, that represent the total space. A higher number of cells can provide a more complex simulation, at the expense of requiring more computing power as there are more elements to simulate.[102] Under the selected boundary conditions, a series of mathematical models, commonly the Navier-Stokes equations, are used to calculate the parameters needed for the flow simulation at the individual cells.[122] Using CFD is possible to evaluate flow velocities, generation of phenomena such as vortexes, mass transfer of species or even heat exchange profiles[102]. For example, in figure 6B the influence in mixing of an oscillatory motion through baffles was evaluated. The concentration distribution was estimated by simulating a tracer species, and the velocity profiles at different points of the oscillation were also calculated. As the same 3D model is used for both manufacturing and simulations, it is possible therefore to adjust all the mixing elements to tailor their performance before even producing the reactor. Finally, CFD experiments can be validated by performing RTD studies with the manufactured reactor and compare the simulated and obtained data.[123] The understanding of the impact of geometry in the flow behaviour can generate a workflow loop of evaluation-fine tuning until the requirements are satisfied.[6] Thanks to this, it's possible to reduce generated waste and shorten reactor development times, as the tested reactors could already have been validated with CFD and employ a theoretically optimised geometry for the initial experiments.

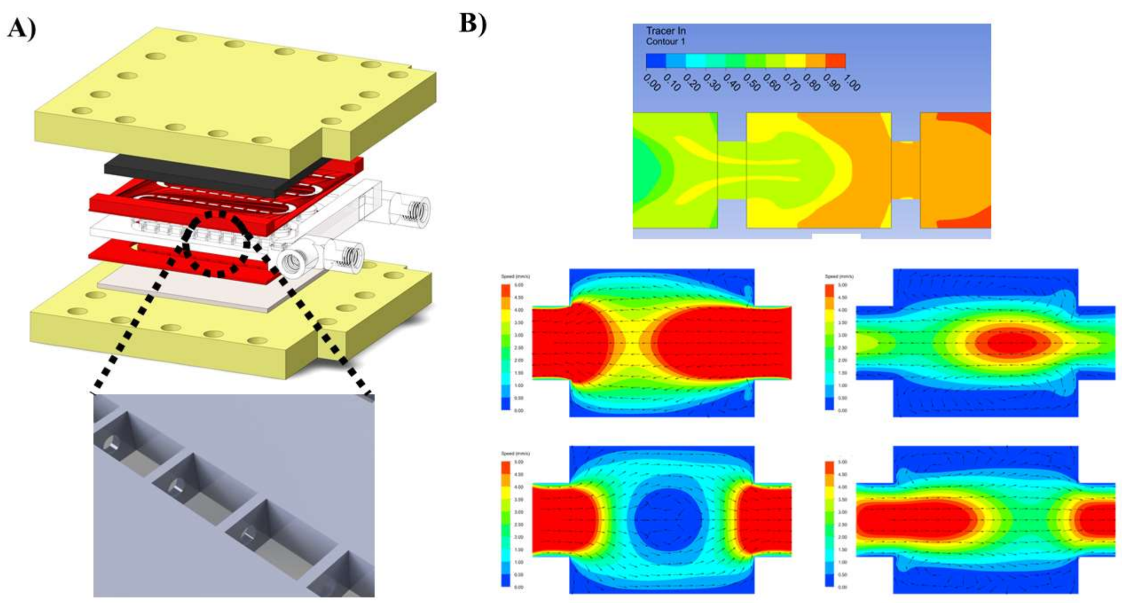

Figure 6. A) Components of a CAD-designed reactor B) CFD simulations for tracer concentration and velocity profiles in the reactor. Reproduced from [88]

CFD has been used to discover new flow regimes with experimental applications. Kappe's group studied the impact of oscillatory flow in a split-and-recombine reactor as a way to transport solid suspensions avoiding their deposition, and used it sucesfully.[90, 124] McDonough *et al.* used CFD to develop a novel flow pattern for oscillatory baffled reactor by adding an helicoidal structure with a central rod to enhance the generation of vortexes in straight channels. The complex structure was easily manufactured thanks to 3D printing, compared to the traditional means, so the simulations were rapidly validated in the laboratory with residence time distribution (RTD) studies.[125] In a similar way, they have developed other structures that can be 3D printed with different dimensions, like helical pitch or radius, to evaluate their impact in the process.[126] The MASP group, in collaboration with Prof. Raúl Martínez Cuenca (UJI) has applied this to evaluate the impact of oscillatory flow in the performance of electrochemical flow reactors. The CFD simulations revealed how the combination of baffles and oscillation enhanced the mass transport of species to electrode surface, enabling the increase of interelectrode distance.[88]

1.4.2 3D Printing

Additive manufacturing, commonly known as 3D printing (3DP), is the result of the combination of different technologies for the production of three-dimensional objects starting from a 3D model. The name of additive manufacturing derives from the principle of the technique, as objects are created by the addition of material layer by layer until the model is completed. This is opposed to traditional production methods (like cutting, machining or grinding) that are based on the subtractive method of production, as material is removed to conform the final product. The easiness of operation for producing complex items with great reproducibility, transitioning directly from the virtual 3D model to the physical object, has awakened a great interest in the technique that keeps growing.[127] The decreasing cost of printers has enabled their easy acquisition, even for hobbyists at home, for rapid prototyping and development of custom pieces at laboratories. Additionally, as the material is not removed but added precisely, there is a notably decrease of produced waste during production. Considering this, 3DP has become an important asset in the transition to more sustainable manufacturing processes.[1]

The first requirement to use 3D printing is to have a virtual model of the object that is going to be produced. It can be done using CAD software previously discussed, albeit over the last years there have been initiatives to share models online in order to increase the reproducibility between laboratories.[128] One of the most widely supported file formats for 3DP is *.stl*, that transforms the modelled geometries into a combination of triangles, and was developed for the firsts 3DP techniques.[129] Next, the file has to be introduced into a slicing software, that will divide the model into the series of layers that will be printed. Depending on the desired accuracy for the print, different layer thickness can be chosen, ranging from tens to hundreds of microns. A lower layer thickness yields a better z-axis resolution, albeit this increases printing time, hence this balance must be considered depending on the final applications. Slicing can be done using specific software, but many printers use proprietary printing software that slices while simultaneously processing other printing parameters. After all, layers contain information about the material-containing sections, so the printing software programs the needed commands, like printhead location or exposure time, during slicing. Finally, the file can be loaded to the 3D printer and it begins, taking from minutes or days depending on item size, method chosen and resolution.

3DP is an umbrella term that covers different techniques, aggrouped in seven different types according to the ISO/ASTM 52900:2015, with different working principles but with the same objective. These categories are: material extrusion, vat photopolymerization, material jetting, binder jetting, powder bed fusion, direct energy deposition and sheet lamination.[130] The choice of printing technique will be mainly conditioned by the properties of the printing material, item geometry and desired resolution. Some of these 3DP methods that were focus of the present thesis will be highlighted and discussed during this section.

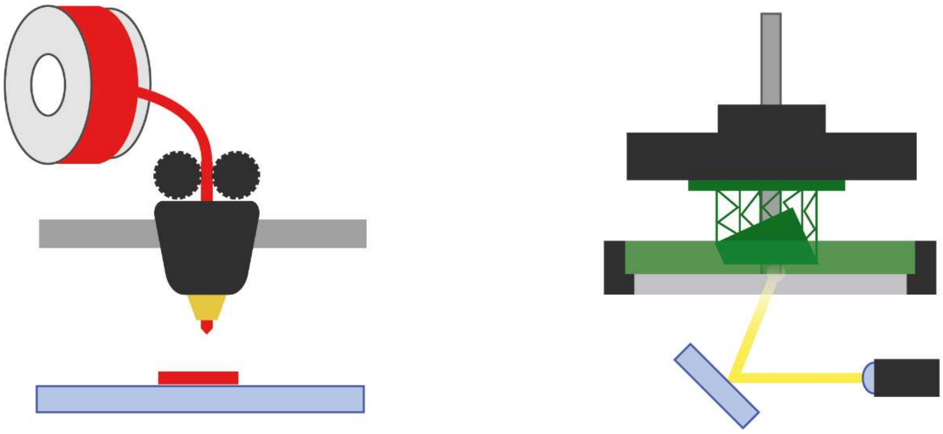

Fused Filament Fabrication (FFF) **Stereolithography (SLA)**

Digital Light Processing (DLP) **Masked Stereolithography (MSLA)**

Figure 7. Schematic representation of highlighted 3D printing techniques.

Fused Filament Fabrication (FFF).

Extrusion based technique that uses thermoplastics for producing the final objects. The selected material is used in filament form and heated at a nozzle to the required temperature, so it melts and is extruded for its deposition. Filament is typically loaded into a spool that feeds it to the nozzle, a series of motors move it to the required positions of the printing platform and the filament is deposited according to the layer data (a simplification can be seen in Figure 7). Even though, theoretically, FFF printers can achieve XYZ resolutions under 10µm, minimum feature size is limited by nozzle diameter. Details of up to 20 µm can be printed with 0.4mm nozzles, but variability between prints is not completely reliable.[131] However, the achievable level of details is low compared with other techniques, the different layers can be observed with the naked eye, produced items might have issues in applications involving fluids (as they may present a degree of porosity), or have poor mechanic properties (as problems of adhesion between layers might cause part breakage). Anyways, this technique can be used for rapid prototyping structures without complex details, or accessories for the lab, and since materials have a low cost, it has experienced a wide application. Additionally, by adjusting the infill density of the pieces, porosity can be controlled, and objects can be printed in a tilted angle to increase mechanical strength.

FFF has seen great use for creating setups by assembling elements tailored to the dimensions of already available elements on the laboratory. For example, there are different series of open-sourced modules for photoreactions. They were designed in a way that users can download the files and easily adjust the configuration depending on parameters, like the reaction is in flow or batch or reaction volume, and then print the required pieces.[92, 132] The same principle can be applied to develop elements like syringe pumps onsite, by using core elements like motors, syringes or Arduinos and print the housing or other parts.[56, 133] But not only outer elements can be printed using FFF, the reactor can also be fabricated for running chemical reactions, always having in mind the chemical robustness of the material. In this regard, polypropylene is a material readily available, widely used in 3D printing and with great compatibility with many chemical reaction conditions,[134] albeit there are other alternatives like PEEK that are more challenging to print.[103] In that regard, they been applied to build different reactors, for either batch[134] or flow cells,[133, 135] and mixing elements, like helical coils, can even be embedded in the design to be printed.[103] Another factor to be considered in the selection of material is the possibility to use their properties for expand the functionalities of printed parts. Pumera's group has developed numerous electrochemical systems featuring 3D-printed electrodes, with filaments that combine polymers with conductive materials, like copper[136] or graphite,[137] that even allow to tailor the conductivity at different points by adjusting the extrusion temperature. Other possibilities include the use of the material as a way to control heat conductivity at different points by adjusting wall thickness[138] or materials that enable the support of catalysts.[139]

Vat photopolymerization.

This family of techniques combine a source of light and liquid resins, containing monomers and a photoinitiator, for producing 3D solids by selectively polymerizing selected areas. The photopolymerizable resin is contained in a vat placed over the light source, and there is a motor that moves a platform holding the printed object. It should be noted that the printing surface must be transparent to the light source, typically UV light, so vats feature a window of materials such as fluorinated ethylene propylene (FEP). For each individual layer the platform is immersed in the resin, the light polymerizes the required areas according to the slicing data for the selected exposure time, and the platform goes up. Noticeably, in the more usual configuration of this setups, the objects are hanging from a platform that goes up and down, generating the risk of pieces dropping during the print. Additionally, after each layer, the platform must overcome the adhesion forces between the newly formed layer and vat surface, thereby there is a risk of the model falling while the platform is pulling back. For overcoming this, supports need to be included for improving stability of the printed element and their adhesion to the platform. Supports are pillar-like structures that connect the platform with small areas of the models and serve as an anchor for preventing them from dropping. Furthermore, orientation of the models is really important, as large flat surfaces have higher adhesion to the bottom of the bath, and hence the risk of prints falling. Moreover, if the force that needs to be overcome is too big, it might deform the final product. The most recommended solution in those cases is to tilt the model 45º before slicing and adding supports. Another issue that must be considered is that pieces require post-treatment: they need to be washed to remove rests of resin (usually with isopropanol) and cured to achieve the final mechanical properties (using UV light and/or temperature), increasing the associated labour. Nevertheless, taking this into consideration vat photopolymerization techniques are a useful asset for producing highly detailed pieces with details in the micron order.

Depending on the mechanism used for irradiating the resin, different types of vat polymerization techniques can be identified, their basic mechanisms are represented in Figure 7. Stereolitography (SLA) was one the first methods developed in the 80s by Hull, who also founded 3D System, a pioneering company also responsible of the creation of the *.stl* format. This technique uses a laser to accurately polymerize the required points, therefore XY resolution depends on the radius the laser beam, making possible to reach even 5µm.[140] Digital Light Processing (DLP) uses a light beam with an array of mirrors to irradiate selected parts by generating a 2D image for each layer. DLP can be faster than SLA, as the whole layer is polymerized simultaneously instead of moving the laser point by point, at the expense of detail but resolution in the XY plane can be in the order of 35µm.[141] A variation over this concept is Masked Stereolitography (MSLA), where light is generated by an array of LEDs that has to pass through an LCD screen. The pixels of the screen allow or block the light path according to the layer data, therefore XY resolution of this technique depends on pixel size of the screen, and there are reports of printers with a pixel size of approximately 50µm.[142] Thanks to the low cost of the units, it has become a useful tool for laboratories, with manufacturers pursuing better screen resolutions for increased the level of detail with this technique. Nevertheless, it should be noted that the values here commented are illustrative, as they can only be achieved in ideal conditions, with an exhaustive optimization of all the printing parameters and resin formulation.

One of the main advantages of vat photopolymerization 3D printing over extrusion-based techniques is the achievable level of detail, hence more complex and intricate structures can be printed. Thanks to this, it is possible to fabricate reactors with integrated mixers in their structure that are really hard to produce with another methods.[143] For example, the implementation of helical mixers[144] or coiled reactors that feature an internal coiled structure, further improving mixing.[7] In this regard, the MASP group has extensive experience in the development of structures for diverse applications fabricated using diverse vat photopolymerization techniques. Using SLA, an oscillatory baffled reactor was fabricated for improved particle size control in the synthesis of silver nanoparticles.[53] On the other hand, with MSLA systems custom formulations were developed for really diverse applications, ranging from embedding perovskite crystals for photocatalysis,[145] build luminescent structures by stabilizing quantum dots,[146] fabricate elements with antimicrobial properties[147] or formulations that allow the support of ionic liquids for CO_2

conversion to added value chemicals.[83] But not only organic polymers can be produced with these techniques, the development of formulations for 3D-printing alternative materials like ceramic is being explored, with applications such as the production of structures, like honeycombs, that serve as a support for enzymes.[81]

1.4.3 Digital interfaces, inline analytics, and automation

An objective of the digitalisation of chemical processes is to decrease physical interaction with the setups by transforming laboratory operations into commands entered digitally. In this regard, flow reactors have great synergy with digitalisation, as there is no required manual interaction with the reactor during the process, pumps can be digitally controlled and product is collected at the output. Therefore, reaction parameters (temperature, pressure, concentration, flow…) can be set up by introducing a series of inputs in software, minimizing the number of uncontrolled variables or differences caused by human intervention, enhancing process reproducibility, as well as improving safety by decreasing exposure to chemicals of the operators.[4] Additionally, the integration of inline analytics techniques can provide additional information in real time about the products, and give insight about the causes of possible variations. Thereby, appropriate digital interfaces need to be developed for controlling all the different devices and process the acquired data, but for also performing different series of experiments and even self-optimize reaction conditions.

All the digital structure for a flow platform can be self-developed in the laboratory, albeit it requires knowledge of programming language, like Python or C++, that might be out of reach for chemist-profile researchers.[148] The easiest choice to avoid this is to use readily available in the market flow platforms, that include proprietary software for controlling the different components (pumps, reactors, detectors…). They usually lack flexibility, as they are limited to the intended components by the company, although some companies like Vapourtec feature the possibility of controlling it externally for pairing along other tools.[149] Initially, some laboratories automated bespoke platforms were developed in LabVIEW a visual programming language, as it decreases the level of abstraction required, since operations are introduced by connecting blocks, akin to a process flowchart. LabVIEW allows to communicate with the instrument, and also generates a digital interface for selecting the required inputs. Additionally, there are available libraries for a great number of instrument drivers and shared knowledge, simplifying their implementation. Also, it can be paired with MATLAB for data processing and output optimization.[150] However, in many occasions, due to programming made by non-specialists, it is difficult to replace or remove a component without issues, increasing the labour related to automation. In order to solve this, there are initiatives for lowering the entry barrier, like OpenFlowChem mainly based on LabVIEW[151] or the Python-based LABS,[152] that simplify instrument connection and setup. Anyways, new researcher profiles more oriented to programming are appearing, these "digital chemists" are more dedicated to the integration of devices and swift development of platforms in more flexible and open-source languages such as Python. Ideally, the different devices, like pumps, would be easily swapped without issues, allowing to share reaction data or synthesis protocols as a series of commands for their replication in another laboratory.[148]

Another objective of process digitalization is the acquisition of data in real time for a better control and understanding, not only about the product but also intermediate steps. Continuous temperature and pressure recording is a basic way to monitor reactor status, verify selected conditions are matched, and identify variations that might affect the final product. In electrochemical processes, the logging of current or voltage can also give information in real time about variations in mixing or the formation of gas bubbles.[88, 153] For more detailed insight about the reaction, on-line or in-line analytics can be used. On-line analytics are techniques where aliquots redirected from the output to an analysis system, like a chromatograph or mass spectrometer.[5] Meanwhile, in-line analytics are constantly recording information from the flow at selected points. It's important to consider that techniques selected for in-line analytics must be non-destructive, as the flow must be unaffected by the measurement while continuing the path. Thereby, some examples of methodologies used for monitor in real time include image recognition,[99] UV-VIS absorption,[154] photoluminescence measurements,[155] X-Ray diffraction[59] or Nuclear Magnetic Resonance.[156] Additionally, inline analytics make possible to study reaction intermediates or crystallization kinetics by monitoring different parts of the reactor, as time of reaction is directly correlated with physical position within the reactor.[155]

In the end, with the combination of these principles is possible not to simply develop flow synthesis systems but full digital flow platforms adapted to different processes. For example, Jamison's group developed a modular platform that enabled the rapid exchange of modules to adapt the setup to the operations needed for each synthesis of organic compounds. The different products could be monitored in real time by using FT-IR, Raman, mass spectrometry and HPLC depending on the process needs.[150] For further minimizing interaction, Gilmore's group developed a platform for the synthesis of organic compounds that featured a radial structure with a central rotating 16-way valve. Depending on the required steps, the modules would be rotated to connect the reactors accordingly and it was monitored by NMR and FT-IR.[157] In the case of advanced materials, for example, Abolhasani's group has dedicated many works to the construction of digital flow platforms for the synthesis of perovskite quantum dots. By coupling inline analytics and digital control over reaction parameters, it was possible to study many different synthesis conditions using minimum amounts of sample, saving time and minimizing the use of resurces.[155] Further developments over this concept lead to platforms including self-optimization algorithms that use the obtained data to adjust in real time synthesis conditions, like achieving maximum performance by adjusting dopant concentration[64] or fine tuning for achieving materials with very specific optoelectronic properties.[112] All of these examples show the potential of code programmed in LabVIEW for controlling complex setups, but for more flexibility, and the aim of making the code open-source, Python would be the next step. In this regard, Cronin's group has extensive experience in the creation of Python-based chemical flow platforms, having developed a code structure for directly transforming chemical reactions into digital commands to be sent to the required devices, coining the concept of *chemputation.*[148] With this, they have demonstrated its use in the optimization electrochemical systems,[158] organic synthesis[159] or perform multiple kinetic studies.[160]

Considering the described benefits for digital flow platforms, there is an interest in the transition from traditional syntheses. However, the adaptation is non-trivial due to the increased complexity of systems featuring many different components. The field remains full of challenges to overcome and knowledge gaps to cover for each particular case, therefore, the present thesis aims to contribute in furthering the development said digital flow platforms. The fundamentals described during the introduction are applied to the design of systems for tackling different challenges, with the aim of developing knowledge that can also be transferred to other problems. For each of them, reaction conditions need to be initially studied for considering a favourable transition into flow. Next, the flow platform for the corresponding transformations needs to be designed, including proper reagent delivery methods, tubing, reactor design or the selection of mixing features according to reaction needs among others. Finally, for more enhanced developments, components can be digitally designed, validated, and produced for further optimization of performance. And digital control of the whole setup can be achieved, for a more robust regulation of process conditions and eventual automation.

In the field of chemical synthesis, continuous flow has proven improvements in yield and selectivity, while decreasing waste. However, mass transfer of species might impose limitations in the final yield of the reactions, requiring the development of new tailored geometries.[9] The digital design of reactors can help in finding innovative structured and carefully tune them according to reaction parameters. More specifically, the conversion of carbon dioxide to added value products is a process of interest, not only because it's a way to recycle a common byproduct, but also because reactions like cycloadition to epoxide are able to yield the product with a 100% atom efficiency.[161] Alkenes are commonly more accessible than their respective epoxides, therefore there is interest in processes that produce the epoxide as intermediate species for the following cycloaddition.[162, 163] This remains a challenge for diverse reasons, including the search for compatible conditions for the two reactions for while achieving sufficient selectivity a yield. There are reports of sequential oxidation and cycloaddition, but its application as a multi-step continuous flow process has not been deeply studied and there is room for improvement.[164] In this regard, electrochemical oxidation shows potential as a greener alternative for the oxidation of alkenes to epoxide,[93] and the development of new reactor geometries, along digitalization of the setup, can aid in improving the overall yield of the process.

Another field where digital flow platforms are of great interest is crystallization, more specifically of advanced materials. It has been previously highlighted their application for the preparation of materials like perovskite quantum dots,[112] but the flow crystallization of perovskite single crystals remains quite unexplored. This family of materials, of great interest in applications such as X-Ray sensors[165] or solar cells,[166] has been traditionally synthesized in batch with the aid of techniques like antisolvent crystallization of temperature lowering. These methods are slow, requiring days or weeks, something that complicates their industrial fabrication. Over the last years, Inverse Temperature Crystallization (ITC) has emerged as an alternative as it allows to obtain millimetre sized crystals in hours. This technique is based in reverse solubility that certain salt and solvent combinations present, meaning that by increasing temperature in a controlled manner the solubility decreases and the crystal is obtained.[167] However, one of the main issues this technique presents low reproducibility of experiments due to loss of control during the process done in batch.[168] As this lack of control could be attributed to the generation of hotspots or concentration gradients along the reactor profile, the implementation of flow and the digitalization of the process is expected to improve the reproducibility of the crystals.

1.5 References

(1) European comission; 2030 Digital Compass: the European way for the Digital Decade. 2021.
(2) CEFIC. Digital technologies for sustainabilit y in the european chemical industry. 2023.
(3) Burger, B.; Maffettone, P. M.; Gusev, V. V.; Aitchison, C. M.; Bai, Y.; Wang, X.; Li, X.; Alston, B. M.; Li, B.; Clowes, R.; et al. A mobile robotic chemist. *Nature* **2020**, *583* (7815), 237-241. DOI: 10.1038/s41586-020-2442-2.
(4) Dragone, V.; Sans, V.; Henson, A. B.; Granda, J. M.; Cronin, L. An autonomous organic reaction search engine for chemical reactivity. *Nature Communications* **2017**, *8* (1), 15733. DOI: 10.1038/ncomms15733.
(5) Browne, D. L.; Wright, S.; Deadman, B. J.; Dunnage, S.; Baxendale, I. R.; Turner, R. M.; Ley, S. V. Continuous flow reaction monitoring using an on-line miniature mass spectrometer. *Rapid Communications in Mass Spectrometry* **2012**, *26* (17), 1999-2010. DOI: 10.1002/rcm.6312.
(6) Bettermann, S.; Kandelhard, F.; Moritz, H.-U.; Pauer, W. Digital and lean development method for 3D-printed reactors based on CAD modeling and CFD simulation. *Chemical Engineering Research and Design* **2019**, *152*, 71-84. DOI: 10.1016/j.cherd.2019.09.024.
(7) McDonough, J. R.; Armett, J.; Law, R.; Harvey, A. P. Coil-in-Coil Reactor: Augmenting Plug Flow Performance by Combining Different Geometric Features Using 3D Printing. *Industrial & Engineering Chemistry Research* **2019**, *58* (47), 21363-21371. DOI: 10.1021/acs.iecr.9b04239.
(8) Hone, C. A.; Kappe, C. O. Towards the Standardization of Flow Chemistry Protocols for Organic Reactions. *Chemistry–Methods* **2021**, *1* (11), 454-467. DOI: 10.1002/cmtd.202100059.
(9) Noël, T.; Cao, Y.; Laudadio, G. The Fundamentals Behind the Use of Flow Reactors in Electrochemistry. *Accounts of Chemical Research* **2019**, *52* (10), 2858-2869. DOI: 10.1021/acs.accounts.9b00412.
(10) Mallapragada, D. S.; Dvorkin, Y.; Modestino, M. A.; Esposito, D. V.; Smith, W. A.; Hodge, B.-M.; Harold, M. P.; Donnelly, V. M.; Nuz, A.; Bloomquist, C.; et al. Decarbonization of the chemical industry through electrification: Barriers and opportunities. *Joule* **2023**, *7* (1), 23-41. DOI: 10.1016/j.joule.2022.12.008.
(11) Mahin, J.; Torrente-Murciano, L. Continuous synthesis of monodisperse iron@iron oxide core@shell nanoparticles. *Chemical Engineering Journal* **2020**, *396*, 125299. DOI: 10.1016/j.cej.2020.125299.
(12) Hartman, R. L.; McMullen, J. P.; Jensen, K. F. Deciding Whether To Go with the Flow: Evaluating the Merits of Flow Reactors for Synthesis. *Angewandte Chemie International Edition* **2011**, *50* (33), 7502-7519. DOI: 10.1002/anie.201004637.
(13) Webb, D.; Jamison, T. F. Continuous flow multi-step organic synthesis. *Chemical Science* **2010**, *1* (6), 675-680, 10.1039/C0SC00381F. DOI: 10.1039/C0SC00381F.
(14) Sebastian, V. Toward continuous production of high-quality nanomaterials using microfluidics: nanoengineering the shape, structure and chemical composition. *Nanoscale* **2022**, *14* (12), 4411-4447, 10.1039/D1NR06342A. DOI: 10.1039/D1NR06342A.
(15) Newman, S. G.; Jensen, K. F. The role of flow in green chemistry and engineering. *Green Chemistry* **2013**, *15* (6), 1456-1472. DOI: 10.1039/C3GC40374B.
(16) Fogler, H. S. *Elements of chemical reaction engineering*; Third edition. Upper Saddle River, N.J. : Prentice Hall PTR, 1999.

(17) Yoshida, J.-i.; Kim, H.; Nagaki, A. "Impossible" Chemistries Based on Flow and Micro. *Journal of Flow Chemistry* **2017**, *7* (3), 60-64. DOI: 10.1556/1846.2017.00017.
(18) Plutschack, M. B.; Pieber, B.; Gilmore, K.; Seeberger, P. H. The Hitchhiker's Guide to Flow Chemistry. *Chemical Reviews* **2017**, *117* (18), 11796-11893. DOI: 10.1021/acs.chemrev.7b00183.
(19) Zaquen, N.; Rubens, M.; Corrigan, N.; Xu, J.; Zetterlund, P. B.; Boyer, C.; Junkers, T. Polymer Synthesis in Continuous Flow Reactors. *Progress in Polymer Science* **2020**, *107*, 101256. DOI: 10.1016/j.progpolymsci.2020.101256.
(20) Terry, S. C.; Jerman, J. H.; Angell, J. B. A gas chromatographic air analyzer fabricated on a silicon wafer. *IEEE Transactions on Electron Devices* **1979**, *26*, 1880-1885. DOI: 10.1109/t-ed.1979.19791.
(21) Manz, A.; Graber, N.; Widmer, H. M. Miniaturized total chemical analysis systems: A novel concept for chemical sensing. *Sensors and Actuators B: Chemical* **1990**, *1* (1), 244-248. DOI: 10.1016/0925-4005(90)80209-I.
(22) Woolley, A. T.; Sensabaugh, G. F.; Mathies, R. A. High-Speed DNA Genotyping Using Microfabricated Capillary Array Electrophoresis Chips. *Analytical Chemistry* **1997**, *69* (11), 2181-2186. DOI: 10.1021/ac961237+.
(23) Jensen, K. Smaller, faster chemistry. *Nature* **1998**, *393* (6687), 735-737. DOI: 10.1038/31590.
(24) Burns, J. R.; Ramshaw, C. Development of a Microreactor for Chemical Production. *Chemical Engineering Research and Design* **1999**, *77* (3), 206-211. DOI: 10.1205/026387699526106.
(25) McDonald, J. C.; Duffy, D. C.; Anderson, J. R.; Chiu, D. T.; Wu, H.; Schueller, O. J.; Whitesides, G. M. Fabrication of microfluidic systems in poly(dimethylsiloxane). *Electrophoresis* **2000**, *21* (1), 27-40. DOI: 10.1002/(sici)1522-2683(20000101)21:1<27::Aid-elps27>3.0.Co;2-c From NLM.
(26) Wang, J.; Sui, G.; Mocharla, V. P.; Lin, R. J.; Phelps, M. E.; Kolb, H. C.; Tseng, H.-R. Integrated Microfluidics for Parallel Screening of an In Situ Click Chemistry Library. *Angewandte Chemie International Edition* **2006**, *45* (32), 5276-5281. DOI: 10.1002/anie.200601677.
(27) Kitson, P. J.; Rosnes, M. H.; Sans, V.; Dragone, V.; Cronin, L. Configurable 3D-Printed millifluidic and microfluidic 'lab on a chip' reactionware devices. *Lab on a Chip* **2012**, *12* (18), 3267-3271, 10.1039/C2LC40761B. DOI: 10.1039/C2LC40761B.
(28) Besenhard, M. O.; LaGrow, A. P.; Famiani, S.; Pucciarelli, M.; Lettieri, P.; Thanh, N. T. K.; Gavriilidis, A. Continuous production of iron oxide nanoparticles via fast and economical high temperature synthesis. *Reaction Chemistry & Engineering* **2020**, *5* (8), 1474-1483. DOI: 10.1039/D0RE00078G.
(29) Su, M.; Gao, Y. Air–Liquid Segmented Continuous Crystallization Process Optimization of the Flow Field, Growth Rate, and Size Distribution of Crystals. *Industrial & Engineering Chemistry Research* **2018**, *57* (10), 3781-3791. DOI: 10.1021/acs.iecr.7b05236.
(30) Huang, H.; du Toit, H.; Ben-Jaber, S.; Wu, G.; Panariello, L.; Thanh, N. T. K.; Parkin, I. P.; Gavriilidis, A. Rapid synthesis of gold nanoparticles with carbon monoxide in a microfluidic segmented flow system. *Reaction Chemistry & Engineering* **2019**, *4* (5), 884-890. DOI: 10.1039/C8RE00351C.
(31) Das Adhikari, S.; Masi, S.; Echeverría-Arrondo, C.; Miralles-Comins, S.; Sánchez, R. S.; Fernandes, J. A.; Chirvony, V.; Martínez-Pastor, J. P.; Sans, V.; Mora-Seró, I. Continuous-Flow Synthesis of Orange Emitting Sn(II)-Doped CsBr Materials. *Advanced Optical Materials* **2021**, *9* (21), 2101024. DOI: 10.1002/adom.202101024.

(32) Baxendale, I. R.; Brocken, L.; Mallia, C. J. Flow chemistry approaches directed at improving chemical synthesis. *Green Processing and Synthesis* **2013**, *2* (3), 211-230. DOI: 10.1515/gps-2013-0029.

(33) Kim, H.; Min, K.-I.; Inoue, K.; Im, D. J.; Kim, D.-P.; Yoshida, J.-i. Submillisecond organic synthesis: Outpacing Fries rearrangement through microfluidic rapid mixing. *Science* **2016**, *352* (6286), 691-694. DOI: 10.1126/science.aaf1389.

(34) Nagy, B. S.; Llanes, P.; Pericas, M. A.; Kappe, C. O.; Ötvös, S. B. Enantioselective Flow Synthesis of Rolipram Enabled by a Telescoped Asymmetric Conjugate Addition–Oxidative Aldehyde Esterification Sequence Using in Situ-Generated Persulfuric Acid as Oxidant. *Organic Letters* **2022**, *24* (4), 1066-1071. DOI: 10.1021/acs.orglett.1c04300.

(35) Mallia, C. J.; Baxendale, I. R. The Use of Gases in Flow Synthesis. *Organic Process Research & Development* **2016**, *20* (2), 327-360. DOI: 10.1021/acs.oprd.5b00222.

(36) Kockmann, N.; Thenée, P.; Fleischer-Trebes, C.; Laudadio, G.; Noël, T. Safety assessment in development and operation of modular continuous-flow processes. *Reaction Chemistry & Engineering* **2017**, *2* (3), 258-280. DOI: 10.1039/C7RE00021A.

(37) Plouffe, P.; Macchi, A.; Roberge, D. M. From Batch to Continuous Chemical Synthesis—A Toolbox Approach. *Organic Process Research & Development* **2014**, *18* (11), 1286-1294. DOI: 10.1021/op5001918.

(38) Dong, Z.; Wen, Z.; Zhao, F.; Kuhn, S.; Noël, T. Scale-up of micro- and milli-reactors: An overview of strategies, design principles and applications. *Chemical Engineering Science: X* **2021**, *10*, 100097. DOI: 10.1016/j.cesx.2021.100097.

(39) Yang, C.-G.; Xu, Z.-R.; Lee, A. P.; Wang, J.-H. A microfluidic concentration-gradient droplet array generator for the production of multi-color nanoparticles. *Lab on a Chip* **2013**, *13* (14), 2815-2820, 10.1039/C3LC50254F. DOI: 10.1039/C3LC50254F.

(40) Schoenitz, M.; Grundemann, L.; Augustin, W.; Scholl, S. Fouling in microstructured devices: a review. *Chemical Communications* **2015**, *51* (39), 8213-8228. DOI: 10.1039/C4CC07849G.

(41) Laybourn, A.; Robertson, K.; Slater, A. G. Quid Pro Flow. *Journal of the American Chemical Society* **2023**, *145* (8), 4355-4365. DOI: 10.1021/jacs.2c13670.

(42) Browne, D. L.; Deadman, B. J.; Ashe, R.; Baxendale, I. R.; Ley, S. V. Continuous Flow Processing of Slurries: Evaluation of an Agitated Cell Reactor. *Organic Process Research & Development* **2011**, *15* (3), 693-697. DOI: 10.1021/op2000223.

(43) Reizman, B. J.; Jensen, K. F. Feedback in Flow for Accelerated Reaction Development. *Accounts of Chemical Research* **2016**, *49* (9), 1786-1796. DOI: 10.1021/acs.accounts.6b00261.

(44) Holtze, C.; Boehling, R. Batch or flow chemistry? – a current industrial opinion on process selection. *Current Opinion in Chemical Engineering* **2022**, *36*, 100798. DOI: 10.1016/j.coche.2022.100798.

(45) Hartman, R. L. Flow chemistry remains an opportunity for chemists and chemical engineers. *Current Opinion in Chemical Engineering* **2020**, *29*, 42-50. DOI: 10.1016/j.coche.2020.05.002.

(46) Pedersen, M. J.; Skovby, T.; Mealy, M. J.; Dam-Johansen, K.; Kiil, S. Redesign of a Grignard-Based Active Pharmaceutical Ingredient (API) Batch Synthesis to a Flow Process for the Preparation of Melitracen HCl. *Organic Process Research & Development* **2018**, *22* (2), 228-235. DOI: 10.1021/acs.oprd.7b00368.

(47) Polyzos, A.; O'Brien, M.; Petersen, T. P.; Baxendale, I. R.; Ley, S. V. The Continuous-Flow Synthesis of Carboxylic Acids using CO2 in a Tube-In-Tube Gas Permeable Membrane Reactor. *Angewandte Chemie International Edition* **2011**, *50* (5), 1190-1193. DOI: 10.1002/anie.201006618.

(48) Köckinger, M.; Hone, C. A.; Gutmann, B.; Hanselmann, P.; Bersier, M.; Torvisco, A.; Kappe, C. O. Scalable Continuous Flow Process for the Synthesis of Eflornithine Using Fluoroform as Difluoromethyl Source. *Organic Process Research & Development* **2018**, *22* (11), 1553-1563. DOI: 10.1021/acs.oprd.8b00318.
(49) Miao, Y.; Siri-Nguan, N.; Sornchamni, T.; Jovanovic, G. N.; Yokochi, A. F. CO2 reduction in wet ionic liquid solution in microscale-based electrochemical reactor. *Chemical Engineering Journal* **2018**, *333*, 300-309. DOI: 10.1016/j.cej.2017.09.052.
(50) Pinho, B.; Torrente-Murciano, L. Dial-A-Particle: Precise Manufacturing of Plasmonic Nanoparticles Based on Early Growth Information—Redefining Automation for Slow Material Synthesis. *Advanced Energy Materials* **2021**, *11* (32), 2100918. DOI: 10.1002/aenm.202100918.
(51) Li, C.; Ding, B.; Zhang, L.; Song, K.; Tao, S. 3D-printed continuous flow reactor for high yield synthesis of CH3NH3PbX3 (X = Br, I) nanocrystals. *Journal of Materials Chemistry C* **2019**, *7* (30), 9167-9174. DOI: 10.1039/C9TC02390A.
(52) Guo, F.; Chen, B. Numerical Study on Taylor Bubble Formation in a Micro-channel T-Junction Using VOF Method. *Microgravity Science and Technology* **2009**, *21* (1), 51-58. DOI: 10.1007/s12217-009-9146-4.
(53) Okafor, O.; Weilhard, A.; Fernandes, J. A.; Karjalainen, E.; Goodridge, R.; Sans, V. Advanced reactor engineering with 3D printing for the continuous-flow synthesis of silver nanoparticles. *Reaction Chemistry & Engineering* **2017**, *2* (2), 129-136. DOI: 10.1039/C6RE00210B.
(54) Asche, S.; Cooper, G. J. T.; Keenan, G.; Mathis, C.; Cronin, L. A robotic prebiotic chemist probes long term reactions of complexifying mixtures. *Nature Communications* **2021**, *12* (1), 3547. DOI: 10.1038/s41467-021-23828-z.
(55) Iglesias, D.; Tinajero, C.; Luis-Gómez, J.; Aranda, C. A.; Martinez Cuenca, R.; Zanatta, M.; Sans, V. 3D printed flow reactors for the synthesis of single crystal perovskites. *Materials Today Energy* **2024**, *39*, 101476. DOI: 10.1016/j.mtener.2023.101476.
(56) Baas, S.; Saggiomo, V. Ender3 3D printer kit transformed into open, programmable syringe pump set. *HardwareX* **2021**, *10*, e00219. DOI: 10.1016/j.ohx.2021.e00219.
(57) Murray, P. R. D.; Browne, D. L.; Pastre, J. C.; Butters, C.; Guthrie, D.; Ley, S. V. Continuous Flow-Processing of Organometallic Reagents Using an Advanced Peristaltic Pumping System and the Telescoped Flow Synthesis of (E/Z)-Tamoxifen. *Organic Process Research & Development* **2013**, *17* (9), 1192-1208. DOI: 10.1021/op4001548.
(58) Claes, J.; Vancleef, A.; Segers, M.; Brabants, B.; Leblebici, M. E.; Kuhn, S.; Moens, L.; Thomassen, L. C. J. Synthesis of amines: From a microwave batch reactor to a continuous milliflow reactor with heterogeneous feed and product. *Chemical Engineering and Processing - Process Intensification* **2023**, *183*, 109252. DOI: 10.1016/j.cep.2022.109252.
(59) Levenstein, M. A.; Wayment, L.; Scott, C. D.; Lunt, R.; Flandrin, P.-B.; Day, S. J.; Tang, C. C.; Wilson, C. C.; Meldrum, F. C.; Kapur, N.; et al. Dynamic Crystallization Pathways of Polymorphic Pharmaceuticals Revealed in Segmented Flow with Inline Powder X-ray Diffraction. *Analytical Chemistry* **2020**, *92* (11), 7754-7761. DOI: 10.1021/acs.analchem.0c00860.
(60) Wong, W. K.; Yap, S. K.; Lim, Y. C.; Khan, S. A.; Pelletier, F.; Corbos, E. C. Robust, non-fouling liters-per-day flow synthesis of ultra-small catalytically active metal nanoparticles in a single-channel reactor. *Reaction Chemistry & Engineering* **2017**, *2* (5), 636-641. DOI: 10.1039/C7RE00072C.
(61) Iglesias, D.; Tinajero, C.; Marchetti, S.; Roppolo, I.; Zanatta, M.; Sans, V. Multi-step oxidative carboxylation of olefins with carbon dioxide by combining electrochemical

and 3D-printed flow reactors. *Green Chemistry* **2023**, *25* (23), 9934-9940. DOI: 10.1039/D3GC03360K.

(62) Choi, Y. M.; Choi, H. M.; Lee, S. H.; Kang, W. Characteristic test methods of the thermal mass flow controller. *Journal of Mechanical Science and Technology* **2014**, *28* (3), 907-914. DOI: 10.1007/s12206-013-1158-8.

(63) Prieschl, M.; García-Lacuna, J.; Munday, R.; Leslie, K.; O'Kearney-McMullan, A.; Hone, C. A.; Kappe, C. O. Optimization and sustainability assessment of a continuous flow Ru-catalyzed ester hydrogenation for an important precursor of a β2-adrenergic receptor agonist. *Green Chemistry* **2020**, *22* (17), 5762-5770. DOI: 10.1039/D0GC02225J.

(64) Bateni, F.; Sadeghi, S.; Orouji, N.; Bennett, J. A.; Punati, V. S.; Stark, C.; Wang, J.; Rosko, M. C.; Chen, O.; Castellano, F. N.; et al. Smart Dope: A Self-Driving Fluidic Lab for Accelerated Development of Doped Perovskite Quantum Dots. *Advanced Energy Materials* **2024**, *14* (1), 2302303. DOI: 10.1002/aenm.202302303.

(65) *Flow Chemistry – Fundamentals Volume 1*; De Gruyter, 2021. DOI: doi:10.1515/9783110693676.

(66) Lee, C.-Y.; Wang, W.-T.; Liu, C.-C.; Fu, L.-M. Passive mixers in microfluidic systems: A review. *Chemical Engineering Journal* **2016**, *288*, 146-160. DOI: 10.1016/j.cej.2015.10.122.

(67) Liu, B.; Ran, B.; Chen, C.; Shi, L.; Liu, Y.; Chen, H.; Zhu, Y. A low-cost and high-performance 3D micromixer over a wide working range and its application for high-sensitivity biomarker detection. *Reaction Chemistry & Engineering* **2022**, *7* (11), 2334-2347. DOI: 10.1039/D2RE00103A.

(68) Sobieszuk, P.; Aubin, J.; Pohorecki, R. Hydrodynamics and Mass Transfer in Gas-Liquid Flows in Microreactors. *Chemical Engineering & Technology* **2012**, *35* (8), 1346-1358. DOI: 10.1002/ceat.201100643.

(69) Cao, Y.; Padoin, N.; Soares, C.; Noël, T. On the performance of liquid-liquid Taylor flow electrochemistry in a microreactor – A CFD study. *Chemical Engineering Journal* **2022**, *427*, 131443. DOI: 10.1016/j.cej.2021.131443.

(70) Sans, V.; Karbass, N.; Burguete, M. I.; García-Verdugo, E.; Luis, S. V. Residence time distribution, a simple tool to understand the behaviour of polymeric mini-flow reactors. *RSC Advances* **2012**, *2* (23), 8721-8728. DOI: 10.1039/C2RA20903A.

(71) Reis, M. H.; Varner, T. P.; Leibfarth, F. A. The Influence of Residence Time Distribution on Continuous-Flow Polymerization. *Macromolecules* **2019**, *52* (9), 3551-3557. DOI: 10.1021/acs.macromol.9b00454.

(72) Marre, S.; Jensen, K. F. Synthesis of micro and nanostructures in microfluidic systems. *Chemical Society Reviews* **2010**, *39* (3), 1183-1202. DOI: 10.1039/B821324K.

(73) Cambié, D.; Zhao, F.; Hessel, V.; Debije, M. G.; Noël, T. A Leaf-Inspired Luminescent Solar Concentrator for Energy-Efficient Continuous-Flow Photochemistry. *Angewandte Chemie International Edition* **2017**, *56* (4), 1050-1054. DOI: 10.1002/anie.201611101.

(74) Nagy, K. D.; Shen, B.; Jamison, T. F.; Jensen, K. F. Mixing and Dispersion in Small-Scale Flow Systems. *Organic Process Research & Development* **2012**, *16* (5), 976-981. DOI: 10.1021/op200349f.

(75) Fang, Y.; Tranmer, G. K. Continuous flow photochemistry as an enabling synthetic technology: synthesis of substituted-6(5H)-phenanthridinones for use as poly(ADP-ribose) polymerase inhibitors. *MedChemComm* **2016**, *7* (4), 720-724. DOI: 10.1039/C5MD00552C.

(76) Khosravi Parsa, M.; Hormozi, F.; Jafari, D. Mixing enhancement in a passive micromixer with convergent–divergent sinusoidal microchannels and different ratio of

amplitude to wave length. *Computers & Fluids* **2014**, *105*, 82-90. DOI: 10.1016/j.compfluid.2014.09.024.

(77) Ansari, M. A.; Kim, K.-Y. Mixing performance of unbalanced split and recombine micomixers with circular and rhombic sub-channels. *Chemical Engineering Journal* **2010**, *162* (2), 760-767. DOI: doi.org/10.1016/j.cej.2010.05.068.

(78) Woitalka, A.; Kuhn, S.; Jensen, K. F. Scalability of mass transfer in liquid–liquid flow. *Chemical Engineering Science* **2014**, *116*, 1-8. DOI: 10.1016/j.ces.2014.04.036.

(79) McDonough, J. R.; Ahmed, S. M. R.; Phan, A. N.; Harvey, A. P. A study of the flow structures generated by oscillating flows in a helical baffled tube. *Chemical Engineering Science* **2017**, *171*, 160-178. DOI: 10.1016/j.ces.2017.05.032.

(80) Liu, K.; Yang, Q.; Chen, F.; Zhao, Y.; Meng, X.; Shan, C.; Li, Y. Design and analysis of the cross-linked dual helical micromixer for rapid mixing at low Reynolds numbers. *Microfluidics and Nanofluidics* **2015**, *19* (1), 169-180. DOI: 10.1007/s10404-015-1558-4.

(81) Valotta, A.; Maier, M. C.; Soritz, S.; Pauritsch, M.; Koenig, M.; Brouczek, D.; Schwentenwein, M.; Gruber-Woelfler, H. 3D printed ceramics as solid supports for enzyme immobilization: an automated DoE approach for applications in continuous flow. *Journal of Flow Chemistry* **2021**, *11* (3), 675-689. DOI: 10.1007/s41981-021-00163-4.

(82) González-Castaño, M.; Baena-Moreno, F.; Carlos Navarro de Miguel, J.; Miah, K. U. M.; Arroyo-Torralvo, F.; Ossenbrink, R.; Odriozola, J. A.; Benzinger, W.; Hensel, A.; Wenka, A.; et al. 3D-printed structured catalysts for CO2 methanation reaction: Advancing of gyroid-based geometries. *Energy Conv. Manag.* **2022**, *258*, 115464. DOI: 10.1016/j.enconman.2022.115464.

(83) Valverde, D.; Porcar, R.; Zanatta, M.; Alcalde, S.; Altava, B.; Sans, V.; García-Verdugo, E. Towards highly efficient continuous-flow catalytic carbon dioxide cycloadditions with additively manufactured reactors. *Green Chemistry* **2022**, *24* (8), 3300-3308. DOI: 10.1039/D1GC04593H.

(84) Chen, Z.; Pei, Z.; Zhao, X.; Zhang, J.; Wei, J.; Hao, N. Acoustic microreactors for chemical engineering. *Chemical Engineering Journal* **2022**, *433*, 133258. DOI: 10.1016/j.cej.2021.133258.

(85) Dong, Z.; Zondag, S. D. A.; Schmid, M.; Wen, Z.; Noël, T. A meso-scale ultrasonic milli-reactor enables gas–liquid-solid photocatalytic reactions in flow. *Chemical Engineering Journal* **2022**, *428*, 130968. DOI: 10.1016/j.cej.2021.130968.

(86) Wang, G. R.; Yang, F.; Zhao, W. There can be turbulence in microfluidics at low Reynolds number. *Lab on a Chip* **2014**, *14* (8), 1452-1458. DOI: 10.1039/C3LC51403J.

(87) Eze, V. C.; Fisher, J. C.; Phan, A. N.; Harvey, A. P. Intensification of carboxylic acid esterification using a solid catalyst in a mesoscale oscillatory baffled reactor platform. *Chemical Engineering Journal* **2017**, *322*, 205-214. DOI: https://doi.org/10.1016/j.cej.2017.04.038.

(88) Alvarez, E.; Romero-Fernandez, M.; Iglesias, D.; Martinez-Cuenca, R.; Okafor, O.; Delorme, A.; Lozano, P.; Goodridge, R.; Paradisi, F.; Walsh, D. A.; et al. Electrochemical Oscillatory Baffled Reactors Fabricated with Additive Manufacturing for Efficient Continuous-Flow Oxidations. *ACS Sustainable Chemistry & Engineering* **2022**, *10* (7), 2388-2396. DOI: 10.1021/acssuschemeng.1c06799.

(89) Vranckaert, M.; Gemoets, H. P. L.; Dangreau, R.; Van Aken, K.; Breugelmans, T.; Hereijgers, J. An electrochemical oscillatory flow reactor with pillar array electrodes improving mass transfer in electrosynthesis. *Electrochimica Acta* **2022**, *436*, 141435. DOI: 10.1016/j.electacta.2022.141435.

(90) Hammer, S.; Nanto, F.; Canu, P.; Ötvös, S. B.; Kappe, C. O. Application of an Oscillatory Plug Flow Reactor to Enable Scalable and Fast Reactions in Water Using a

Biomass-Based Polymeric Additive**. *ChemSusChem* **2024**, *17* (2), e202301149. DOI: 10.1002/cssc.202301149.

(91) Bianchi, P.; Williams, J. D.; Kappe, C. O. Oscillatory flow reactors for synthetic chemistry applications. *Journal of Flow Chemistry* **2020**, *10* (3), 475-490. DOI: 10.1007/s41981-020-00105-6.

(92) Masson, T. M.; Zondag, S. D. A.; Schuurmans, J. H. A.; Noël, T. Open-source 3D printed reactors for reproducible batch and continuous-flow photon-induced chemistry: design and characterization. *Reaction Chemistry & Engineering* **2024**. DOI: 10.1039/D4RE00081A.

(93) Jud, W.; Kappe, C. O.; Cantillo, D. One-pot multistep electrochemical strategy for the modular synthesis of epoxides, glycols, and aldehydes from alkenes. *Electrochemical Science Advances* **2021**, *1* (3), e2100002. DOI: 10.1002/elsa.202100002.

(94) Capaldo, L.; Wen, Z.; Noël, T. A field guide to flow chemistry for synthetic organic chemists. *Chemical Science* **2023**, *14* (16), 4230-4247. DOI: 10.1039/D3SC00992K.

(95) Jud, W.; Kappe, C. O.; Cantillo, D. A Continuous Flow Cell for High-Temperature/High-Pressure Electroorganic Synthesis. *ChemElectroChem* **2020**, *7* (13), 2777-2783. DOI: 10.1002/celc.202000696.

(96) Lölsberg, J.; Starck, O.; Stiefel, S.; Hereijgers, J.; Breugelmans, T.; Wessling, M. 3D-Printed Electrodes with Improved Mass Transport Properties. *ChemElectroChem* **2017**, *4* (12), 3309-3313, Article. DOI: 10.1002/celc.201700662 Scopus.

(97) Kisukuri, C. M.; Seidler, J.; Gärtner, T.; Rohrmann, D. F.; Waldvogel, S. R. Scalable Electrochemical Reduction of Nitrobenzotrifluorides to 3-Trifluoromethylanilines. *Organic Process Research & Development* **2024**, *28* (5), 1474-1485. DOI: 10.1021/acs.oprd.3c00067.

(98) von Keutz, T.; Cantillo, D.; Kappe, C. O. Enhanced mixing of biphasic liquid-liquid systems for the synthesis of gem-dihalocyclopropanes using packed bed reactors. *Journal of Flow Chemistry* **2019**, *9* (1), 27-34. DOI: 10.1007/s41981-018-0026-1.

(99) Labes, R.; Pastre, J. C.; Ingham, R. J.; Battilocchio, C.; Marçon, H. M.; Damião, M. C. F. C. B.; Tran, D. N.; Ley, S. V. Automated multistep synthesis of 2-pyrazolines in continuous flow. *Reaction Chemistry & Engineering* **2024**, *9* (3), 558-565. DOI: 10.1039/D3RE00515A.

(100) Asano, S.; Miyamura, H.; Matsushita, M.; Kudo, S.; Kobayashi, S.; Hayashi, J.-i. Impact of gas-solid direct contact on gas-liquid-solid reaction performance in a flow reactor. *Journal of Flow Chemistry* **2024**, *14* (1), 329-335. DOI: 10.1007/s41981-023-00295-9.

(101) Barrulas, R. V.; Tinajero, C.; Ferreira, D. P. N.; Illanes-Bordomás, C.; Sans, V.; Carrott, M. R.; García-González, C. A.; Zanatta, M.; Corvo, M. C. Poly(ionic liquid)-based aerogels for continuous-flow CO2 upcycling. *J. CO2 Util.* **2024**, *83*, 102771. DOI: 10.1016/j.jcou.2024.102771.

(102) Parra-Cabrera, C.; Achille, C.; Kuhn, S.; Ameloot, R. 3D printing in chemical engineering and catalytic technology: Structured catalysts, mixers and reactors. *Chem. Soc. Rev.* **2018**, *47* (1), 209-230, Review. DOI: 10.1039/c7cs00631d Scopus.

(103) Harding, M. J.; Brady, S.; O'Connor, H.; Lopez-Rodriguez, R.; Edwards, M. D.; Tracy, S.; Dowling, D.; Gibson, G.; Girard, K. P.; Ferguson, S. 3D printing of PEEK reactors for flow chemistry and continuous chemical processing. *React. Chem Eng.* **2020**, *5* (4), 728-735, Article. DOI: 10.1039/c9re00408d Scopus.

(104) Lebl, R.; Zhu, Y.; Ng, D.; Hornung, C. H.; Cantillo, D.; Kappe, C. O. Scalable continuous flow hydrogenations using Pd/Al2O3-coated rectangular cross-section 3D-printed static mixers. *Catalysis Today* **2022**, *383*, 55-63. DOI: 10.1016/j.cattod.2020.07.046.

(105) VapourtecLtd. *The V-3 pump – Active pressure regulator*. https://www.vapourtec.com/products/e-series-reagent-pumping/active-pressure-control/ (accessed 6/2024).
(106) Robertson, K.; Seeberger, P. H.; Gilmore, K. Rapid optimisation of API crystallisation in a segmented flow reactor with a continuous, variable temperature gradient. *Reaction Chemistry & Engineering* **2023**, *8* (1), 77-83. DOI: 10.1039/D2RE00183G.
(107) Contente, M. L.; Dall'Oglio, F.; Tamborini, L.; Molinari, F.; Paradisi, F. Highly Efficient Oxidation of Amines to Aldehydes with Flow-based Biocatalysis. *ChemCatChem* **2017**, *9* (20), 3843-3848. DOI: 10.1002/cctc.201701147.
(108) Winterson, B.; Rennigholtz, T.; Wirth, T. Flow electrochemistry: a safe tool for fluorine chemistry. *Chemical Science* **2021**, *12* (26), 9053-9059. DOI: 10.1039/D1SC02123K.
(109) Whipple, D. T.; Finke, E. C.; Kenis, P. J. A. Microfluidic Reactor for the Electrochemical Reduction of Carbon Dioxide: The Effect of pH. *Electrochemical and Solid-State Letters* **2010**, *13* (9), B109. DOI: 10.1149/1.3456590.
(110) Coley, C. W.; Eyke, N. S.; Jensen, K. F. Autonomous Discovery in the Chemical Sciences Part II: Outlook. *Angewandte Chemie International Edition* **2020**, *59* (52), 23414-23436. DOI: 10.1002/anie.201909989.
(111) Jose, N. A.; Kovalev, M.; Bradford, E.; Schweidtmann, A. M.; Chun Zeng, H.; Lapkin, A. A. Pushing nanomaterials up to the kilogram scale – An accelerated approach for synthesizing antimicrobial ZnO with high shear reactors, machine learning and high-throughput analysis. *Chemical Engineering Journal* **2021**, *426*, 131345. DOI: 10.1016/j.cej.2021.131345.
(112) Epps, R. W.; Bowen, M. S.; Volk, A. A.; Abdel-Latif, K.; Han, S.; Reyes, K. G.; Amassian, A.; Abolhasani, M. Artificial Chemist: An Autonomous Quantum Dot Synthesis Bot. *Advanced Materials* **2020**, *32* (30), 2001626. DOI: 10.1002/adma.202001626.
(113) Duros, V.; Grizou, J.; Xuan, W.; Hosni, Z.; Long, D.-L.; Miras, H. N.; Cronin, L. Human versus Robots in the Discovery and Crystallization of Gigantic Polyoxometalates. *Angewandte Chemie International Edition* **2017**, *56* (36), 10815-10820. DOI: 10.1002/anie.201705721.
(114) Granda, J. M.; Donina, L.; Dragone, V.; Long, D.-L.; Cronin, L. Controlling an organic synthesis robot with machine learning to search for new reactivity. *Nature* **2018**, *559* (7714), 377-381. DOI: 10.1038/s41586-018-0307-8.
(115) Chatre, L.; Socci, J.; Adams, S. J.; Denissenko, P.; Cherkasov, N. Design of 3D-printed structures for improved mass transfer and pressure drop in packed-bed reactors. *Chemical Engineering Journal* **2021**, *420*, 129762. DOI: 10.1016/j.cej.2021.129762.
(116) SolidWorks. *Solidworks 3D CAD*. https://www.solidworks.com/product/solidworks-3d-cad (accessed 07/2024).
(117) Autodesk. *Fusion 369*. https://www.autodesk.com/eu/products/fusion-360/overview (accessed 07/24).
(118) FreeCAD. *FreeCAD*. https://www.freecad.org/index.php (accessed 07/24).
(119) Tenorio-Suárez, M. I.; Gómez-Ortega, A.; Canales, H.; Piedra, S.; Pérez-Barrera, J. MaSMaker: An open-source, portable software to create and integrate maze-like surfaces into arbitrary geometries. *SoftwareX* **2022**, *19*, 101203. DOI: 10.1016/j.softx.2022.101203.
(120) Hyperganic. *HyDesign*. https://www.hyperganic.com/hydesign/ (accessed 07/2024).

(121) Hou, W.; Bubliauskas, A.; Kitson, P. J.; Francoia, J.-P.; Powell-Davies, H.; Gutierrez, J. M. P.; Frei, P.; Manzano, J. S.; Cronin, L. Automatic Generation of 3D-Printed Reactionware for Chemical Synthesis Digitization using ChemSCAD. *ACS Central Science* **2021**, *7* (2), 212-218. DOI: 10.1021/acscentsci.0c01354.

(122) Padoin, N.; Matiazzo, T.; Riella, H. G.; Soares, C. A perspective on the past, the present, and the future of computational fluid dynamics (CFD) in flow chemistry. *Journal of Flow Chemistry* **2024**, *14* (1), 239-256. DOI: 10.1007/s41981-024-00313-4.

(123) Bracconi, M.; Ambrosetti, M.; Okafor, O.; Sans, V.; Zhang, X.; Ou, X.; Da Fonte, C. P.; Fan, X.; Maestri, M.; Groppi, G.; et al. Investigation of pressure drop in 3D replicated open-cell foams: Coupling CFD with experimental data on additively manufactured foams. *Chemical Engineering Journal* **2019**, *377*, 120123. DOI: 10.1016/j.cej.2018.10.060.

(124) Nanto, F.; Ötvös, S. B.; Kappe, C. O.; Canu, P. Experimental and computational investigation of fluid flow and solid transport in split-and-recombine oscillatory flow reactors for organic chemistry in water. *J. Ind. Eng. Chem.* **2024**. DOI: 10.1016/j.jiec.2024.04.016.

(125) McDonough, J. R.; Ahmed, S. M. R.; Phan, A. N.; Harvey, A. P. The development of helical vortex pairs in oscillatory flows – A numerical and experimental study. *Chemical Engineering and Processing - Process Intensification* **2019**, *143*, 107588. DOI: 10.1016/j.cep.2019.107588.

(126) McDonough, J. R.; Murta, S.; Law, R.; Harvey, A. P. Oscillatory fluid motion unlocks plug flow operation in helical tube reactors at lower Reynolds numbers ($Re \leq 10$). *Chemical Engineering Journal* **2019**, *358*, 643-657. DOI: 10.1016/j.cej.2018.10.054.

(127) Dilberoglu, U. M.; Gharehpapagh, B.; Yaman, U.; Dolen, M. The Role of Additive Manufacturing in the Era of Industry 4.0. *Procedia Manufacturing* **2017**, *11*, 545-554. DOI: 10.1016/j.promfg.2017.07.148.

(128) Diederich, B.; Müllenbroich, C.; Vladimirov, N.; Bowman, R.; Stirling, J.; Reynaud, E. G.; Andreev, A. CAD we share? Publishing reproducible microscope hardware. *Nature Methods* **2022**, *19* (9), 1026-1030. DOI: 10.1038/s41592-022-01484-5.

(129) Balletti, C.; Ballarin, M.; Guerra, F. 3D printing: State of the art and future perspectives. *Journal of Cultural Heritage* **2017**, *26*, 172-182. DOI: 10.1016/j.culher.2017.02.010.

(130) Wu, H.; Fahy, W. P.; Kim, S.; Kim, H.; Zhao, N.; Pilato, L.; Kafi, A.; Bateman, S.; Koo, J. H. Recent developments in polymers/polymer nanocomposites for additive manufacturing. *Progress in Materials Science* **2020**, *111*, 100638. DOI: 10.1016/j.pmatsci.2020.100638.

(131) Tothill, A. M.; Partridge, M.; James, S. W.; Tatam, R. P. Fabrication and optimisation of a fused filament 3D-printed microfluidic platform. *Journal of Micromechanics and Microengineering* **2017**, *27* (3), 035018. DOI: 10.1088/1361-6439/aa5ae3.

(132) Schiel, F.; Peinsipp, C.; Kornigg, S.; Böse, D. A 3D-Printed Open Access Photoreactor Designed for Versatile Applications in Photoredox- and Photoelectrochemical Synthesis. *ChemPhotoChem* **2021**, *5* (5), 431-437. DOI: 10.1002/cptc.202000291.

(133) Neumaier, J. M.; Madani, A.; Klein, T.; Ziegler, T. Low-budget 3D-printed equipment for continuous flow reactions. *Beilstein J Org Chem* **2019**, *15*, 558-566. DOI: 10.3762/bjoc.15.50.

(134) Kitson, P. J.; Marie, G.; Francoia, J.-P.; Zalesskiy, S. S.; Sigerson, R. C.; Mathieson, J. S.; Cronin, L. Digitization of multistep organic synthesis in reactionware for on-

demand pharmaceuticals. *Science* **2018**, *359* (6373), 314-319. DOI: doi:10.1126/science.aao3466.

(135) van Melis, C. G. W.; Penny, M. R.; Garcia, A. D.; Petti, A.; Dobbs, A. P.; Hilton, S. T.; Lam, K. Supporting-Electrolyte-Free Electrochemical Methoxymethylation of Alcohols Using a 3D-Printed Electrosynthesis Continuous Flow Cell System. *ChemElectroChem* **2019**, *6* (16), 4144-4148, Article. DOI: 10.1002/celc.201900815 Scopus.

(136) Perales-Rondon, J. V.; Rojas, D.; Gao, W.; Pumera, M. Copper 3D-Printed Electrodes for Ammonia Electrosynthesis via Nitrate Reduction. *ACS Sustainable Chemistry & Engineering* **2023**, *11* (18), 6923-6931. DOI: 10.1021/acssuschemeng.2c06851.

(137) Iffelsberger, C.; Jellett, C. W.; Pumera, M. 3D Printing Temperature Tailors Electrical and Electrochemical Properties through Changing Inner Distribution of Graphite/Polymer. *Small* **2021**, *17* (24), 2101233. DOI: 10.1002/smll.202101233.

(138) Okafor, O.; Robertson, K.; Goodridge, R.; Sans, V. Continuous-flow crystallisation in 3D-printed compact devices. *Reaction Chemistry & Engineering* **2019**, *4* (9), 1682-1688. DOI: 10.1039/C9RE00188C.

(139) Ye, J.; Chu, T.; Chu, J.; Gao, B.; He, B. A Versatile Approach for Enzyme Immobilization Using Chemically Modified 3D-Printed Scaffolds. *ACS Sust. Chem. Eng.* **2019**, *7* (21), 18048-18054, Article. DOI: 10.1021/acssuschemeng.9b04980 Scopus.

(140) Stansbury, J. W.; Idacavage, M. J. 3D printing with polymers: Challenges among expanding options and opportunities. *Dental Materials* **2016**, *32* (1), 54-64. DOI: 10.1016/j.dental.2015.09.018.

(141) Caprioli, M.; Roppolo, I.; Chiappone, A.; Larush, L.; Pirri, C. F.; Magdassi, S. 3D-printed self-healing hydrogels via Digital Light Processing. *Nature Communications* **2021**, *12* (1), 2462. DOI: 10.1038/s41467-021-22802-z.

(142) Mohamed, M. G. A.; Kumar, H.; Wang, Z.; Martin, N.; Mills, B.; Kim, K. Rapid and Inexpensive Fabrication of Multi-Depth Microfluidic Device using High-Resolution LCD Stereolithographic 3D Printing. *Journal of Manufacturing and Materials Processing* **2019**, *3* (1), 26. DOI: 10.3390/jmmp3010026.

(143) Capel, A. J.; Edmondson, S.; Christie, S. D. R.; Goodridge, R. D.; Bibb, R. J.; Thurstans, M. Design and additive manufacture for flow chemistry. *Lab on a Chip* **2013**, *13* (23), 4583-4590. DOI: 10.1039/C3LC50844G.

(144) Feng, Y.; Zhang, H.; Wang, J.; Yang, Y. Performance Evaluation and Scale-Up Behavior of an Engineered In-Line Mixer for 3D Printing. *Industrial & Engineering Chemistry Research* **2021**, *60* (30), 11568-11578. DOI: 10.1021/acs.iecr.1c02320.

(145) Miralles-Comins, S.; Zanatta, M.; Gualdrón-Reyes, A. F.; Rodriguez-Pereira, J.; Mora-Seró, I.; Sans, V. Polymeric ionic liquid-based formulations for the fabrication of highly stable perovskite nanocrystal composites for photocatalytic applications. *Nanoscale* **2023**, *15* (10), 4962-4971. DOI: 10.1039/D2NR07254H.

(146) Luangwanta, T.; Turren-Cruz, S.-H.; Masi, S.; Das Adhikari, S.; Recalde, I. B.; Zanatta, M.; Iglesias, D.; Rodríguez-Pereira, J.; Gené-Marimon, S.; Martinez-Ferrero, E.; et al. Enabling white color tunability in complex 3D-printed composites by using lead-free self-trapped exciton 2D perovskite/carbon quantum dot inks. *Nanoscale* **2024**, *16* (21), 10262-10272. DOI: 10.1039/D4NR00707G.

(147) Miralles-Comins, S.; Zanatta, M.; Embid, S. G.; Alleva, M.; Chiappone, A.; Roppolo, I.; Mitchell, S. G.; Sans, V. Development of high-resolution 3D printable polymerizable ionic liquids for antimicrobial applications. *Device* **2024**, *2* (2), 100224. DOI: 10.1016/j.device.2023.100224.

(148) Hammer, A. J. S.; Leonov, A. I.; Bell, N. L.; Cronin, L. Chemputation and the Standardization of Chemical Informatics. *JACS Au* **2021**, *1* (10), 1572-1587. DOI: 10.1021/jacsau.1c00303.

(149) VapourtecLtd. *R-Series software – OPC-UA server and client.* https://www.vapourtec.com/products/r-series-control/r-series-software-opc-ua-server-and-client/ (accessed 06/2024).

(150) Bédard, A.-C.; Adamo, A.; Aroh, K. C.; Russell, M. G.; Bedermann, A. A.; Torosian, J.; Yue, B.; Jensen, K. F.; Jamison, T. F. Reconfigurable system for automated optimization of diverse chemical reactions. *Science* **2018**, *361* (6408), 1220-1225. DOI: doi:10.1126/science.aat0650.

(151) Cherkasov, N.; Bai, Y.; Expósito, A. J.; Rebrov, E. V. OpenFlowChem – a platform for quick, robust and flexible automation and self-optimisation of flow chemistry. *Reaction Chemistry & Engineering* **2018**, *3* (5), 769-780. DOI: 10.1039/C8RE00046H.

(152) Hielscher, M. M.; Dörr, M.; Schneider, J.; Waldvogel, S. R. LABS: Laboratory Automation and Batch Scheduling – A Modular Open Source Python Program for the Control of Automated Electrochemical Synthesis with a Web Interface. *Chemistry – An Asian Journal* **2023**, *18* (14), e202300380. DOI: 10.1002/asia.202300380.

(153) Maljuric, S.; Jud, W.; Kappe, C. O.; Cantillo, D. Translating batch electrochemistry to single-pass continuous flow conditions: an organic chemist's guide. *Journal of Flow Chemistry* **2020**, *10* (1), 181-190. DOI: 10.1007/s41981-019-00050-z.

(154) Yue, J.; Falke, F. H.; Schouten, J. C.; Nijhuis, T. A. Microreactors with integrated UV/Vis spectroscopic detection for online process analysis under segmented flow. *Lab on a Chip* **2013**, *13* (24), 4855-4863. DOI: 10.1039/C3LC50876E.

(155) Epps, R. W.; Felton, K. C.; Coley, C. W.; Abolhasani, M. Automated microfluidic platform for systematic studies of colloidal perovskite nanocrystals: towards continuous nano-manufacturing. *Lab on a Chip* **2017**, *17* (23), 4040-4047. DOI: 10.1039/C7LC00884H.

(156) Sans, V.; Porwol, L.; Dragone, V.; Cronin, L. A self optimizing synthetic organic reactor system using real-time in-line NMR spectroscopy. *Chemical Science* **2015**, *6* (2), 1258-1264. DOI: 10.1039/C4SC03075C.

(157) Chatterjee, S.; Guidi, M.; Seeberger, P. H.; Gilmore, K. Automated radial synthesis of organic molecules. *Nature* **2020**, *579* (7799), 379-384. DOI: 10.1038/s41586-020-2083-5.

(158) Laws, K.; Tze-Kiat Ng, M.; Sharma, A.; Jiang, Y.; Hammer, A. J. S.; Cronin, L. An Autonomous Electrochemical Discovery Robot that Utilises Probabilistic Algorithms: Probing the Redox Behaviour of Inorganic Materials. *ChemElectroChem* **2024**, *11* (1), e202300532. DOI: 10.1002/celc.202300532.

(159) Leonov, A. I.; Hammer, A. J. S.; Lach, S.; Mehr, S. H. M.; Caramelli, D.; Angelone, D.; Khan, A.; O'Sullivan, S.; Craven, M.; Wilbraham, L.; et al. An integrated self-optimizing programmable chemical synthesis and reaction engine. *Nature Communications* **2024**, *15* (1), 1240. DOI: 10.1038/s41467-024-45444-3.

(160) Matysiak, B. M.; Thomas, D.; Cronin, L. Reaction Kinetics using a Chemputable Framework for Data Collection and Analysis. *Angewandte Chemie International Edition* **2024**, *63* (9), e202315207. DOI: 10.1002/anie.202315207.

(161) Dabral, S.; Schaub, T. The Use of Carbon Dioxide (CO2) as a Building Block in Organic Synthesis from an Industrial Perspective. *Advanced Synthesis & Catalysis* **2019**, *361* (2), 223-246. DOI: 10.1002/adsc.201801215.

(162) Podrojková, N.; Oriňak, A.; Garcia-Verdugo, E.; Sans, V.; Zanatta, M. On the role of multifunctional ionic liquids for the oxidative carboxylation of olefins with carbon dioxide. *Catalysis Today* **2023**, *418*, 114128. DOI: 10.1016/j.cattod.2023.114128.

(163) Wang, L.; Que, S.; Ding, Z.; Vessally, E. Oxidative carboxylation of olefins with CO2: environmentally benign access to five-membered cyclic carbonates. *RSC Advances* **2020**, *10* (15), 9103-9115. DOI: 10.1039/C9RA10755J.
(164) Calmanti, R.; Selva, M.; Perosa, A. Tandem catalysis: one-pot synthesis of cyclic organic carbonates from olefins and carbon dioxide. *Green Chemistry* **2021**, *23* (5), 1921-1941. DOI: 10.1039/D0GC04168H.
(165) Wei, H.; Fang, Y.; Mulligan, P.; Chuirazzi, W.; Fang, H.-H.; Wang, C.; Ecker, B. R.; Gao, Y.; Loi, M. A.; Cao, L.; et al. Sensitive X-ray detectors made of methylammonium lead tribromide perovskite single crystals. *Nature Photonics* **2016**, *10* (5), 333-339. DOI: 10.1038/nphoton.2016.41.
(166) Alsalloum, A. Y.; Turedi, B.; Almasabi, K.; Zheng, X.; Naphade, R.; Stranks, S. D.; Mohammed, O. F.; Bakr, O. M. 22.8%-Efficient single-crystal mixed-cation inverted perovskite solar cells with a near-optimal bandgap. *Energy & Environmental Science* **2021**, *14* (4), 2263-2268. DOI: 10.1039/D0EE03839C.
(167) Saidaminov, M. I.; Abdelhady, A. L.; Maculan, G.; Bakr, O. M. Retrograde solubility of formamidinium and methylammonium lead halide perovskites enabling rapid single crystal growth. *Chemical Communications* **2015**, *51* (100), 17658-17661. DOI: 10.1039/C5CC06916E.
(168) Amari, S.; Verilhac, J.-M.; Gros D'Aillon, E.; Ibanez, A.; Zaccaro, J. Optimization of the Growth Conditions for High Quality CH3NH3PbBr3 Hybrid Perovskite Single Crystals. *Crystal Growth & Design* **2020**, *20* (3), 1665-1672. DOI: 10.1021/acs.cgd.9b01429.

Chapter 2. Objectives

Objectives

The relevance of the development new digital processes towards more sustainable production methods has been highlighted in the previous chapter. The aim of this thesis is to apply these concepts to develop different digitalized flow setups in the context of sustainable process development. The challenges faced involve the evaluation of alternative synthesis routes for a more efficient use of resources, and the development of new methodologies to produce materials for renewable energies. The Sustainable Development Goals mainly impacted by the present work are: *7. Affordable and clean energy*, *9. Industry, innovation and infrastructure*, *12. Responsible consumption and productio*n and *13. Climate action.* From a sustainable chemistry point of view, the main principles targeted are atom economy, design for energy efficiency and catalysis. The work developed can be divided into two theme areas: (1) sustainable synthesis and (2) advanced materials crystallization. Specific objectives for each area will be later detailed, but the global objectives (GO) of the work are the following:

- **GO1:** To develop flow setups for improved yield and selectivity. The focus is on creating systems that make a more efficient use of resources (reagents, solvents) and employs milder process conditions (P, T) than the state of the art.
- **GO2:** To incorporate digitalisation principles to those setups to further improve control over reaction outputs, by implementing digital control of reaction parameters and continuous monitorization of the products formed.
- **GO3:** To develop advanced reactor geometries, by combining CAD design and 3D printing, for improvements in parameters such as mixing, scalability or overall process yield.

(1) New routes for improved synthesis sustainability

The transition to more sustainable syntheses requires the review of multiple parameters, including improvements over reaction economy, the reuse of byproducts in alternative synthesis routes or the development of new catalytic routes. In this regard, flow chemistry has shown enhancements in selectivity and yield due to more efficient control over reaction conditions and enhanced mass transfer. The development of advanced reactor geometries, along the use of thermocatalysis or electrochemistry, can further improve the results obtained in these processes compared to batch. The coupling of these technologies may enable new synthesis routes, more energy efficient, safer and with reduced waste generation. The specific objectives (SO) of this area are:

- **SO1.1:** To develop new reactor geometries with improved mass transport for different synthetic applications.
- **SO1.2:** To apply continuous-flow synthetic methodologies to improve yield and selectivity compared to traditional batch technologies. The transformation of CO_2 to cyclic carbonates was selected as case of study.
    - Optimization of the electrochemical oxidation of olefins to epoxides.
    - Study the cycloaddition of CO_2 to the epoxide.

(2) Development of platforms for crystallization of advanced materials

Hybrid inorganic–organic perovskites are a material of great interest in the development of optoelectronic devices like solar cells. Polycrystalline thin films are widely used for device production, but grain boundaries impose limitations to their maximum performance. Single crystals are a proposed solution, but their synthesis by traditional methods is slow. Inverse Temperature Crystallization (ITC), in which solubility of the perovskite decreases as temperature increases, greatly improves growth speed, but poor control overgrowth conditions greatly hinder batch-to-batch reproducibility. The objectives in this area are:

- **SO2.1:** To develop a platform for the continuous growth of perovskite single crystals based on ITC.
- **SO2.2:** To improve control over crystal nucleation and growth to yield large single crystals with improved quality.
- **SO2.3:** To enable the fabrication of novel materials only possible with the digital platforms developed in this work. Mixed halide multi-material perovskites are demonstrated as proof of principle.

Chapter 3. Electrochemical Oscillatory Baffled Reactors Fabricated with Additive Manufacturing for Efficient Continuous-Flow Oxidations.

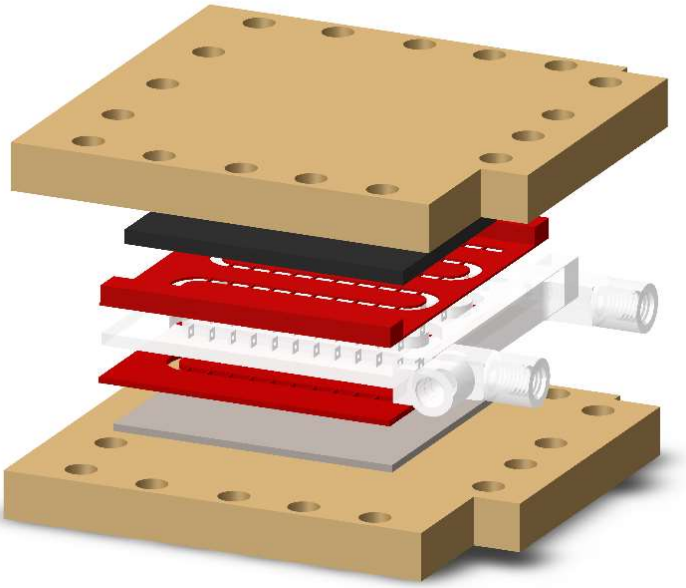

The results described during the present chapter have been already published. Reproduced from *ACS Sustainable Chemistry & Engineering* **2022**, *10* (7), 2388-2396.

3.1 Main text

3.1.1 Abstract

Electrochemical continuous-flow reactors offer a great opportunity for enhanced and sustainable chemical syntheses. Here we present a novel application of electrochemical continuous-flow oscillatory baffled reactors (ECOBRs) that combines advanced mixing features with electrochemical transformations to enable efficient electrochemical oxidations under continuous-flow at millimeter distance between electrodes. Different Additive Manufacturing techniques have been employed to rapidly fabricate the reactors. The electrochemical oxidation of NADH, a very sensitive substrate key for the regeneration of enzymes in biocatalytic transformations, has been employed as a benchmark reaction. The oscillatory conditions improved bulk mixing, facilitating the contact of reagents to the electrodes. Under oscillatory conditions, the ECOBR demonstrated improved performance in the electrochemical oxidation of NADH, attributed to improved mass transfer associated to the oscillatory regime.

3.1.2 Introduction

Continuous-flow synthetic methodologies are becoming a key technology for sustainable and efficient chemical manufacturing. [1] Electrochemical flow reactors are gaining interest as alternative methodologies to perform chemical transformations in a clean and efficient fashion, [2-7] especially when considering that energy can be obtained from renewable sources. This enables efficient transformations and reduces the amount of waste generated by avoiding the need for additives and auxiliary reagents to perform redox reactions. However, the performance of continuous-flow electro-reactors can be affected by mass-transfer limitations of reagents and products to the electrodes if the reactor geometry is not carefully controlled. [2] To address this, the electrodes are typically held apart by a few hundreds of microns, which improves mass transfer due to the small distances and it also minimises ohmic losses. [6] These inter-electrode distance requirements impose considerable limitations in the design of reactor architectures for continuous flow electro-reactors. Typically, flat parallel electrode configurations are chosen. [3] Advanced reactor architectures could help to overcome these limitations by improving mixing, thus enabling efficient performance at higher electrode distance. The higher reactor volume would in turn enable the integration of other enabling technologies for novel applications.[8]

In this regard, additive manufacturing (AM), commonly known as 3D printing, can offer new opportunities for the development of continuous-flow reactors, [9-11] advanced reactor architectures [12] and other continuous-flow applications like crystallizers, [13, 14] calorimeters [15] or magnetic resonance probes. [16] The digitalisation of the fabrication process enables the coupling of advanced and lean design techniques, like computational fluid dynamics (CFD), to allow the generation of optimised reactor structures[17] and the production of reactor geometries which are easily adaptable to commercial set-ups. [7] Moreover, with the aid of CFD simulations, the shape of the reactor and the position of other elements like static mixers can be fine-tuned to optimize flow dynamics and consequently reactor performance before manufacturing.[18]

A key advantage of flow chemistry is the ability to finely control mixing, which can be done by adding elements without moving parts (passive), [19] or with the use of an external energy source that produces changes in the flow resulting in better mixing. [20] The use of AM to generate advanced structures that enhance mixing in electrochemical flow systems is gaining attention. [8, 21, 22]. Indeed, the design of simple structures to improve mixing in parallel plate continuous-flow electro-reactors has been recently demonstrated, showcasing the potential of AM to improve the performance of electrochemical transformations under flow conditions. [23] Continuous-flow oscillatory baffled reactors (COBRs) are a specific class of chemical reactors that combine both passive and active mixing: the coupling of periodic constrictions and a mechanically generated oscillatory flow enables the generation of turbulent flow at low Reynolds (Re) numbers. [24, 25] The employment of additive manufacturing to generate miniaturised continuous oscillatory baffled reactors has been demonstrated previously by our group. [12]

Here, we report for the first time the design and fabrication of an electrochemical oscillatory baffled continuous flow reactor (ECOBR), which combines enhanced mixing in electrochemical systems, allowing for efficient anodic oxidations. The improved mixing was demonstrated by CFD studies and preliminary work with the designed reactor show the effect of oscillation in improving the cell performance. Enhanced performance of the ECOBR can be comparable to a commercial parallel plate flow cell for electrochemical oxidations of NADH under continuous-flow and opens the door to couple multiple enabling technologies, like electrochemical transformations, continuous-flow and other enabling technologies (e.g. biocatalysis).[26]

3.1.3 Experimental section

Production of the Additively Manufactured electrochemical flow reactor

Reactor: The baffled reactor was designed with CAD software (Creo Parametrics) and fabricated by laser sintering from nylon polyamide 12 (PA12) with an EOS P100 selective laser sintering (SLS) printer. Parts were built with 21W laser power (16W contour), 2500 mm s^{-1} scan speed, 0.25 mm scan spacing, 172.5°C build temperature, with the removable platform at 150°C.

Gaskets: Gaskets were initially printed in Formlabs Form 2 stereolithography (SLA) and Form 3 low force stereolithography (LFS) 3D printers using commercially available resins (Formlabs Flexible). Gaskets with the shape of the reactor and the baffles with a thickness of 0.5-1 mm were successfully fabricated. Alternatively, 0.5 mm thick gaskets were fabricated using an Ultimaker S5 fused filament printer, employing red thermoplastic polyurethane (TPU95) filament purchased from Ultimaker.

Outer casing: Parts were modelled using 3D design software and fabricated using a Formlabs 3 low force stereolitography (LFS) printer loaded with Formlabs Clear resin.

Proof of concept of the Additively Manufactured electrochemical flow reactor

Proof of concept experiments were carried out using the AM electroreactor equipped with 6x6 cm^2 electrodes (working electrode (WE): glassy carbon; counter electrode (CE): stainless steel 316). Cell performance was monitored using potentiometry with a two-electrode system on a μStat400 potentiostat (Metrohm Dropsens) using the cables supplied by the manufacturer, at a flow rate of 0.1 mL min^{-1} and 15 μA cm^{-2} current, using as electrolyte 0.1 M aqueous 2-amino-2-(hydroxymethyl)propane-1,3-diol hydrochloride (Tris-HCl) which had been pH adjusted to *ca.* 6.7 with sodium hydroxide. Oscillatory flow regimes were generated by a C3000 programmable pump (Tricontinent) equipped with a 5 mL syringe.

Electrochemical oxidation of NADH

Cyclic voltammetries (CV) for evaluating the electrochemical oxidation of NADH were recorded using an Autolab PGSTAT302 (EcoChemie) with a three electrode configuration (WE: glassy Carbon; RE: silver; CE: platinum). The concentration of Tris-HCl was 80 and 100 mM and NADH was 15 mM. The pH was varied at 7 and 8.8.

An Ammonite8 spiral cell (100x0.2x0.5 cm) equipped with 8.5 cm electrodes (WE: carbon/PVDF; CE: stainless steel) was used as a control experiment for the electrochemical oxidation of NADH enzymatic cofactor. The AM electroreactor was equipped with square 6x6 cm^2 electrodes (WE: glassy carbon; CE: Stainless steel 316) and the oscillation was controlled by a programmable Tricontinent C3000 pump equipped with a 5 mL syringe. Experiments for both reactors were performed using an aqueous solution of 1 mM of NADH in Tris-HCl (10 mM, pH=7), electrical current was controlled using an Autolab PGSTAT302 (EcoChemie). The current density (A cm^{-2}) and normalized reactor productivity ($mol_{NAD+}\cdot mol_{NADH}^{-1}\cdot min^{-1}\cdot cm^{-2}$) were calculated as follows:

$$Current\ density\ = \frac{I}{area_{elec.}} \qquad \text{(Eq. 1)}$$

$$Normalized\ reactor\ productivity\ (NRP)\ = \frac{mol_{NAD^+}}{mol_{NADH}\cdot t_{res}\cdot area_{elec.}} \qquad \text{(Eq. 2)}$$

$$Current\ efficiency\ (\%)\ = \frac{e^- oxidation}{e^- supplied}\cdot 100 = \frac{2\cdot mol_{NAD^+}\cdot F}{I\cdot t_{res}}\cdot 100 \qquad \text{(Eq. 3)}$$

where I is the intensity of current set with the potentiostat, $area_{elec}$ corresponds to the geometric area of the electrode in contact with the reaction media; mol_{NAD+} and mol_{NADH} are the mols of product and reagent respectively; t_{res} is the residence time. F is the Faraday constant (96485 C mol^{-1}).

Quantification of NAD^+ concentration

In a typical experiment, a NADH solution in Tris-HCl was pumped through the reactor in order to fully load it and to reach the steady state conditions. The residence time was calculated as the ratio between the volumetric flow rate and the total volume of the reactor. The NADH solution was pumped for the equivalent of two bed volumes, i.e. twice the residence time. Then it was assumed that steady state had been reached. The cell was maintained at constant current through this transient period and continued during the steady state experiments. Applied currents were chosen using the Faraday equation (Eq. S1) applied to the reaction conditions (flow rate, concentration), with the aim of driving full conversion during the residence time. The NADH cofactor oxidation was quantified through its use in the enzymatic transformation of glucose into glucolactone employing a commercially available glucose dehydrogenase (GDH) enzyme. After the enzymatic reaction, the samples were analysed in UV-visible spectrophotometer at 340 nm and quantified through a calibration curve of NAD^{+} (Figures S1 and S2).

CFD Simulations

The flow dynamics were resolved using the ANSYS-CFX 20 solver, based on the element-based finite volume method. [27].Given the reduced Reynolds number (Re) [27, 28] of the flow, a transitional shear stress transport (SST) k–ω model turbulence model was used and the liquid was described as a Newtonian incompressible fluid. Two tracers were added to the flow, with a molecular diffusivity of 10^{-8} m^2 s and a Schmidt number (ratio between turbulent eddy viscosity and eddy mass diffusivity) [27, 29] for turbulent dispersion of 0.9. The first tracer (inert tracer) entered through the inlet side and served to characterize the inlet flow mixing. The second tracer was generated as a mass flux, tracer mass (m_{tracer}) per unit area and time, at the electrodes at a rate given by:

$$\frac{\partial m_{tracer}}{\partial A\, \partial t} = k\, \frac{(C_{sat} - C_{tracer})}{C_{sat}} \qquad \text{(Eq. 4)}$$

In the simulations, $C_{sat} = 0.1\, kg\, m^{-3}$ and $k = 1\, mg\, mm^2 s^{-1}$. C_{tracer} was the tracer volume concentration right next to the electrode, and was calculated by the solver as it depends on the flow conditions.

Two transient simulations were performed to reproduce the flow advancement through the reactor. The inlet was modelled as an opening boundary condition so the fluid can enter and leave the flow domain. The velocity at this boundary was set as:

$$U(t) = U_{mean}\left[1 + A\, sin\left(2\pi \frac{t}{T}\right)\right] \qquad \text{(Eq. 5)}$$

with the values $U_{mean} = 1\ \mathrm{mm\ s^{-1}}$ and $T = 2$ s. The amplitude was set to 0 for the steady state case and $A = 10$ for the pulsating one.

Results and discussion

The initial design of the baffled reactor was based on a modification of a previously reported AM mCOBR reactor configuration. [12] The channels were designed with a square section and open on both sides to accommodate the electrodes on the upper and lower walls of the reactor (Figure 1A). The reactor module is sandwiched with the electrodes on top and bottom and the whole structure is completed with AM gaskets and support structures that are bolted together (Figure 1B). The reactor modules were printed by selective laser sintering (SLS) in polyamide-12 (PA12) (Figure 1C). Nylon is a robust, chemically resistant and versatile material to generate structures that could be subsequently modified to add functionality. [30] The structure is separated by gaskets fabricated with thermoplastic polyurethane (TPU95, Ultimaker) employing fused filament fabrication (FFF) technology (Figure 1D). The gaskets (0.5 mm thickness) were printed with geometries matching the baffles. Alternatively, the gaskets were fabricated with commercial flexible SLA resin (Flexible resin, Formlabs), but they were damaged upon utilization in the electrochemical set-up (Figure S3). The design of the gaskets was modified to adapt to the size of the different electrodes. Stainless steel plates were cut to the size of the reactor chips and therefore required flat gaskets from the same size. The glassy carbon electrodes had narrower dimensions. Hence, the gaskets were modified to fill the gap between the electrode and the reactor module, thus facilitating the assembly of the ECOBR device, which was bolted together and tightened until no leak was observed by pumping distilled water through the reactor chamber at controlled flow rates. The pump flow rates were calibrated in the assembled set-up to ensure there were no leaks.

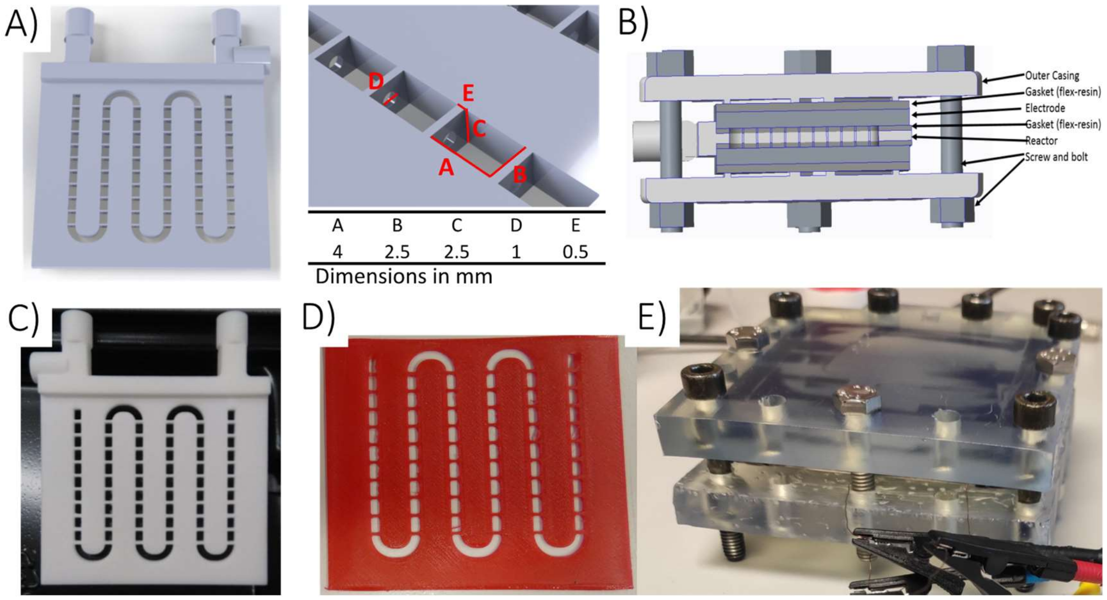

Figure 1 *A) General CAD design of the baffled section of the reactor (left), with a detailed view of the baffles (right) including the characteristic dimensions. B) Schematic representation of ECOBR assembly. C) Baffled reactor section fabricated in nylon employing selective laser sintering (SLS). D) Gasket with tailored design matching baffles fabricated in TPU95 employing fused filament fabrication (FFF). E) ECOBR assembly detail.*

Proof-of-concept experiments were performed using the ECOBR assembled as previously described (Figure 1E), similarly to our previously reported method[12]. A potentiostat was employed to measure the difference of electric potential under a constant current employing a two-electrode system, glassy carbon was used as the working electrode and stainless steel as the counter electrode (Figure S4). Oscillatory conditions were achieved by controlling the Tricontinent C3000 pump with in-house developed code using Labview (Figure S5). The parameters controlled by the user were frequency and amplitude of the oscillations, the latter actually controlling how much volume is displaced back and forth; it should be considered that due to the nature of oscillatory movement, the net flow of the oscillatory action is zero.

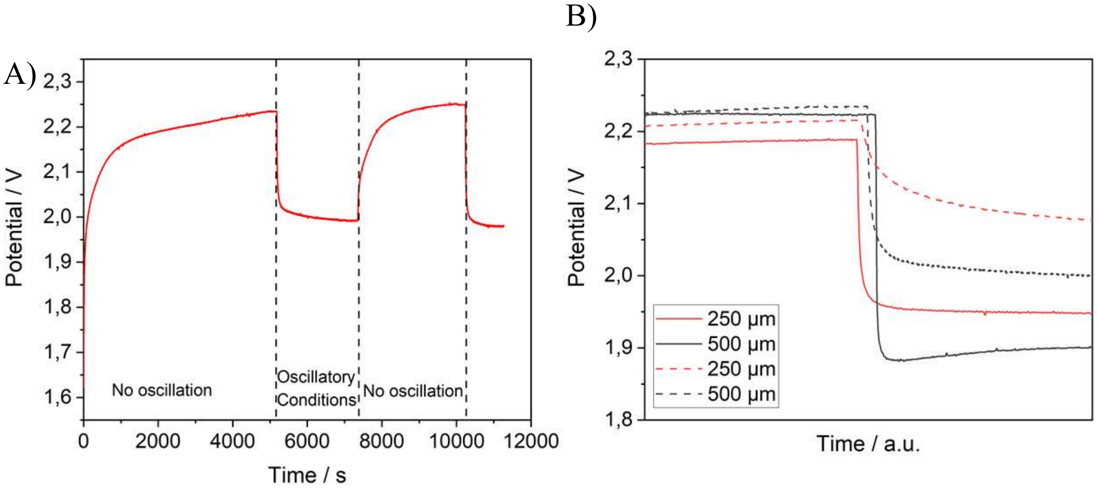

Figure 2. Chronoamperometry measurements of the ECOBR showing the effect of oscillatory conditions; A) Activation and deactivation of the conditions. B) Potential drop for different parameter combinations (Amplitude: 250 µm for red line, 500 µm for black line. Frequency: 1Hz for dashed lines, 5Hz for solid lines).

The observed variations of the cell potential were due to the impact that oscillatory conditions on the observed electrochemical process, presumably the electrolysis of the electrolyte (Tris-HCl). A flow of 0.1 mL min^{-1} was constantly pumped through the ECOBR while a current of 4.1 µA cm^{-2} was applied. Changes in potential were observed due to the differences of the operation of the reactor associated to different mixing conditions. We noted that when the cell was arranged with the cathode on top, the cell started behaving erratically and large bubbles were observed in the reactor outlet. Hence, the cathode was placed in the bottom to prevent gas evolution. Initially, no oscillatory regime was induced and the chamber was left to stabilise for 3 minutes. Afterwards, a rapid increase in the potential was initially observed, followed by a stabilisation period. The cell potential increased to above 2.2 V after 5000 s electrolysis (Figure 2A). However, once the syringe pump was activated and oscillatory conditions were initiated, the potential suddenly dropped then slowly stabilized until it stabilized at below 2.0 V. If oscillation stopped, the potential grew again until it reached values similar to the original ones (Figure 2A).

The combined effect of oscillatory conditions and the baffled design of the reactor was expected to improve mass transport within the cell.[31] This means that the transformation promoted by the ECOBR would be facilitated under oscillatory conditions.

The effect of the oscillation parameters on ΔV, i.e. the difference of potential observed before the oscillation started (V_0) and the potential observed upon stabilization under oscillatory conditions, was examined. As seen in Table 1, an increase in frequency from 1 Hz to 5 Hz is correlated with a decrease of the cell potentials (Table 1, entries 1 and 4). The effect of frequency achieved a maximum, evidenced by the lack of significant improvement at 10 Hz (Table 1, entry 7), in line with the behaviour reported for COBRs in the literature [12, 25]. This has been explained as once a threshold frequency is trespassed, the effect of the oscillatory flow dominates over the net flow, the continuous reactor operates more likely to a batch reactor and mixing is hindered.[32]

Table 1 Decrease in cell potential for different oscillation parameter combinations

Entry	**Amplitude / µm**	**Frequency / Hz**	**$\Delta V\ V_o^{-1}$ / %**
1	125	1	5.1
2	250	1	7.5
3	500	1	12.0
4	125	5	10.2
5	250	5	11.0
6	500	5	14.0
7	250	10	11.0

Flow dynamics were simulated in a virtual reactor with similar dimensions and operating conditions as the one used in the experimental part (Figure S7) to illustrate the enhanced mixing provided by the oscillating flow. The results demonstrate that the pulses of the oscillating conditions significantly enhance the mixing of the flow, thus improving the contact of the fluid with the walls of the reactor, which correspond to the electrodes.

Figure 3 shows the concentration of the inert tracer across the reactor cross-section. In the non-oscillating state (Figure 3A), the tracer remains close to the reactor axis (note the distribution in the central cell). The tracer distribution in the oscillating state is shown in Figure 3B. In this case, the tracer is distributed across the whole cell section, reaching the walls in a higher proportion, which should favour the electrochemical processes.

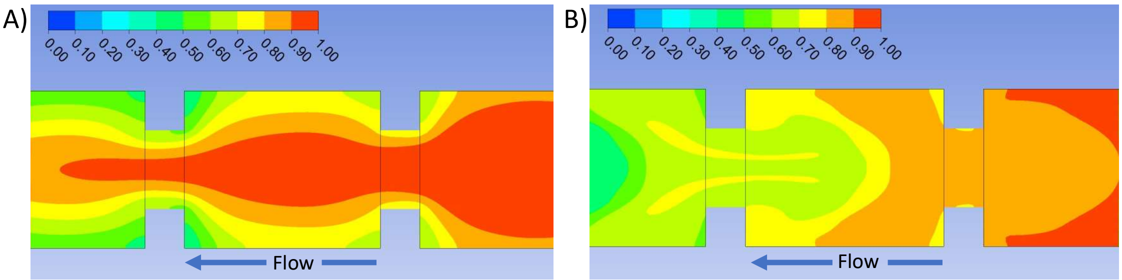

Figure 3 CFD simulation of concentration of inert tracer for: A) non-oscillating conditions and B) oscillating conditions.

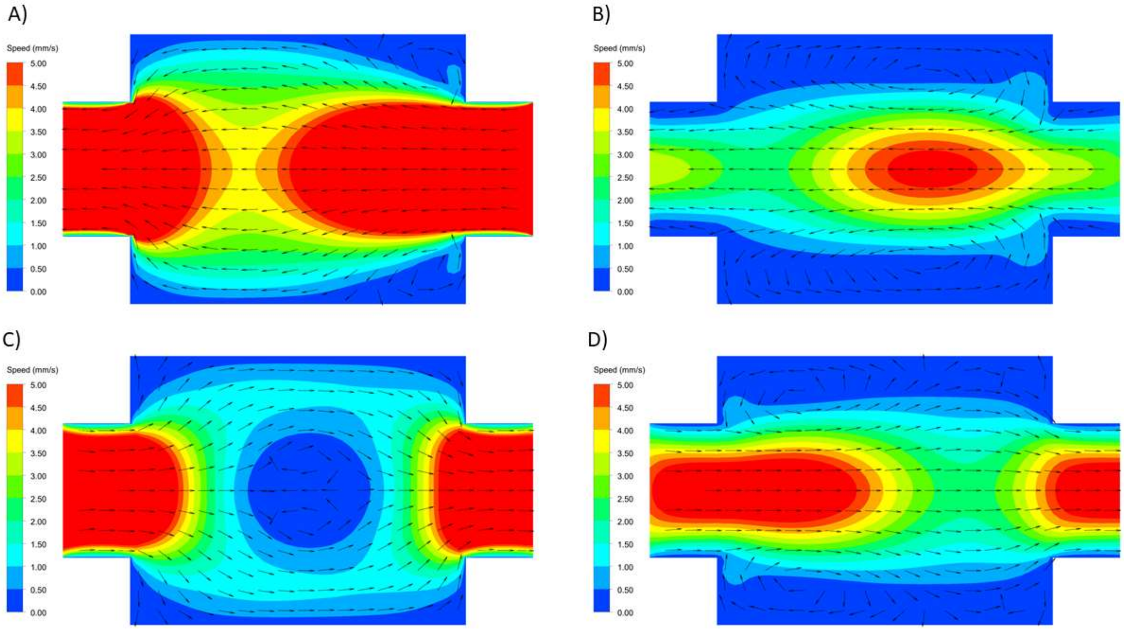

Figure 4. . Results from CFD simulations for the velocity fields under oscillatory conditions. Colour represents flow speed and arrows indicate flow direction (arrow size scales with velocity). Images from A) to D) correspond to different oscillation times inside half cycle

The improved mixing is due to the change of the flow paths, i.e., it is not related to flow induced turbulence. This can be noted in the Figure 4, which represents the CFD calculated velocity fields at four different times within half an oscillating cycle. The flow in the non-oscillating case (Figure S8) is limited to the central region, flowing smoothly from the cell inlet towards the cell outlet. As the cell section is bigger than the tubular region, the flow slightly spreads, but cannot efficiently reach the electrodes. Figures 4A to 4D show the flow at different time steps under oscillatory conditions. These figures clearly show the formation of mixing vortexes (Figure 4B and 4D) and strong flow-reversal conditions (Figure 4C) near the electrodes. This flow field enhances the mixing compared to the non-oscillatory conditions, characterized by low speeds near the electrodes and an even flow distribution.

Once the concept of the ECOBR was demonstrated, the next step was to evaluate its efficacy in a reaction process. The use of biocatalysts in industrial environments has grown since they allow the use of environmentally friendlier conditions and offer great selectivity. However many enzymes require cofactors in their catalytic pathways, and since the cost of cofactors is usually high, their regeneration is essential. [33] The NADH/NAD+ is a cofactor redox couple that intervenes in numerous interesting reactions, such as those catalysed by dehydrogenase enzymes. [34] Furthermore, the electrooxidation of NADH to NAD^+ has been thoroughly studied over the years [35-37] and used in applications such as biosensors. [34] For all these reasons, the NADH oxidation was chosen for evaluate our proposed reactor.

Before proceeding with the experiments using the reactor, a cyclic voltammetry was performed using NADH 15mM in Tris-HCl buffer to verify that the electro oxidation could take place in the reaction medium (Figure 5A, additional conditions and blank CVs described in Figure S4). The voltammogram showed that NADH was oxidized to NAD+ (Figure 5A) at 0.6 V as previous works using glassy carbon have established [38], thus confirming that oxidation could be carried out in the ECOBR.

Initially, the testing under continuous-flow conditions was undertaken in a commercial Ammonite8 electrochemical flow cell, which served as a benchmark of the oxidation reaction, which later was performed in the ECOBR. It is important to note that the reactor conditions are not strictly comparable in terms of performance and productivity due to the use of different current densities and electrode materials. The design of the Ammonite 8 reactor features a circular cell with a carved spiral pathway that the solution has to traverse while in contact with electrodes placed on the top and bottom walls of the reactor. The amount of NAD^+ generated was quantified employing an enzymatic method (see SI for more details and Figures S1-S2), this also demonstrated that the electrochemically oxidated/regenerated cofactor is active in enzymatic reactions. Preliminary tests with a solution of NADH (1mM) were performed with the cell potential fixed at 1V, higher than required for the oxidation of NADH (Figure 5B), which caused the current to increase to 0.18 A and presumably caused the observed overoxidation (Figure 5C). The oxidation of NADH is a two-electron process, given a faradaic efficiency of 100%, the amount of charge transferred would be equal to the amount of charge supplied of 2 F·mol^{-1} (F being 96485 C). Hence, the current intensity was set to a value calculated with Eq. S1, providing the required amount of charge for a complete conversion during the residence time. For a residence time of 100 min, and a molar flow rate of 0.01 mmol·min^{-1} (calculated as concentration x volumetric flow rate), eq. S1 predicted a required current of 32A. Under these conditions a stable regime was observed and steady state was easily achieved. When a current above the calculated with Eq. S1 was applied a negative effect on the yield of NADH was observed (Figure 5D and Table S1). This is presumably due to the overoxidation of the substrate at high current values.

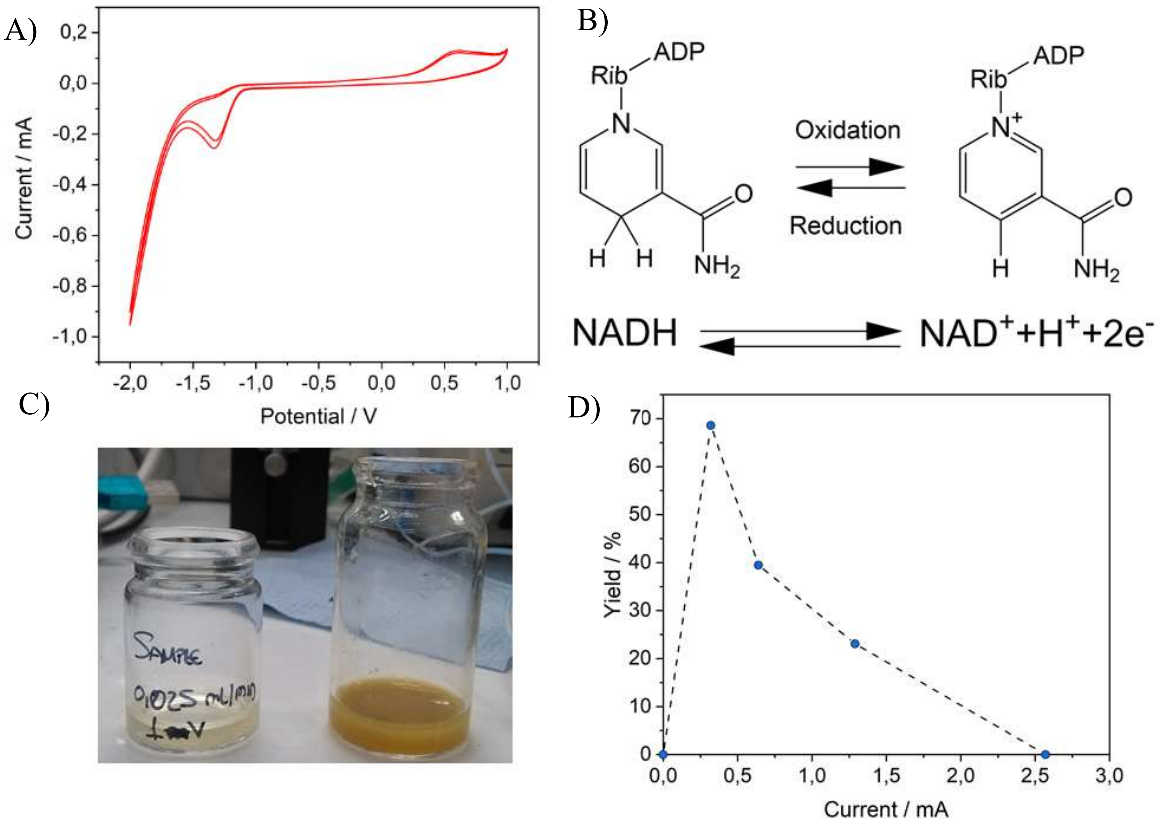

Figure 5. A) Cyclic voltammetry of the oxidation of NADH 15mM in Tris-HCl 100mM (pH 7.0). WE glassy carbon, CE platinum, reference AgCl, scan rate = 500 mV s^{-1} B) Redox reaction of NADH. C) Degraded samples after applying a high current. D) Graph

of yield vs current using Ammonite 8 spiral reactor. Flow rate = 0.01 mL min^{-1}; t_{res} = 100 min; room temperature, [NADH] = 10 mM

Table 2 Results of the NADH oxidation for different continuous-flow conditions

Entry	**Reactor**	**Flow / mL min^{-1}**	**t_{Res} / min**	**I / µA**	**Curr. dens. / µA cm^{-2}**	**Faradaic Efficiency / %**	**Normalized reactor productivity·10^4 / mol_{NAD+} mol_{NADH}^{-1} min^{-1} cm^{-2}**
1	Amm8	0.01	100	32	1.6	81	4.1
2	Amm8	0.02	50	64	3.2	39	3.9
3	Amm8	0.05	20	160	8.1	14	3.5
4	ECOBR	0.01	230	32	4.2	62	3.5
5	ECOBR	0.02	115	64	8.3	56	6.3
6	ECOBR	0.05	46	160	20.8	27	7.6
7	ECOBR	0.1	23	320	41.5	11	6.2

The normalized reactor productivity (NRP) parameter (Eq.2) was employed to compare the performance of the different experiments. Here, the NRP was calculated as the productivity of the reactor in terms of molar flow rate of product (mol NAD$^+$ min^{-1}) per mol of reagent (NADH) and electrode surface area along the reactor channels. Different values of current and flow rates were evaluated for the Ammonite8 cell (Table 2, entries 1-3) and for the AM ECOBR without oscillatory regime (Table 2, entries 4-7). In both reactors, the highest yield was achieved with the lowest flow rate, thus with longer residence time (Table 2, entry 1). The NRP of the reactor did not drop significantly as the flow rate was changed, which suggests that mass transfer in the cell was relatively efficient. It is important to keep in mind that the electrode distance is of *ca.* 0.2 mm. Next, the AM reactor was evaluated without using oscillatory conditions in order to find the optimum flow for this reactor. In this case, the electrodes are placed about 3 mm from each other, which is an order of magnitude higher than in the commercial cell. This enables the integration of supplementary features, like the baffles, which can play additional roles for enhanced performance. Like for the commercial reactor, the highest yield was obtained with the lowest flow rate evaluated, corresponding to the highest residence time (Table 2, entry 4). The productivity correlates the moles of product formed with the residence time of the reaction, representing the amount of product generated per unit of time. Hence, the productivity does not necessarily correlate with the highest yield, but with the highest reaction rate. Indeed, it was achieved with a residence time of 46 minutes (Table 2, entry 6). Therefore, these conditions were chosen for the oscillatory experiments.

In order to elucidate the effect of the oscillations on the NRP, the current density was selected based on eq. S1, which as previously mentioned calculates the stoichiometric amount of charge required for a full conversion of the electrolyzed reagents and it showed optimal performance with the Ammonite cell (see Figure 5D and Table S1, entry 2). Different combinations of amplitude and frequency were set using the flow rate and current previously selected, and their impact on the oxidation of NADH was evaluated in the ECOBR. The NRP values observed were higher than for non-oscillating conditions under most of the combinations studied, except the one with lowest amplitude (Table 3, entry 2). The best performance was achieved at an amplitude of 1 mm and a frequency of 0.5 Hz (Table 3, entry 3). The productivity observed was 2.2-fold higher than the same conditions without oscillating conditions.

Table 3 Results of the NADH oxidation for different conditions using the AM flow reactor with different oscillation conditions.

Entry	**λ / Hz**	**A / µm**	**Faradaic Efficiency / %**	**NRP $\cdot 10^4$ / mol$_{NAD+}$ mol$_{NADH}^{-1}$ min^{-1} cm^{-2}**
1	0	0	27	7.6
2	1	500	20	5.6
3	0.5	1000	60	16.9
4	1	1000	42	11.8
5	2	1000	31	8.7
6	1	1500	32	9.0

Reaction conditions. Flow rate = 0.05 mL min^{-1}; t_{res} = 46 min; I = 160 µA; current density = 20.8 µA cm^{-2}

The oscillatory regime of the ECOBR demonstrated an effect on the yield of NAD$^+$ observed. Indeed, an increase in frequency led to lower yields (Figure 6A), while amplitude did not show a defined trend (Figure 6B). The generation of oscillations enhanced the performance of the ECOBR in terms of mols of NADH generated per unit of time and surface area of electrode.

Improving mass transport in the liquid phase can undoubtedly improve the performance of electrochemical flow reactors. In micro and millireactors, laminar flow is predominant so there are different strategies to solve this problem, one of them is giving the reagents enough time to allow mixing by either lowering the flow or increasing the pathway. [39] It is demonstrated that as previously seen in the CFD simulations, the oscillations generated in the baffled reactor produce vortexes that improve the mixing, which could work as a different strategy to improve performance in electrochemical reactors (Figure 6C).

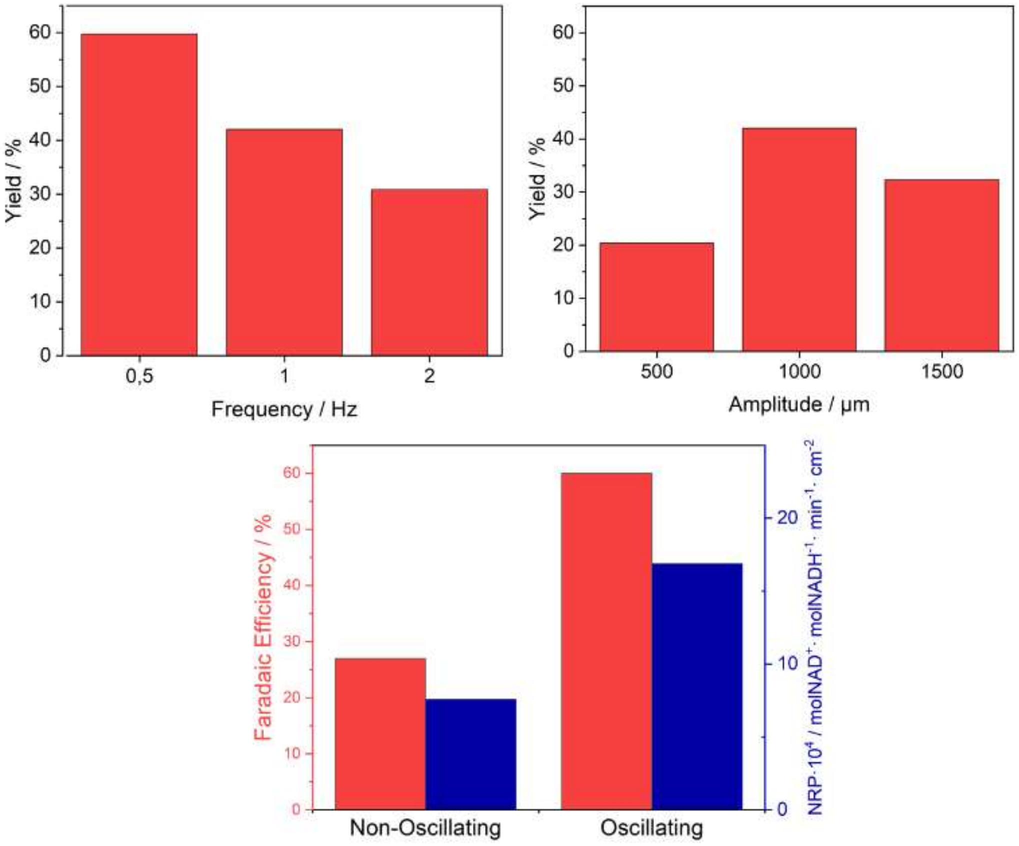

Figure 6. A) Influence of oscillation frequency on the yield of the AM ECOBR reactor (amplitude used: 1000 µm). B) Influence of oscillation amplitude on the yield (frequency used: 1Hz). C) Faradaic efficiency and normalized reactor productivity (NRP) for the ECOBR under oscillating (l=0.5 Hz, A = 1mm) and non-oscillating conditions, both experiments at flow rate = 0.05 mL min^{-1}; t_{res} = 46 min; I = 160 µA; current density = 20.8 µA cm^{-2}.

3.1.4 Conclusions

In the present work an electrochemical continuous-flow oscillatory baffled reactor was manufactured with different AM techniques. The design features a pathway segmented by numerous baffles that under a continuous oscillatory flow promote the generation of vortexes, which improve the mixing in the reactor. Different parameters of amplitude and frequency of the oscillations, flow and current were evaluated for the oxidation of NADH. The ECOBR under oscillatory flow conditions showed improved performance.

The simplicity of this reactor architecture paves the way for new applications that may arise thanks to the easy tuning enabled by AM. Additionally, the materials can be adapted to optimize each reaction system and the different components can even be functionalized to broaden their range of applications, thus envisioning the possibility of efficiently combining multiple processes in integrated devices, this offering novel windows of opportunity for sustainable chemical manufacturing.

3.1.5 References

1. Gutmann, B.; Cantillo, D.; Kappe, C. O., Continuous-Flow TechnologyA Tool for the Safe Manufacturing of Active Pharmaceutical Ingredients. *Angew. Chem.-Int. Ed.* **2015,** *54* (23), 6688-6728, DOI: 10.1002/anie.201409318.

2. Noël, T.; Cao, Y.; Laudadio, G., The Fundamentals Behind the Use of Flow Reactors in Electrochemistry. *Acc. Chem. Res.* **2019,** *52* (10), 2858-2869, DOI: 10.1021/acs.accounts.9b00412.

3. Walsh, F. C.; Ponce de León, C., Progress in electrochemical flow reactors for laboratory and pilot scale processing. *Electrochim. Acta* **2018,** *280*, 121-148, DOI: https://doi.org/10.1016/j.electacta.2018.05.027.

4. Maljuric, S.; Jud, W.; Kappe, C. O.; Cantillo, D., Translating batch electrochemistry to single-pass continuous flow conditions: an organic chemist's guide. *J. Flow Chem.* **2020,** *10* (1), 181-190, DOI: 10.1007/s41981-019-00050-z.

5. Kabeshov, M. A.; Musio, B.; Ley, S. V., Continuous direct anodic flow oxidation of aromatic hydrocarbons to benzyl amides. *React. Chem Eng.* **2017,** *2* (6), 822-825, DOI: 10.1039/C7RE00164A.

6. Brown, R. C. D., The Longer Route can be Better: Electrosynthesis in Extended Path Flow Cells. *Chem. Rec.* **2021,** *21*, 1– 17 DOI: https://doi.org/10.1002/tcr.202100163.

7. van Melis, C. G. W.; Penny, M. R.; Garcia, A. D.; Petti, A.; Dobbs, A. P.; Hilton, S. T.; Lam, K., Supporting-Electrolyte-Free Electrochemical Methoxymethylation of Alcohols Using a 3D-Printed Electrosynthesis Continuous Flow Cell System. *Chemelectrochem* **2019,** *6* (16), 4144-4148, DOI: 10.1002/celc.201900815.

8. Sans, V., Emerging trends in flow chemistry enabled by 3D printing: Robust reactors, biocatalysis and electrochemistry. *Curr. Opin. Green Sustain. Chem.* **2020,** *25*, 100367, DOI: https://doi.org/10.1016/j.cogsc.2020.100367.

9. Kitson, P. J.; Rosnes, M. H.; Sans, V.; Dragone, V.; Cronin, L., Configurable 3D-Printed millifluidic and microfluidic 'lab on a chip' reactionware devices. *Lab Chip* **2012,** *12* (18), 3267-3271, DOI: 10.1039/c2lc40761b.

10. Penny, M. R.; Rao, Z. X.; Peniche, B. F.; Hilton, S. T., Modular 3D Printed Compressed Air Driven Continuous-Flow Systems for Chemical Synthesis. *Eur. J. Org. Chem.* **2019,** *2019* (23), 3783-3787, DOI: https://doi.org/10.1002/ejoc.201900423.

11. Rao, Z. X.; Patel, B.; Monaco, A.; Cao, Z. J.; Barniol-Xicota, M.; Pichon, E.; Ladlow, M.; Hilton, S. T., 3D-Printed Polypropylene Continuous-Flow Column Reactors: Exploration of Reactor Utility in SNAr Reactions and the Synthesis of Bicyclic and Tetracyclic Heterocycles. *Eur. J. Org. Chem.* **2017,** *2017* (44), 6499-6504, DOI: https://doi.org/10.1002/ejoc.201701111.

12. Okafor, O.; Weilhard, A.; Fernandes, J. A.; Karjalainen, E.; Goodridge, R.; Sans, V., Advanced reactor engineering with 3D printing for the continuous-flow synthesis of silver nanoparticles. *React. Chem Eng.* **2017,** *2* (2), 129-136, DOI: 10.1039/c6re00210b.

13. Okafor, O.; Robertson, K.; Goodridge, R.; Sans, V., Continuous-flow crystallisation in 3D-printed compact devices. *React. Chem Eng.* **2019,** *4* (9), 1682-1688, DOI: 10.1039/c9re00188c.

14. Thomas, K. M.; Kwon, S.; Lakerveld, R., Continuous Protein Crystallization in Mixed-Suspension Mixed-Product-Removal Crystallizers. *Crys. Growth Des.* **2021,** *21* (2), 757-769, DOI: 10.1021/acs.cgd.0c00885.

15. Maier, M. C.; Leitner, M.; Kappe, C. O.; Gruber-Woelfler, H., A modular 3D printed isothermal heat flow calorimeter for reaction calorimetry in continuous flow. *Reaction Chem. Eng.* **2020,** *5* (8), 1410-1420, DOI: 10.1039/d0re00122h.

16. Xie, J.; You, X.; Huang, Y.; Ni, Z.; Wang, X.; Li, X.; Yang, C.; Zhang, D.; Chen, H.; Sun, H.; Chen, Z., 3D-printed integrative probeheads for magnetic resonance. *Nat. Commun.* **2020,** *11* (1), 5793, DOI: 10.1038/s41467-020-19711-y.

17. Bracconi, M.; Ambrosetti, M.; Okafor, O.; Sans, V.; Zhang, X.; Ou, X.; Da Fonte, C. P.; Fan, X.; Maestri, M.; Groppi, G.; Tronconi, E., Investigation of pressure drop in 3D replicated open-cell foams: Coupling CFD with experimental data on additively manufactured foams. *Chem. Eng. J.* **2019,** *377*, 120123, DOI: https://doi.org/10.1016/j.cej.2018.10.060.

18. Bettermann, S.; Kandelhard, F.; Moritz, H. U.; Pauer, W., Digital and lean development method for 3D-printed reactors based on CAD modeling and CFD simulation. *Chem. Eng. Res. Des.* **2019,** *152*, 71-84, DOI: 10.1016/j.cherd.2019.09.024.

19. Lee, C.-Y.; Chang, C.-L.; Wang, Y.-N.; Fu, L.-M., Microfluidic Mixing: A Review. *Int. J. Mol. Sci.* **2011,** *12* (5), 3263-3287, DOI: 10.3390/ijms12053263.

20. Hessel, V.; Löwe, H.; Schönfeld, F., Micromixers—a review on passive and active mixing principles. *Chem. Eng. Sci.* **2005,** *60* (8), 2479-2501, DOI: https://doi.org/10.1016/j.ces.2004.11.033.

21. Walsh, F. C.; Arenas, L. F.; Ponce de León, C., Editors' Choice—Critical Review—The Bipolar Trickle Tower Reactor: Concept, Development and Applications. *J. Electrochem. Soc.* **2021,** *168* (2), 023503, DOI: 10.1149/1945-7111/abdd7a.

22. Ambrosi, A.; Shi, R. R. S.; Webster, R. D., 3D-printing for electrolytic processes and electrochemical flow systems. *J. Mater. Chem. A* **2020,** *8* (42), 21902-21929, DOI: 10.1039/D0TA07939A.

23. Márquez-Montes, R. A.; Collins-Martínez, V. H.; Pérez-Reyes, I.; Chávez-Flores, D.; Graeve, O. A.; Ramos-Sánchez, V. H., Electrochemical Engineering Assessment of a Novel 3D-Printed Filter-Press Electrochemical Reactor for Multipurpose Laboratory Applications. *ACS Sustain. Chem. Eng.* **2020,** *8* (9), 3896-3905, DOI: 10.1021/acssuschemeng.9b07368.

24. McDonough, J.; Armett, J.; Law, R.; Harvey, A. P., Coil-in-Coil Reactor: Augmenting Plug Flow Performance by Combining Different Geometric Features Using 3D Printing. *Ind. Eng. Chem. Res.* **2019,** *58* (47), 21363-21371, DOI: 10.1021/acs.iecr.9b04239.

25. Reis, N.; Vicente, A. A.; Teixeira, J. A.; Mackley, M. R., Residence times and mixing of a novel continuous oscillatory flow screening reactor. *Chem. Eng. Sci.* **2004,** *59* (22), 4967-4974, DOI: https://doi.org/10.1016/j.ces.2004.09.013.

26. Porcar, R.; Sans, V.; Ríos-Lombardía, N.; Gotor-Fernández, V.; Gotor, V.; Burguete, M. I.; García-Verdugo, E.; Luis, S. V., Stereoselective Chemoenzymatic Synthesis of Enantiopure 2-(1H-imidazol-yl)cycloalkanols under Continuous Flow Conditions. *ACS Catal.* **2012,** *2* (9), 1976-1983, DOI: 10.1021/cs300282w.

27. ANSYS® Academic Research, Release 20.2, Help System, ANSYS CFX Reference Guide, ANSYS Inc.

28. Fogler, S. H., *Elements of Chemical Reaction Engineering,*. 5th ed.; Prentice Hall International: New Jersey, 2011.

29. Tominaga, Y.; Stathopoulos, T., Turbulent Schmidt numbers for CFD analysis with various types of flowfield. *Atmos. Environ.* **2007,** *41*, 8091-8099, DOI.

30. Peris, E.; Okafor, O.; Kulcinskaja, E.; Goodridge, R.; Luis, S. V.; Garcia-Verdugo, E.; O'Reilly, E.; Sans, V., Tuneable 3D printed bioreactors for transaminations under continuous-flow. *Green Chem.* **2017,** *19* (22), 5345-5349, DOI: 10.1039/c7gc02421e.

31. Lölsberg, J.; Starck, O.; Stiefel, S.; Hereijgers, J.; Breugelmans, T.; Wessling, M., 3D-Printed Electrodes with Improved Mass Transport Properties. *ChemElectroChem* **2017,** *4* (12), 3309-3313, DOI: 10.1002/celc.201700662.

32. Avila, M.; Fletcher, D. F.; Poux, M.; Xuereb, C.; Aubin, J., Mixing performance in continuous oscillatory baffled reactors. *Chem. Eng. Sci.* **2020,** *219*, 115600, DOI: https://doi.org/10.1016/j.ces.2020.115600.

33. Bommarius, A. S.; Paye, M. F., Stabilizing biocatalysts. *Chem. Soc. Rev.* **2013,** *42* (15), 6534-6565, DOI: 10.1039/C3CS60137D.

34. Bartlett, P. N.; Simon, E.; Toh, C. S., Modified electrodes for NADH oxidation and dehydrogenase-based biosensors. *Bioelectrochem.* **2002,** *56* (1), 117-122, DOI: https://doi.org/10.1016/S1567-5394(02)00047-6.

35. Moiroux, J.; Elving, P. J., Effects of adsorption, electrode material, and operational variables on the oxidation of dihydronicotinamide adenine dinucleotide at carbon electrodes. *Anal. Chem.* **1978,** *50* (8), 1056-1062, DOI: 10.1021/ac50030a015.

36. Gorton, L.; Domínguez, E., Electrochemistry of NAD(P)+/NAD(P)H. In *Encyclopedia of Electrochemistry*, A.J. Bard: 2007; pp 67-134.

37. Immanuel, S.; Sivasubramanian, R., Electrochemical studies of NADH oxidation on chemically reduced graphene oxide nanosheets modified glassy carbon electrode. *Mater. Chem. Phys.* **2020,** *249*, 123015, DOI: https://doi.org/10.1016/j.matchemphys.2020.123015.

38. Wang, S.; Yao, Z.; Yang, T.; Zhang, Q.; Gao, F., An Enzymatic Electrode Integrated with Alcohol Dehydrogenase and Chloranil in Liquid-Crystalline Cubic Phases on Carbon Nanotubes for Sensitive Amperometric Detection of NADH and Ethanol. *J. Electrochem. Soc.* **2019,** *166* (10), G116-G121, DOI: 10.1149/2.1341910jes.

39. Maier, M. C.; Lebl, R.; Sulzer, P.; Lechner, J.; Mayr, T.; Zadravec, M.; Slama, E.; Pfanner, S.; Schmölzer, C.; Pöchlauer, P.; Kappe, C. O.; Gruber-Woelfler, H., Development of customized 3D printed stainless steel reactors with inline oxygen sensors for aerobic oxidation of Grignard reagents in continuous flow. *React. Chem Eng.* **2019,** *4* (2), 393-401, DOI: 10.1039/c8re00278a.

3.2 Supporting information

NAD+ quantification

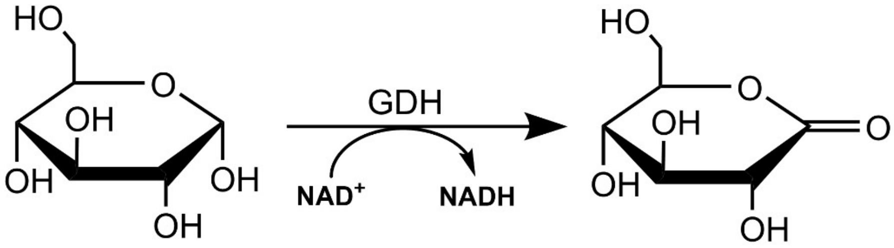

Figure S1 Reaction used for the NAD$^+$ quantification

The NADH cofactor oxidation was quantified through its use in the enzymatic transformation of glucose into glucolactone employing GDH enzyme. After the enzymatic reaction, the samples were analysed in UV-vis spectrophotometer at 340 nm and quantified through a calibration curve of NAD+.

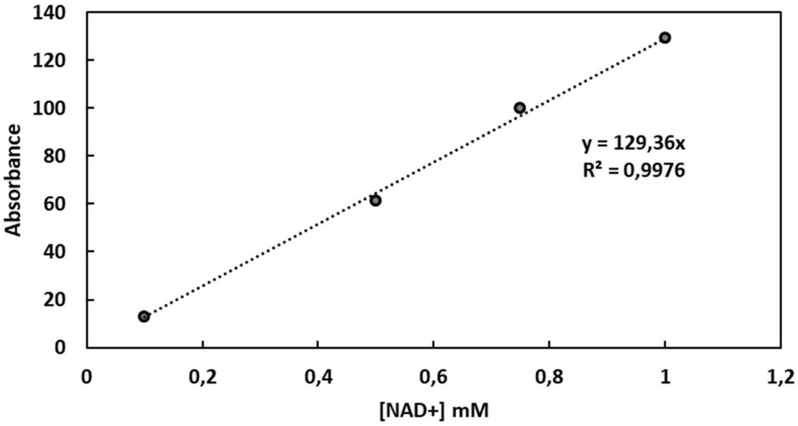

[NAD+] / mM	Absorbance / a.u.
0,1	12,9
0,5	61,4
0,75	99,7
1	129

Figure S2. Calibration curve for NAD+ concentration

Gaskets

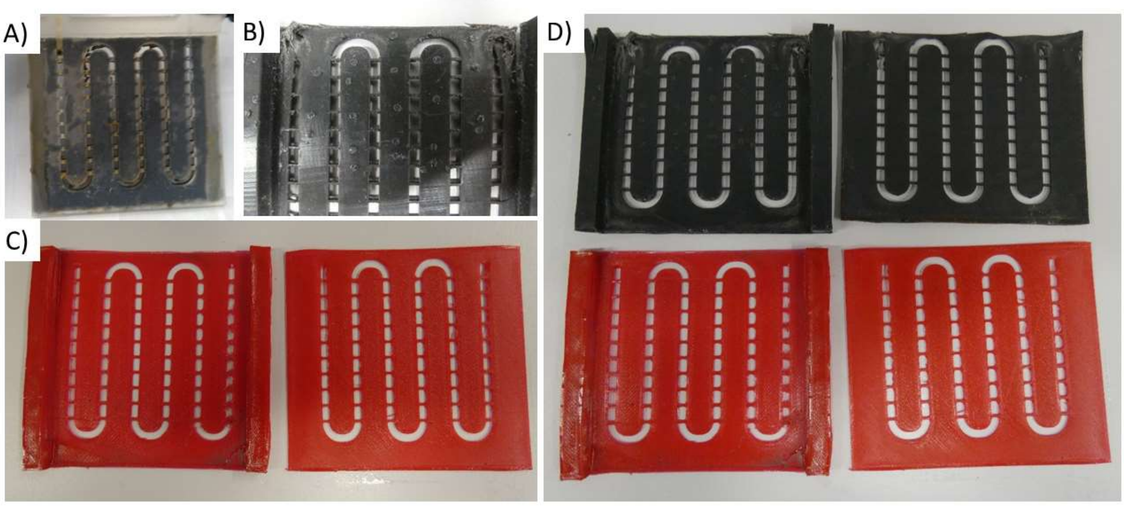

Figure S3 A) Flexible resin gaskets degraded after working without limited current. B) Flexible resin gaskets status after a batch of experiments. C) TPU gaskets after a batch of experiments D) Comparison of the status between flexible resing and TPU gaskets.

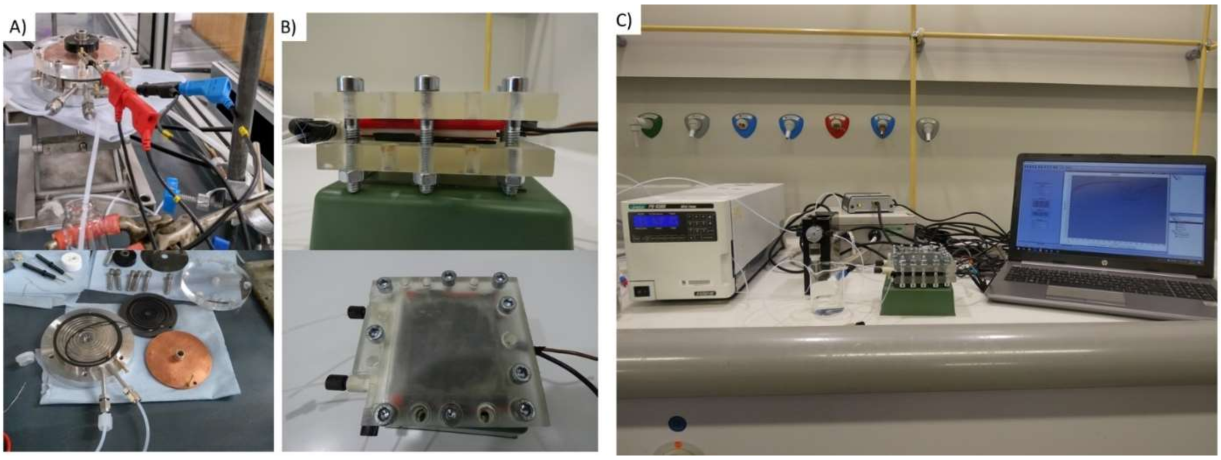

Figure S4 A) Ammonite8 Spiral Reactor B) 3D Printed ECOBR C) Setup used for the ECOBR experiments.

Programming of the syringe pump used for oscillation

A Labview VI was developed to control the syringe pump that generates the oscillating flow. The front panel for the executable can be seen at figure S5A, there the user can input the desired oscillating conditions. The block diagram comprises a series of cases that activate different functions, including the start/stop of the oscillation and other processes like pump cleaning or initialization, an example can be seen at figure S5B.

Finally, the oscillation order is sent to the pump as a string of commands in the required format generated using the code seen in figure S5C.

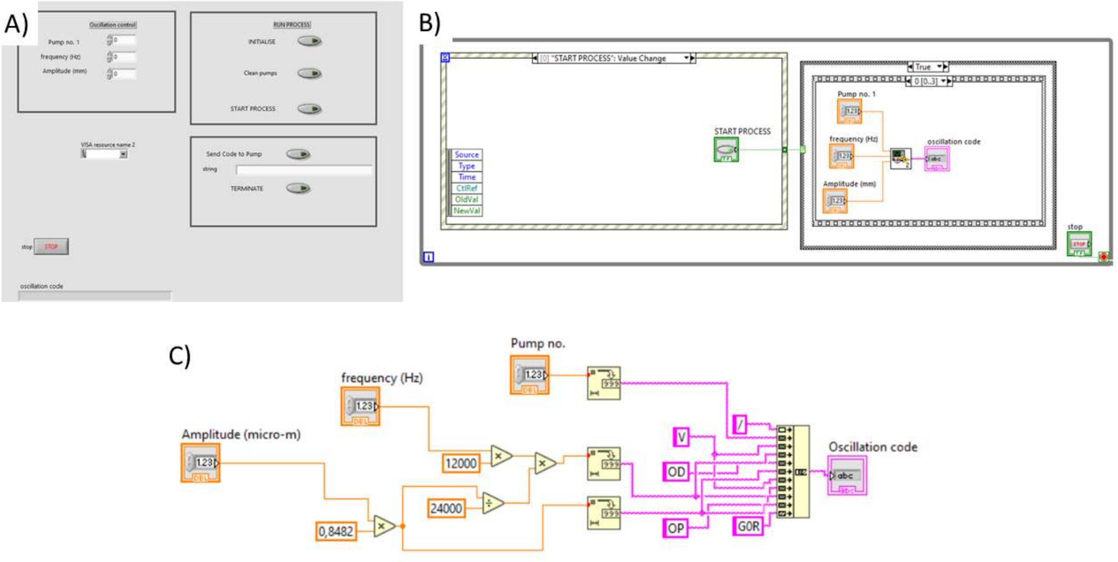

Figure S5 A) Front panel of the VI executable where user can select conditions. B) Part of the block diagram. C) Block diagram for the generation of the oscillation code.

CV of the oxidation of Tris-HCl

The voltage variations recorded in the proof of concept experiments observed were presumably due to the oxidation of Tris-HCl. A CV for Tris-HCl was performed.

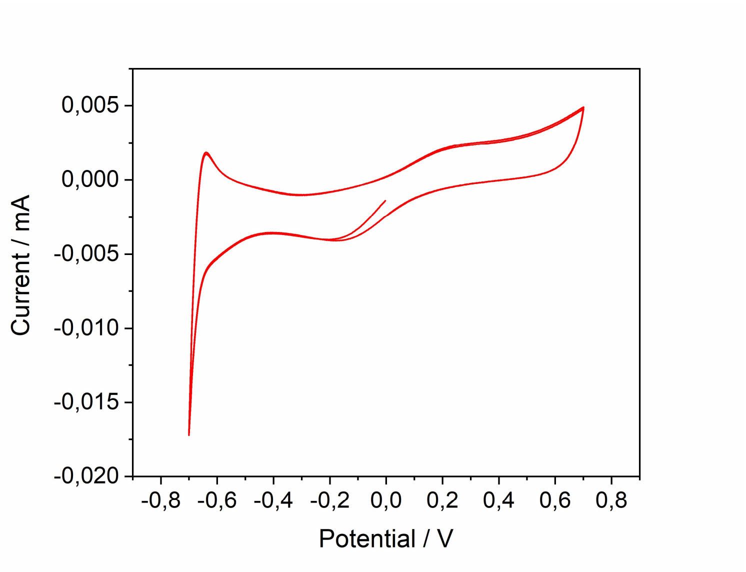

Figure S6. Cyclic voltammetry of the oxidation of NADH

Geometry used for the CFD simulations

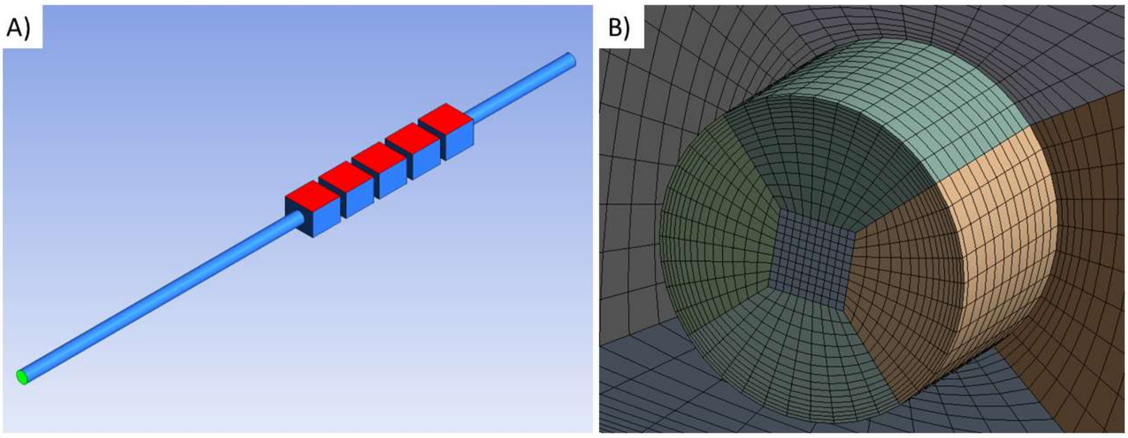

Figure S7 A) Simplified 3D geometry used for the simulation. Red: electrodes. Green: inlet and outlet B) structure of the mesh

To accelerate the calculations, a subset of 5 cells was simulated (figure S4A), with proper inlet and outlet separation to minimize the effects of boundary conditions on the flow inside the cells. The surfaces marked in red represent the cell electrodes. Figure S4B shows a detail of the fully structured 3D mesh that was generated, which is based on the O-GRID approach for the tubular regions.

Simulated flow field for non-oscillatory conditions

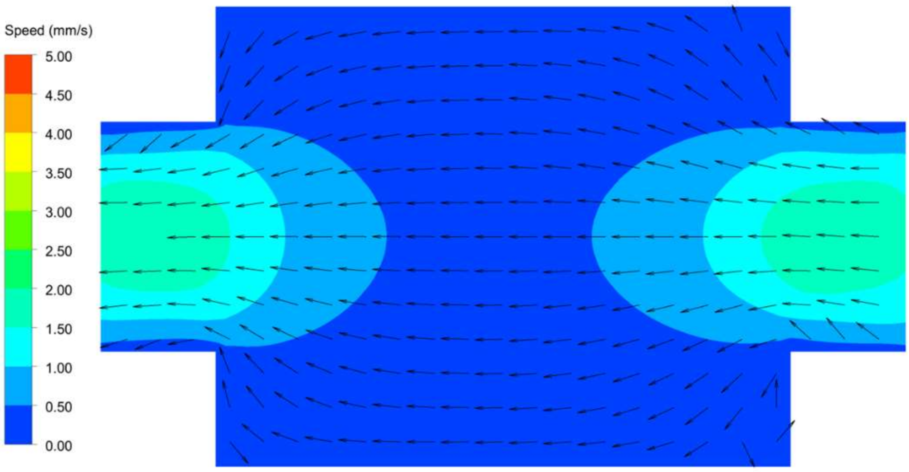

Figure S8 Flow field for the non-oscillatory conditions.

The flow is distributed evenly when the reactor is working under non-oscillatory conditions. Also, flow speed is extremely low and near the electrodes.

Study of higher currents in reaction

The use of higher currents lowered the yield presumably due to overoxidation of the substrate. Therefore, definitive experimental currents were selected using Faraday's law, considering the concentraion of NADH used, the cell's volume, residence time and flow.

$$i = \frac{m \cdot n \cdot F}{t} \qquad \text{(Eq. S1)}$$

Where i = current, m = mol, n = electron number, F = Faraday constant, t = time.

Table S1 Results for experiments using higher currents in a commercial Ammonite 8 cell reactor at a concentration of NADH 10 mM.

Entry	Flow / mL min^{-1}	t_{Res} / min	I / mA	Curr. dens. / mA cm^{-2}	Yield / %
1	0.01	100	0	0.0000	0
2	0.01	100	0.32	0.0160	68.59
3	0.01	100	0.64	0.0320	39.48
4	0.01	100	1.29	0.0645	23.08
5	0.01	100	2.57	0.1285	0

Chapter 4. Multi-step oxidative carboxylation of olefins with carbon dioxide by combining electrochemical and 3D-printed flow reactors

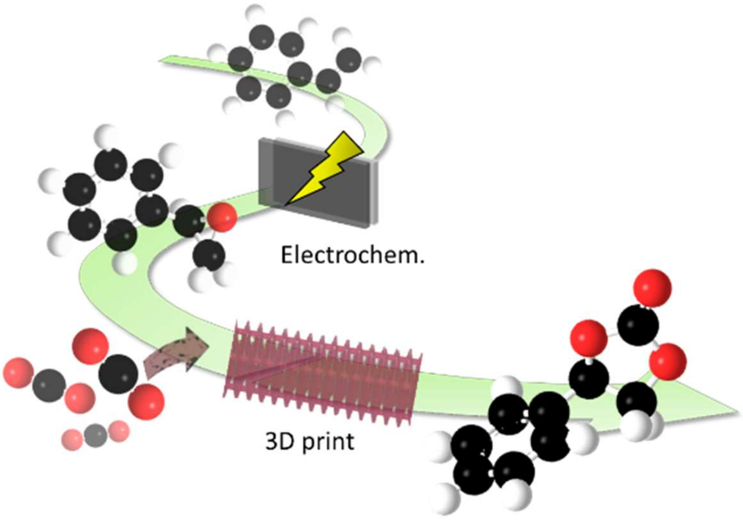

The results described during the present chapter have been already published. Reproduced from *Green Chemistry* **2023**, *25* (23), 9934-9940 with permission from Royal Society of Chemistry.

4.1 Main text

4.1.1 Abstract:

The selective oxidation of alkenes to form epoxides followed by the cycloaddition of CO_2 is a sustainable and cost-efficient method to generate functional cyclic carbonates. The use of continuous-flow process allows to seamlessly integrate both reactions sequentially with tailored and optimised conditions for each of the transformations to produce the cyclic carbonates. Here, we successfully demonstrate olefin electrooxidation, followed by the cycloaddition of CO_2 to produce cyclic carbonates employing 3D printed (3DP) reactors in continuous-flow and without the need for intermediate purification steps. This approach is highly convenient since the electrolyte (ammonium salt) from the electrochemical reaction acts also as a catalyst in the cycloaddition reaction. Different parameters in the electrochemical oxidation were evaluated (e.g. solvent, electrode, electrolyte, concentrations and current intensity). Complete conversion and high selectivity (>80%) towards the formation of epoxide were observed. The electrolyte served as catalyst for the cycloaddition reaction. The digital design of the 3DP reactor played a crucial role to efficiently undertake the cycloaddition reaction, showing increased productivity (space time yield of 4.38 $g_{prod}h^{-1}L^{-1}$) compared to a coil and a packed bed reactors. Consecutive CO_2 cycloaddition reaction were also evaluated and a global yield of 83% to cyclic carbonate was observed for styrene. The system exhibited stability and stable activity for at least 20 h.

4.1.2 Introduction

The use of CO_2 as a building block for the synthesis of high-value heterocyclic compounds is receiving more interest in the framework of sustainable and green chemistry. [1, 2] The reaction between carbon dioxide and epoxides is 100% atom efficient and one of the few industrially feasible processes for producing cyclic carbonates. Organic carbonates are functional molecules that can be used as starting materials for the synthesis of polycarbonate and polyurethane, green solvents, fuel additives, and fine chemical intermediates. Recently, one-pot "oxidative carboxylation," or the direct synthesis of cyclic carbonates from alkenes and CO_2, has drawn a lot of attention since alkenes are more readily available and less expensive than the related epoxides. Such a procedure would eliminate the necessity for isolating and purifying epoxides, which are frequently unstable and extremely reactive. In this field, the synthetic approach can be divided into two main groups*:* *(i)* direct oxidation and carboxylation in only one step, and[3, 4] *(ii) one-pot.* [4, 5] Despite the CO_2 cycloaddition to epoxide is well-known in the literature, [6-8] catalytic methods for generating organic carbonates from olefins are considerably scarcer. [9] Additionally, to design a multifunctional catalyst efficient and selective for both the reactions still remains a big challenge. [5, 10]

An oxidant is essential to carry out the epoxidation reaction, but it is incompatible with the carboxylation catalyst system which usually employs a Lewis base. The use of organic oxidants, like tert-Butyl hydroperoxide (TBHP), is common for epoxidation reactions, but has several disadvantages due to its hazardous nature, flammability, toxicity, poor atom-economy, and the generation of waste. A greener alternative is hydrogen peroxide, as it produces water as the only by-product, however this leads to a biphasic epoxidation reaction (as most olefins are hydrophobic) and hence requires long reaction times as mass transfer across the aqueous–organic interface controls the rate of the reaction. [11] Within this context, electrochemical oxidation appears as a green and non-toxic alternative for this reaction. Recently Cantillo *et. al.* (2021) [12] presented the development of a selective approach for the synthesis of epoxides, diols, and aldehydes from a single set of electrochemical reaction components. The modularity permits the selection of the desired product in batch conditions. Alternatively, the use of continuous flow processes emerges as a solution for reducing heat and mass transfer limitations, something particularly important in multiphasic reaction systems. [13-15] Even though the CO_2 cycloaddition to epoxides under continuous-flow has been explored, [16-21] the direct oxidative carboxylation of olefins to yield cyclic carbonate using it is still an almost unexplored field. [11, 14, 22] In 2021, Perosa *et. al.* [9] highlighted the necessity for the development of continuous-flow direct oxidative carboxylation processes, since only two studies have been reported to date. In 2014, Jamison *el. at.* [22] demonstrated a multi-step flow system to perform oxidative carboxylation of olefins the using n-bromosuccinimide (NBS) and 1,8-Diazabicyclo(5.4.0)undec-7-ene (DBU), resulting in 43-89% of yield of cyclic carbonate. In 2017, Rioux and co-workers[11] described a flow reactor based on a rhenium catalyzed epoxidation of the olefin followed by trapping the epoxide by CO_2 in the presence of an aluminum catalyst and iodide salt, resulting in yield from 48-98%.

Motivated by these researches, the main focus of the present study will be on implementing a continuous flow setup to enhance production capacity of olefins carboxylation. [12] The epoxidation of olefins will be performed using electrochemical oxidation, avoiding the use of reagents incompatible with the next step. The cycloaddition step will be done in a bespoke reactor produced using 3D printing. Additive manufacturing techniques (AM), also known as three-dimensional printing (3DP), have been recently receiving attention for designing and fabricating objects with specific shapes. [23] 3DP allows to produce reactor geometries that improve mass transfer during flow reactions[24] and the development of tailored formulations for 3DP to use in specific applications, such as catalysis or materials, is a growing and attractive area. [25-31] In this regard, recently, we have demonstrated the application of a 3D printed catalytic reactor in a flow system to convert CO_2 into cyclic carbonate using an epoxide as starting point. [28]

In this work, we successfully demonstrate the oxidative carboxylation of olefins with CO_2 to produce cyclic carbonates under continuous flow. The system performs the transformation in two steps with compatible conditions, avoiding the need of intermediate purification. Furthermore, the electrolyte employed in the first reaction serves as catalyst for the CO_2 cycloaddition, reducing the atom economy of the process. The geometry of a tailored designed 3DP reactor played a crucial role in the improvement of the contact between the phases, thus allowing to selectively produce the cyclic carbonates under mild conditions of pressure ($P<8$ bar). Overall, a global yield of transformation from olefin to cyclic carbonate of 83% was observed.

4.1.3 Results and Discussion

Electrochemical epoxidation

A Vapourtec electrochemical Ion cell with a parallel electrode configuration was employed to explore the electrochemical oxidation of styrene as the model substrate. The effect of the electrode nature, electrolyte, solvent and current on the reaction were extensively examined. Hydrogen was generated in the cathode, which was observed in the outlet, where the flow was multiphasic. An initial screening of solvent and electrolyte was performed in order to select the best parameters to proceed the reaction (Table S1). A mixture MeCN/H_2O (80:20 v:v) showed promising selectivity towards the products that can be used as reagents for the cycloaddition reaction (styrene oxide and halohydrin, **Figure 1A**), while other solvents (DMSO, THF, acetone) showed more selectivity towards the aldehyde, which is undesirable in this case. The use of TBA.Br resulted in higher selectivity towards the epoxide, compared to other ammonium salts evaluated

(TBA.Cl, TBA.Br and TEA.BF_4, Table S1 and S2,). Conveniently, TBA.Br is an efficient catalyst for the subsequent cycloaddition reaction. [32] The effect of working electrode was also evaluated (flexible graphite and glassy carbon, Table S2). Glassy carbon was selected due to its higher long-term stability and better reproducibility.

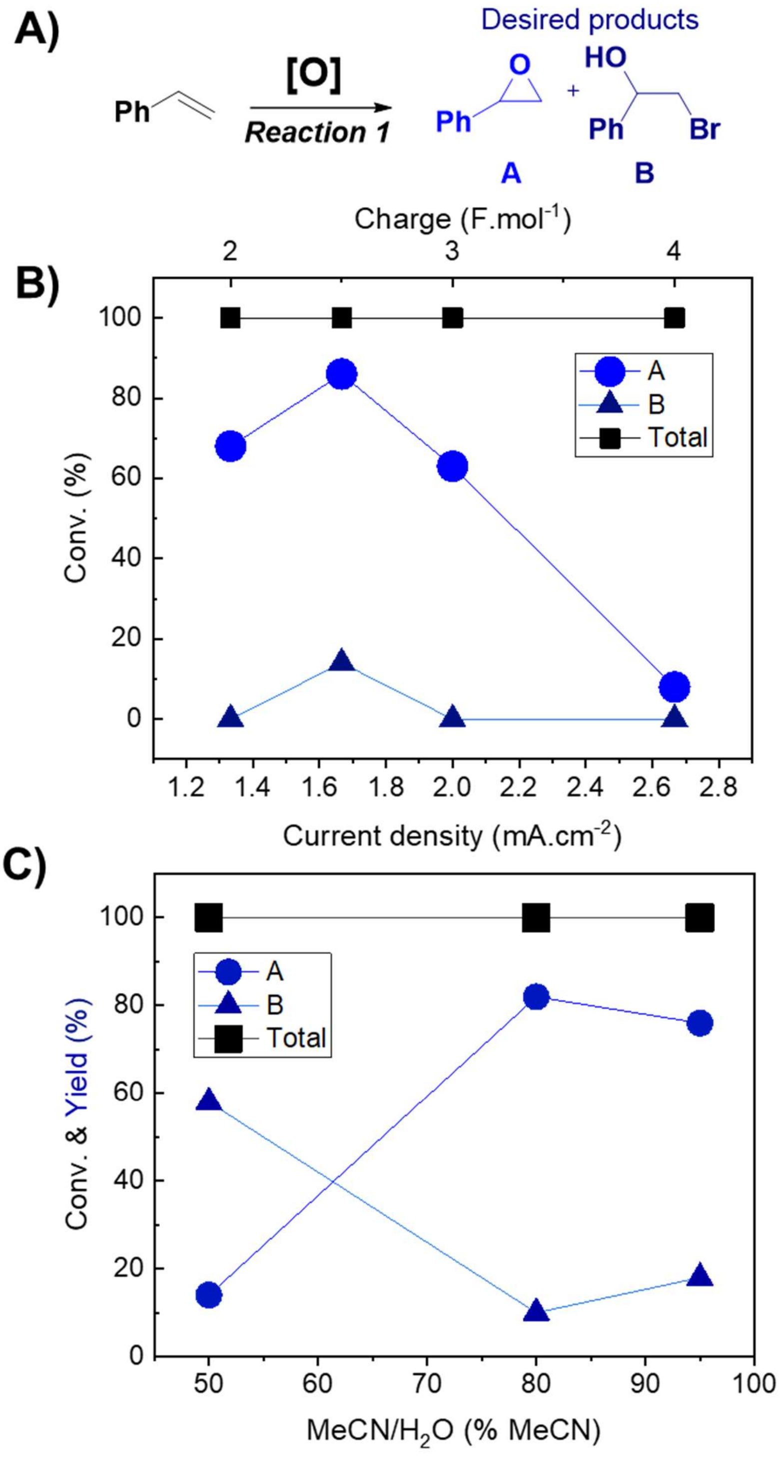

Figure 1. Optimization of epoxidation flow reaction using styrene. A) General reaction. *Reaction conditions:* 1 mmol of styrene, 2 mmol of electrolyte, 20 mL of solvent, 0.05

mL min^{-1} flow rate, resulting in 12 min of residence time. Glassy carbon as working electrode and stainless steel as the counter electrode. B) Current density effect. C) Solvent effect.

The effect of current density **(Figure 1B**) and solvent proportion (**Figure 1C**) were then studied, using previous reaction parameters (solvent, electrode and electrolyte) where only products A and B were formed. Both products (**A** and **B**) were of interest since it is possible to further convert them into cyclic carbonate. The current density range to be studied was selected based on previously reported studies in the literature, [12] with charge varying from 2 $F \cdot mol^{-1}$ to 4 $F \cdot mol^{-1}$. Calculation of the respective current densities in electrode surface was done employing Eq. 1 and Eq. 2 (see experimental section for more details). The current density of 1.66 mA cm^{-2} clearly presented better results (**Figure 1B**), whereas other values of current density facilitated the formation of byproducts, such as aldehydes and bromo alkenes. Notably, the success of this reaction depended on the presence of a small amount of water, as observed in the solvent effect (**Figure 1C**). Changing the amount of water in the MeCN solution, the majoritarian product also changed, as well as the conversion (**Figure 1C**). The best result was observed with 80% of MeCN, resulting in 86% selectivity towards epoxide, using a current of 20 mA (a charge of 2.5 $F \cdot mol^{-1}$) with a residence time of 12 minutes, and this mixture was used for further reactions. Finally, control tests with different pressure conditions were evaluated, however the reaction was not successful, resulting in the formation of solid products that began to accumulate on the electrodes. For this reason, atmospheric pressure was selected for further oxidation reactions. Overall, the results obtained for the reaction performed in flow highlighted its potential over batch experiments. In 2021, Cantillo *et. al.* [12] reported a selectivity of 53% using a current of 20mA, with a charge of 3.5 $F \cdot mol^{-1}$. Meanwhile, *Qian et. al.* (2022) [33] reported a selectivity of 97% towards epoxide using a current of 30 mA for 4 hours.

CO_2 cycloaddition with 3DP reactor

The evaluation of CO_2 cycloaddition to an epoxide to produce cyclic carbonates was also conducted. Building upon our prior research, a variety of 3DP reactors were specifically designed to investigate their impact on the reaction. [28] A new formulation was employed to improve the printing resolution (see SI for more details). Two reactor designs with a helicoidal shape, namely **R1** and **R2** (as shown in **Figure 2A**), were successfully printed using masked stereolithography (mSLA). These structures were designed to fit into a commercially available Omnifit™ column (L: 15cm, Ø: 1.0cm) enabling their use under flow conditions (**Figure 2A**). Both designs are based on a helicoidal structure with four built-in columns to improve its mechanical resistance and flow distribution by representing obstacles to the pathway. Each geometry featured a different helix pitch: **R1** had a distance of 4 mm between each complete spin, while **R2** had 2.5 mm. STL files of the geometries can be found in the SI.

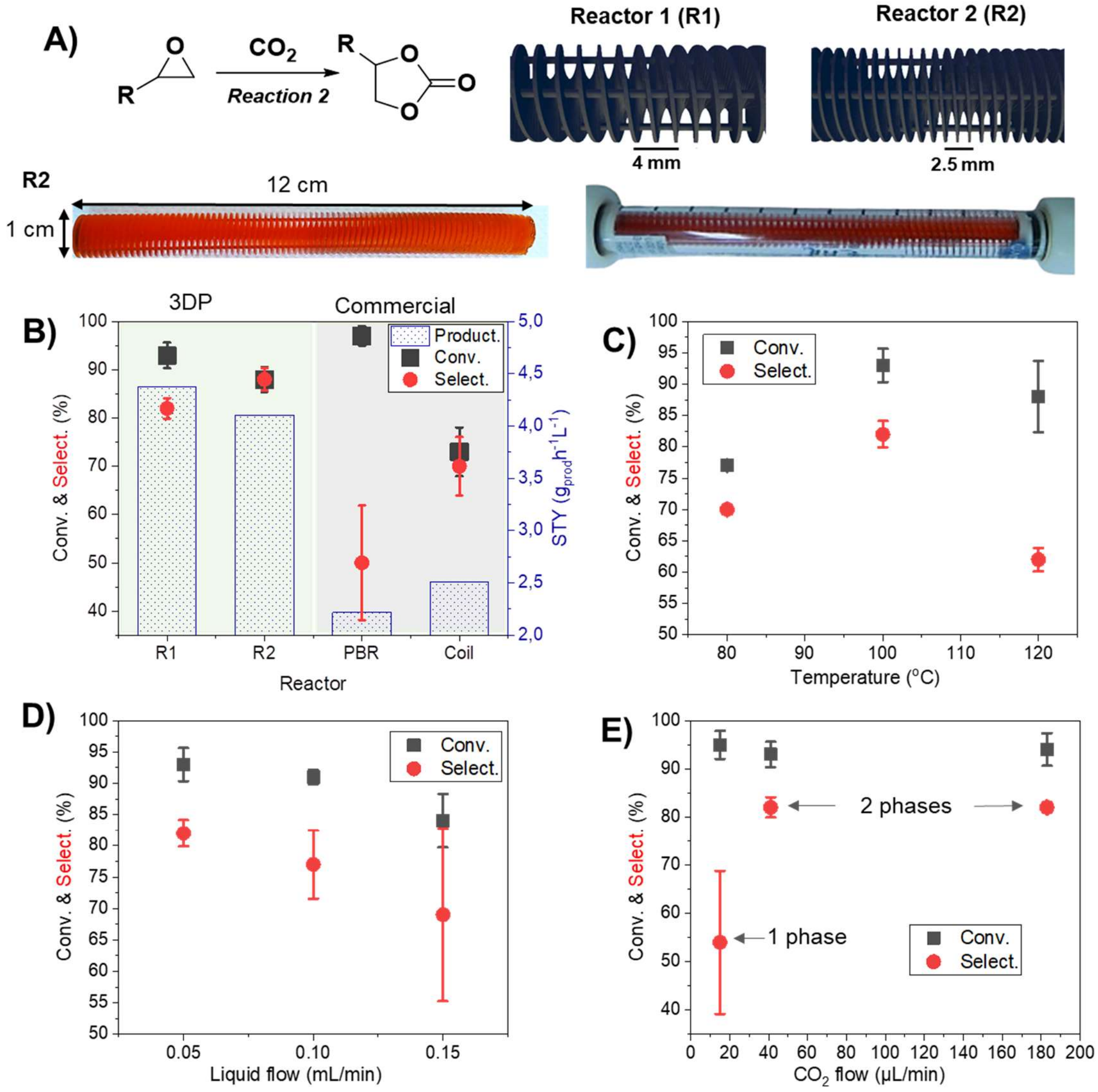

Figure 2. Optimization of CO_2 cycloaddition reaction in flow using styrene oxide. *Reaction conditions:* 1 mmol of styrene oxide, 2 mmol TBAB, 20 mL of solvent (MeCN /H_2O) (80:20) (v:v). *Standard flow conditions:* 0.05 mL/min liquid flow rate, 41 µL min^{-1} gas flow rate, 100 °C. A) Top left: CO_2 cycloaddition reaction; Top right: Computer-aided design (SolidWorks or CAD) of structured reactors; bottom left: photo R2 3D printed; bottom right: photo R2 in Omnifit^{TM} column. B) Evaluation of different flow

reactors; Productivity normalized according to residence time (see experimental part): R1 = 47 min; R2 = 51 min; PBR = 55 min; coil = 60 min. C) Temperature effect. D) Liquid flow evaluation E) CO_2 flow evaluation.

In order to optimize the parameters of the cycloaddition reaction (**Figure 2A**), a mixture of styrene oxide, TBA.Br in MeCN:H_2O (80:20) (v:v) was used. The variation of the reactor structure demonstrated its strong influence over the selectivity and reproducibility of the reaction (**Figure 2B**). Notably, the employment of 3DP reactors led to a substantial improvement in both conversion and selectivity (R1 = 93±3% conversion, 82±2% selectivity), as compared to the use of a conventional packed bed reactor (PBR) (97±2% conversion, 50±12% selectivity) containing beads of a commercial polymeric resin (Purolite ECR8209M, average diameter 500 µm) of similar formulation to our 3DP polymers, or a coiled tubular reactor (73±5% conversion, 70±6% selectivity). This result was more evident when comparing the space time yield (STY) of the different systems, the values of R1 (4.38 $g_{prod}h^{-1}L^{-1}$) and R2 (4.11 $g_{prod}h^{-1}L^{-1}$) significatively decrease to 2.22 $g_{prod}h^{-1}L^{-1}$ for PBR and 2.51 $g_{prod}h^{-1}L^{-1}$ for the coil. This result suggested a more uniform flow distribution in the 3DP reactor compared to the PBR. Furthermore, conventional reactors (PBR and coil) were affected by several issues, such as challenges regarding pressure control and difficulty to achieve steady state. This was evidenced by the difficulty to collect fractions of product solution with equal volumes at even time distributions, and also the low reproducibility of the results, as denoted by the high error bars (**Figure 2B**). Alternatively, the use of 3DP structures improved the homogeneity of the fluid flow, sample collection volume and internal pressure of the column; overall it led to more stable flows and higher productivities. The spiral configuration of the reactor, complemented with four internal columns, apparently enhanced the interfacial area between the liquid and gas phases, [34] and thus improving the mass transfer, contact between reactants and catalyst and overall reaction rates (Figure S1). Moreover, the internal columns improved the stability of the structure: without them, some deformation of the helicoidal structure was observed due to swelling (Figure S2). The long-term stability of the 3DP reactor with internal columns was further demonstrated and will be discussed in more detail in Figure 3D. Although the results obtained from **R1** and **R2** were similar, **R1** presented slightly superior productivity, evidenced by the higher value of STY. Additionally, R1 showed superior durability and longer potential usage (see supporting information figure S2), for this reason it was chosen for the subsequent phase of the experiment. In addition, noteworthy achievements are evident when comparing our system with previous PBRs documented in the literature for CO_2 cycloaddition to epoxide. In fact, Valverde *et al.* (2021)[35] reported 53% conversion under the operating conditions of 140 bar and 150 °C. Likewise, Yin *et al.* (2021)[36] reported >76% conversion while operating at 20 bar and 90 °C.

The increase in the temperature to 120ºC demonstrated a decrease in the selectivity favoring the formation of diol (**Figure 2C**). For this reason, 100ºC was selected to the further reactions. The flow of liquid was optimized, and as observed in **Figure 2D,** the best results were obtained with smaller flow to represent higher residence time (47 min for 0.05 mL min^{-1}; 30 min 0.10 mL min^{-1}; and 22 min 0.15 mL min^{-1}; respectively).

The flow of CO_2 is also directly related to selectivity. While less concentration favored the hydrolysis yielding diol (**Figure 2E**), higher concentration of CO_2 resulted in higher formation of cyclic carbonate until a maximum point (40 µL min^{-1}). From this point, the increases in the CO_2 flow did not suppose any significant change in the reaction. Another interesting point to consider is that passing from 15 µL min^{-1} to 40 µL min^{-1} the system transitioned from 1 phase (liquid) to 2 phases (gas-liquid). This discovery stems from the constrained solubility of CO_2 within our solvent under our working pressure conditions (6 bar). At lower flow rates, we observed complete dissolution of CO_2 in the liquid phase. In contrast, as the flow rate increased, we witnessed partial solubility, resulting in a two-phase system. This alteration in phase behavior may indeed impact the reaction mechanism and kinetics within the reactor, which can be the responsible for the different conversion observed at this point.[37] It has been studied how a two-phase flow promotes the apparition of vortexes inside the different phases.[38] This generated vortexes enhance the mixing and mass transfer, and thus they can also be linked to the observed results.

Combined reactions

After optimizing the individual reactions, we combined the reactor sequence to perform the direct oxidative carboxylation (**Figure 3A** and Figure S12). The epoxidation and carboxylation reactors were identical to those described above. The solution containing the olefin and TBA.Br was pushed employing an HPLC pump towards the inlet of the ionic electrochemical reactor. The resulting product (a mixture of liquid and H_2 gas) is collected in an intermediate collection vessel, allowing the gas separation. The liquid phase was subsequently pumped with a second HPLC pump into a T-mixer and mixed with CO_2 driven by a peristaltic pump. A back-pressure regulator (BPR) of 6.5 bar was added between the peristaltic pump and the T-mixer to ensure the control over gas flow rate. This, in addition to the use of two check valves at the respective flow inlets, allowed for a uniform mixing between the two phases. The multiphasic reaction mixture entered the 3DP reactor at a temperature of 100ºC, where the cycloaddition takes place. A BPR regulator controlled the pressure of the reactor at 6 bar. The products were collected employing an automated fraction collector in triplicate in vial after reaching steady state. The complete system can be observed in **Figure 3B**.

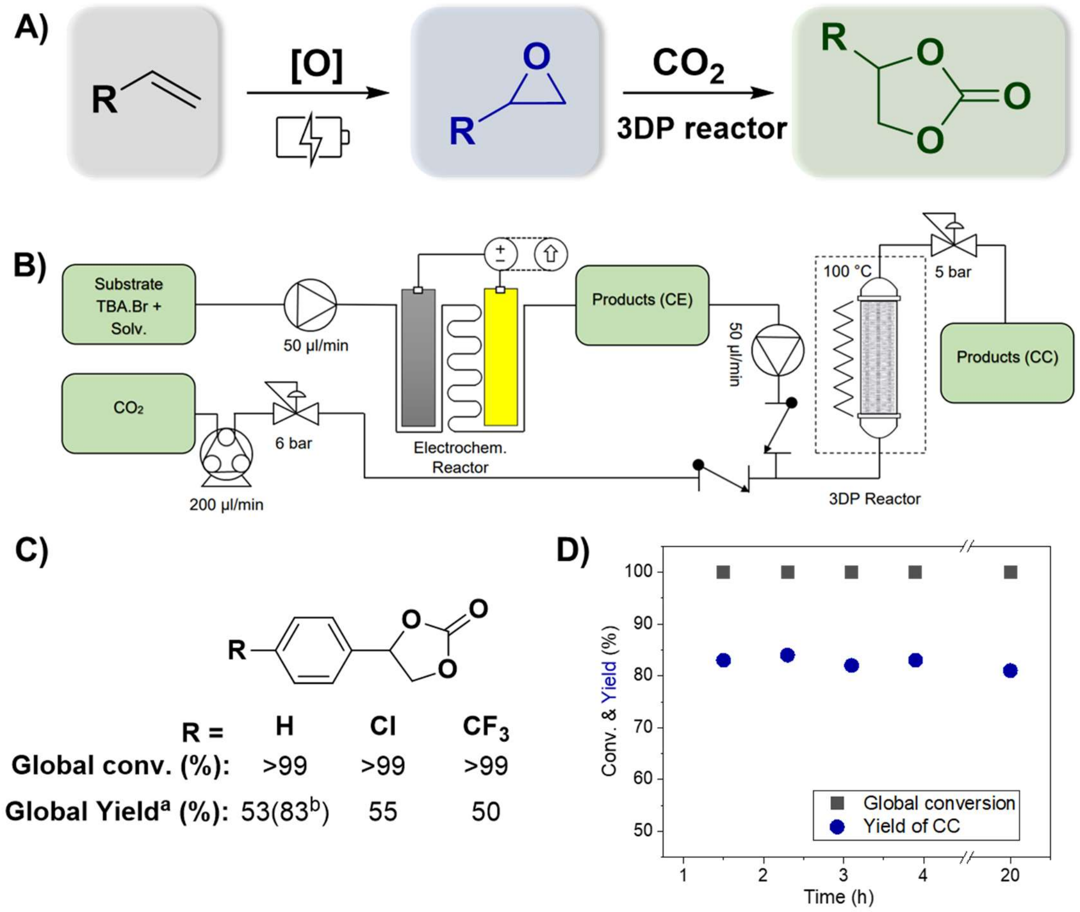

Figure 3. A) Overview of the consecutive reactions for direct oxidative carboxylation of olefins (Figure S12). B) Schematic representation of continuous-flow system. C) Substrates used for the scope ([a]47 min residence time, [b]94 min of residence time). D) System stability using styrene as substrate in combined reactions.

Using this system, different olefins were tested, and the production of correspondent cyclic carbonate can be seen on **Figure 3C**. Complete global conversion was observed for all reactions, and no residual olefins were detected in the ^{1}H NMR spectrum (refer to figures S9-S11). However, a slight decrease in the reaction rate was observed for this combined reaction. After the first hour, the yield of cyclic carbonate was 53% for styrene, 55% for 4-(chloro)styrene, and 50% for 4-(trifluoromethyl)styrene. However, this was easily fixed by the increasing of residence time, where the styrene increases the global yield from 53% to 83%. Additional tests using electron-donor substituents (-OMe) were conducted; however, these experiments did not yield the desired product in the oxidation step. This outcome highlights the significance of the substituent's role in activating the epoxide. It is likely that substituents with stronger electron-withdrawing properties create a more electron-deficient carbon, which makes it more susceptible to nucleophilic attack of the bromide of (TBA.Br).[39, 40] Finally, the stability of the system can be observed in **Figure 3D**, where, after reaching the steady state, the yield of the desired product (CC) remained constant for at least 4 hours.

4.1.4 Conclusions

In this study, we have effectively showcased the continuous flow synthesis of cyclic organic carbonates from olefins and carbon dioxide has been demonstrated. Our system accomplishes this transformation in two sequential steps, maintaining compatible conditions throughout the process, thus eliminating the requirement for intermediate purification steps. An integrated system for synthesizing combination of electrochemical and chemical steps, with TBA.Br as electrolyte and catalyst reduces the use of expensive catalysts and waste generating oxidizing agents. The utilization of 3DP reactors present significant advancements in terms of conversion and selectivity when compared to conventional PBRs or coiled tubular reactors. The improvement is more evident when comparing productivity, calculated using STY, where approximately half of the STY was observed for the commercial reactor compared to the 3DP reactor (R1 = 4.38 $g_{prod}h^{-1}L^{-1}$, R2 = 4.11 $g_{prod}h^{-1}L^{-1}$, PBR = 2.22 $g_{prod}h^{-1}L^{-1}$, and coil = 2.51 $g_{prod}h^{-1}L^{-1}$). Our methodology employs cost-effective catalysts, enables the execution of reactions under relatively low temperatures and pressures, and achieves rapid reaction times. These findings highlight the promising potential of 3D-printed reactors in enhancing the efficiency and sustainability of chemical reactions in various industries. While scaling up is not the primary focus of this paper, these factors combined with the continuous flow are relevant in terms of scalability and may represent a promising alternative for the future. Future research can further optimize this approach and explore its applicability to other catalytic systems.

4.1.5 Experimental section

Reactions conditions:

Epoxidation reaction: The oxidation reaction was performed using described procedure with some adaptation to the flow system. [33] In a typical catalytic reaction procedure, 1.0 mmol (0.104 g) of styrene (or styrene derivatives), 2 mmol (0.644 g) of TBA.Br, 16 mL of CH_3CN, and 4 mL of H_2O were pumped into an Ion electrochemical reactor (Vapourtec, UK) using a 0.05 mL min^{-1} flow rate. Glassy carbon was used as the working electrode and a stainless steel as the counter electrode, the surface area was of 12 cm^2 (0,6 mL with a height of 0.5 mm). The catalytic reaction was performed under a constant current of 20 mA at 25 °C with a residence time of 12 minutes. The conversion and selectivity to the products was calculated by ^{1}H NMR spectroscopy.

Current density (mA cm^{-2}) and faradaic efficiency were calculated as follows

$$Current\ Density = \frac{I}{area_{elec}} \qquad (1)$$

$$\frac{F}{mol} = \frac{I(A)}{Q\left(\frac{mL}{s}\right) \cdot C\left(\frac{mol}{mL}\right) \cdot 2F} \qquad (2)$$

Where, *Q* is the flow rate, *I* is the current, *C* is the concentration and *F* the Faraday constant.

Cycloaddition reaction: In a typical catalytic reaction procedure the reaction mixture from epoxidation reaction or a mixture containing 1.0 mmol (0. 120 g) of styrene oxide 2 mmol (0.644 g) of TBA.Br, 16 mL of CH_3CN, and 4 mL of H_2O was pumped using a HPLC pump at a rate of 0.05 mL min^{-1}. CO_2 was pumped at a flow rate of 0.20 mL/min (nominal value) and mixture with the liquid phase using a T-mixer. The experimental CO_2 flow rate was determined to be 41 µL min^{-1}, taking into account gas compression and solubility calculations in the solvent at a temperature of 25°C. CO_2 was pumped at a flow rate of 0.20 mL min^{-1} (nominal value) directly into a back pressure regulator, which aimed to ensure a pressure line that would enable a constant flow of gas to mix with the liquid phase in a T-mixer. The experimental flow rate of CO_2 was determined to be 41 µL min^{-1} by calculating the difference between the total flow rate (of the gas-liquid mixture) and the flow rate of the incompressible liquid in a known volume of tubing and selected time. This calculation yielded the actual CO_2 inlet flow rate, taking into account the system's pressure conditions. The reaction was performed inside a column reactor containing the 3DP structure, at 100 °C and 6 bar with a residence time of 47-60 minutes according to the reactor structure used (R1 = 47 min; R2 = 51 min; PBR = 55 min; coil = 60 min). The conversion and selectivity to the products was calculated by ^{1}H NMR spectroscopy.

The residence time was calculated using the equation (3):

$$Residence\ time\ (RT) = \frac{Vr(mL)}{Q\left(\frac{mL}{min}\right)} \qquad (3)$$

Where Vr is the volume of the reactor (R1 = 4.30 mL; R2 = 4.63 mL; PBR = 5.46 mL; coil = 5 mL), Q is the flow rate, calculated by adding up the flow rate of gas (experimentally determined) and liquid.

The productivity was calculated considering the space time yield (STY) (equation 4):

$$STY = \frac{product\ weight}{volume\ reactor * residence\ time} = \frac{gprod}{L.h} \qquad (4)$$

Combined reaction: In a typical catalytic reaction procedure, 1.0 mmol (0.104 g) of styrene (or styrene derivatives), 2 mmol (0.644 g) of TBA.Br, 6 mL of CH_3CN, and 4 mL of H_2O were pumped into an ion electrochemical reactor using a 0.05 mL min^{-1} flow rate. Glassy carbon was used as the working electrode and a stainless steel as the counter electrode. The catalytic reaction was performed under a constant current of 20 mA at 25 °C with a residence time of 12 minutes. The reaction mixture obtained in this part was pumped to the second reactor with a flow rate of 0-05 mL min^{-1} and mixed with CO_2 (flow rate nominal of 0.20 mL/min, that correspond to 41 μL min^{-1}) using a T-mixer [1]. The reaction was performed inside a column reactor containing the 3DP structure, at 100 °C and 6 bar with a residence time of 47 minutes. The conversion and selectivity to the products was calculated by ^{1}H NMR spectroscopy.

4.1.6 References

1. Q. Liu, L. Wu, R. Jackstell and M. Beller, *Nature Communications*, 2015, **6**, 5933.

2. S. Dabral and T. Schaub, *Advanced Synthesis & Catalysis*, 2019, **361**, 223-246.

3. Q. Han, B. Qi, W. Ren, C. He, J. Niu and C. Duan, *Nature Communications*, 2015, **6**, 10007.

4. N. Podrojková, A. Oriňak, E. Garcia-Verdugo, V. Sans and M. Zanatta, *Catalysis Today*, 2023, **418**, 114128.

5. L. Wang, S. Que, Z. Ding and E. Vessally, *RSC Advances*, 2020, **10**, 9103-9115.

6. L. Guo, K. J. Lamb and M. North, *Green Chemistry*, 2021, **23**, 77-118.

7. H. Büttner, L. Longwitz, J. Steinbauer, C. Wulf and T. Werner, *Topics in Current Chemistry*, 2017, **375**, 50.

8. T. K. Pal, D. De and P. K. Bharadwaj, *Coordination Chemistry Reviews*, 2020, **408**, 213173.

9. R. Calmanti, M. Selva and A. Perosa, *Green Chemistry*, 2021, **23**, 1921-1941.

10. X. Yang, J. Wu, X. Mao, T. F. Jamison and T. A. Hatton, *Chemical Communications*, 2014, **50**, 3245-3248.

11. A. A. Sathe, A. M. K. Nambiar and R. M. Rioux, *Catalysis Science & Technology*, 2017, **7**, 84-89.

12. W. Jud, C. O. Kappe and D. Cantillo, *Electrochemical Science Advances*, 2021, **1**, e2100002.

13. H. Seo, L. V. Nguyen and T. F. Jamison, *Advanced Synthesis and Catalysis*, 2019, **361**, 247-264.

14. H. Seo, L. V. Nguyen and T. F. Jamison, *Advanced Synthesis & Catalysis*, 2019, **361**, 247-264.

15. H. Luo, J. Ren, Y. Sun, Y. Liu, F. Zhou, G. Shi and J. Zhou, *Chinese Chemical Letters*, 2023, **34**, 107782.

16. H. Yasuda, L.-N. He, T. Takahashi and T. Sakakura, *Applied Catalysis A: General*, 2006, **298**, 177-180.

17. M. North, P. Villuendas and C. Young, *Chemistry – A European Journal*, 2009, **15**, 11454-11457.

18. X. Wu, M. Wang, Y. Xie, C. Chen, K. Li, M. Yuan, X. Zhao and Z. Hou, *Applied Catalysis A: General*, 2016, **519**, 146-154.

19. A. Sainz Martinez, C. Hauzenberger, A. R. Sahoo, Z. Csendes, H. Hoffmann and K. Bica, *ACS Sustainable Chemistry & Engineering*, 2018, **6**, 13131-13139.

20. J. A. Kozak, J. Wu, X. Su, F. Simeon, T. A. Hatton and T. F. Jamison, *Journal of the American Chemical Society*, 2013, **135**, 18497-18501.

21. X.-B. Lu, J.-H. Xiu, R. He, K. Jin, L.-M. Luo and X.-J. Feng, *Applied Catalysis A: General*, 2004, **275**, 73-78.

22. J. Wu, J. A. Kozak, F. Simeon, T. A. Hatton and T. F. Jamison, *Chemical Science*, 2014, **5**, 1227-1231.

23. S. Miralles-Comins, M. Zanatta and V. Sans, *Polymers*, 2022, **14**, 5121.

24. C. Parra-Cabrera, C. Achille, S. Kuhn and R. Ameloot, *Chemical Society Reviews*, 2018, **47**, 209-230.

25. M. R. Penny and S. T. Hilton, *Reaction Chemistry & Engineering*, 2020, **5**, 853-858.

26. C. R. Tubío, J. Azuaje, L. Escalante, A. Coelho, F. Guitián, E. Sotelo and A. Gil, *Journal of Catalysis*, 2016, **334**, 110-115.

27. J. Wu, Y. Yan, L. Zhang, Z. Qin and S. Tao, *Advanced Materials Technologies*, 2018, DOI: 10.1002/admt.201800515.

28. D. Valverde, R. Porcar, M. Zanatta, S. Alcalde, B. Altava, V. Sans and E. García-Verdugo, *Green Chemistry*, 2022, **24**, 3300-3308.

29. S. Rossi, A. Puglisi and M. Benaglia, *ChemCatChem*, 2018, **10**, 1512-1525.

30. V. Saggiomo, in *Catalyst Immobilization*, 2020, pp. 369-408.

31. M. R. Penny, Z. X. Rao, R. Thavarajah, A. Ishaq, B. J. Bowles and S. T. Hilton, *Reaction Chemistry & Engineering*, 2023, **8**, 752-757.

32. Y. Chen, P. Xu, M. Arai and J. Sun, *Advanced Synthesis & Catalysis*, 2019, **361**, 335-344.

33. Y. Zhang, A. Iqbal, J. Zai, S.-Y. Zhang, H. Guo, X. Liu, I. ul Islam, H. Fazal and X. Qian, *Organic Chemistry Frontiers*, 2022, **9**, 436-444.

34. M. Berton, J. M. de Souza, I. Abdiaj, D. T. McQuade and D. R. Snead, *Journal of Flow Chemistry*, 2020, **10**, 73-92.

35. D. Valverde, R. Porcar, P. Lozano, E. García-Verdugo and S. V. Luis, *ACS Sustainable Chemistry & Engineering*, 2021, **9**, 2309-2318.

36. J. Sun, Z. Li and J. Yin, *Journal of CO2 Utilization*, 2021, **53**, 101723.

37. J. Lefebvre, S. Bajohr and T. Kolb, *Fuel*, 2019, **239**, 896-904.

38. C. Yao, Y. Zhao, H. Ma, Y. Liu, Q. Zhao and G. Chen, *Chemical Engineering Science*, 2021, **229**, 116017.

39. N. Panza, R. Soave, F. Cargnoni, M. I. Trioni and A. Caselli, *Journal of CO2 Utilization*, 2022, **62**, 102062.

40. S. Marmitt and P. F. B. Gonçalves, *Journal of Computational Chemistry*, 2015, **36**, 1322-1333.

4.2 Supporting information

4.2.1 Experimental details

Materials

All reagents and solvents used were commercially available: Glycidyl methacrylate (97%, Aldrich), Pentaerythritol-tetraacrylate (PETA) (>99%, Aldrich), phenyl-bis-(2,4,6-trimethylbenzoyl)phosphine oxide (97%, Aldrich), ink (ELEGOO translucent LCD UV-Curing), styrene oxide (97%, Aldrich), styrene, 4-(trifluromethyl)styrene (98%, Aldrich),, 4-(methoxy)styrene (97%, Aldrich), tetrabutylammonium chloride (TBA.Cl) (97%, Aldrich) and tetrabutylammonium bromide (TBA.Br) (99%, Aldrich). All the solvents were used as received from Scharlab.

General characterization protocols

Fourier Transform Infrared (FT-IR) spectra were acquired with a Pike single-reflection ATR diamond/ZnSe accessory in a JASCO FT/IR-4700 instrument.

Thermal gravimetric analysis was performed on TGA-DSC3 analyser from Mettler Toledo. Samples for TGA analysis were heated in an inert atmosphere up to 800 ºC with a heating rate of 10 ºC min^{-1}.

3D printers: A DLP printer (Asiga PICO2) and a MSLA printer (Elegoo mars 2 Pro), were the 3D printers employed. The DLP printing system was equipped with a LED light source operating at 405 nm. The Elegoo Mars 2 Pro printer was equipped with a 2560 × 1620 mono liquid crystal display (LCD), illuminating at 405 nm. The CAD files were designed and converted to STL-type files using SolidWorks CAD software. The digital light processing fabrication in both printers began by slicing the 3D CAD model into individual 2D images for projecting onto the photocurable liquid. For Asiga PICO2 printer, the additive manufacturing software used to create slices was Asiga Composer. For the Elegoo Mars 2 Pro 3D printer the slicer software employed was ChituBox.

The conversion of CO_2 cycloaddition reactions was calculated by ^1H NMR spectra, carried out using a Bruker Avance III HD 300 or 400 spectrometer (300 or 400 MHz for ^1H).

3P printing methodology

3DP-SIL composition: The printer tank was filled with 50.0 mL a monomeric solution containing 60% by weight of GMA, 40% by weight of PETA, and 2w% of the photoinitiator (Phenyl-bis-(2,4,6-trimethylbenzoyl)phosphine oxide) regarding the monomers, 0,1 phr Pentaerythritol tetrakis (3,5-di-tert-butyl-4-hydroxyhydrocinnamate) and 0,1 phr Methyl Red (only for the R2 reactor). The 3D structure was obtained according to the digital design downloaded in the printer (column R1 and R2). Once the 3D structure was printed, the object was extracted from the platform, washed with IPA (3 x 25 mL) and cured at 60 ºC for 15 min under UV lamp.

Printing Parameters of 3DP objects: All the objects were printed in Elegoo mars 2 Pro, in vertical position. **R1:** column length: 11.5 cm, column diameter: 0.95 cm, 18 s exposure time, 22 s bottom exposure time, total printing time: 17 h. **R2:** column length: 11.5 cm, column diameter: 0.95 cm, 18 s exposure time, 22 s bottom exposure time, total printing time: 17 h.

4.2.2 Results

Oxidation reaction

Table S1. Evaluation of solvent and electrolyte for epoxidation reaction. [a]

Ent.	Solvent (vol%)	Electrolyte	I (mA)	Aldehyde	Epoxide	Halohydrin
1	$DMSO_{80}/ H_2O_{20}$	$TEA.BF_4$	20	-	-	-
2	$Acetone_{80}/ H_2O_{20}$	$TEA.BF_4$	20	✓	-	-
3	$Acetone_{80}/ H_2O_{20}$	$TEA.BF_4$	27	✓	-	-
4	THF_{50}/ H_2O_{50}	$TEA.BF_4$	20	✓	-	-
5	THF_{50}/ H_2O_{50}	$TEA.BF_4$	27	✓	-	-
6	THF_{80}/ H_2O_{20}	$TEA.BF_4$	20	✓	-	-
7	THF_{80}/ H_2O_{20}	$TEA.BF_4$	27 [b]	✓	-	-
8	$MeCN_{80}/ H_2O_{20}$	$TEA.BF_4$	20	✓	-	-
9	$MeCN_{80}/ H_2O_{20}$	$TEA.BF_4$	27	✓	-	-
10	$MeCN_{80}/ H_2O_{20}$	TBA.Br	20	-	✓	-
11 [c]	$MeCN_{80}/ H_2O_{20}$	TBA.Br	20	-	✓	✓

[a] *Reaction conditions:* 0.5 mmol of styrene,1 mmol of electrolyte, 10 mL of solvent, 0.05 mL min^{-1} flow rate, maximum power set to 12 V. Carbon sheet as working electrode and a stainless steel as the counter electrode. [b] Degradation. [c] Membrane reactor.

Table S2. Evaluation of electrode for epoxidation reaction. [a]

Entry	Working electrode	Electrolyte	Conv. (%)	Conv. Epoxide (%)	Conv. Halohydrin (%)
1	Flexible graphite	TBA.Br	100	72	16
2	Glassy carbon	TBA.Br	100	80	10
3	Glassy carbon	TBA.Cl	100	50	-

[a] *Reaction conditions:* 0.5 mmol of styrene,1 mmol of electrolyte, 10 mL of solvent (MeCN 80%/ H_2O 20%), 0.05 mL min^{-1} flow rate, 20 mA. Stainless steel as the counter electrode.

3D printed structures and characterization

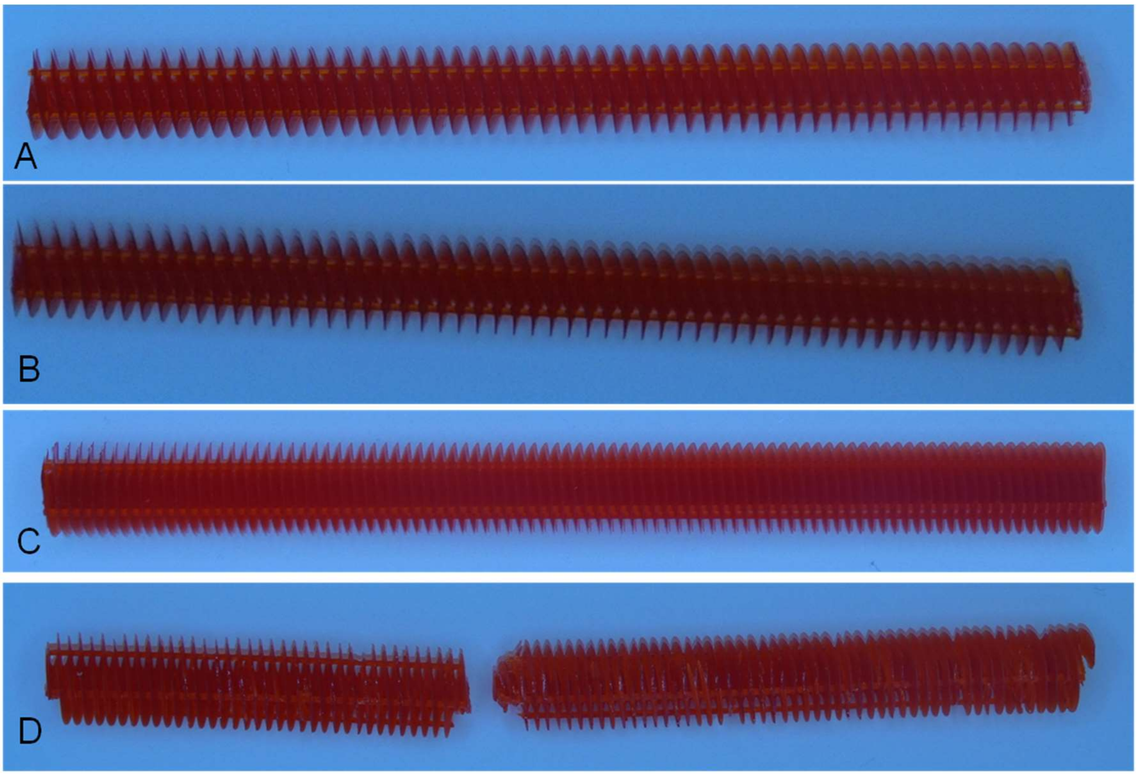

Figure S1. Photos of the reactors before and after reaction: A) Design R1 before reaction; B) Design R1 after reaction C) Design R2 before reaction; D) Design R2 after reaction.

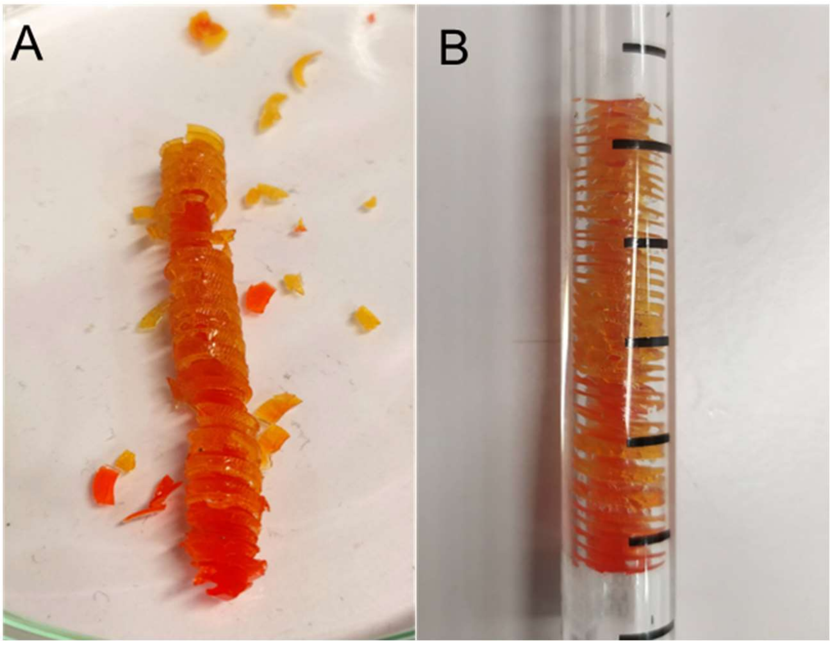

Figure S2. Photos reactors after reaction. A) first design without columns. B) first design with 4 columns.

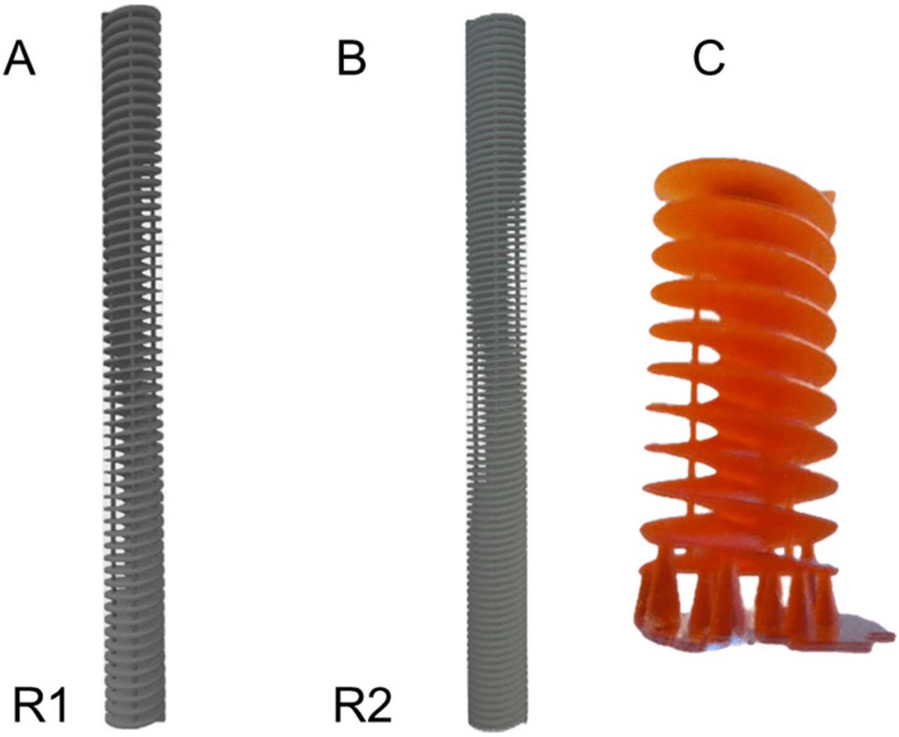

Figure S3. Computer-aided design (SolidWorks or CAD) of structured reactors A) Design R1; B) Design R2; C) Shorter version of printed column before remove the supports.

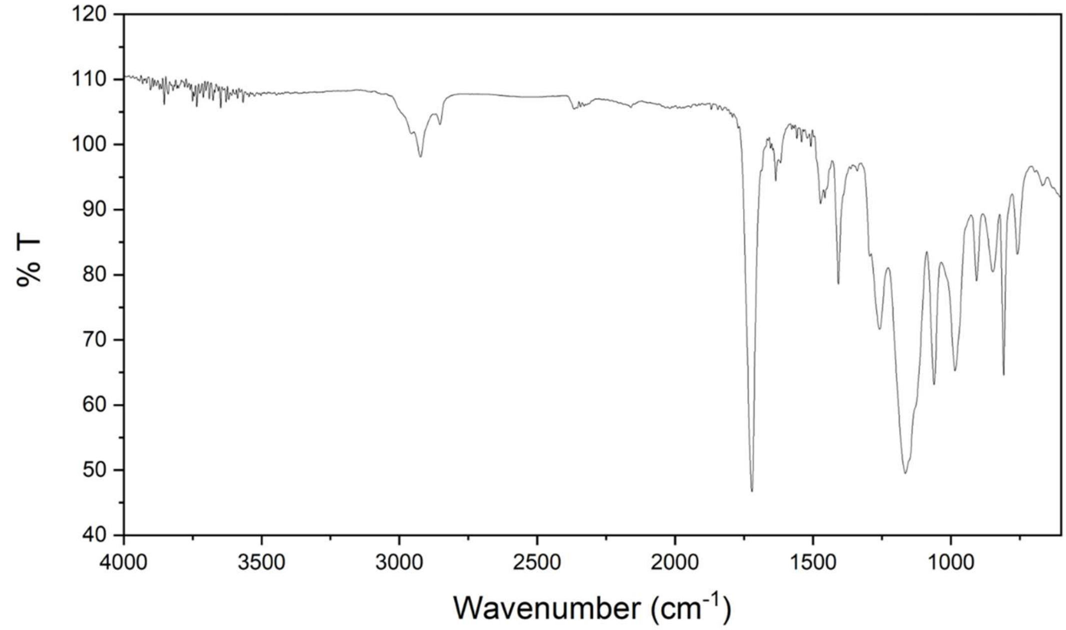

Figure S4. FTIR spectra of optimized formulation used to print the reactor.

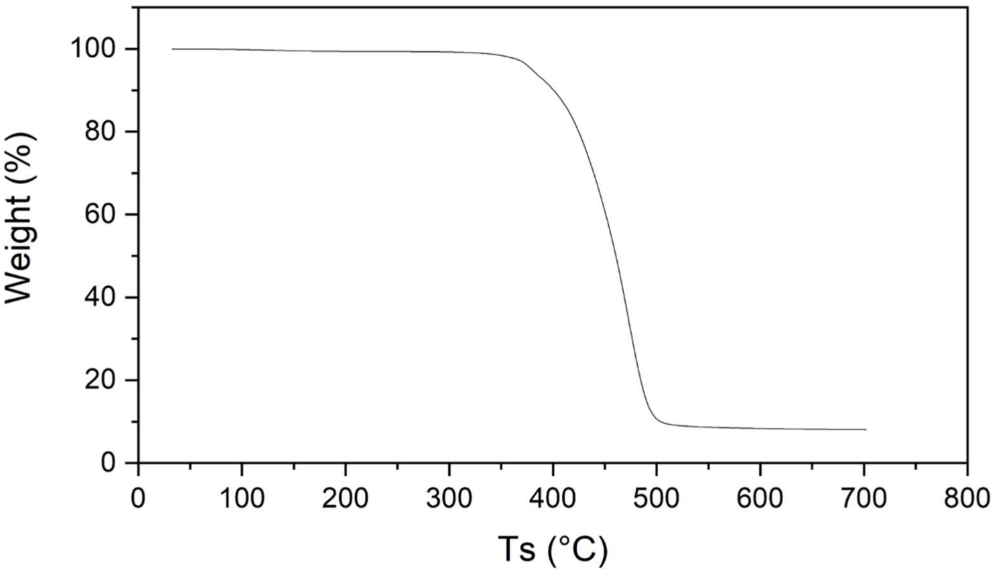

Figure S5. TGA analysis of optimized formulation used to print the reactor.

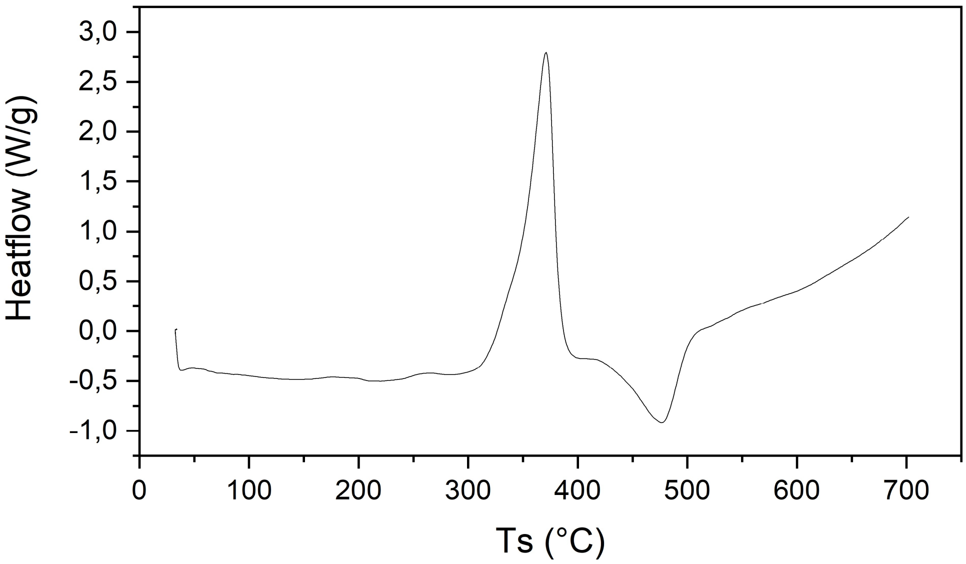

Figure S6. DSC analysis of optimized formulation used to print the reactor.

NMR analysis of oxidative carboxylation reaction

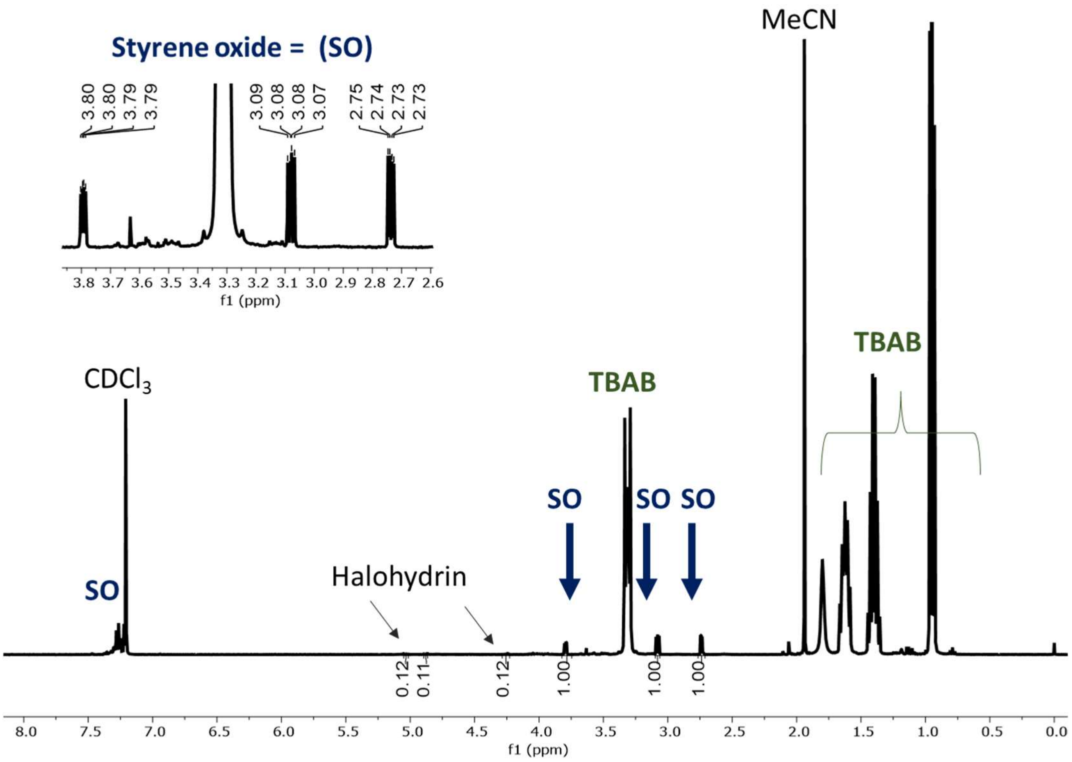

Figure S7. ^{1}H NMR (400 MHz, $CDCl_3$) of reaction 1 (electrochemical oxidation) using styrene as substrate (optimized condition).

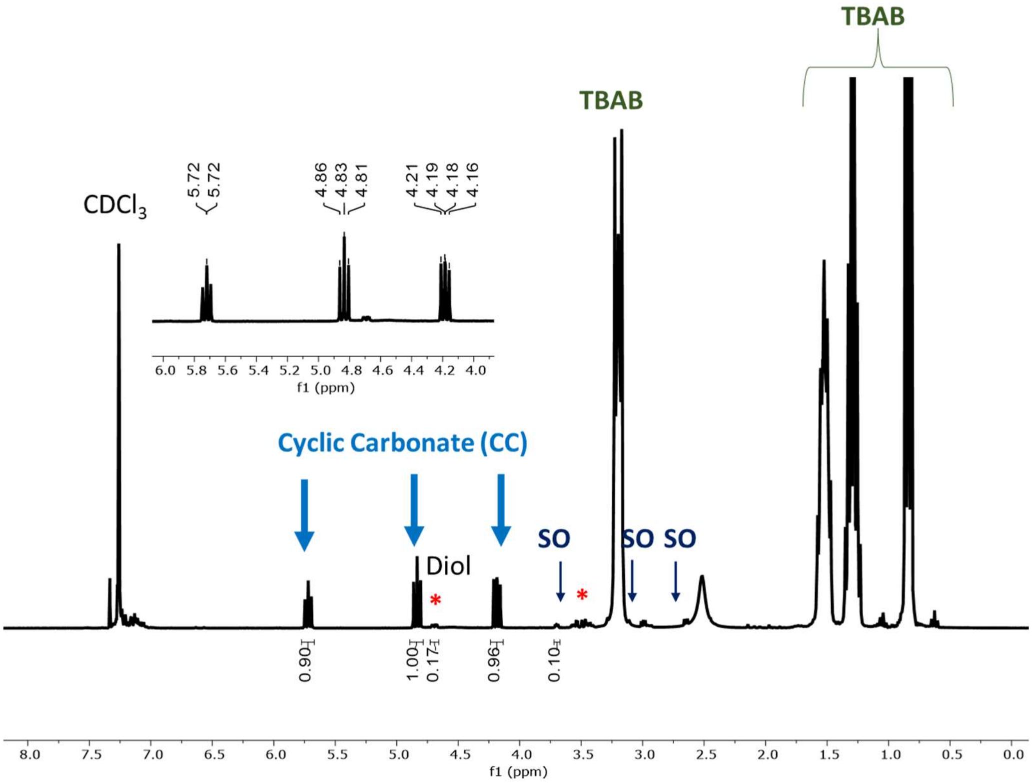

Figure S8. ^{1}H NMR (400 MHz, $CDCl_3$) of reaction 2 (CO_2 cycloaddition) using styrene oxide as substrate (optimized condition).

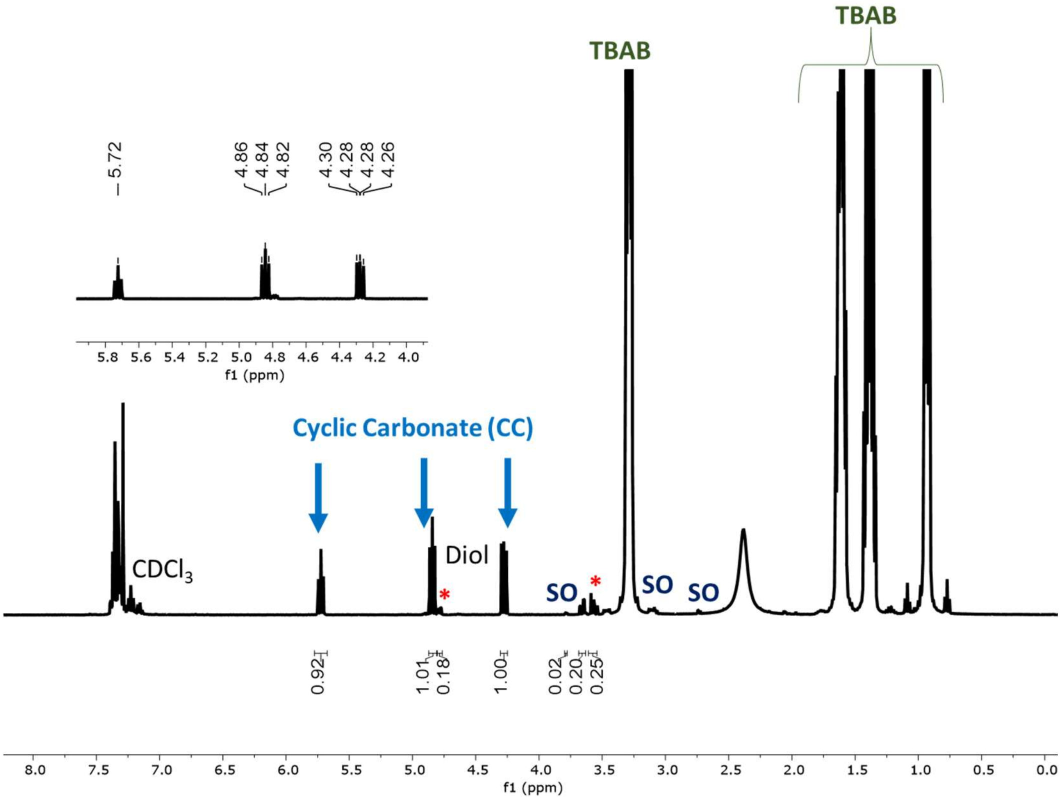

Figure S9. ^{1}H NMR (400 MHz, $CDCl_3$) of combined reaction using styrene as substrate.

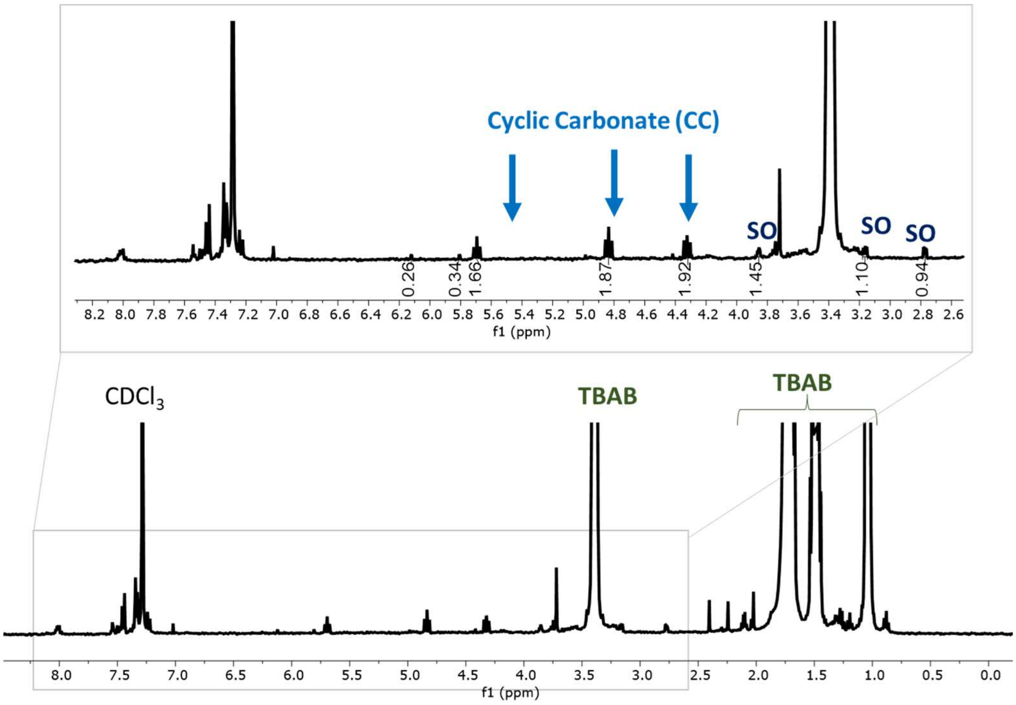

Figure S10. ^{1}H NMR (400 MHz, $CDCl_3$) of combined reaction using 4-(chloro)styrene as substrate.

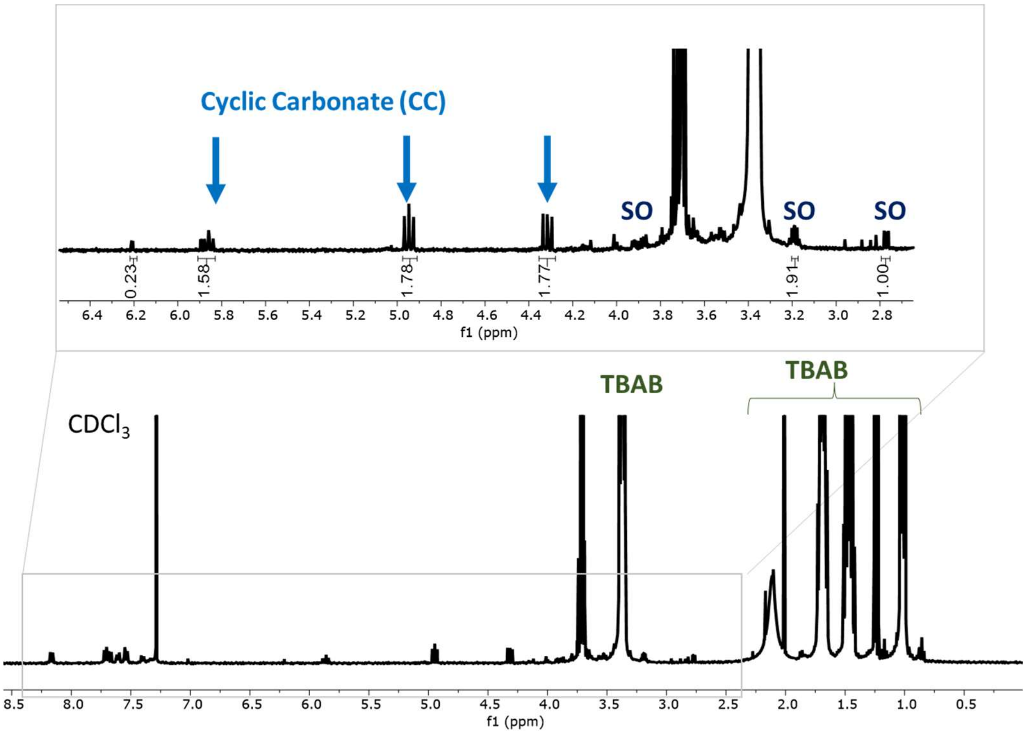

Figure S11. ^{1}H NMR (400 MHz, $CDCl_3$) of combined reaction using 4-(trifluoromethyl)styrene as substrate.

Continuous flow apparatus

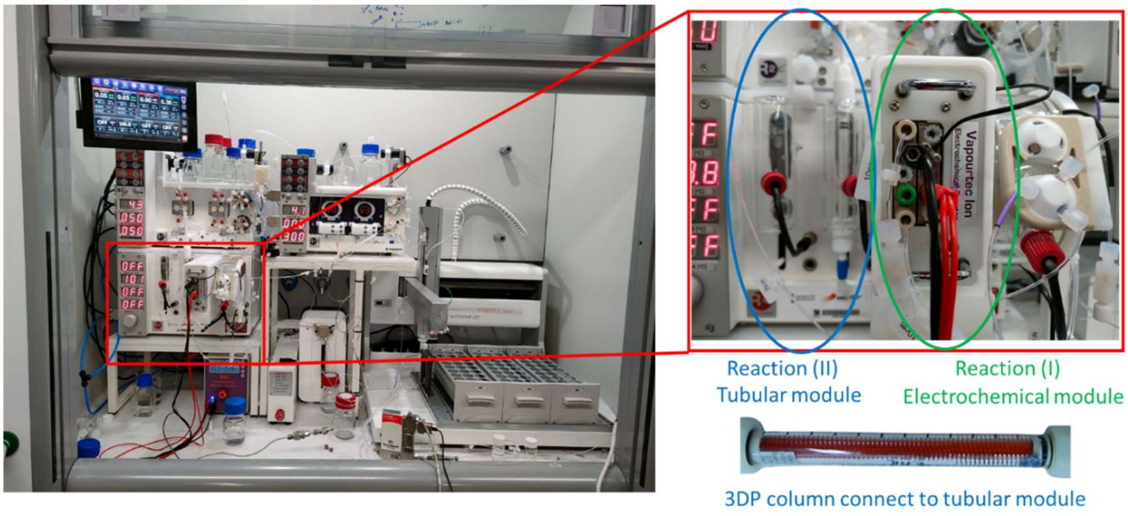

Figure S12. Vapourtec continuous flow system combining electrochemical and tubular modules

Chapter 5. 3D printed flow reactors for the synthesis of single crystal perovskites

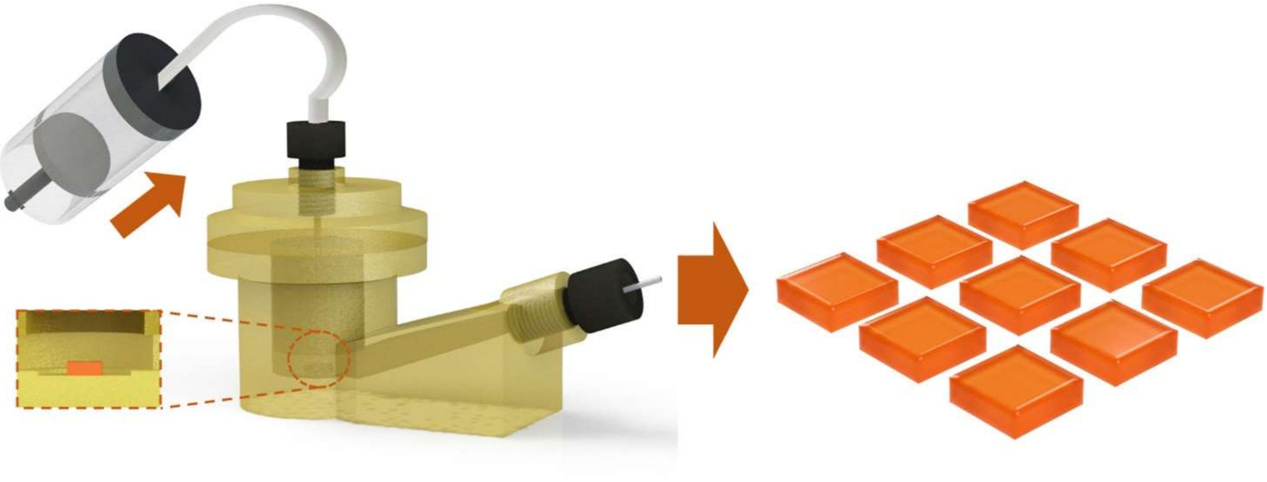

The results described during the present chapter have been already published. Reproduced from *Materials Today Energy* **2024**, *39*, 101476. with permission from Elsevier.

5.1 Main text

Abstract:

Defect-free single crystal perovskites have unique photophysical properties that makes them highly attractive for a range of optoelectronic applications. However, their syntheses largely rely on batch protocols, which are limited in terms of reproducibility and scalability. Here, a new methodology is presented to develop tailored continuous-flow platforms for the synthesis of lead halide perovskites. The digital design of the reactors and their manufacturing with 3D printing, employing commercially available resins and low-cost stereolithography, was achieved. The reactor chamber was designed to facilitate the continuous slow addition of reagents to the reaction chamber, thus maintaining a constant concentration of reagents inside the reactor. The highly controlled synthetic conditions allowed for a high reproducibility of the crystallization process, with yields ranging between 8 and 15% in weight in eight consecutive reaction cycles. The crystals produced were characterized and demonstrated excellent photoluminescence properties.

5.1.1 Introduction

The interest in hybrid organic–inorganic perovskites (HOIP) has risen in the last years due to their extraordinary optoelectronic properties. This family of semiconductor materials is easily synthesizable under mild conditions via solution-based methods [1], and display tunable semiconductor and properties that make them interesting materials for solar cells [2], LED and optoelectronics. Currently, optoelectronic devices are produced using polycrystalline HOIP thin films (with $MAPbX_3$ structure), but the presence of grain boundaries limits them to achieve their full potential [3], Single crystals have been proposed as a solution to this problem making them highly desirable for the development of new photovoltaic devices [4, 5]. Moreover, single crystals present slower degradation rates under moisture conditions compared to their polycrystalline counterparts [6], and therefore the resulting devices are more stable, acting as helpful models for studying the properties of this family of materials [7, 8].

There is a wide diversity of methods for synthesizing single crystals, including controlled cooling of solutions or the use of antisolvents, but these classical methods are slow, requiring even days to achieve good quality crystals and they typically suffer from low reproducibility. The Inverse Temperature Crystallization (ITC) method was developed based on the loss of solubility of specific salt-solvent pairs at elevated temperatures, allowing to produce millimeter sized crystals in a few hours [4]. Nevertheless, to produce single crystals without structural defects in a reproducible way it is of utmost importance to control the nucleation process. There are several contributions in literature addressing this problem, paying attention to factors like precursor purity [9], the relationship between solution concentration and temperature [10] or the use of crystal seeds [11, 12]. There are also more advanced strategies like controlling the solution concentration via solvent diffusion through another phase [13] or a combination of crystal seeds with a ramped heating profile [7].

One of the issues of the synthesis in batch is the variability of material properties between batches, which is caused mainly by inhomogeneous distribution of temperature and concentration in the reactor [14]. Industry is looking for the transition to flow reactions since they offer improvements regarding these issues, but other benefits include improvements over parameters like scalability, energy efficiency or waste generation [15]. Furthermore, it eases the integration of monitoring techniques [16], that would aid the full digitalization of the process to increase its reproducibility and, eventually, its automation [17]. Indeed, there is work done for transitioning the synthesis of perovskite quantum dots into flow [18, 19] and even automatic platforms that self-optimize their synthesis conditions had been designed [20].

Additive manufacturing (AM), also known as 3D printing (3DP), has been gaining attention during the last years since enables to construct layer by layer complex geometries in a rapid, cost-efficient and simple fashion [21]. AM allows to adapt reactor geometry to the requirements of each system, tailoring the mixing and temperature profiles along the reactor. Furthermore, with the aid of computational fluid dynamics is even possible to simulate these distributions before even producing the reactor [22]. This synergy between flow and 3DP has been applied to the crystallization of really diverse compounds, like proteins [23], perovskite quantum dots [19] or silver nanoparticles [24].

Here we present a new concept for the development of efficient systems for the generation of high-quality single crystal perovskites in a scalable and reproducible fashion, employing a simple 3D printed set-up. We report the first 3DP system for the synthesis of perovskite single crystals, for improved reproducibility in the synthesis by combining two different principles. First, the use of an adequate polymeric 3D resin, a material with low heat conductivity, as the body of the reactor serves to smoothen the heating of the solution, avoiding a temperature gradient that could negatively affect the crystallisation processes. And, secondly, the use of continuous-flow addition of reagent facilitates the control of the concentration of reagents within the reactor chamber. Controlled and reproducible single crystals can be generated with this approach.

5.1.2 Results and Discussion

3DP techniques based on stereolithography (SLA) were selected for this work due to the combination of high resolution, low-cost and availability of commercial resins [25]. The compatibility of the selected resins with the organic and conditions employed for the synthesis of the perovskites was the first issue to be addressed. Commercially available High Temperature Resin (HTR) from Formlabs was selected due to its solvent compatibility with low swelling in a broad range of organic solvents and high thermal resistance (up to 230 ºC). Its low heat conductivity (0.282 W mK^{-1}) compared to glass vials commonly used for the synthesis of single crystals allows for gentle heating profiles that damp thermal inhomogeneities [26]. Furthermore, ramped heating, akin to other published works [7], could be performed without the need of programmable heating equipment.

3DP vials and discs were fabricated with a Form 3 printer, using HTR resin (Figure 1A) to study their compatibility with the conditions employed in the literature for the single perovskite crystallisation. N,N-Dimethylformamide (DMF) and a 1 M precursor solution of methylammonium lead bromide ($MAPbBr_3$) in DMF were introduced into different 3DPvials and kept at 80 ºC for 24 hours, with no visually observed degradation of the material. Swelling of the discs submerged in these solutions was minimal, with a mass increment of only 2%. Thermogravimetric analyses (TGA) showed no noticeable mass loss until 300 ºC for the control experiment (Figure 1B). The samples submerged in DMF (Disc-DMF), and precursor solution (Disc-PVSK) presented a 3% weight loss at the 150-240 ºC interval, consistent with the boiling point of DMF (153 ºC). No other differences were observed. All samples started to degrade above 350 ºC.

The effect of the solutions on the material surface was studied. FT-IR spectra of the different sample discs are shown in Figure 1C. An slightly increase of intensity of the bands around 3000, 1700, 1455 and 1155 cm^{-1} could be observed in the samples submerged in solution, which were assigned to DMF [27]. These increases are consistent with the previously reported swelling. There are not remarkable differences between the sample Disc-DMF and Disc-PVSK, except a small peak at 866 cm^{-1} that could be assigned to the methylammonium cation [28]. Surfaces roughness was not affected by the organic materials, as evidenced by profilometry images (Figure S1A). The difference in surface height was less than 10 µm in all cases, with a root mean square deviation of the peaks (middle point in the three samples) in the micron order (Figure S1B). These values are smaller than the ones stablished by manufacturer of the 3D printer for the printing process (30 µm standard deviation for 1 mm prints) [29]. With all this information, Formlabs HTR was deemed compatible with the working conditions and acceptable to be used in the development of the flow platform.

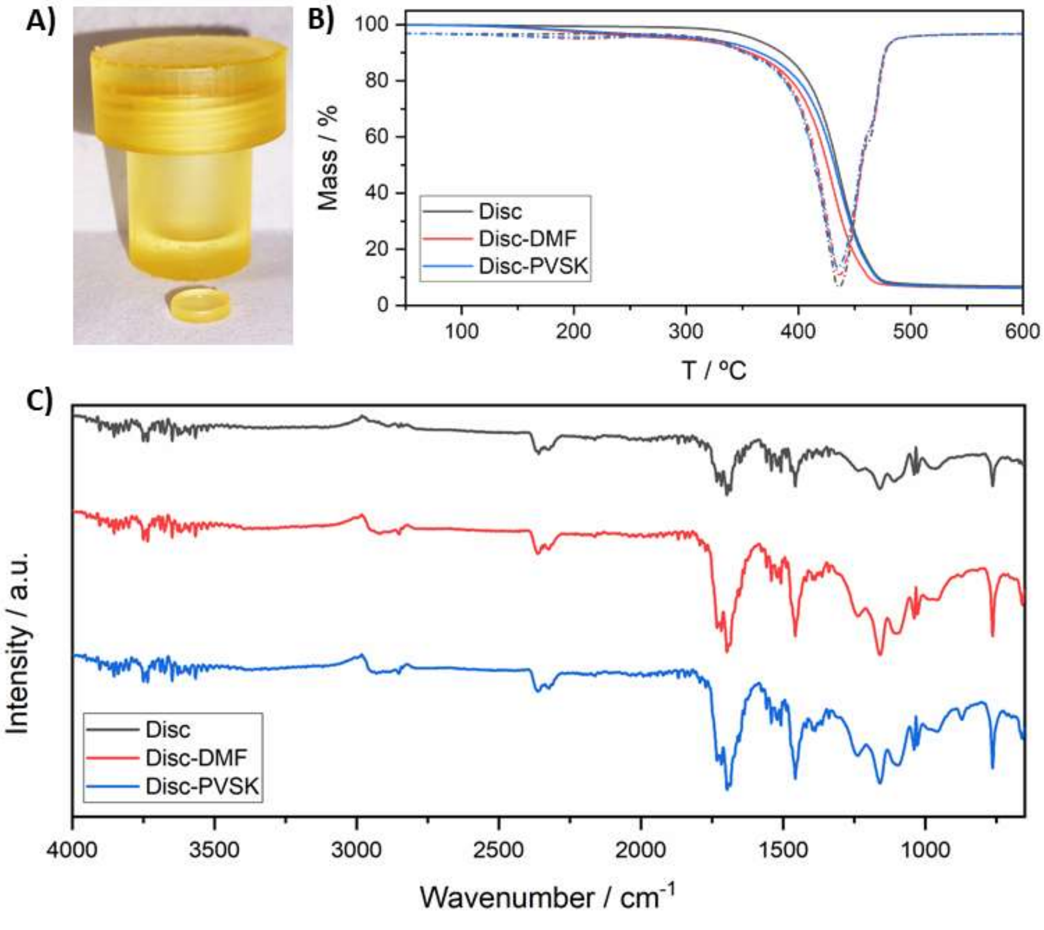

Figure 1. A) 3D printed vial and disc of the HTR resin employed in this work. B) Solid lines: TGA analysis of the same samples. Dashed lines: First derivative of the TGA curve. C) FT-IR spectra of the 3DP resin, resin after 24 hours in DMF at 80 ºC, resin after 24 hours in $MAPbBr_3$ 1 M solution in DMF at 80 ºC.

The first iteration of the crystallization, named **V0**, was composed of two pieces (Figure S2). The top part featured a threaded port with standard 1/4-28 threads, compatible with standard fitting connectors, designed to feed the solution and a diffusor to distribute the flow homogenously into the reactor chamber. The bottom part included a seat for glass substrates and output holes around the substrate that merged at a collection channel with a 1.5 mm diameter at the bottom. An o-ring was placed between parts to ensure sealing, and the system was easily closed together with a vacuum clamp. Total volume inside the reactor was 3.94 mL. During the initial experiments at 80 °C using the same perovskite precursor solution as in the preliminary tests, uncontrolled nucleation happened fast, as seen on figure 2A. This was due to the placement of collection channels in the bottom of the reactor and their lower wall thickness compared to the target zone, causing that local temperature at the channels was higher. Furthermore, limited space within the channels accelerated crystallization, therefore nucleation was preferred on their inside and clogging of the output took place them as can be observed.

The second generation of the reactor, named **V1**, is shown in figure 2A along detailed measurements. In this design, two parts were designed, the top part, comprising of flow inlet and diffusor; and the bottom part, with the reactor area and the outflow channel. The top piece was designed as a cylinder, featuring a flow line split into seven channels to homogeneously distribute the flow towards the reactor. The bottom was modified with respect to **V0** to avoid the undesired precipitation of the Pb based materials. The inner diameter of the reactor was 17 mm an indentation 10.5 mm diameter of 1 mm depth was created in the centre to conveniently place a glass substrate. The crystallisation zone was located at the bottom part of the reactor. The outlet channel was in a ramp at 19º inclination, while the base of the part was kept flat. In this way, the channel was designed as a wide ramp starting at the exit of the reactor chamber and going upwards, out of the heating zone. This resulted in an increase in wall thickness from 6 to 15 mm, while the wall above the channel was kept at a constant thickness of 2 mm with respect to the fluidic conduct. This was done intentionally to gradually reduce heating from the bottom while aiding the cooling from the top (a diagram detailing the full setup during experiments can be seen at Figure S3A). The top and bottom parts were sealed with an o-ring and closed with a clamp. Total volume inside the system was 3.05 mL.

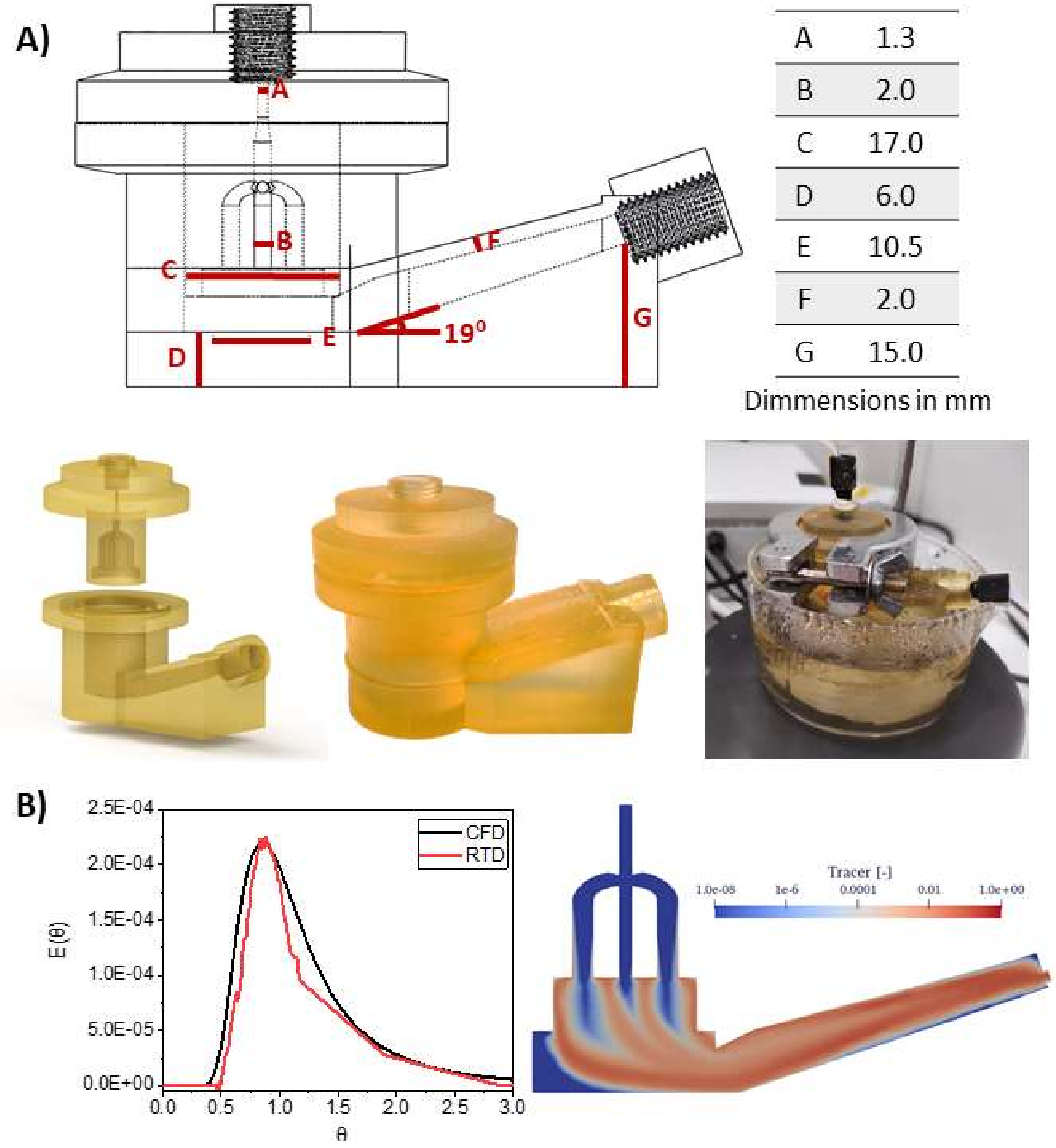

Figure 2. 3DP reactor design A) V1 reactor with detailed measurements, 3D model and during experiments B) CFD simulation of flow patterns inside the reactor chamber. Comparison of experimental (RTD) and simulated (CFD) curves for tracer experiments.

To evaluate the overall behaviour of the reactor through a quantitative measure of internal mixing within the system, Residence Time Distribution (RTD) studies of the V1 was performed (a diagram detailing the setup is shown on figure S3B). This knowledge is crucial in achieving a desired flow pattern during reactor design, significantly contributing to its efficiency and performance [30]. The Figure 2B displays the E(θ) curve as a function of time (θ) for the pulse experiment evaluation. This curve exhibits a normal distribution with a mean residence time of 5300 seconds and a slight tracer tail, indicating the presence of a certain degree of internal mixing within the reactor. Importantly, the employed flow conditions (50 μL min^{-1}) in the experiment rule out possibilities of significant channelling, stagnation, and internal recirculation issues. These findings demonstrate the effectiveness of control and assurance against potential future problems during the reactor's operational lifespan.

The CFD simulation of the tracer experiment was performed in similar conditions to the experiment with a flowrate of 50 μL min^{-1}. A tracer pulse with constant concentration (1 mg/L) and a duration of 60 seconds was went through the reactor's inlet. The simulation was ran to study its evolution over 20000 seconds. For the simulation, the fluid was considered as a Newtonian fluid with kinematic viscosity of 4.9×10^{-6} m^2 s^{-1} and a density of 1425 kg m^{-3}. The kinematic diffusivity of the tracer was set to 10^{-8} m^2 s^{-1}. Given the flow conditions, an isothermal laminar flow was considered.

The simulation results show a good agreement with the experiments (see Fig. 2B) Despite the differences in shape, the location of the peaks and the distribution widths are reasonably close. The contour plot illustrates the tracer distribution inside the reactor for a time close to the peak of the RTD. For a better representation, the tracer concentration was normalized to its maximum value and a logarithmic scale was used for the representation. This plot provides a good insight into the reactor's hydrodynamic behavior: the inlet flow is distributed over the lateral channels giving rise to a set of streams that fill the main chamber of the reactor except for a small region in the side that is opposed to the outlet (left side in the contour plot). It is important to note that part of the tracer is accumulated near the entrances to the main chamber, and the fact that the stream coming from the channel on the left side lies behind the other streams. Also, note that these streams conveniently combine in the ascending part of the outlet so that there is no tracer accumulation in this region.

V1 reactor was employed to generate $MAPbBr_3$ single crystals. Perovskite crystallization yield and crystal quality, in this sense, of different solution flows needed to be tested using reactor **V1**. Considering that the reactor was partially submerged in the oil bath (Figure 2A), a thermal gradient was expected within the system.[31] Therefore, a calibration of the temperature difference between the oil bath employed to heat the reactor and the inner temperature of the reactor was done using a high-resolution contact thermometer on the surface of the reactor, after waiting two hours (Figure S4). The observed difference arises from the temperature gradient caused by the continuous injection of a precursor solution at room temperature into the preheated reactor, and the partial immersion of the reactor in the oil bath. The temperature of reaction was selected to facilitate the crystallisation of a 1 M solution of precursors, corresponding to 67 ºC at the target zone. Different flow rates were evaluated, producing crystals in all cases (Figure 3A) that remained still at the bottom of the reactor once they have nucleated. Multiple crystals were generated per experiment, in the case of 25 $\mu L\ min^{-1}$ they were homogenously shaped and sized, featuring smoother surfaces observed under the microscope compared to lower flows, that featured noticeable growth rings. Furthermore, at this flow rate, similar crystal sizes were achieved in half the time compared to other conditions.

The observable surface differences and growth rate of crystals can be attributed to the use of flow, since there is a continuous regeneration of the boundary layer at the surface of the crystal. During the growth of the crystals from the precursor solution, once the solute is incorporated to the crystal, the degree of supersaturation in the solution surrounding the crystal decreases and a boundary layer is formed [32]. In this area, crystallization kinetics are greatly decreased, as they are dependent on perovskite concentration [13]. The use of flow decreases the thickness of this boundary layer by enhancing the transport of saturated solution to the crystal surface. It is worth noting that an increase of flow to 50 $\mu L\ min^{-1}$ did not increase the crystallization yield compared to 25 $\mu L\ min^{-1}$, suggesting that at these flow rates the growth was not limited by mass transfer. This signals that optimum concentration values and flow rates should be explored for the different stages of crystallization process, particularly for eventual longer or larger scale experiments. This would be done by gradually changing flowrates or generating concentration gradients using a secondary pump. Moreover, the difference of mass transfer between flows also affected the morphology of the crystals. As seen on Figure 3A, at lower flows, crystals showed a higher number of inhomogeneities, featuring a concentric ring shape, something that could be attributed to an intermittent growth or formation of inclusions caused by poor mass transfer to the crystal surface. The appearance of secondary crystals could affect the morphology of the surrounding ones, as an excess of crystals might disrupt the flow, reducing mass transfer and causing instability on surfaces during crystal growth. This issue must be considered along the three-dimensionality of the system, as the relative the direction of the crystals against the flow can influence the movement of islands, enhance or even inhibit crystal growth in some directions [33].

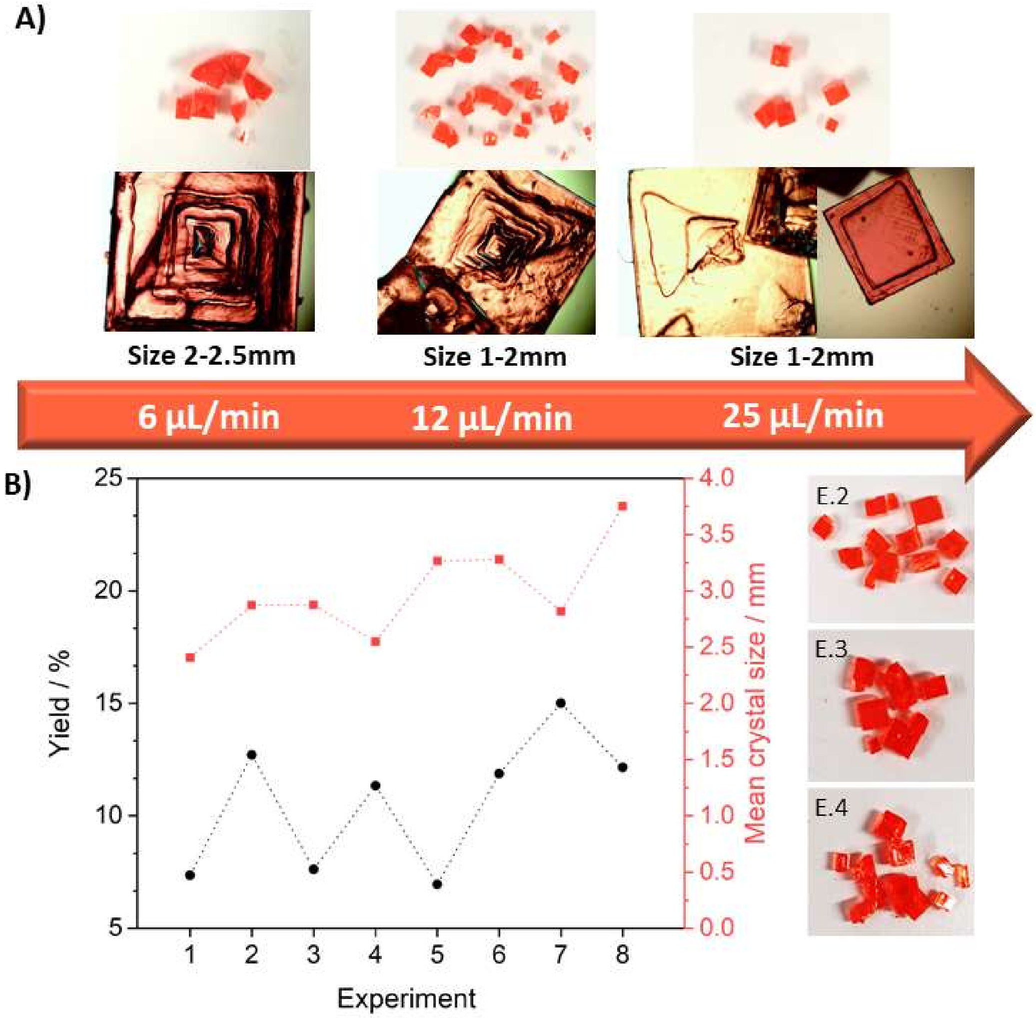

Figure 3. A) Influence of flow rate in crystallization. B) Reproducibility at 25 µL min^{-1} flow and examples of obtained crystals in representative experiments

The next step was to evaluate the experimental reproducibility of the platform. To this end, a number of reaction experiments were carried out in the same set-up in different days. The conditions employed were the same as in previous experiments, *i.e.* a flow rate of 25 µL min^{-1}, a temperature of 67 ºC on the inside, 1 M $MAPbBr_3$ precursor solution and a total run time of 240 minutes. In all cases, high quality single crystals, as it can be observed in XRD spectra, were obtained, and their results are shown in Figure 3B. The average crystals produced per run was 7, total crystal yield (calculated with eq. 1) obtained per run ranged between 7 and 15%, and mean crystal size comprised from 2.4 to 3.7 mm. A trend could be observed in the majority of the experiments, where mass obtained and mean crystal size were inversely related. This could also be correlated to the number of crystals (Figure S5). A higher number of nucleated crystals produced more simultaneous growth sites and higher total mass was achieved. However, these sites competed between each other in the incorporation of perovskite from solution, and thus produced crystals were smaller. Overall, crystal yield in the flow platform was stable during the different experiments, but for further improving the results next iterations of the design will be needed. The main focus would be to reduce the number initial nucleation sites and inhibit secondary nucleation, as it would enable to have better control over the growth of the present crystals, and minimize perturbations in morphology caused by surrounding crystals.

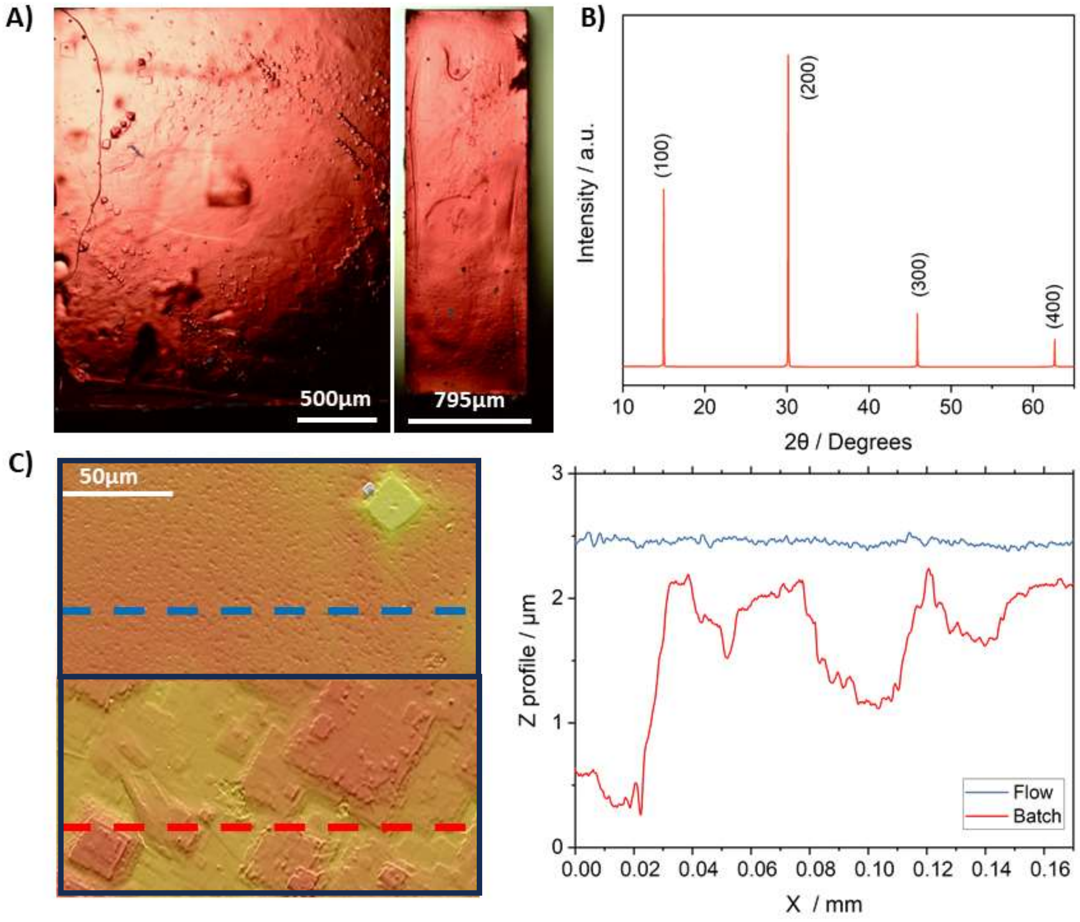

Figure 4 A) Top and transversal pictures of a selected crystal observed in an optical microscope. B) XRD spectra of a $MAPbBr_3$ crystal. C) Profilometry image of the crystal surface and profile of marked section

Selected crystals were characterized to evaluate their properties. The crystal shown in figure 4A had a square aspect ratio with size of 2.5x2.5mm and thickness of 0.8mm. The crystal exhibited a homogeneous structure, with neither visible cracks on the inside as observed in the microscope pictures nor inward angles between adjacent facets, something used as a sign to identify polycrystalline samples [7]. Nevertheless, some superficial defects are observed that can be attributed to previously discussed factors such as influence of other crystals in the vicinity. Also, crystals that grew over the resin and not the glass substrate showed growth rings (Figure S6), indicating an effect of reactor surface roughness on the crystal grow. X-Ray diffraction spectra of the crystal presented diffraction peaks at 14.97º, 30.14º. 45.90º and 62.63º, as seen in Figure 4B, that are attributed to the (100), (200), (300) and (400) facets. This indicates that only cubic $MAPbBr_3$ perovskite crystals were grown in the system [34] as with the traditional method (figure S7A). A profilometry image of the crystal under 50x magnification shown in figure 4C revealed a regular surface for the glass grown crystals. In contrast, batch crystals showed more pronounced height variations an artifacts, as can be seen in figure 4C. A more detailed area measurement with atomic force microscopy (AFM) revealed a local a root mean-squared roughness of 9.38 nm (Figure S7B), an order of magnitude lower than polycrystalline [35] and the 30.7nm measured in batch synthesized crystals (Figure S7C). Finally, the synthesized crystals optical properties were evaluated, and they presented an absorption curve with a sharp edge around 555 nm (Figure S7D) and a photoluminescence in a peak located at 542 nm. These results are in line of other reported values for synthesized $MAPbBr_3$ [34, 36, 37].

To substantiate the superior optoelectronic characteristics of perovskite crystals grown in a flow-reactor compared to those grown using the conventional batch method, we conducted measurements of photoluminescence (PL) in both steady-state emission and time-resolved photoluminescence (TRPL) (Figure 5). The steady-state PL has the same maximum at 542 nm, but the intensity is approximately twice as high for the flow-reactor-grown crystal, implying a reduction in defect concentration and consequently a decrease in non-radiative processes. Furthermore, when examining the normalized PL (Figure 5B), a distinct secondary peak at longer wavelengths (575 nm) is evident in the batch-grown crystal, a feature commonly attributed in the literature to self-absorption within the perovskite material [38, 39].

Self-absorption significantly hampers the light extraction efficiency, resulting in diminished optical transparency of perovskite crystals and consequently impairing their photodetection performance. Photodetection currently represents a crucial application for perovskite single crystals [40, 41]. Interestingly, our findings indicate that this self-absorption effect is notably mitigated in crystals grown using a flow-reactor method. This observation suggests that the flow-reactor approach may serve as a promising initial step for producing higher-quality perovskite single crystals.

To further substantiate this claim, we conducted time-resolved photoluminescence (TRPL) measurements, revealing a significant one-order-of-magnitude disparity in the long-lived (bulk) lifetime values: τ_F = 335 ns for flow-reactor-grown crystals and τ_B = 45 ns for batch-grown crystals. These results point to a distinct reduction in defect density within the bulk crystal produced using the flow-reactor method as opposed to the batch method. While acknowledging the necessity for further statistical analysis and in-depth investigations, these preliminary findings serve as a proof of concept for the novel methodology proposed herein.

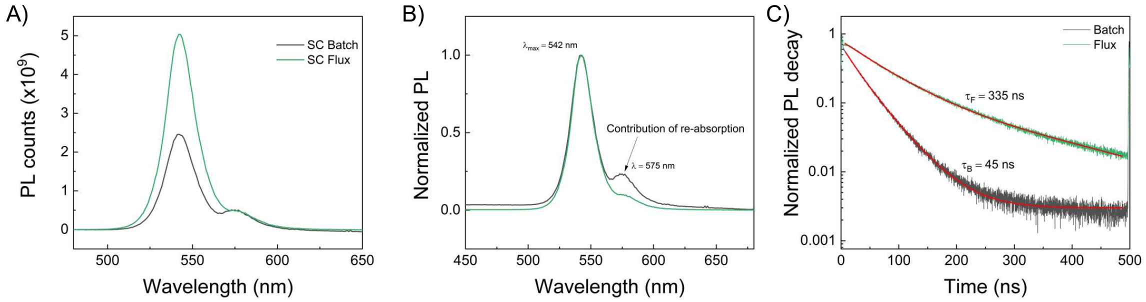

Figure 5. Comparison of photoluminescence response between SC grown in batch and in flow reactor using laser diode of 375 nm wavelength excitation source. A) PL emission of both crystals. Black color corresponds to the SC in batch and green color to the one from flow reactor. Note the 2 times higher intensity for the crystal from reactor. B) Normalized PL emission showing the second peak at 575 nm for the spectra corresponding to batch crystal. C) TRPL for the crystals showing one order of magnitude difference in the long-lived (bulk) lifetime values.

5.1.3 Conclusion

To sum up, a new concept for the syntheses of high-quality single crystal perovskites has been demonstrated here. The employment of 3DP employing commercially available resins for SLA printers allows for the development of tailored reactors for single crystal perovskite synthesis employing ITC methodologies. This is a very interesting proposition, since it allows to carefully control the heating profile continuously, and to add reagents into the reaction chamber without the need to open or manipulate the sample in any way. This is clearly advantageous compared to traditional batch crystallisation processes.

In this work, commercially available compatible resins with the challenging reaction conditions (DMF, high temperature) have been identified and evaluated under relevant working conditions. Two different flow reactors have been designed, printed and evaluated under different flow conditions. The optimal reactor configuration demonstrated the ability to generate single crystal $MAPbBr_3$ perovskites with high reproducibility over several synthetic iterations and improved photoluminescence properties.

5.1.4 Methodology

3D printed reactor fabrication.

Reactors were modelled using CAD software (Solidworks) and converted to STL. They were fabricated using a Formlabs 3 low force stereolithography (LFS) printer loaded with off-the-self Formlabs High Temp resin. STL files were sliced in Preform and printed with a layer height of 50 μm using the default settings of the manufacturer. EPDM O-rings were purchased from RTC Couplings. Clamps were purchased from Leybold.

Reactor material characterization

Thermogravimetric analyses (TGA) of the samples were performed using a TGA/DSC3 from Metler Toledo. Samples were heated at a 10 ºC/min heating rate under nitrogen atmosphere. Fourier transformed Infrared spectra (FT-IR) of the discs were collected using a JASCO FT/IR-4700 spectrometer equipped with a Miracle single-reflection ATR diamond/ZnSe accessory from Pike. Profilometric images of the samples were performed using an optical profilometer PLμ2300 from Sensofar. Images were taken under 50x magnification for an area of 254.64 x 190.90 μm. Thermal conductivity of the resin was measured using a C-Therm TCi from Mathis Instruments.

CFD simulations

The CFD simulation of the 3DP reactor was carried out using Openfoam®. The model was meshed with cubic cells (0.35 mm side), refinement controls for curvature (minimum cell size of 87.5 μm) and inflation layers near the walls for a better resolution of the flow in the regions with higher velocity gradients. As a result, the final mesh was composed by 940000 cells. The simulation was run in two separate configurations.

The first configuration was a steady-state resolution using the simpleFoam solver with a convergence criterion based on the RMS of the flow equations (10^{-4} for pressure, 10^{-5} for velocity components). The second configuration was a transient resolution using the scalarTransportFoam solver. The velocity and pressure fields resulting from the first configuration were used to solve the transport of the tracer over a frozen flow.

RTD studies

The experiment was carried out using the apparatus depicted in Figure S6. This setup includes two syringe pumps: one to control the primary flow rate, and the other to load a 50 μL loop into an automated 6-way Rheodyne valve. This valve was employed to simplify the process of injecting a tracer pulse into the flow stream. The Rheodyne valve was linked to a commercial flow cell, which allowed a light beam to pass through and be detected by a fixed-wavelength UV-visible spectrometer. All connections were made using 1/16-inch PEEK capillary tubes. The experiments utilized isopropanol and a Methyl Red (tracer) solution (1 mg L^{1}) in the same solvent, with a flow rate of 50 μL min^{-1}. The variation of the tracer concentration over time was determined by the absorbance peak at 525 nm in UV-VIS spectra (Figure S3B).

Precursor solution preparation.

In a typical synthesis, 1.12g of CH_3NH_3Br (>99 wt %, Great Cell Solar Materials) and 3.67g of $PbBr_2$ (>98 wt %, Alfa Aesar) were dissolved at 1:1 molar ratio in 10mL of DMF (> 99.9 wt %, anhydrous, VWR) to produce a 1 M solution of $MAPbBr_3$. Solutions were kept at room temperature under stirring and filtered before starting the crystallization, using 0.2 μm pore size PTFE filters in order to remove insoluble particles.

Continuous-flow growth experiments.

Flow experiments were performed using a programmable Tricontinent C3000 pump equipped with a 5 mL syringe. The previously prepared 1M $MAPbBr_3$ solution was loaded into the reactor and continuously fed by controlling the pump with an in-house developed code using Labview. Temperature was kept at 67 ºC inside the reactor, flow rate varied between 6 μL min^{-1} and 25 μL min^{-1}. In a standard experiment lasting 2 hours, once crystal formation occurred, the reactor was subsequently opened to remove the crystals and underwent cleaning in preparation for a new experiment (Figure S3A).

Yield was calculated using the equation (1)

$$Yield\ (\%) = \frac{m}{C \cdot (V + f \cdot t)} \cdot 100 \tag{1}$$

Where *m* is the mass of crystals obtained, *C* is the perovskite solution concentration in g mL^{-1}, *V* the volume of the reactor in mL (3.05 mL in the case of reactor V1), f the volumetric flow rate and *t* crystallization running time.

Synthesized crystal characterization

Images of the crystals were taken under a 4x magnification using a BA310E microscope from Motic equipped with a MoticamBTW camera.

XRD spectra was measured using a Bruker D8-Advance diffractometer, using CuKα radiation (λ = 1.5406 Å) by mounting the crystal in a sample holder to directly record it.

Atomic force microscopy images were made using JSPM-5200 Scanning Probe Microscope from Jeol. Images were taken in contact mode for an area of 2 x 2 µm with a pixel resolution of 256 x 256.

Profilometric images of the samples were performed using an optical profilometer PLµ2300 from Sensofar. Images were taken under 50x magnification for an area of 254.64 x 190.90 µm.

UV–vis absorption spectra was measured in a Jasco V-780 spectrometer (400-900nm) by mounting the crystal in a 3D printed holder. The holder was produced using an Ultimaker S5 printer equiped with Black Though PLA filament from Ultimaker. It consisted of a rectangle (12.5 mm wide, 42.5 mm height and 4 mm depth), to be fitted in the cuvette slot of the spectrometer, featuring a sample slot and windows fit to crystal size.

PL and TRPL measurements were performed with use of Edinburgh Instrument FLS 1000 fluorimeter with a picosecond pulsed diode laser EPL 375 nm as the excitation source. The pulse period was setteld at 200 ns for steady state PL and increased up to 500 ns for the TRPL performance with a time scale of 500 ns.

Conflicts of interest

There are no conflicts to declare.

Acknowledgements

This work was supported by FEDER/Ministerio de Ciencia e Innovación – Agencia Estatal de Investigación (PID2020-119628RB-C33). MZ and VS thank the funding received from the European Union's Horizon 2020 research and innovation programme under the Marie Skłodowska-Curie Individual Fellowships (GA no. 101026335). VS thanks Generalitat Valenciana (CIDEGENT 2018/036) for funding. The authors are grateful to the SCIC of the Universitat Jaume I for technical support. J. L-G. is supported by FPU21/03740 doctoral grant from the Spanish Ministry of Universities. CAA thanks the Spanish Ministry of Science and Innovation under contract number (TED2021-129758B-C33) MCIN/AEI/10.13039/501100011033/ European Union NextGeneration EU/PRTR provided gratefully acknowledged financial support. CT thanks the Generalitat Valenciana for a doctoral grant through the program Santiago Grisolía (CIGRIS/2021/075). The authors thank Dr. Vladimir Chirvony from Universidad of Valencia and Dr. Francisco García Moscoso from Universidad Pablo de Olavide for their valuable support in the performance of the optical and transient measurements.

5.1.5 References

(1) Manser, J. S.; Saidaminov, M. I.; Christians, J. A.; Bakr, O. M.; Kamat, P. V. Making and Breaking of Lead Halide Perovskites. *Accounts of Chemical Research* **2016**, *49* (2), 330-338. DOI: 10.1021/acs.accounts.5b00455.

(2) Kim, J. Y.; Lee, J.-W.; Jung, H. S.; Shin, H.; Park, N.-G. High-Efficiency Perovskite Solar Cells. *Chemical Reviews* **2020**, *120* (15), 7867-7918. DOI: 10.1021/acs.chemrev.0c00107.

(3) Liu, Y.; Yang, Z.; Liu, S. Recent Progress in Single-Crystalline Perovskite Research Including Crystal Preparation, Property Evaluation, and Applications. *Advanced Science* **2018**, *5* (1), 1700471. DOI: https://doi.org/10.1002/advs.201700471.

(4) Saidaminov, M. I.; Abdelhady, A. L.; Maculan, G.; Bakr, O. M. Retrograde solubility of formamidinium and methylammonium lead halide perovskites enabling rapid single crystal growth. *Chemical Communications* **2015**, *51* (100), 17658-17661, 10.1039/C5CC06916E. DOI: 10.1039/C5CC06916E.

(5) Trivedi, S.; Prochowicz, D.; Parikh, N.; Mahapatra, A.; Pandey, M. K.; Kalam, A.; Tavakoli, M. M.; Yadav, P. Recent Progress in Growth of Single-Crystal Perovskites for Photovoltaic Applications. *ACS Omega* **2021**, *6* (2), 1030-1042. DOI: 10.1021/acsomega.0c04593.

(6) Wang, Q.; Chen, B.; Liu, Y.; Deng, Y.; Bai, Y.; Dong, Q.; Huang, J. Scaling behavior of moisture-induced grain degradation in polycrystalline hybrid perovskite thin films. *Energy & Environmental Science* **2017**, *10* (2), 516-522, 10.1039/C6EE02941H. DOI: 10.1039/C6EE02941H.

(7) Amari, S.; Verilhac, J.-M.; Gros D’Aillon, E.; Ibanez, A.; Zaccaro, J. Optimization of the Growth Conditions for High Quality CH3NH3PbBr3 Hybrid Perovskite Single Crystals. *Crystal Growth & Design* **2020**, *20* (3), 1665-1672. DOI: 10.1021/acs.cgd.9b01429.

(8) García-Batlle, M.; Mayén Guillén, J.; Chapran, M.; Baussens, O.; Zaccaro, J.; Verilhac, J.-M.; Gros-Daillon, E.; Guerrero, A.; Almora, O.; Garcia-Belmonte, G. Coupling between Ion Drift and Kinetics of Electronic Current Transients in MAPbBr3 Single Crystals. *ACS Energy Letters* **2022**, *7* (3), 946-951. DOI: 10.1021/acsenergylett.1c02578.

(9) Tisdale, J. T.; Smith, T.; Salasin, J. R.; Ahmadi, M.; Johnson, N.; Ievlev, A. V.; Koehler, M.; Rawn, C. J.; Lukosi, E.; Hu, B. Precursor purity effects on solution-based growth of MAPbBr3 single crystals towards efficient radiation sensing. *CrystEngComm* **2018**, *20* (48), 7818-7825, 10.1039/C8CE01498A. DOI: 10.1039/C8CE01498A.

(10) Liu, Y.; Zhang, Y.; Zhao, K.; Yang, Z.; Feng, J.; Zhang, X.; Wang, K.; Meng, L.; Ye, H.; Liu, M.; et al. A 1300 mm2 Ultrahigh-Performance Digital Imaging Assembly using High-Quality Perovskite Single Crystals. *Advanced Materials* **2018**, *30* (29), 1707314, https://doi.org/10.1002/adma.201707314. DOI: https://doi.org/10.1002/adma.201707314 (acccessed 2022/06/30).

(11) Liu, Y.; Zhang, Y.; Yang, Z.; Feng, J.; Xu, Z.; Li, Q.; Hu, M.; Ye, H.; Zhang, X.; Liu, M.; et al. Low-temperature-gradient crystallization for multi-inch high-quality perovskite single crystals for record performance photodetectors. *Materials Today* **2019**, *22*, 67-75. DOI: https://doi.org/10.1016/j.mattod.2018.04.002.

(12) Liu, Y.; Yang, Z.; Cui, D.; Ren, X.; Sun, J.; Liu, X.; Zhang, J.; Wei, Q.; Fan, H.; Yu, F.; et al. Two-Inch-Sized Perovskite CH3NH3PbX3 (X = Cl, Br, I) Crystals: Growth and Characterization. *Advanced Materials* **2015**, *27* (35), 5176-5183, https://doi.org/10.1002/adma.201502597. DOI: https://doi.org/10.1002/adma.201502597 (acccessed 2022/06/28).

(13) Yao, F.; Peng, J.; Li, R.; Li, W.; Gui, P.; Li, B.; Liu, C.; Tao, C.; Lin, Q.; Fang, G. Room-temperature liquid diffused separation induced crystallization for high-quality perovskite single crystals. *Nature Communications* **2020**, *11* (1), 1194. DOI: 10.1038/s41467-020-15037-x.

(14) Sebastian, V. Toward continuous production of high-quality nanomaterials using microfluidics: nanoengineering the shape, structure and chemical composition. *Nanoscale* **2022**, *14* (12), 4411-4447, 10.1039/D1NR06342A. DOI: 10.1039/D1NR06342A.

(15) Newman, S. G.; Jensen, K. F. The role of flow in green chemistry and engineering. *Green Chemistry* **2013**, *15* (6), 1456-1472, 10.1039/C3GC40374B. DOI: 10.1039/C3GC40374B.

(16) Marre, S.; Jensen, K. F. Synthesis of micro and nanostructures in microfluidic systems. *Chemical Society Reviews* **2010**, *39* (3), 1183-1202, 10.1039/B821324K. DOI: 10.1039/B821324K.

(17) Sans, V.; Cronin, L. Towards dial-a-molecule by integrating continuous flow, analytics and self-optimisation. *Chemical Society Reviews* **2016**, *45* (8), 2032-2043, 10.1039/C5CS00793C. DOI: 10.1039/C5CS00793C.

(18) Liang, X.; Baker, R. W.; Wu, K.; Deng, W.; Ferdani, D.; Kubiak, P. S.; Marken, F.; Torrente-Murciano, L.; Cameron, P. J. Continuous low temperature synthesis of MAPbX3 perovskite nanocrystals in a flow reactor. *Reaction Chemistry & Engineering* **2018**, *3* (5), 640-644, 10.1039/C8RE00098K. DOI: 10.1039/C8RE00098K.

(19) Li, C.; Ding, B.; Zhang, L.; Song, K.; Tao, S. 3D-printed continuous flow reactor for high yield synthesis of CH3NH3PbX3 (X = Br, I) nanocrystals. *Journal of Materials Chemistry C* **2019**, *7* (30), 9167-9174, 10.1039/C9TC02390A. DOI: 10.1039/C9TC02390A.

(20) Abdel-Latif, K.; Bateni, F.; Crouse, S.; Abolhasani, M. Flow Synthesis of Metal Halide Perovskite Quantum Dots: From Rapid Parameter Space Mapping to AI-Guided Modular Manufacturing. *Matter* **2020**, *3* (4), 1053-1086. DOI: https://doi.org/10.1016/j.matt.2020.07.024.

(21) Capel, A. J.; Edmondson, S.; Christie, S. D. R.; Goodridge, R. D.; Bibb, R. J.; Thurstans, M. Design and additive manufacture for flow chemistry. *Lab on a Chip* **2013**, *13* (23), 4583-4590, 10.1039/C3LC50844G. DOI: 10.1039/C3LC50844G.

(22) Bettermann, S.; Kandelhard, F.; Moritz, H.-U.; Pauer, W. Digital and lean development method for 3D-printed reactors based on CAD modeling and CFD simulation. *Chemical Engineering Research and Design* **2019**, *152*, 71-84. DOI: https://doi.org/10.1016/j.cherd.2019.09.024.

(23) Thomas, K. M.; Kwon, S.; Lakerveld, R. Continuous Protein Crystallization in Mixed-Suspension Mixed-Product-Removal Crystallizers. *Crystal Growth & Design* **2021**, *21* (2), 757-769. DOI: 10.1021/acs.cgd.0c00885.

(24) Okafor, O.; Weilhard, A.; Fernandes, J. A.; Karjalainen, E.; Goodridge, R.; Sans, V. Advanced reactor engineering with 3D printing for the continuous-flow synthesis of silver nanoparticles. *Reaction Chemistry & Engineering* **2017**, *2* (2), 129-136, 10.1039/C6RE00210B. DOI: 10.1039/C6RE00210B.

(25) Miralles-Comins, S.; Zanatta, M.; Sans, V. Advanced Formulations Based on Poly(ionic liquid) Materials for Additive Manufacturing. *Polymers* **2022**, *14* (23), 5121. DOI: 10.3390/polym14235121.

(26) Okafor, O.; Robertson, K.; Goodridge, R.; Sans, V. Continuous-flow crystallisation in 3D-printed compact devices. *Reaction Chemistry & Engineering* **2019**, *4* (9), 1682-1688, 10.1039/C9RE00188C. DOI: 10.1039/C9RE00188C.

(27) *https://sdbs.db.aist.go.jp/sdbs/cgi-bin/cre_index.cgi*. (accessed.

(28) Mhamdi, A.; Mehdi, H.; Bouazizi, A. Effect of solvents and annealing treatment on the properties of the methylammonium lead tribromide perovskite thin films. *Journal of Materials Science: Materials in Electronics* **2021**, *32* (2), 2302-2311. DOI: 10.1007/s10854-020-04994-0.

(29) *https://3d.formlabs.com/form-3-dimensional-accuracy-report/*. (accessed.

(30) Sans, V.; Karbass, N.; Burguete, M. I.; García-Verdugo, E.; Luis, S. V. Residence time distribution, a simple tool to understand the behaviour of polymeric mini-flow reactors. *RSC Advances* **2012**, *2* (23), 8721-8728, 10.1039/C2RA20903A. DOI: 10.1039/C2RA20903A.

(31) Dong, Q.; Fang, Y.; Shao, Y.; Mulligan, P.; Qiu, J.; Cao, L.; Huang, J. Electron-hole diffusion lengths > 175 μm in solution-grown CH₃NH₃PbI₃ single crystals. *Science* **2015**, *347* (6225), 967-970. DOI: doi:10.1126/science.aaa5760.

(32) Stefan-Kharicha, M.; Kharicha, A.; Zaidat, K.; Reiss, G.; Eßl, W.; Goodwin, F.; Wu, M.; Ludwig, A.; Mugrauer, C. Impact of hydrodynamics on growth and morphology of faceted crystals. *Journal of Crystal Growth* **2020**, *541*, 125667. DOI: https://doi.org/10.1016/j.jcrysgro.2020.125667.

(33) Maes, D.; Lutsko, J. F. Molecular Viewpoint on the Crystal Growth Dynamics Driven by Solution Flow. *Crystal Growth & Design* **2020**, *20* (4), 2294-2304. DOI: 10.1021/acs.cgd.9b01434.

(34) Boopathi, K. M.; Martín-García, B.; Ray, A.; Pina, J. M.; Marras, S.; Saidaminov, M. I.; Bonaccorso, F.; Di Stasio, F.; Sargent, E. H.; Manna, L.; et al. Permanent Lattice Compression of Lead-Halide Perovskite for Persistently Enhanced Optoelectronic Properties. *ACS Energy Letters* **2020**, *5* (2), 642-649. DOI: 10.1021/acsenergylett.9b02810.

(35) Li, X.; Bi, D.; Yi, C.; Décoppet, J.-D.; Luo, J.; Zakeeruddin, S. M.; Hagfeldt, A.; Grätzel, M. A vacuum flash–assisted solution process for high-efficiency large-area

perovskite solar cells. *Science* **2016**, *353* (6294), 58-62. DOI: doi:10.1126/science.aaf8060.

(36) Wang, K.-H.; Li, L.-C.; Shellaiah, M.; Wen Sun, K. Structural and Photophysical Properties of Methylammonium Lead Tribromide (MAPbBr3) Single Crystals. *Scientific Reports* **2017**, *7* (1), 13643. DOI: 10.1038/s41598-017-13571-1.

(37) Wu, B.; Nguyen, H. T.; Ku, Z.; Han, G.; Giovanni, D.; Mathews, N.; Fan, H. J.; Sum, T. C. Discerning the Surface and Bulk Recombination Kinetics of Organic–Inorganic Halide Perovskite Single Crystals. *Advanced Energy Materials* **2016**, *6* (14), 1600551. DOI: https://doi.org/10.1002/aenm.201600551.

(38) Fang, Y.; Wei, H.; Dong, Q.; Huang, J. Quantification of re-absorption and re-emission processes to determine photon recycling efficiency in perovskite single crystals. *Nature Communications* **2017**, *8* (1), 14417. DOI: 10.1038/ncomms14417.

(39) Schötz, K.; Askar, A. M.; Peng, W.; Seeberger, D.; Gujar, T. P.; Thelakkat, M.; Köhler, A.; Huettner, S.; Bakr, O. M.; Shankar, K.; et al. Double peak emission in lead halide perovskites by self-absorption. *Journal of Materials Chemistry C* **2020**, *8* (7), 2289-2300, 10.1039/C9TC06251C. DOI: 10.1039/C9TC06251C.

(40) Jin, T.; Liu, Z.; Luo, J.; Yuan, J.-H.; Wang, H.; Xie, Z.; Pan, W.; Wu, H.; Xue, K.-H.; Liu, L.; et al. Self-wavelength shifting in two-dimensional perovskite for sensitive and fast gamma-ray detection. *Nat. Commun.* **2023**, *14* (1), 2808. DOI: 10.1038/s41467-023-38545-y.

(41) Zhao, X.; Niu, G.; Zhu, J.; Yang, B.; Yuan, J.-H.; Li, S.; Gao, W.; Hu, Q.; Yin, L.; Xue, K.-H.; et al. All-Inorganic Copper Halide as a Stable and Self-Absorption-Free X-ray Scintillator. *J. Phys. Chem. Lett.* **2020**, *11* (5), 1873-1880. DOI: 10.1021/acs.jpclett.0c00161.

5.2 Supporting information

Profilometry of printed resin surface

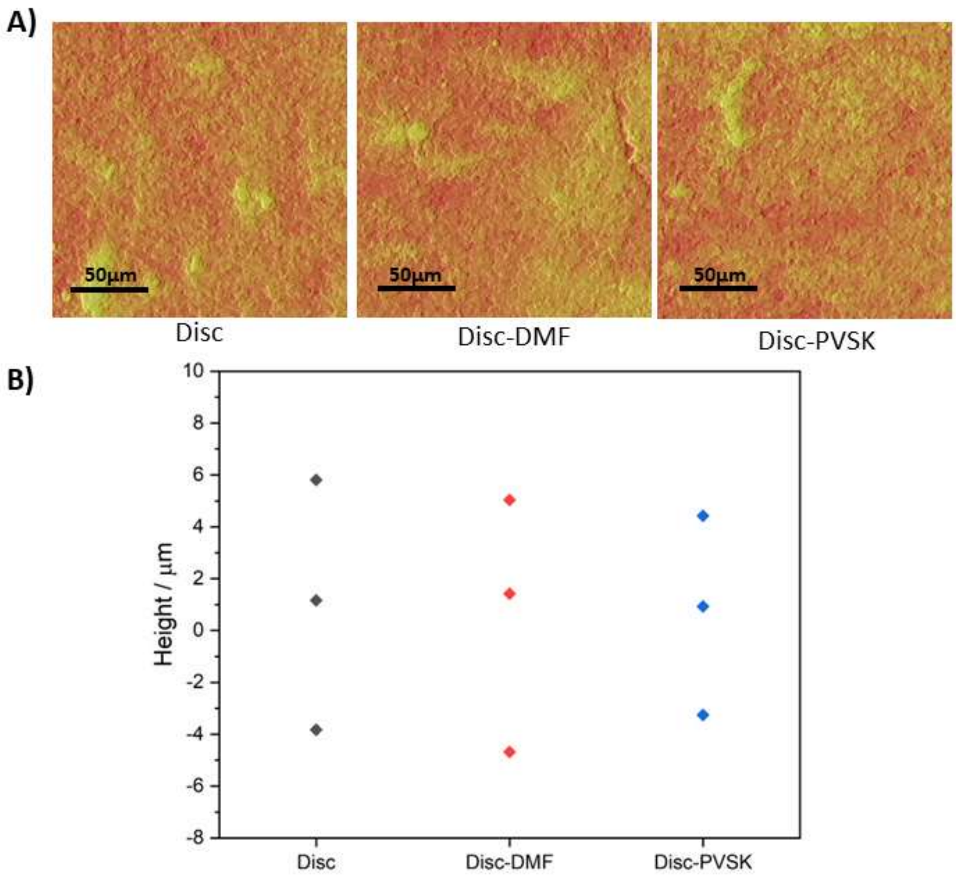

Figure S1. A) Profilometry pictures of the printed discs surfaces B) From top to bottom in each sample: maximum height, root mean square deviation and minimum height.

Preliminary reactor design

Figure S2. Reactor V0, 3D model and printed model.

Schematics of setups using during flow experiments

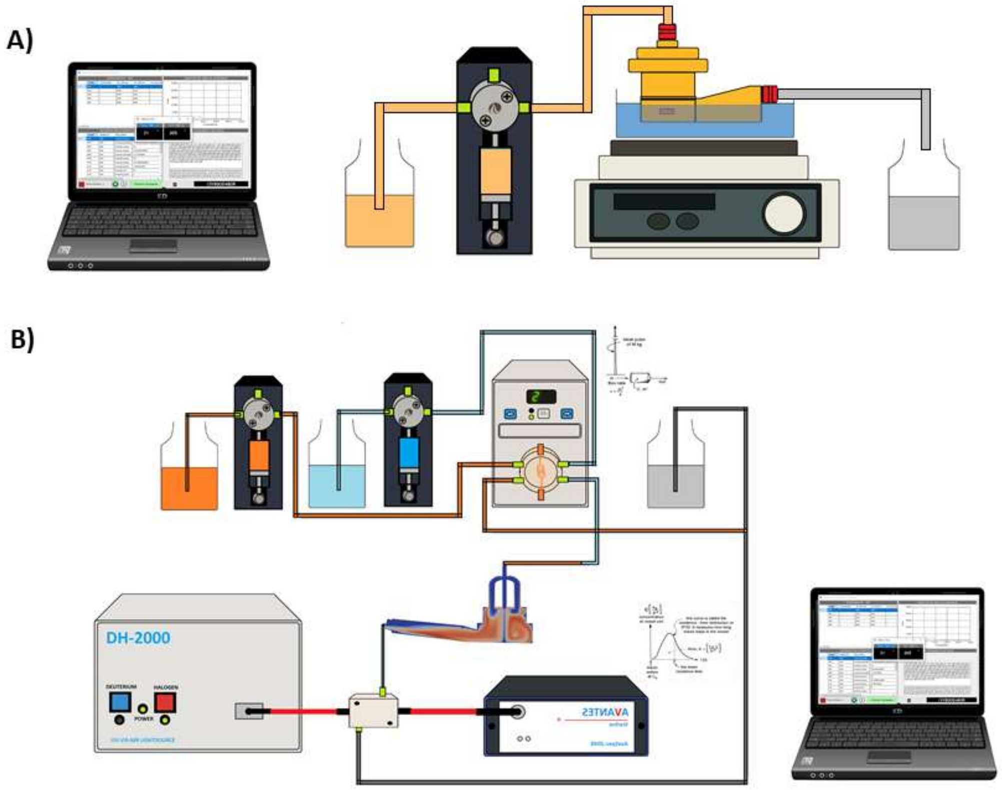

Figure S3. A) Schematic for crystallization experiments. B) Schematic for RTD studies.

Calibration of reactor chamber temperature

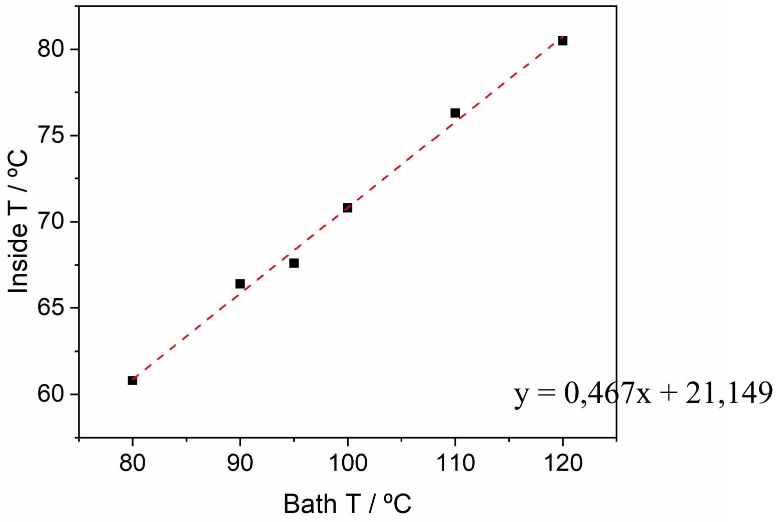

Figure S4. Relationship between heating bath temperature and temperature in the bottom part of the interior of the reactor after 2 hours of waiting time.

Relationship between number of crystals, crystal size and yield of crystallisation

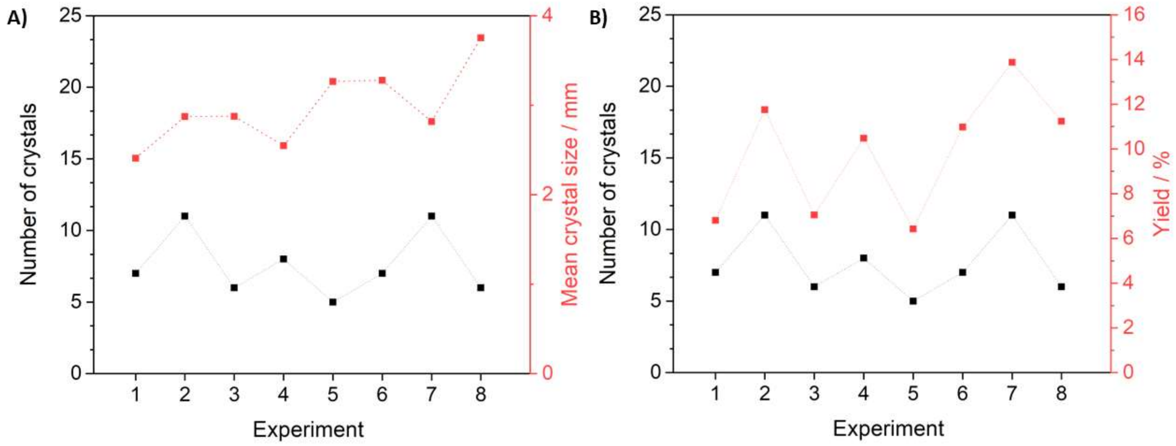

Figure S5. A) Number of crystals and mean crystal size for each experiment. B) Number of crystals and yield for each experiment.

Influence of reactor surface over crystal homogeneity

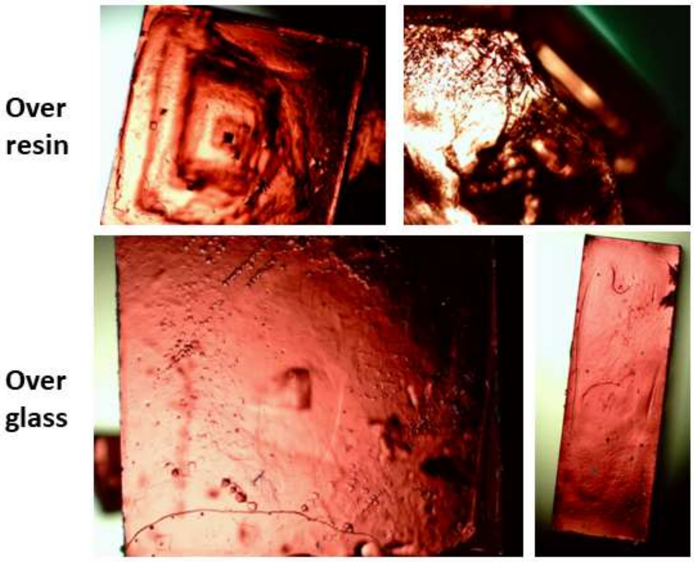

Figure S6. Difference of homogeneity between crystals grown over resin and over glass

Supplemental characterization data

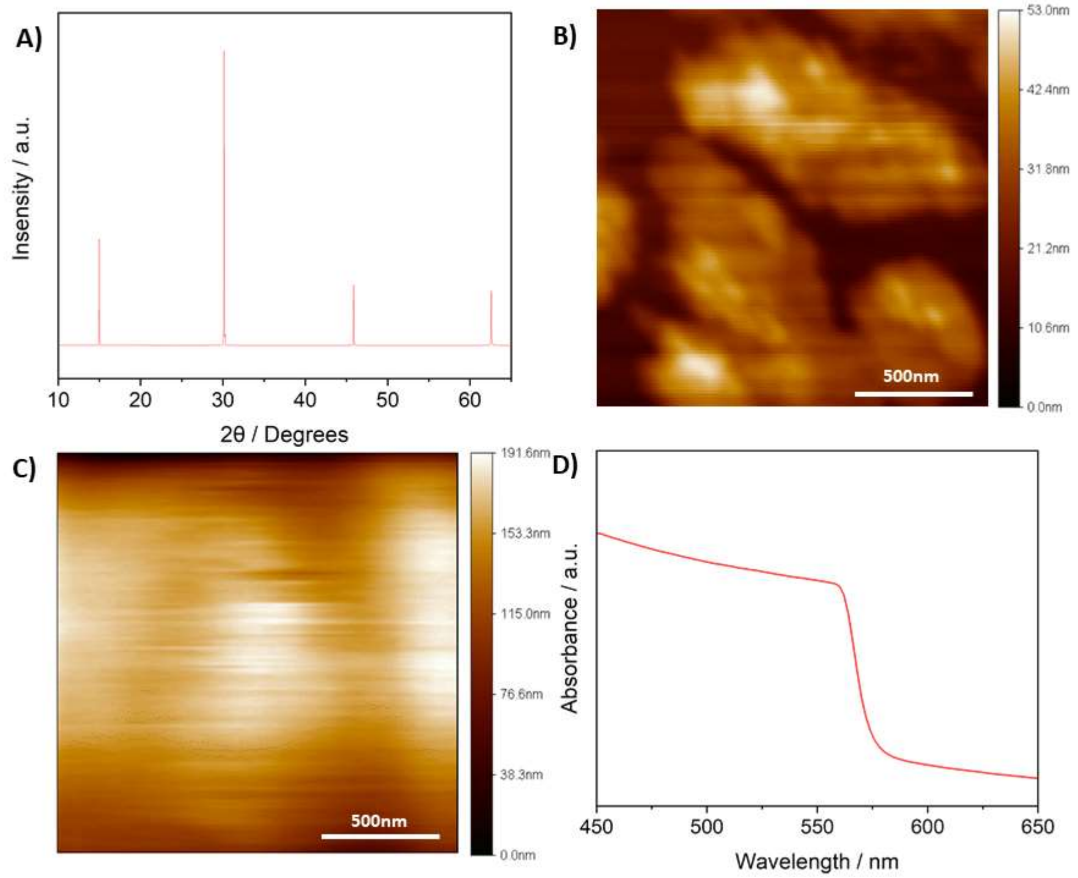

Figure S7. A) B) XRD spectra of batch synthesized $MAPbBr_3$ crystal. V) AFM image of the flow synthesized crystal surface. C) AFM image of the batch synthesized crystal surface D) Absorption spectra of flow synthesized crystal

Table S1. Results of the PL decay kinetics fitting by a sum of two exponential decay curves with lifetimes τ_i and relative amplitudes A_i.

Sample	τ_1 (ns)	A_1	τ_2 (ns)	A_2
Batch	23.83	0.28	44.91	0.39
Flow-reactor	70.73	0.69	334.95	0.11

Chapter 6. Digital flow platform for the synthesis of high-quality multi-material perovskites

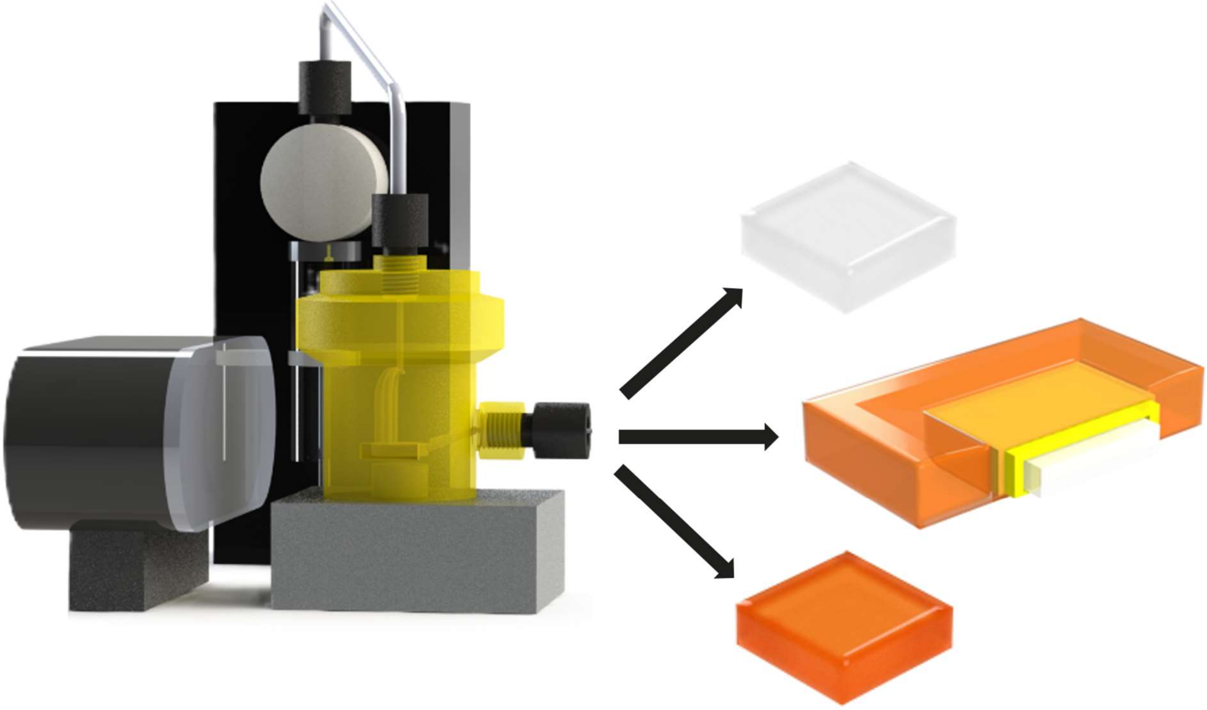

The results described during the present chapter are under the process of submission. The current version of the paper is publicly available as preprint.

6.1 Main Text

Abstract

Perovskite materials have demonstrated great potential for a wide range of optoelectronic applications due to their exceptional electronic and optical properties. However, synthesising high-quality perovskite films remains a significant challenge, often hindered by batch-wise processes that suffer from limited control over reaction conditions, scalability and reproducibility. In this study, we present a novel approach for synthesising single-crystal perovskites with an optimised continuous-flow reactor. Our methodology utilises a 3D printed system that enables precise control over reactant concentrations, reaction times, and temperature profiles. The reaction chamber was designed and optimised by combining residence time distribution (RTD) studies and computational fluid dynamics (CFD) simulations. High-quality single-crystal perovskites with different formulations were obtained employing seeding and seedless conditions. The possibility of synthesising mixed halide single crystal perovskites with different compositions along its structure was demonstrated by simply shifting the feedstock solution during the crystallisation, demonstrating the versatility of this technology.

1. Introduction

Over the recent decade, the interest in hybrid organic-inorganic perovskites has greatly risen. Thanks to their widely tuneable semiconductive and optoelectronic properties, this family of materials has seen great developments in fields like solar cells, [1] X-ray sensors, [2] LEDs[3] or memristors. [4] Part of the interest is due to the possibility of their synthesis under mild conditions using solution-based approaches. Most of the applications using these materials employ polycrystalline thin films, but the boundaries between grains hinder the maximum performance of the resulting devices and can induce material degradation paths. [5] In this regard, the use of monocrystalline perovskites offers superior properties in terms of lower trap density, longer carrier diffusion lengths, and resistance to degradation by moisture. [6]

Perovskite single crystals have been classically grown in batch with techniques like antisolvent crystallisation, [7] solvent evaporation[8] or solution temperature lowering. [9] Achieving millimetre-sized crystals with these methods required days. In contrast, the inverse temperature crystallisation method (ITC), based on the retrograde solubility of the perovskite (solubility decreases as temperature is increased), allows it to grow crystals in a matter of hours. [10] One of the main problems derived from its use is the loss of control over nucleation, as the increase in temperature also accelerates crystallisation kinetics, resulting in a decrease in crystal quality and reproducibility between experiments. [11] This is reflected in the range of electronic defect concentrations reported, even for the monocrystalline structures[12]. Different strategies have been used to overcome these issues, including control over precursor quality, [13] slow ramped heating of solution, use of seeds[14] or localised heating. [15] Nevertheless, batch synthesis has limitations since the maximum crystal size is dependent on the volume and concentration of the starting solution, and the inhomogeneous distribution of temperature and precursor concentration within the crystallisation chamber might affect the quality of the crystals.

Continuous flow synthesis has become an important asset in the transition to more sustainable processes. In complex processes like crystallisation, the use of continuous flow reduces mass and heat transfer limitations, resulting in more homogeneous product distribution compared to batch, improving the overall reproducibility. [16,17] In the field of perovskites, there are numerous reports of their application for the synthesis of crystalline materials, often upgrading the properties of their batch-synthesised counterparts. [18,19] The synthesis of nanostructured perovskite materials is typically carried out in coil reactors with cross sections under 1 mm. [20] In the case of higher lateral area materials, like millimetre-sized monocrystalline perovskites, the cross-section of the tubing severely limits their growth. Meanwhile, as the cross-section increases, mass and heat transfer limitations present in batch might arise[16]. Therefore, there is a need for developing new geometries where crystals have sufficient space for their growth while maintaining the advantages of continuous flow.

Digital reactor design combines computer-aided design (CAD), computational fluid dynamics (CFD) and additive manufacturing to produce advanced reactors with tailored geometries and advanced mixing features. [21, 22] Modelled geometries can be used for simulating the resulting flow pattern with CFD, calculating parameters like flow streamlines, velocity and temperature fields, or tracer transport to validate the model. The analysis of CFD permits the detection of flow maldistributions (short-circuits, dead volumes, etc.) to optimise the CAD geometry. [23] Finally, thanks to 3D printing (3DP), validated reactors can be swiftly manufactured onsite for their experimental application.[24,25] Another significant step towards highly controlled and reproducible synthetic platforms is the development of digital flow platforms. Reaction conditions can be transformed into digital inputs; therefore, solution delivery or reactor temperature can be controlled through an interface for setting up experiments. Additionally, the implementation of in-line analytics allows recording data, like absorbance[26] or photoluminescence, [27] for monitoring crystal growth in real-time. With this, variability caused by human intervention is minimised, and products obtained can be directly correlated with acquired data to better understand the process. It could even be possible to implement self-optimisation algorithms for achieving synthesis by selecting target properties directly. [20,28,29] Digital flow platforms have been successfully used for the synthesis of crystalline materials, [27,30,31] and very recently, the growth of high-quality perovskites has been monitored by employing in-situ video imaging. [32] We presented in our previous work their potential in the synthesis of perovskite single crystals, [19] albeit further developments were required to better control the number of crystals synthesised and to improve their quality.

Thanks to the flow platform developed during this work, we achieved a high degree of reproducibility, allowing for the synthesis of perovskite single crystals with consistent properties and minimal batch-to-batch variations. Moreover, the continuous-flow approach offers improved reaction kinetics, leading to enhanced crystallinity, homogeneity and reduced defect density in the resulting perovskite films. We also investigate the impact of various reaction parameters, such as precursor flow rates, reaction temperatures, and solvent compositions, on the properties of the resulting films and device performance. Furthermore, we use the same platform for the synthesis of different perovskite materials, and its design enables the change of material without interrupting the process. XPS and X-ray diffraction (XRD) have confirmed that the successive perovskite films obtained are stoichiometrically and structurally homogeneous. Hence, our study demonstrates the successful synthesis of high-quality perovskite films under continuous-flow conditions, offering a scalable and reproducible method to produce perovskite-based optoelectronic devices. The continuous-flow approach presents an exciting avenue for advancing the field of perovskite research, enabling improved device performance and paving the way for large-scale commercialisation of perovskite-based technologies.

2. Results and discussion

2.1 Design of flow platform

The main aim of the work was to build a low-cost platform for consistently producing perovskite single crystals with improved properties. In this regard, a strategy addressing multiple fronts for controlling the crystallisation process was developed. As a starting point, we used the combination of flow and a 3D printed reactor to develop a system capable of yielding perovskite single crystals based on previous work. [19] However, further developments of the technique were required to demonstrate an optimised control over the crystallisation processes. To achieve this, a platform was designed (Figure 1) with an optimised flow diffuser to generate a pattern for homogeneous precursor distribution in the crystallisation chamber. The localised homogeneous heating of the surface of the crystallisation chamber aimed to improve control over nucleation and crystallisation.

In parallel, the implementation of a vision control algorithm allows the monitoring of growth kinetics in real time. Finally, the implementation of flow control methodologies with multiple programmable pumps was developed to dynamically control the composition of the crystallisation environment, thus enabling the development of innovative single-crystal multi-materials.

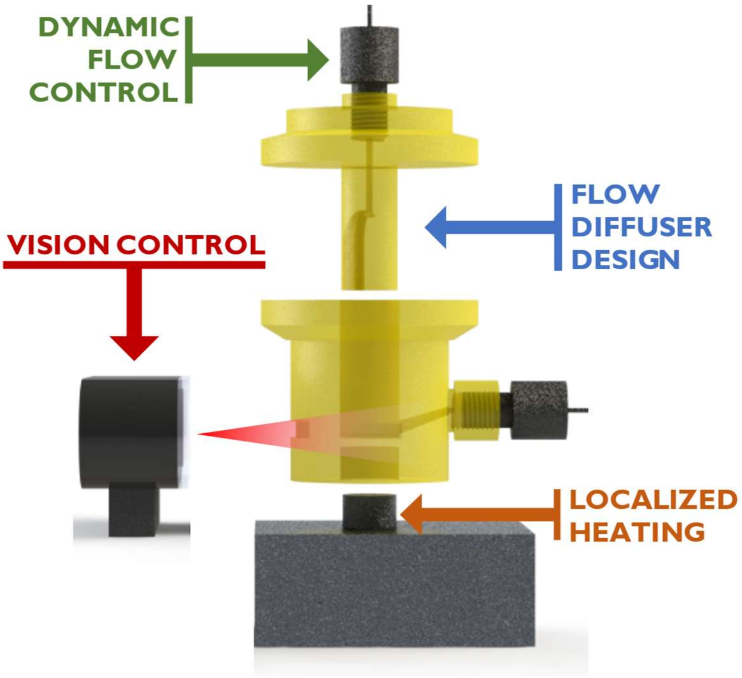

Figure 1. General overview of the digital flow platform developed in this work

The core reactor was designed as a two-bodied system, plus additional accessories for controlling flow, monitorisation, and heating. The bottom part featured a 10.5 mm diameter circular hole for introducing glass substrates and an outlet to maintain steady state flow conditions. The top part was designed as a cylinder, featuring flow channels to act as an inlet, that was inserted into the reactor body. Once both parts were connected and the system closed using a clamp, a small chamber of 1.5 mm height was created to grow crystals with a volume of 0.13 mL (more detailed measurements can be seen in Figure S1). The pieces were manufactured using 3D printing techniques based on stereolithography, which is based on the focused polymerisation of a thin layer of ink inside the vat using a laser beam. [33] The photopolymerisable resin selected was High Temp Resin (HRT) from Formlabs, as we previously demonstrated its compatibility with conditions used for the Inverse Temperature Crystallisation (ITC) of the $MAPbBr_3$ perovskite. [19]

2.2 Optimised design based on flow dynamics

The first step was the study of the flow inlet configuration to achieve a more homogeneous flow distribution in the crystallisation chamber compared to the previous model of the designed reactor. In the original iteration, the flow diffusor, which includes the flow inlet and the diffuser, was designed as a cylinder featuring a flow line divided into seven channels to distribute the flow homogeneously into the reactor. [19] Different flow diffusers for the reactor were fabricated with a varying number of holes and orientations relative to the reactor's lower outlet. An orienting arrow was added to the upper design to aid positioning, as shown in Figure 2A.

To evaluate the impact of different flow diffusor configurations, pulse tracer-based residence time distribution (RTD) studies were conducted as a quantitative measure of the internal mixing within the reactor. [31,34] Here, an inert tracer pulse was injected into the reactor, and the output was constantly recorded with a UV-VIS spectrophotometer. With this, the residence time distribution function ($E(\theta)$) can be calculated to evaluate differences in residence time of fluid particles. Figure 2B shows the $E(\theta)$ curves of the different geometries studied. Initially, the number of inlets in the reactor's flow diffusor was evaluated (1, 3, 7 inlets), all oriented in an initial 180° configuration to the outlet, using a liquid flow rate of 50 $\mu L\ min^{-1}$. The curve corresponding to the flow diffusor with three inlets, referred to as CAP 3 ENT, presents a distribution closer to the ideal normalised distribution time of 1, while the other two show premature tracer breakthrough, suggesting issues such as channelling or short-circuiting.

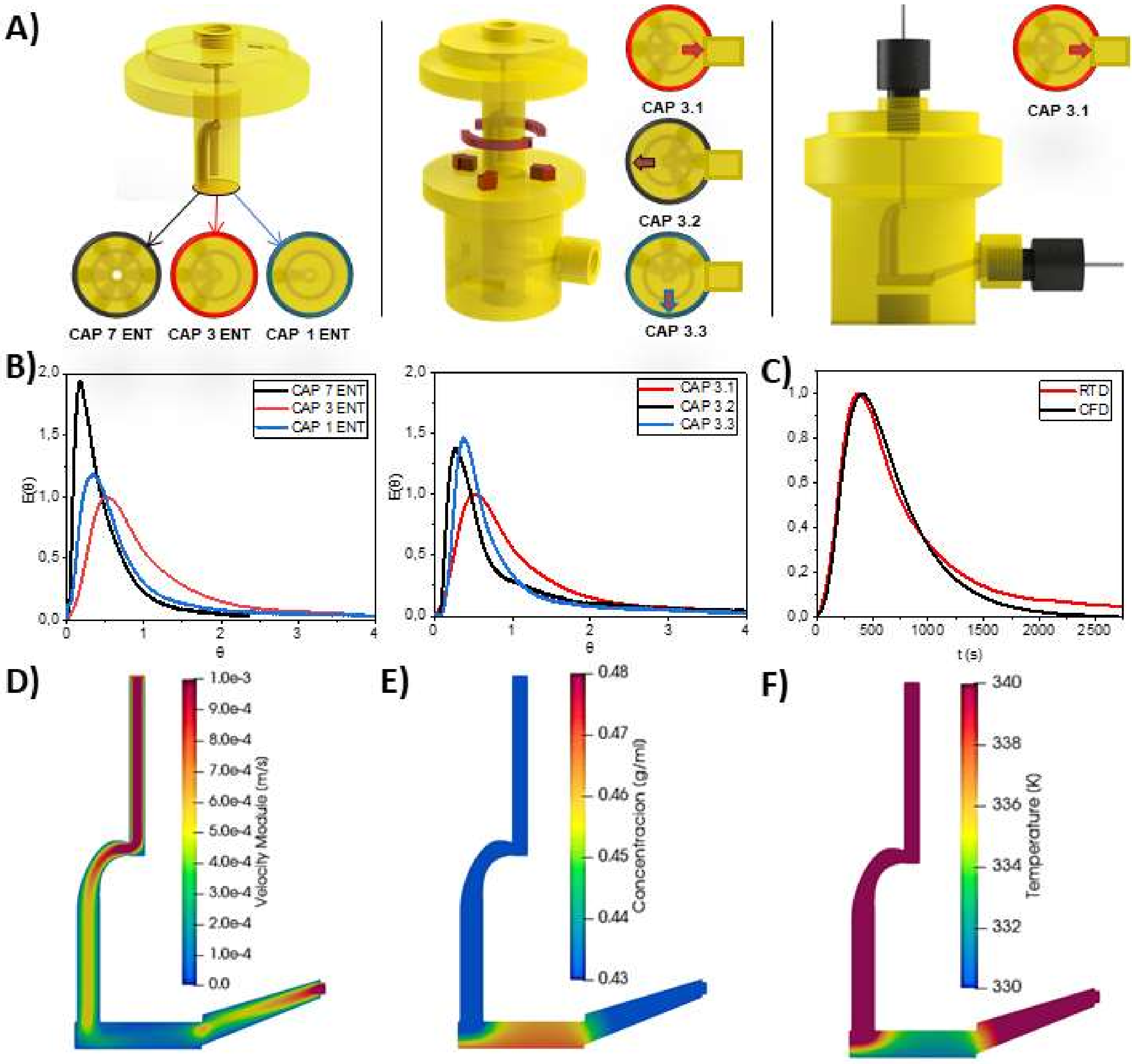

Figure 2. A) Flow diffuser development studied by residence time distribution (RTD) and CFD. B) Left: analyses of multiple inlet flow diffuser geometries. Right: geometry orientations are studied as a function of the angle between the inlet and outlet orientations. C) Comparison of RTD study and CFD simulation for the optimal flow diffuser geometry. CFD simulations of: D) velocity profile inside the reactor; E) temperature distribution field; F) solubility field of $MAPbBr_3$ in dimethylformamide (DMF).

Once it was established that the configuration with three inlets (CAP 3 ENT) offers better flow distribution compared to the 1 and 7 inlet designs, the orientation of the inlets was studied. The orientation CAP 3.1, in which the three inlets of the reactor's upper part are situated opposite the outlet, showed a more homogeneous flow distribution compared to the other inlet angles studied, which showed a less homogeneous tracer concentration. To validate these results, a CFD simulation of the system was performed. As shown in Figure

2C, an overall agreement between the RTD experimental curve and validated the CFD simulations performed. The experimental curve experiences a slightly longer tail associated with wall effects and inhomogeneities of the structured reactor.

The heating system was designed to provide heat specifically directed towards the crystallisation surface, thus avoiding undesired secondary nucleation and crystal growth. An aluminium block connected to a heating resistance controlled by a PID (Proportional-Integral-Derivative) temperature controller was fabricated featuring a little pivot connected with the cavity of the bottom part of the main body of the reactor. A thin wall of 1.8 mm separated the glass substrate and the heating block pivot. The rest of the reactor and heating block were adequately insulated from the environment using thick polymer walls. A calibration of the relationship between the nominal temperature of the PID controller and the inside of the chamber was performed (Figure S2).

The flow and temperature gradients within the crystallisation chamber play a key role in the uniformity of the perovskite concentration and uniformity during the crystallisation process. Therefore, using the values previously validated at the RTD, heat exchange and velocity profiles at the interior of the crystallisation chamber were modelled using CFD. A flow of precursor solution through the reactor passing through the crystallization chamber was simulated while simultaneously, the bottom section of the reactor was constantly heated. In Figure 2D, it can be noticed that the orientation of the inlets promotes a smooth transition from high to low velocities, allowing the solution to homogenise near the bottom where crystallisation starts occurring, also promoting steady, regular crystal growth. Regarding temperature, the contour in Figure 2E shows the formation of a steady gradient of temperature in the chamber that decreases with the distance to the heating wall, as expected. Also, it can be noticed the effect due to the entrance of the cold stream at the rear part of the chamber. The temperature increases as the flow advances through the chamber, promoting nucleation in the middle/frontal region of the reactor. This temperature distribution (T) has a direct effect on the solubility concentration (C) of $MAPbBr_3$ in dimethylformamide (DMF) (Eq. 1). [14]

$$C = 0.0023 \times exp\left(\frac{1782}{T+273.15}\right) \tag{1}$$

Figure 2F clearly shows that lower solubilities are observed at the bottom of the reactor, suggesting that saturation will occur in this area, leading to crystal nucleation near the bottom. Additionally, even if some nucleation occurs near the chamber entrance, significant crystal growth is unlikely due to the higher solubility in that region.

2.3 Vision control of growth kinetics of perovskite single crystals

Once the optimal reactor configuration was selected, the platform was ready for the growth of perovskite single crystals. $MAPbBr_3$ was used as the case model, as we previously demonstrated the possibility of its growth using continuous flow and the ITC method. [19] The monitoring was conducted using the setup illustrated in Figure 3A. The system features a 3D-printed platform that supports the heating block of the crystalliser, along with two perpendicular mounts that house cameras. These cameras capture images at specified time intervals, which are subsequently processed using the OpenCV library[35] for image recognition and Python scripts for data analysis. The reactor is equipped with two $33mm^2$ rectangular windows, perpendicular to the substrate, that allow for the observation of perovskite crystal growth. During the analysis, the crystal size is normalised using these windows as a reference, ensuring precise and consistent measurement of crystal growth. The analysis software developed for this purpose is available on a supplementary GitHub repository. [36] The methodology was validated by conducting analyses of the vision computing area (VCA), comparing them to the experimental determination of the size of the perovskites, which was measured outside the crystallisation chamber with a calliper. A good experimental correlation was found (Figure 3A). It is important to mention that a negative x0 indicates that the VCA system cannot reliably measure very small perovskites ($<1\ mm^2$). Hence, the system can assess the growth of perovskites, yet the nucleation processes can only be qualitatively evaluated.

A series of experiments were conducted to monitor the growth of $MAPbBr_3$ perovskite single crystals under varying conditions. The concentration of reagents (methylammonium bromide and lead (II) bromide in dimethyl formamide) remained constant at $1.2\ mol\ L^{-1}$, while other parameters were systematically varied. Initially, experiments were conducted without the use of seed crystals, focusing on evaluating the influence of key parameters such as flow rate and temperature on single crystal growth. Growth temperatures were kept as low as possible to minimise the apparition of secondary crystal nuclei while enabling stable crystal growth. A summary of the experimental conditions is provided in Table S1, while Figure 3B illustrates the differences in growth kinetics for different temperatures under the same conditions. The crystal growth kinetics presented a direct dependence on the solution temperature. At 58 ºC, no nucleation was observed until 200 minutes, followed by slow growth. Alternatively, by selecting a temperature of 68 ºC, nucleation started at 50 minutes, and the slope was notably more pronounced. This behaviour was expected since, at higher temperatures, it's easier for an oversaturated system to overcome the nucleation energy for the subsequent formation of nuclei, and the growth kinetics are also favoured at higher temperatures. [11]

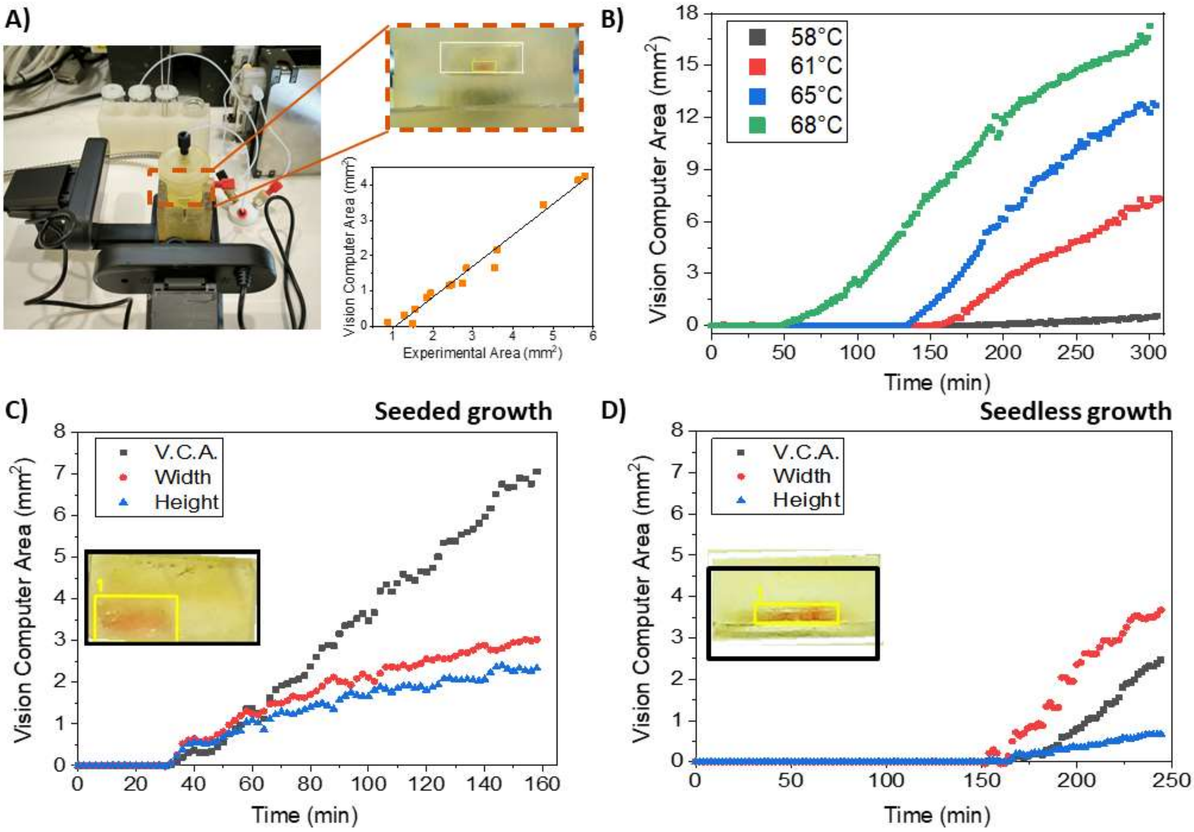

Figure 3. A) Control setup of the growth of perovskite single crystals. The correlation between the vision computing area (VCA) and the experimental area of the perovskites was y=-0.93+0.88x. R^2=0.976. B) Temperature-dependent perovskite growth kinetics for unseeded perovskites. Crystallisation kinetics for C) seeded growth crystals; D) unseeded growth crystals.

While nucleation time decreases at higher temperatures, the probability of uncontrolled nucleation increases. Seed-assisted growth is a way to enable growth at lower temperatures. Here, previously grown and harvested $MAPbBr_3$ single crystals are introduced into the saturated solution to be used as nucleation centres for further growth. For the case of a 1.2 mol L^{-1} $MAPbBr_3$ precursor solution at a 61 ºC temperature, with a 25 µl min^{-1} flowrate, seeded and unseeded experiments were monitored (figures 3C and 3D). Seeded experiments presented a 30-minute induction time where growth was not observed. On the other hand, non-seeded experiments typically present a time of approximately 150 minutes of induction time before crystals are observed. At selected conditions, the solution presents a low supersaturation level. Hence, further nucleation is unlikely, [11] thus inhibiting the appearance of secondary crystals. However, this makes seedless growth challenging. Another difference observed is the aspect ratio of crystals, as also seen in Figure 3C. Seeded crystals present more similar growth speeds in both horizontal and horizontal directions, while unseeded crystals favour horizontal growth (Figure 3D), resulting in a higher area-to-thickness ratio. It should be considered that partial redissolution of the seed during the initial minutes increased the supersaturation level in all the surroundings of the crystal. This would cause an acceleration of growth in all directions, as observed in Figure 3C. Alternatively, in seedless experiments, crystals remained thinner, possibly due to a combination of factors that need further exploration, like the temperature difference between the top and bottom, or the effect of the flow parallel to the crystal surface.

Additionally, the platform was tested for the synthesis of $MAPbCl_3$ crystals, as it also presented retrograde solubility when precursors were dissolved into a mixture of dimethyl formamide and dimethyl sulfoxide (1:1). In this case, different solution concentrations were tested at the same conditions used for the previous bromide experiments (61ºC and 25μL min^{-1} flowrate). $MAPbCl_3$ crystals were obtained successfully using a 0.8M solution concentration, demonstrating the possibility of extending the principles of the platform to other systems that can be grown via ITC of the platform. However, $MAPbCl_3$ appeared to be more prone to secondary nucleation, something that can be controlled by a more exhaustive adjustment of crystallisation conditions. Moreover, due to the colourless look of the crystals, growth could not be monitored by the existing setup. Further developments of the platform could implement photoluminescence measurements or other methodologies for overcoming this issue.

2.4 Characterisation of perovskite single crystals

Selected crystals synthesised with the previously discussed methodology were characterised to evaluate their properties. Seedless-grown crystals showed a clear and homogenous structure, as seen in Figure 4A, with no observable morphological defects, while seeded crystals presented a comparable appearance but with the initial seed embedded in the centre. The XRD spectra (Figure 4B) showed diffraction peaks at

14.97º, 30.14º and 45.90º, which can be attributed to the (100), (200), and (300) facets, confirming the growth of the monocrystalline cubic $MAPbBr_3$ perovskite.[37] Atomic force microscopy of the crystal revealed a surface roughness of 2.93 nm for the seedless-grown crystal and 1.46 nm for the seeded crystal (Figure S3), greatly improving the surface smoothness compared to the literature.[19]

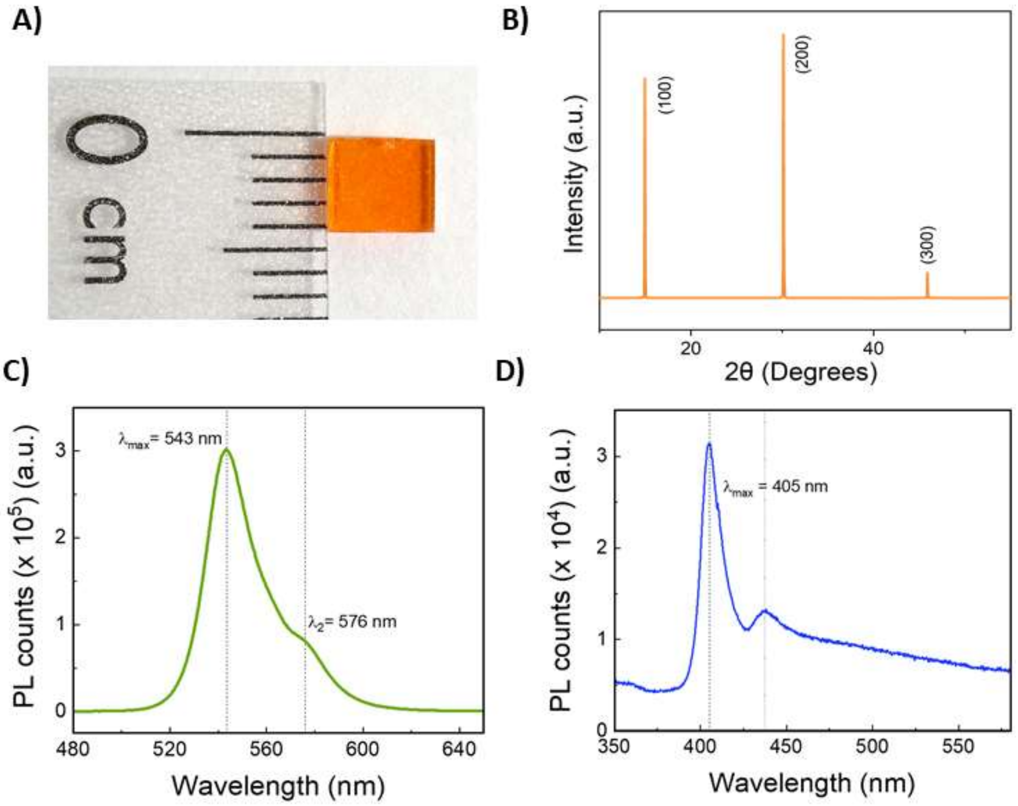

Figure 4. A) Image of a seedless synthesised $MAPbBr_3$ single crystal. B) X-ray diffraction spectra of the seedless-grown $MAPbBr_3$ crystal. C) B) X-ray diffraction spectra of the seedless-grown $MAPbBr_3$ crystal. D) Photoluminescence measurements of a seed containing $MAPbCl_3$ single crystal.

The photoluminescence (PL) properties of the seedless crystals were also evaluated (Figure 4C). Crystal presented an intense peak at 543 nm, corresponding to $MAPbBr_3$ perovskite. A minor secondary peak can be observed at 576 nm, which may be due to reabsorption phenomena observed in monocrystalline materials.[38] Time-resolved photoluminescence (TRPL) decay revealed a τ_F of 181.7 ns (figure S4A), shorter than the values we observed in the previous iteration of the platform.[19] Crystals grown using an initial seed presented higher photoluminescence intensity and a less pronounced shoulder, which indicates lower defect concentration. Interestingly, τ_F was noticeably shorter, with a value of 91.3 ns. It has been reported that the shortening of photoluminescence decay can be related to an increase in crystallinity quality and decreased surface roughness in bulk single crystals. [39] However, there are also reports about how this is linked to a decrease in photoluminescence intensity, as surface defects play a key role in PL emission. Paradoxically, crystals grown in flow with the seed-assisted method presented shorter decay times but higher emission intensity. It can be considered that flow might have a further influence on crystal morphology and their properties, but the complexity of the underlying mechanisms would require extensive exploration. In the case of $MAPbCl_3$ crystals, the maximum PL intensity peak is expected at 405 nm. However, a secondary peak at 440 nm can also be observed (Figure 4D), and, compared to $MAPbBr_3$, it presents a higher relative intensity compared to the main peak. This corroborated that further optimisation of the conditions of the chloride crystals would be required to yield optimal PL properties.

Growth of mixed halide perovskite single crystals

The possibility to adjust the flow rate and composition by employing multiple pumps during the experiment enables the dynamic modification of the crystallization conditions. This is a clear advantage over conventional batch processes, where a change of solution requires stopping the process and the transfer of the crystal to another vessel or diluting the mother liquor by the addition of a new substrate solution. These actions inevitably disturb the growth, as crystals might redissolve partially until supersaturation temperature is reached again, and the manipulation of the crystal might generate surface-level irregularities. In that sense, the use of multiple pumps allows the introduction of different solutions without manipulating the reactor, making this transition smoother. Hence, novel single-crystal multi-materials can be generated with this approach. As a proof of concept, a mixed halide methylammonium lead-based perovskite was synthesised.

Selected materials for the experiments were $MAPbCl_3$ and $MAPbBr_3$, as they share a cubic structure with the same space group[40] and they were both successfully synthesised in the reactor. The first step was the seed-based growth of a crystal of $MAPbCl_3$ using 0.8 M solution of precursors in a mixture of DMF and dimethylsulfoxide (DMSO) (1:1 (v:v)) at 65ºC with a flow rate of 25 $\mu L\ min^{-1}$ since we already used these conditions successfully. After a selected growth time of 2 h, a step change of feedstock solution to a 1.2 mol L^{-1} of precursors in DMF was performed with a second programmable pump, maintaining the overall flow rate constant at 25 $\mu L\ min^{-1}$. Growth of the coloured bromide containing perovskite was constantly monitored with the vision computing platform (Figure S5). The resulting crystals (Figure 5A) are multi-component, with a clear colour gradient across the surface. The crystals were not flat on the surface, they presented a trapezoidal shape, presumably due to the bigger lattice structure of Br-containing crystals versus the smaller Cl-containing ones. It is noteworthy that growth experiments in reverse order, starting from a $MAPbBr_3$ and then introducing $MAPbCl_3$ solution, were not possible, as the crystal was swiftly dissolved once the solution reached the inside of the crystallisation chamber. $MAPbCl_3$ growth requires a DMF/DMSO 1:1 solution, but $MAPbBr_3$ shows very small retrograde solubility in DMSO, and its solubility is over ten times higher at selected conditions[41]. Thereby, the continuous growth of multiple material single crystals requires a thorough revision of the solvent compatibility for each step.

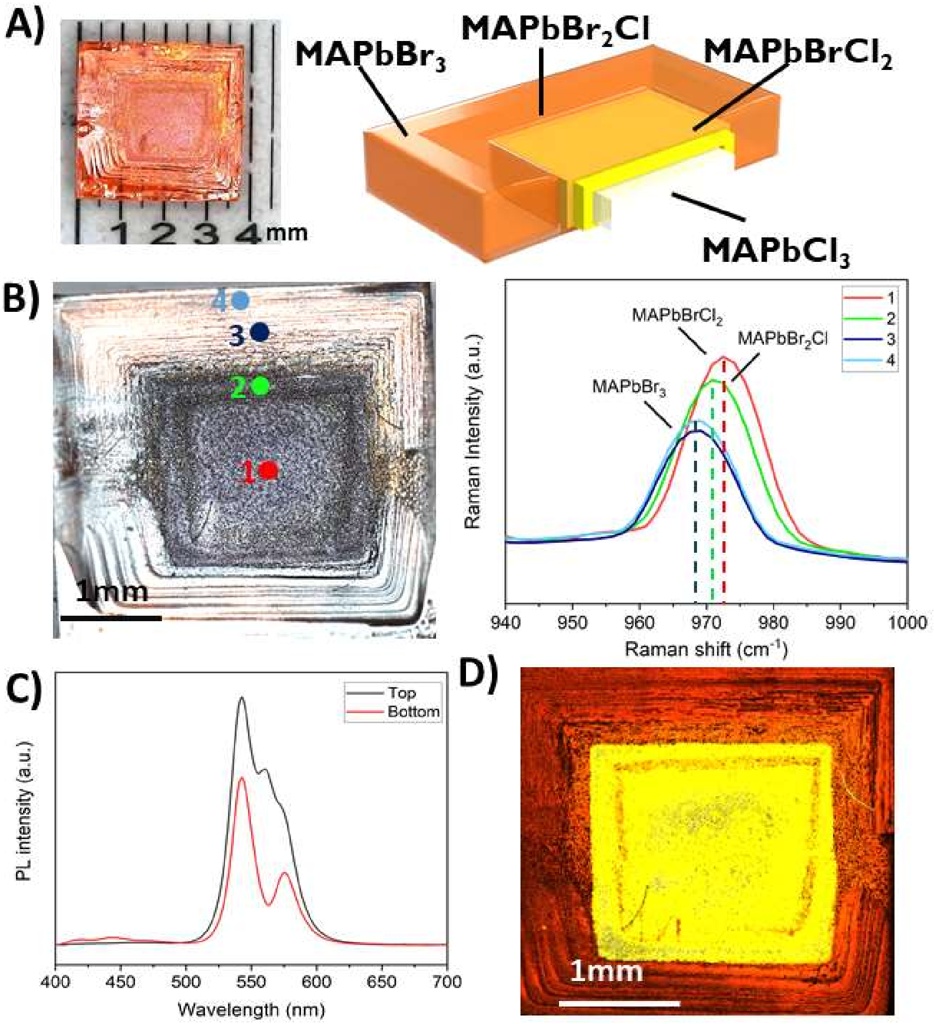

Figure 5. A) Picture of a mixed halides perovskite single crystal and diagram of crystal composition B) Raman shift spectra of selected points. C) Photoluminescence of crystal faces D) Confocal photoluminescence microscope picture of the mixed composition perovskite single crystal.

Raman spectroscopy was employed to probe the composition of the crystal at different points (Figure 5B). The C-N stretching Raman band of the methylammonium (MA) varies as a function of the halide of the corresponding perovskite in the series $MAPbCl_xBr_y$. [40] In Figure 5, point 1 was measured in the centre of the crystal at 5 μm depth (Figure S6), showing a Raman shift of 977 cm^{-1} ($MAPbCl_3$). However, at the same point, but at the surface, the Raman shift observed was 974 cm^{-1} ($MAPbCl_2Br$), thus indicating a compositional from the initial $MAPbCl_3$ perovskite. Furthermore, point 2 at the surface showed a Raman shift of 971 cm^{-1} ($MAPbClBr_2$) Points 3 and 4 clearly correlate to the growth of the crystal under predominantly $PbBr_2$ stock solution. Here, a Raman shift of 968 cm^{-1} confirmed the presence of $MAPbBr_3$ on the surface of the crystal. Interestingly, X-ray photoelectron spectroscopy (XPS) probed at similar points than shown in Figure 5B showed that on the surface (1-10 nm) were bands consistent with $MAPbBr_3$, showing no detectable signals of chlorine (Figures S7 and S8). The core levels of Pb, C, Br, N, and O confirm the spectroscopic homogeneity of the top perovskite film, $MAPbBr_3$.

The photoluminescence properties of the crystal were recorded and a difference in behaviour between the two faces was observed (Figures 5C and S9, Table S3). Both faces presented a maximum emission at 543 nm, attributed to $MAPbBr_3$, but then different secondary peaks appeared. The 560 nm and 576 nm correspond, presumably, to reabsorption processes, and are more noticeable in the top layer, where they might be related to the height differences observed in the surface. On the other hand, the contribution of $MAPbCl_3$ can be detected in the bottom layer at 418 and 443 nm, where $MAPbBr_3$ growth was restricted due to physical limitations of space. To give further insight into this observation, confocal photoluminescence microscopy images were taken, with selected wavelengths to detect the perovskites studied (Table S4). Figure 5D reveals an outer shell of $MAPbBr_3$, that corresponds to the transparent orange sections (Figure 5A). Meanwhile, the central section of the crystal features different species that have mixed halide compositions. There is a gradient where proximity to the core of the crystal corresponds to lower wavelengths, signalling species with increasing proportions of chloride. This indicated the growth of perovskite layer by layer with a gradual change of compositions, as the initial medium containing chloride solution is replaced by the bromide.

Interestingly, $MAPbBr_3$ preferentially grew in the horizontal direction, towards the outer edges of the crystal, while it did not cover the central area for the top layers. Also, bromide ion has a higher radius than chloride, therefore as bromide content is increased cell size presents higher values. The combination of these factors could explain the observed difference in behaviour between faces, and the height difference existing between the inner and outer areas (Figure S10).

3. Conclusions

The development of a novel digital flow platform for the controlled synthesis of perovskite single crystals enables the fabrication of advanced high-quality materials in a controlled and reproducible fashion. The optimisation of the heating chamber and flow conditions offered enhances control over the temperature profile within the crystallisation chamber and offers great potential for future scaling up of the process. Vision control can help in the understanding of growth kinetics, allowing a better selection of reaction conditions.

Single crystals with improved surface smoothness were generated with this platform employing seeded and interestingly highly challenging unseeded conditions. The capabilities of the digital and programmable platform were demonstrated by synthesizing novel single-crystal perovskites as individual highly stoichiometric films, even at thicknesses of just a few nanometres. These films could exhibit various halide compositions ($MAPbCl_3$, $MAPbBrCl_2$, $MAPbBr_2Cl$, and $MAPbBr_3$), by simply dynamically switching the precursor solution during a single-crystal growth experiment. A total of four different perovskites were integrated into a single crystal material, thus opening the possibility to the discovery of new materials, especially new combinations of multi-material single-crystal perovskites with advanced optoelectronic properties.

Methodology

Materials. CH_3NH_3Br (>99 wt%) and CH_3NH_3Cl (>99 wt%) were purchased from Great Cell Solar Materials. $PbBr_2$ (>98 wt%), $PbCl_2$ (>98 wt %), DMF (> 99.8 wt%, anhydrous) and DMSO (> 99.9 wt%, anhydrous) were purchased from Merck. Salts and solvents were used as received without any further purification.

Precursor solution preparation. In the typical synthesis used for this work, 1.34 g of CH_3NH_3Br (>99 wt%, Great Cell Solar Materials) and 4.404 g of $PbBr_2$ (>98 wt%, Merck) were dissolved at 1:1 molar ratio in 10 mL of DMF (>99.8 wt%, anhydrous, Merck) under nitrogen atmosphere to produce a 1.2 mol L^{-1} solution of $MAPbBr_3$ and 0.54 g of CH_3NH_3Cl (>99 wt%, Great Cell Solar Materials) and 2.22 g of $PbCl_2$ (>98 wt %, Merck) were dissolved at 1:1 molar ratio in 5 mL of DMF (>99.8 wt%, anhydrous, Merck) and in 5 mL of DMSO (> 99.9 wt %, anhydrous, Merck) under nitrogen atmosphere to produce a 0.8 mol L^{-1} solution of $MAPbCl_3$. Solutions were kept at room temperature under stirring and filtered before starting the crystallisation with 0.2 µm pore size PTFE filter.

3D printed reactor production. The reactor was modelled using Solidworks CAD software and converted to standard tessellation language (STL) format. It was printed using a Formlabs 3 low-force stereolithography printer loaded with off-the-self Formlabs High Temp resin. STL files were sliced using Formlabs slicing software, Preform, and printed with a layer height of 50 µm using the settings recommended by the manufacturer. EPDM O-rings were purchased from RTC Couplings. Clamps were purchased from Leybold.

Heat and temperature control. A homemade setup consisting of a PID temperature controller connected to a cartridge heater was produced. The cartridge was introduced into a bespoken aluminum block and its temperature was monitored by a thermocouple connected to the PID temperature controller. The temperature at the base of the crystallisation chamber was measured with a high-resolution contact thermometer after waiting for two hours. A calibration for the correlation between temperature of the block and temperature at the surface of the crystallisation chamber was done (Equation S1).

RTD studies. The experimental procedure utilized a setup consisting of two syringe pumps: one for controlling the primary flow rate and the other for loading a 50 µL loop into an automated 6-way Rheodyne valve. This valve facilitated the injection of a tracer pulse into the flow stream, simplifying the process. The valve was connected to a commercial flow cell, allowing a light beam to pass through and be detected by a UV-visible spectrometer operating at a fixed wavelength. All components were connected using 1/16-inch PEEK capillary tubing. The experiments were conducted with isopropanol as the solvent and a Methyl Red tracer solution (1 mg L^{-1}) in the same solvent, with a flow rate of 50 µL min^{-1}. The change in tracer concentration over time was monitored by measuring the absorbance peak at 525 nm in the UV-VIS spectra.

CFD studies. The CFD validation for the RTD was performed using OpenFOAM 2112. The 3D geometry was meshed using snappyHexMesh to obtain a mostly tetrahedral non-deformed mesh composed by 400k nodes. The simpleFoam solver was employed to obtain the steady state resolution of the flow in similar conditions to the RTD study with a flowrate of 50 mL min^{-1}. The fluid was considered Newtonian and incompressible (kinematic viscosity of 4.9×10^{-6} m^2 s^{-1} and base density of 1425 kg m-^{3}) while the temperature was set to 20 °C (heating plate was off in this case). Then, a laminar transient simulation with frozen hydrodynamics was performed by using the scalarTransportFoam solver with a kinematic diffusivity of 10^{-8} m^2 s^{-1}. The tracer pulse was injected with a concentration of 1 mg L^{-1} during 60 s and its evolution was solved over 2700 s.

CFD simulations for the heat transfer analysis were performed employing the chtMultiRegionSimpleFoam solver from OpenFOAM 2112, in addition to the conditions previously described for the RTD curve validation. Inlet flow was fixed at a temperature of 20 °C, while the bottom area of the reactor was fixed at 65 °C (this temperature was determined from the steady-state temperature of the heating plate). Reactor walls were modelled with an experimentally determined thermal conductivity coefficient of 0.282 kg m s^{-3} K^{-1}, while external temperature was set at 20 °C to model the heat exchange with the surrounding air in the room.

XPS studies. High-energy resolution X-ray photoelectron spectroscopy (XPS) measurements were conducted using a SPECS GmbH system, with a base pressure of 1.0 × 10−10 mbar. The system featured a PHOIBOS 150 2D CMOS hemispherical analyzer. Photoelectrons were excited using the Al–Kα line (1486.7 eV). Measurements were performed at room temperature with a pass energy of 20 eV. For all HR-XPS measurements, the simples were placed under ultrahigh vacuum (UHV) conditions, with the analysis chamber achieving a base pressure lower than 1.0 × 10−10 mbar.

Continuous-Flow single and multimaterial crystal growth experiments.

Continuous-flow single crystal growth experiments were conducted using two programmable Tricontinent C3000 pumps, each equipped with a 5 mL syringe. These pumps operated in sequence to maintain a continuous flow of the previously prepared precursor solution into the reactor. The pumps were controlled via an interface developed in Visual Studio with Python scripts. The reactor's internal temperature was adjusted between 58 °C and 68 °C and the flow rate between 12 μL min^{-1} and 50 μL min^{-1} for the experiments.

Multi-material crystal growth experiments were conducted similarly to the previous ones, with one key modification: each of the two pumps introduced a different solution, with the first pump delivering a 0.8 M solution of $MAPbCl_3$ in DMF/DMSO 1:1, followed by the second pump, which delivered a 1.2 M solution of $MAPbBr_3$ in DMF.

The procedure was similar to the previous one, with Continuous-flow growth experiments were conducted using two programmable Tricontinent C3000 pumps, each equipped with a 5 mL syringe. These pumps operated in sequence to maintain a continuous flow of different solutions into the reactor. The first pump pumping a solution of 0.8M $MAPbCl_3$ in DMF/DMSO 1:1 v:v, followed by the second pump, which delivered a 1.2 M $MAPbBr_3$ solution in DMF. The pumps were controlled via an interface developed in Visual Studio with Python scripts. The reactor's internal temperature was kept constant at 67 °C, and the flow rate was adjusted between 6 μL min^{-1} and 25 μL min^{-1} for the experiments.

Vision control of growth kinetics of perovskite single crystals

For the monitoring and analysis of perovskite crystal growth in continuous flow, a specialised algorithm was developed in Python, utilizing the OpenCV library for image processing. This algorithm facilitates automated and precise analysis of the images captured from the reactor during the experiments.

The camera system captures images of the reactor at predetermined time intervals, which are automatically loaded for processing. A Region of Interest (ROI) is defined in each image using a polygon with predefined coordinates, delineating the area where perovskite crystal growth is expected to be observed. This polygon is superimposed on the image to facilitate visualisation and analysis of the target area.

The images, originally in BGR format, are converted to the HSV (Hue, Saturation, Value) colour space to improve colour segmentation, thereby aiding in the identification of perovskite crystals. In this case, a specific colour range in the orange spectrum is used to detect lead perovskite. This colour range can be adjusted according to experimental needs, allowing for flexible adaptation to different lighting conditions or variations in sample composition.

Once the regions of interest are segmented based on colour, contours within these regions are detected. Each contour is analysed to determine its area, with those below a predefined threshold being discarded to avoid noise or irrelevant elements. Valid contours are highlighted in the original image to facilitate visual review.

The total area of the crystals detected within the ROI is calculated and stored for subsequent analysis. These area values are normalised based on the known size of the ROI, enabling accurate comparisons over time. Each area measurement is associated with the corresponding image capture time, creating a time series of data.

To improve data interpretation, a smoothing technique using a moving average with a three-point window is applied, reducing variability and highlighting trends in crystal growth. The results are presented in a graph showing the detected area over time, which is saved as a PDF for documentation. Additionally, the processed images are stored in a specific folder for further review.

This automated approach allows for continuous and detailed monitoring of perovskite crystal growth, providing valuable data for process optimisation and scientific research.

Characterisation

XRD spectra was measured in a Bruker D8-Advance diffractometer. CuKα radiation ($\lambda = 1.5406$ Å) was used for the direct recording of the signal by mounting the crystal in a sample holder.

Atomic force microscopy images were made using JSPM-5200 Scanning Probe Microscope from Jeol. Images were taken in contact mode for an area of 2 × 2 μm with a pixel resolution of 256 × 256.

PL and TRPL measurements were performed with the use of Edinburgh Instrument FLS 1000 fluorimeter with a picosecond pulsed diode laser EPL 375 nm as the excitation source. The pulse period was settled at 200 ns for steady-state PL and increased up to 500 ns for the TRPL performance with a time scale of 500 ns.

Raman spectra measurements were performed using a WITec Apyron confocal Raman microscope. A 785nm laser with a laser power of 9.62mW was used as excitation source with a Zeiss EC Epiplan-Neofluar Dic 100x objective.

Confocal fluorescence pictures were taken using a Leica TCS SP8 microscope using a 405nm laser as excitation source. Photolumnescence was acquired by using a series of PMT detectors with wavelength ranges described in Table S2, with a 53.1µm pinhole and a Leica HC PL APO x10 objective.

CONFLICTS OF INTEREST

There are no conflicts to declare.

ACKNOWLEDGMENTS

This work has been funded by the project (PID2020-119628RB-C33, PID2020-119628RB-C32 and PID2020-119628RB-C31), MCIN/AEI/10.13039/501100011033. CT thanks the Generalitat Valenciana (CIGRIS/2021/075) for funding. The authors are grateful to the SCIC of the Universitat Jaume I for technical support. J. L-G. is supported by FPU21/03740 doctoral grant from the Spanish Ministry of Universities. CAA thanks the Spanish Ministry of Science and Innovation under contract number (TED2021-129758B-C33) MCIN/AEI/10.13039/501100011033/European Union NextGeneration EU/PRTR provided gratefully acknowledged financial support. MZ thank the funding received from "la Caixa" Foundation (ID 100010434) under the fellowship number LCF/BQ/PR24/12050016.

Author Contributions: Conceptualisation VS; Methodology VS, MZ, RAB, PB; Software Programming CT, J.L-G.; Validation DI, SM, JMX; Formal analysis DI, CT, VS; Investigation DI, SM, CAA, AMS, MCA; Resources; Data Curation DI, SM, MZ; Writing - Original Draft DI, MZ, CT; Writing - Review & Editing All authors; Visualisation; Supervision VS, MZ, RMC; Project administration VS; Funding acquisition VS, PB, RAB, MCA.

References

1 Alsalloum, A. Y. *et al.* 22.8%-Efficient single-crystal mixed-cation inverted perovskite solar cells with a near-optimal bandgap. *Energy & Environmental Science* **14**, 2263-2268 (2021). https://doi.org:10.1039/D0EE03839C

2 Wei, H. *et al.* Sensitive X-ray detectors made of methylammonium lead tribromide perovskite single crystals. *Nature Photonics* **10**, 333-339 (2016). https://doi.org:10.1038/nphoton.2016.41

3 Nguyen, V.-C., Katsuki, H., Sasaki, F. & Yanagi, H. Single-crystal perovskite CH3NH3PbBr3 prepared by cast capping method for light-emitting diodes. *Japanese Journal of Applied Physics* **57**, 04FL10 (2018). https://doi.org:10.7567/JJAP.57.04FL10

4 Fernandez-Guillen, I. *et al.* Perovskite Thin Single Crystal for a High Performance and Long Endurance Memristor. *Advanced Electronic Materials* **10**, 2300475 (2024). https://doi.org:https://doi.org/10.1002/aelm.202300475

5 Liu, Y., Yang, Z. & Liu, S. Recent Progress in Single-Crystalline Perovskite Research Including Crystal Preparation, Property Evaluation, and Applications. *Advanced Science* **5**, 1700471 (2018). https://doi.org:https://doi.org/10.1002/advs.201700471

6 Wang, Q. *et al.* Scaling behavior of moisture-induced grain degradation in polycrystalline hybrid perovskite thin films. *Energy & Environmental Science* **10**, 516-522 (2017). https://doi.org:10.1039/C6EE02941H

7 Shi, D. *et al.* Low trap-state density and long carrier diffusion in organolead trihalide perovskite single crystals. *Science* **347**, 519-522 (2015). https://doi.org:doi:10.1126/science.aaa2725

8 Gu, Z., Huang, Z., Li, C., Li, M. & Song, Y. A general printing approach for scalable growth of perovskite single-crystal films. *Science Advances* **4**, eaat2390 (2018). https://doi.org:doi:10.1126/sciadv.aat2390

9 Lian, Z. *et al.* Perovskite CH3NH3PbI3(Cl) Single Crystals: Rapid Solution Growth, Unparalleled Crystalline Quality, and Low Trap Density toward 108 cm–3. *Journal of the American Chemical Society* **138**, 9409-9412 (2016). https://doi.org:10.1021/jacs.6b05683

10 Saidaminov, M. I., Abdelhady, A. L., Maculan, G. & Bakr, O. M. Retrograde solubility of formamidinium and methylammonium lead halide perovskites enabling rapid single crystal growth. *Chemical Communications* **51**, 17658-17661 (2015). https://doi.org:10.1039/C5CC06916E

11 Zia, W. *et al.* Impact of Low-Temperature Seed-Assisted Growth on the Structural and Optoelectronic Properties of MAPbBr3 Single Crystals. *Chemistry of Materials* **35**, 5458-5467 (2023). https://doi.org:10.1021/acs.chemmater.3c00780

12 Kumar, S., Hodes, G. & Cahen, D. Defects in halide perovskites: The lattice as a boojum? *MRS Bulletin* **45**, 478-484 (2020). https://doi.org:10.1557/mrs.2020.146

13 Tisdale, J. T. *et al.* Precursor purity effects on solution-based growth of MAPbBr3 single crystals towards efficient radiation sensing. *CrystEngComm* **20**, 7818-7825 (2018). https://doi.org:10.1039/C8CE01498A

14 Amari, S., Verilhac, J.-M., Gros D'Aillon, E., Ibanez, A. & Zaccaro, J. Optimization of the Growth Conditions for High Quality CH3NH3PbBr3 Hybrid Perovskite Single Crystals. *Crystal Growth & Design* **20**, 1665-1672 (2020). https://doi.org:10.1021/acs.cgd.9b01429

15 Kumar, S., Rukban, A., Sinisi, J., Damle, V. H. & Cahen, D. Localized Heating Tailors Nucleation for Reproducible Growth of Thin Halide Perovskite Single Crystals. *Crystal Growth & Design* **22**, 7160-7167 (2022). https://doi.org:10.1021/acs.cgd.2c00833

16 Sebastian, V. Toward continuous production of high-quality nanomaterials using microfluidics: nanoengineering the shape, structure and chemical composition. *Nanoscale* **14**, 4411-4447 (2022). https://doi.org:10.1039/D1NR06342A

17 Iglesias, D., Haddad, D. & Sans, V. Recent Developments in Process Digitalisation for Advanced Nanomaterial Syntheses. *Chemistry-Methods* **2** (2022). https://doi.org:10.1002/cmtd.202200031

18 Das Adhikari, S. *et al.* Continuous-Flow Synthesis of Orange Emitting Sn(II)-Doped CsBr Materials. *Advanced Optical Materials* **9**, 2101024 (2021). https://doi.org:https://doi.org/10.1002/adom.202101024

19 Iglesias, D. *et al.* 3D printed flow reactors for the synthesis of single crystal perovskites. *Materials Today Energy* **39**, 101476 (2024). https://doi.org:https://doi.org/10.1016/j.mtener.2023.101476

20 Epps, R. W. *et al.* Artificial Chemist: An Autonomous Quantum Dot Synthesis Bot. *Advanced Materials* **32**, 2001626 (2020). https://doi.org:https://doi.org/10.1002/adma.202001626

21 Savage, T. *et al.* Machine learning-assisted discovery of flow reactor designs. *Nature Chemical Engineering* **1**, 522-531 (2024). https://doi.org:10.1038/s44286-024-00099-1

22 Lee, C.-Y., Wang, W.-T., Liu, C.-C. & Fu, L.-M. Passive mixers in microfluidic systems: A review. *Chemical Engineering Journal* **288**, 146-160 (2016). https://doi.org:https://doi.org/10.1016/j.cej.2015.10.122

23 Bettermann, S., Kandelhard, F., Moritz, H.-U. & Pauer, W. Digital and lean development method for 3D-printed reactors based on CAD modeling and CFD simulation. *Chemical Engineering Research and Design* **152**, 71-84 (2019). https://doi.org:https://doi.org/10.1016/j.cherd.2019.09.024

24 Gonzalez, G., Roppolo, I., Pirri, C. F. & Chiappone, A. Current and emerging trends in polymeric 3D printed microfluidic devices. *Additive Manufacturing* **55**, 102867 (2022). https://doi.org:https://doi.org/10.1016/j.addma.2022.102867

25 Parra-Cabrera, C., Achille, C., Kuhn, S. & Ameloot, R. 3D printing in chemical engineering and catalytic technology: structured catalysts, mixers and reactors. *Chemical Society Reviews* **47**, 209-230 (2018). https://doi.org:10.1039/C7CS00631D

26 Yue, J., Falke, F. H., Schouten, J. C. & Nijhuis, T. A. Microreactors with integrated UV/Vis spectroscopic detection for online process analysis under segmented flow. *Lab on a Chip* **13**, 4855-4863 (2013). https://doi.org:10.1039/C3LC50876E

27 Epps, R. W., Felton, K. C., Coley, C. W. & Abolhasani, M. Automated microfluidic platform for systematic studies of colloidal perovskite nanocrystals: towards continuous nano-manufacturing. *Lab on a Chip* **17**, 4040-4047 (2017). https://doi.org:10.1039/C7LC00884H

28 Pinho, B. & Torrente-Murciano, L. Dial-A-Particle: Precise Manufacturing of Plasmonic Nanoparticles Based on Early Growth Information—Redefining Automation for Slow Material Synthesis. *Advanced Energy Materials* **11**, 2100918 (2021). https://doi.org:https://doi.org/10.1002/aenm.202100918

29 Bateni, F. *et al.* Smart Dope: A Self-Driving Fluidic Lab for Accelerated Development of Doped Perovskite Quantum Dots. *Advanced Energy Materials* **14**, 2302303 (2024). https://doi.org:https://doi.org/10.1002/aenm.202302303

30 Lignos, I., Maceiczyk, R. M., Kovalenko, M. V. & Stavrakis, S. Tracking the Fluorescence Lifetimes of Cesium Lead Halide Perovskite Nanocrystals During Their Synthesis Using a Fully Automated Optofluidic Platform. *Chemistry of Materials* **32**, 27-37 (2020). https://doi.org:10.1021/acs.chemmater.9b03438

31 Okafor, O. *et al.* Advanced reactor engineering with 3D printing for the continuous-flow synthesis of silver nanoparticles. *Reaction Chemistry & Engineering* **2**, 129-136 (2017). https://doi.org:10.1039/C6RE00210B

32 Haruta, Y. *et al.* Reproducible high-quality perovskite single crystals by flux-regulated crystallization with a feedback loop. *Nature Synthesis* (2024). https://doi.org:10.1038/s44160-024-00576-8

33 Salas, A., Zanatta, M., Sans, V. & Roppolo, I. Chemistry in light-induced 3D printing. *ChemTexts* **9**, 4 (2023). https://doi.org:10.1007/s40828-022-00176-z

34 Sans, V., Karbass, N., Burguete, M. I., García-Verdugo, E. & Luis, S. V. Residence time distribution, a simple tool to understand the behaviour of polymeric mini-flow reactors. *RSC Advances* **2**, 8721-8728 (2012). https://doi.org:10.1039/C2RA20903A

35 *Open CV Library*, <www.opencv.org> (

36 Tinajero, C. *VCA Algorithm*, <https://github.com/catm542-ai/PerovskiteGrowthDetection/blob/main/LICENSE> (

37 Boopathi, K. M. *et al.* Permanent Lattice Compression of Lead-Halide Perovskite for Persistently Enhanced Optoelectronic Properties. *ACS Energy Letters* **5**, 642-649 (2020). https://doi.org:10.1021/acsenergylett.9b02810

38 Schötz, K. *et al.* Double peak emission in lead halide perovskites by self-absorption. *Journal of Materials Chemistry C* **8**, 2289-2300 (2020). https://doi.org:10.1039/C9TC06251C

39 Ding, J., Lian, Z., Li, Y., Wang, S. & Yan, Q. The Role of Surface Defects in Photoluminescence and Decay Dynamics of High-Quality Perovskite MAPbI3 Single Crystals. *The Journal of Physical Chemistry Letters* **9**, 4221-4226 (2018). https://doi.org:10.1021/acs.jpclett.8b01898

40 Niemann, R. G. *et al.* Halogen Effects on Ordering and Bonding of CH3NH3+ in CH3NH3PbX3 (X = Cl, Br, I) Hybrid Perovskites: A Vibrational Spectroscopic Study. *The Journal of Physical Chemistry C* **120**, 2509-2519 (2016). https://doi.org:10.1021/acs.jpcc.5b11256

41 Petrov, A. A., Ordinartsev, A. A., Fateev, S. A., Goodilin, E. A. & Tarasov, A. B. Solubility of Hybrid Halide Perovskites in DMF and DMSO. *Molecules* **26**, 7541 (2021). https://doi.org/10.3390/molecules26247541

6.2 Supporting information

Additional information of the flow platform.

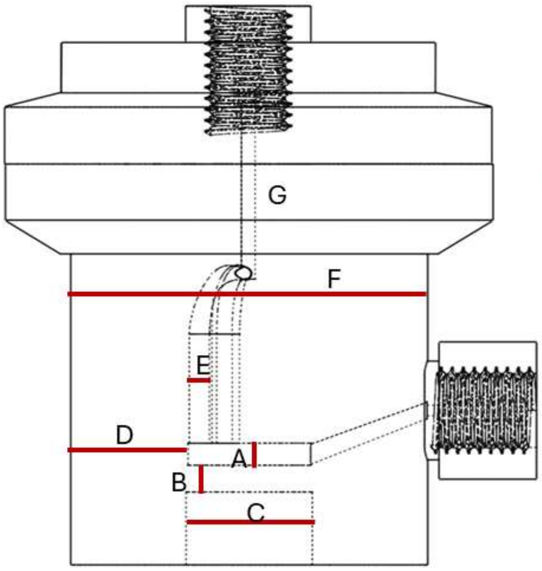

Entry	Size / mm
A	1.6
B	1.8
C	10.5
D	9.5
E	1.5
F	29.2
G	1.2

Figure S1. Detailed measurements of the 3D-printed reactor

Temperature control

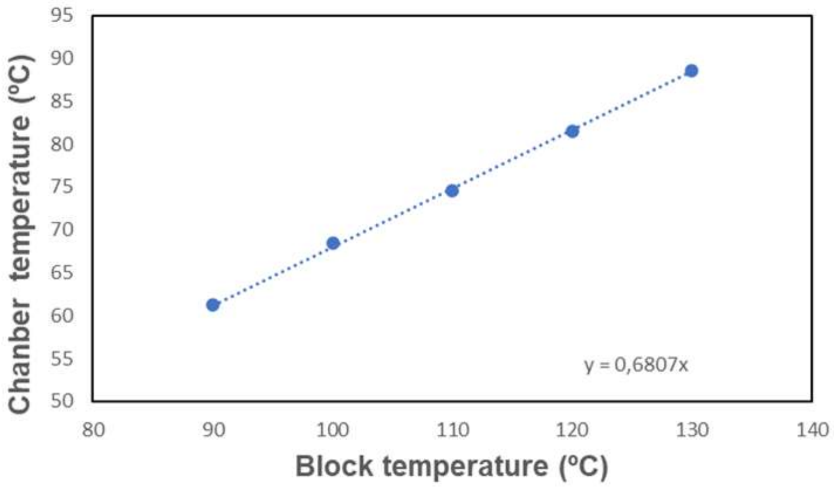

Figure S2. Temperature calibration.

$$y=0.68\,x \qquad \text{Eq. S1}$$

Monitored growth of perovskite single crystals experiments

Table S1. Conditions used in growth monitoring experiments

Entry	**Concentration (M)**	**T heater (°C)**	**Flow (µL min^{-1})**
1	1.2	85	25
2	1.2	85-95	25
3	1.2	90	25
4	1.2	90	12,5
5	1.2	90	50
6	1.2	95	25
7	1.2	100	25

Characterization of synthesized perovskite single crystals

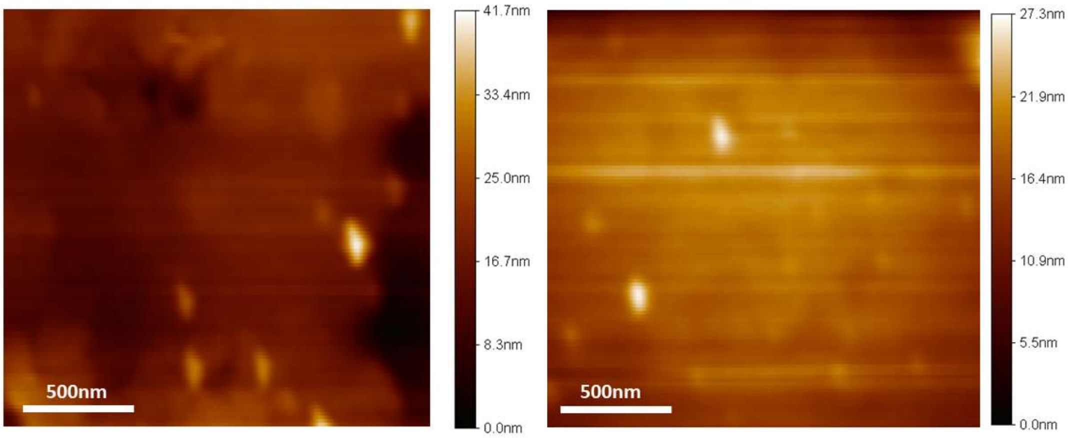

Seedless growth

Seeded growth

Figure S3. Atomic Force Microscopy images of grown crystals

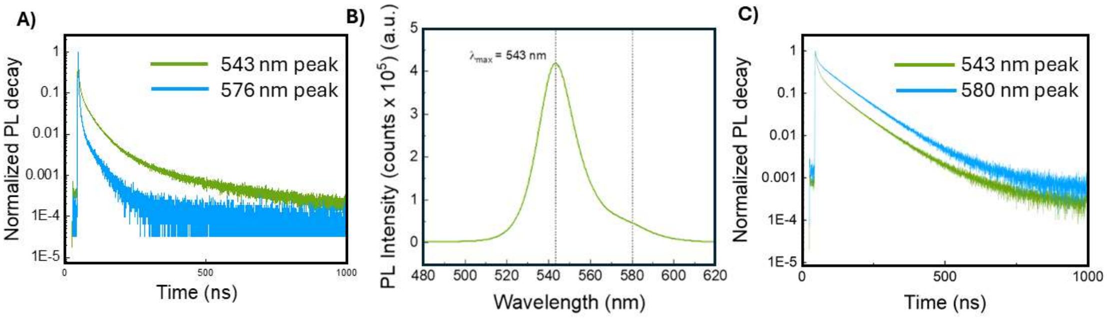

Figure S4. A) TRPL measurement of methylammonium lead bromide perovskite single crystal grown without seed. The lifetimes corresponding to both are shown in Table S2 B) PL spectra of a MAPbBr$_3$ perovskite single crystal grown using seeds. C) TRPL measurement of MAPbBr$_3$ perovskite single crystal grown without seed.

Table S2.

Sample	**τ_1** **(ns)**	**τ_2** **(ns)**	**τ_3** **(ns)**
543 nm peak (Unseeded)	9.04	39.8	181.7
576 nm peak (Unseeded)	5.9	36.7	152
543 peak (Seeded)	6.57	31.33	91.31
580 peak (Seeded)	7.77	60.02	101.94

Growth of mixed composition perovskite single crystal

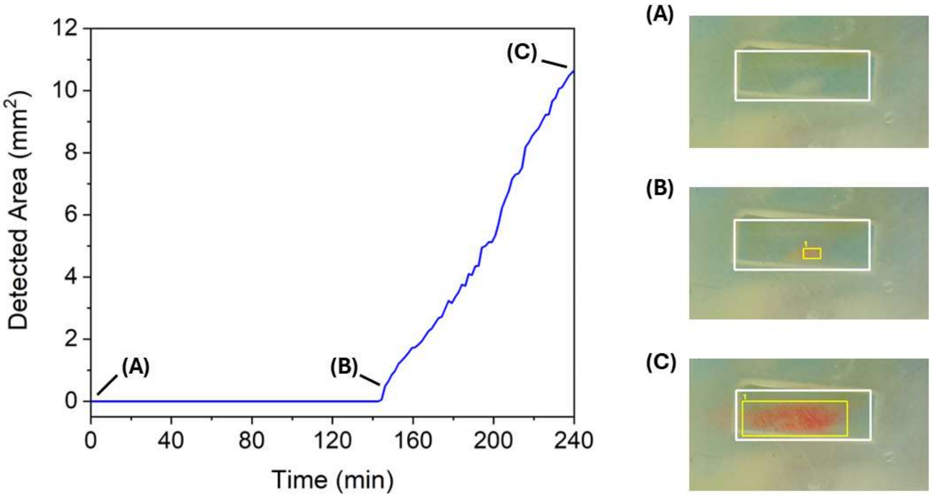

Figure S5. Growth kinetics of mixed composition single crystal

Characterization of synthesized mixed composition single crystal perovskites

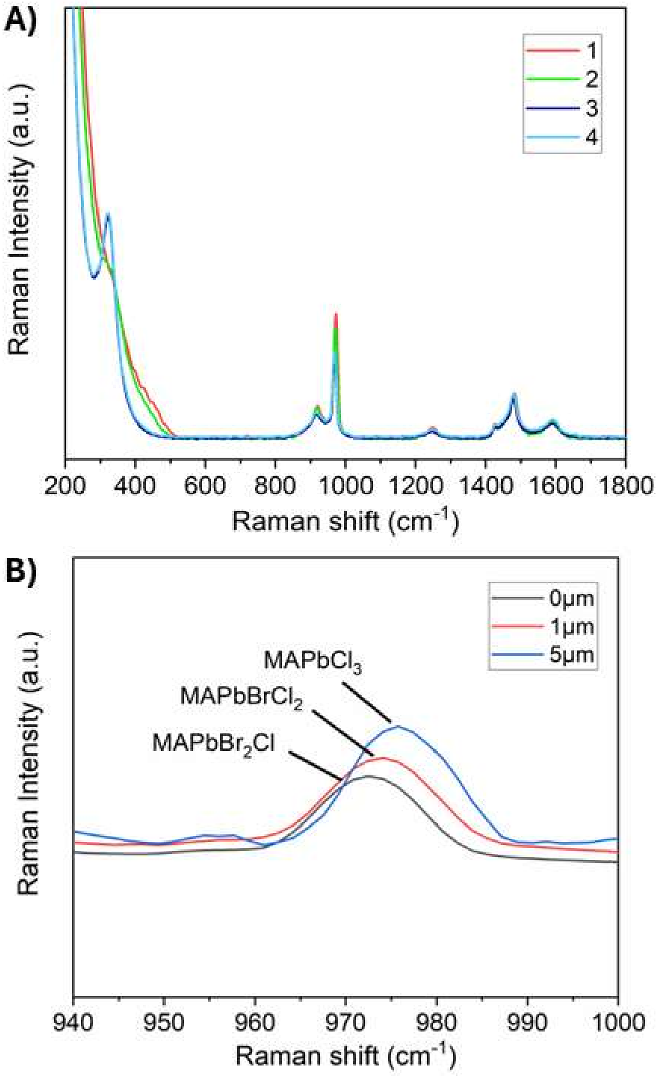

Figure S6. A) Raman spectra of different points of crystal surface. B) Raman shift measurements at the center of the crystal at surface, 1 μm under surface and 5 μm under surface.

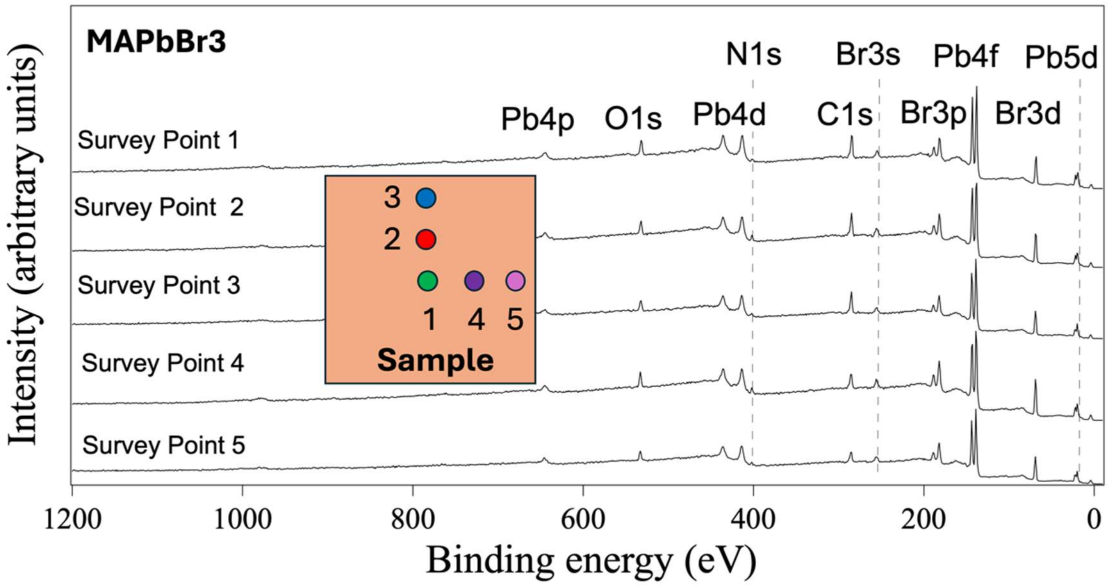

Figure S7. XPS survey spectra from five different positions on the sample, as indicated in the inset. The core levels of Pb, C, Br, N, and O confirm the spectroscopic homogeneity of the top perovskite film, $MAPbBr_3$, with no detectable chlorine core level signals.

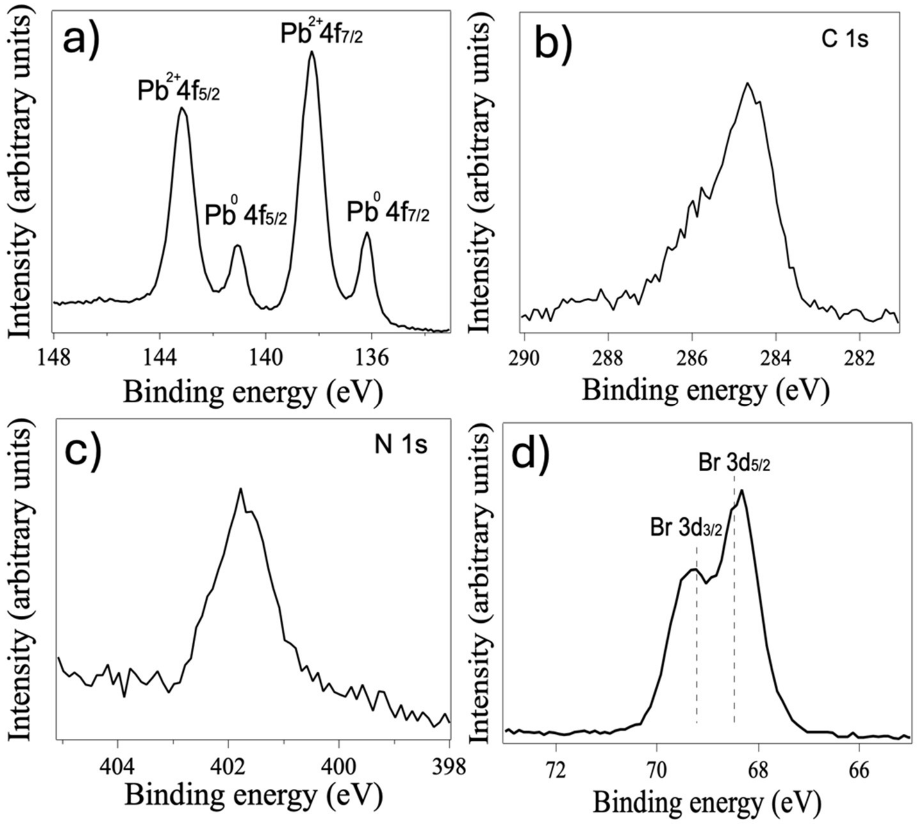

Figure S8. High-resolution XPS spectra of the a) Pb 4f, b) C 1s, c) N 1s, and d) Br 3d peaks measured at point 1 on the sample, as indicated in the inset of Figure 6.

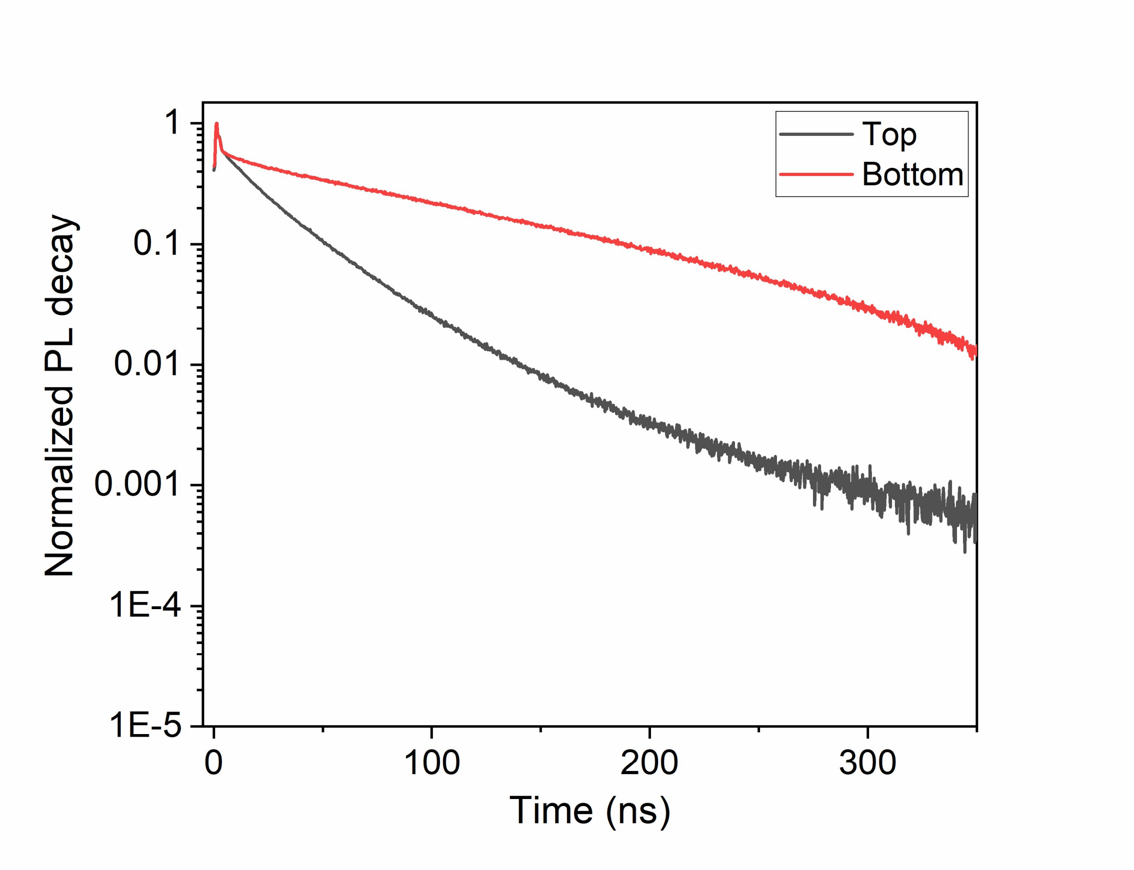

Figure S9. Normalized PL decay comparing the two faces. The lifetimes corresponding to both are shown in Table S3

Table S3. Photoluminescence decay times for mixed composition crystals

Sample	τ_1 (ns)	τ_2 (ns)	τ_3 (ns)	**τ_{avg} (ns)**
Top	1.2	12.3	125	**46.6**
Bottom	1.2	17.8	41.7	**20.2**

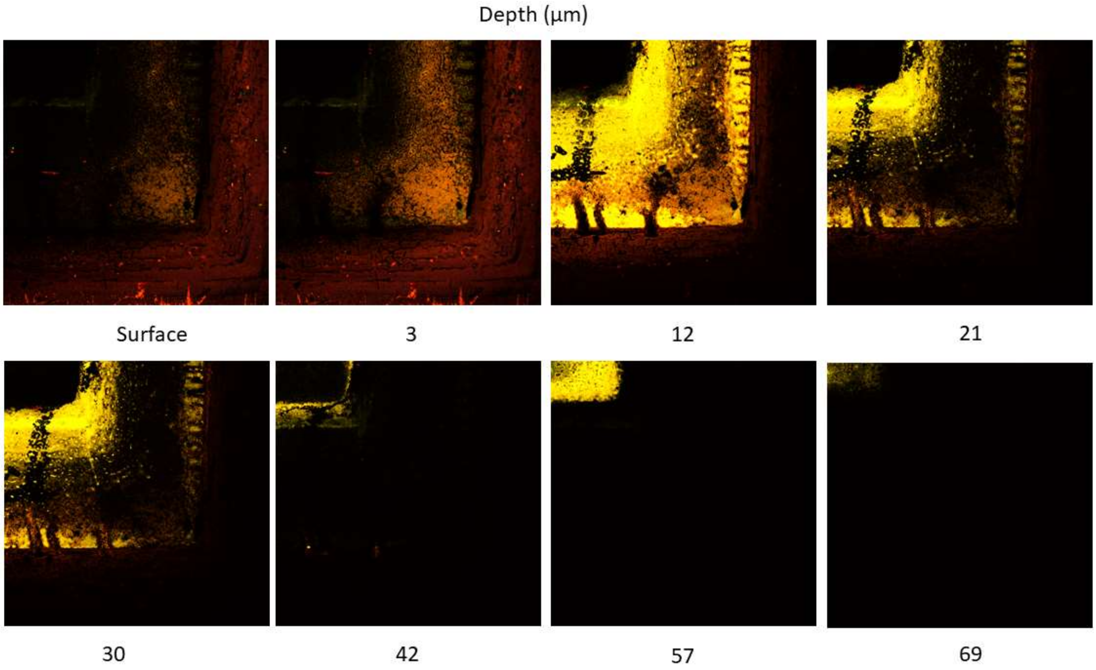

Figure S10. Photoluminescence microscopy image at different depths

Table S4. Channel wavelength range used in confocal photoluminescence images.

Channel	Wavelength range (nm)
1 ($MAPbCl_3$, white)	408-428
2	433-453
3	458-478
4 (Yellow)	482-501
5	507-517
6	527-537
7($MAPbBr_3$, red)	547-557

Chapter 7. Conclusions

Conclusions

During this thesis a series digital flow systems were developed for their application in different processes of interest. In all cases, new reactor geometries were developed in CAD and fabricated using 3D printing, afterwards each case required a thorough study for translating process conditions from batch to flow. Furthermore, we incorporated digital control for achieving superior performance and use of resources in the tested processes. Overall, digitalised systems presented advantages in yield and selectivity compared to their equivalents batch. More specific conclusions of each theme area are detailed below.

New routes for improved synthesis sustainability

A new geometry for electrochemical reactors was developed. The flowpath featured baffles that, combined with an oscillatory motion, resulted in the generation of vortexes that improve mass transport of species to the electrodes. Interelectrode distance is one of the main limitations in the scaling up of electrochemical reactors, but this opens the path to the manufacturing of higher volume electrochemical reactors. The reactor was manufactured with 3D-printing, with the exception of the electrodes, with the possibility to adapt materials to match reaction conditions easily. Components could be further adapted to add functionalities, like supported catalysts, and further developments could make the electrodes 3D-printed onsite.

The electrochemical flow oxidation of olefins to epoxides presented advantages in yield and selectivity over the batch reactions previously described, with a total conversion to species active in the next step. For the cycloaddition of CO_2 to the epoxide and helicoidal structure with pillars was designed in CAD and 3D-printed with a bespoke formulation. This structure improved the mixing of the two phases, resulting in improved yield and selectivity of the cyclic carbonate compared to traditional geometries like packed bed and coiled reactors. Additionally, the tetrabutylammonium bromide served as both the electrolyte in the first step and catalyst in the second one, improving the atom economy of the process. Overall, this two-step reaction highlights the potential of the combination of flow, electrochemistry and 3D-printing for improving the sustainability of chemical synthesis.

Development of platforms for crystallization of advanced materials

A platform for the flow synthesis of perovskite single crystals was developed, with an initial design that highlighted the potential of the technique and a second version that improved overall the reactor design.

The central core of the initial concept platform was a 3D-Printed reactor to be used with the inverse temperature crystallization technique. The resin used for the fabrication of the body, a thermal insulator, served to generate a heating ramp, avoiding uncontrolled temperature spikes. The constant pumping of fresh precursor solution kept the concentration in the crystallization chamber constant, improving kinetics and reducing the generation of defects. Overall, improvements were observed in reproducibility and crystal quality over batch synthesis, with crystals presenting increased photoluminescence activity.

The concept was further developed, with a thorough revision of different components. The heating system was changed to a more localised heating on the crystallization chamber, for better control and more efficient energy used, and the flow distribution was further optimized for achieving a more homogeneous precursor concentration distribution. This resulted in further improvements in nucleation control, something critical for the future implementation of this crystallization technique, and more homogeneous crystals. Additionally, a vision control algorithm was developed for constant monitor of the growth, with the goal of achieving deeper understanding of the influence of parameters over crystallization. Finally, the digital control of the pumps allowed the growth of crystals with varying composition without stopping the process, showing its potential for the development of more complex materials.

In summary, CAD-design of reactor geometries, 3D-printing, digital control of the process and flow chemistry are important assets in the future of the chemical industry. We believed that the works developed during the present thesis contribute to the progress toward more sustainable syntheses, albeit further research is required. Indeed, some of the ideas here presented are being currently explored in work lines of the Materials for Advanced Sustainable Production group, with more advancements coming in the future.